Thèse n° 9331

Dielectric metasurfaces and their applications for optical biosensing

Présentée le 17 mai 2023

Faculté des sciences et techniques de l’ingénieur
Laboratoire de systèmes bionanophotoniques
Programme doctoral en microsystèmes et microélectronique

pour l’obtention du grade de Docteur ès Sciences

par

Yasaman JAHANI

Acceptée sur proposition du jury

Prof. H. Shea, président du jury
Prof. H. Altug, directrice de thèse
Prof. J. F. V. Vaz, rapporteur
Prof. J.-S. Yeo, rapporteur
Prof. C. Guiducci, rapporteuse

École
polytechnique
fédérale
de Lausanne

2023

Dedication

This dissertation is dedicated to the memory of 70 children who perished in Iran when I was working on this text. To Mona Naghib, an eight years old girl whose tiny heart and big hopes were lost to a bullet on the way back from school. To Kian Pirfalak, a ten years old boy, and the creative popsicle boat he made for the science fair, who did not get a chance to fulfill his dream of becoming an inventor.

Acknowledgments

It is with the utmost modesty and gratitude that I acknowledge the invaluable contributions of those who have supported me in the completion of my doctoral dissertation. I am deeply honored to have had the esteemed Prof. Hatice Altug as my advisor, and I extend my sincerest gratitude for her guidance, trust, and unwavering support throughout my years at EPFL. I extend cordial appreciation to the esteemed members of my thesis jury, Prof. José Filipe Vilela Vaz, Prof. Jong-Souk Yeo, Prof. Carlotta Guiducci, and Prof. Herbert Shea, for their kind acceptance of my invitation to serve as my examiners. I am grateful to EPFL, my doctoral program (EDMI), and the Center of MicroNanoTechnology (CMi) for providing a thoughtful multidisciplinary program, excellent state-of-the-art infrastructure, and invaluable support throughout my studies. I would like to express my appreciation to Lucie Auberson, EDMI's administrative assistant, for her kindness, accountability, and beautiful smile, and to Rosana Blanchard, our lab's (BIOS) administrative assistant, for her attentive help and kind availability.

I am deeply grateful to my current and previous colleagues, including Abtin, Saeid, Kosmas, Jihye, Ming, Felix, Clementine, Andreas, Peter, Yeng-Chen, Dordaneh, Maria, Deepthy, Aurelian, and many others in BIOS, for their undeniable contributions to both my academic and personal growth. My warmest appreciation goes to Filiz, a greatly supportive and passionate master's thesis supervisor, colleague, and dear friend. I am also most thankful to another dear friend and colleague, Eduardo, for his ingenious scientific contributions, as well as for his kind and generous spirit that undoubtedly made our lab a better place. I am grateful to all the bachelor and master students, Sara, Kenza, Teodora, Andrea, Shayan, Samuel, Yash, and others, with whom I had the opportunity to practice my training and supervisory skills, for their assistance. I would like to take this opportunity to thank my colleagues and friends in the EPFL photonics chapter (EPC), particularly Furkan, Marie, Nathan, Jorge, and Bingxin.

Indubitably, my days in Switzerland would not have been as delightful as they were without the companionship of my amazing friends, Mina, Rachel, John, baby Ilona, Marco, Amin, Hossein, Fereshteh, Amirhossein, Feresheteh, Shima, Yuji, Dorian, Ramin, Elmira, Saleh, Bahram, Mahsa, Notash, Hoda, Laya, Hesam, Elias, Lucas, Julie, and many others whom I might have unintentionally omitted from this list. I am deeply grateful for the friendship of each and every one of them. I would like to express my sincerest gratitude to Foozieh, my very kind and smart best friend of all time, whose unwavering support and presence undoubtedly made my days brighter and more enjoyable. Their friendship and support have been a constant source of joy and inspiration throughout my time in Switzerland.

My deepest, warmest, and most sincere gratitude goes to my parents, who have taught me the true meaning of love, support, and dedication. They are the reason for who I am today, and I owe everything to them. They not only nurtured my mind and encouraged me to think critically but also instilled in me an adventurous spirit that has led me to explore the world and seek new opportunities. They have always been there to support me through every step of my journey, showering me with love and care and always putting my happiness and success as their top priority. They gave me wings to fly, and for that, I am forever grateful. Their unwavering love and support have been a constant source of strength and motivation throughout my life, and I will always be grateful to them.

My gratitude towards my brother, Mehrad, is eternal. He has been a constant source of care, guidance, and friendship throughout my life. He is truly my most precious treasure; his unwavering love and support have been the main fuel for my motivation. He has always gone above and beyond for my happiness and well-being, always being there for me, even when I have been studying abroad for the past eight years. Hearing his voice over the phone has been one of the brightest parts of my life. He has been the source of my joy, the reason for my loud and joyous chuckles, and he is the smartest, kindest, and funniest being I have ever known. He has the biggest heart, and I am blessed to have him as my brother. He is truly a gem in my life, and I am deeply grateful for everything he has done for me.

I am truly blessed to have Ehsan by my side throughout my Ph.D. studies. He has been a constant source of encouragement, comfort, and support throughout the entire journey. He has been the most patient, kind, and understanding person that I have ever known, always putting my needs and well-being first. I could always rely on him for anything. He has been the light in my darkest days, the rock in my toughest moments, and the driving force behind my success. His unwavering devotion and contributions are immeasurable, and I am deeply grateful for everything he has done for me. I love him to the moon and back, and I am extremely lucky to have him in my life.

Lausanne, 16 January 2023

Abstract

Over the past century, our understanding of life has been focused on its most fundamental building blocks: molecules. Biological molecules, such as proteins found in blood, other body fluids, or tissues, are excellent guides to identifying a normal or abnormal process, condition, or disease. Nonetheless, their minuscule scale presents challenges in accurately quantifying protein molecules. Photonic biosensors provide a convenient method for probing analytes using light. Nanophotonics, the study of light's interaction with nanoscale structures, has emerged as a promising platform to tightly confine the light and overcome the scale barrier between minuscule biomarkers and electromagnetic fields.

Metasurfaces have recently garnered considerable attention as an auspicious platform for biosensing applications. These two-dimensional engineered structures or artificial electromagnetic media are made of unit cells much smaller than their operating wavelength. High-index dielectric nanostructures are excellent candidates because of their ability to confine and scatter light strongly with relatively low absorption losses. Due to their unique optical characteristics, dielectric metasurfaces can realize sharp resonances that are highly sensitive to the minute changes of refractive index in the vicinity of the nanoresonators, making them favorable for label-free refractometric sensing and providing reliable quantitative information.

This doctoral thesis aims to demonstrate state-of-the-art metasurface technology for imaging-based refractometric biosensing in both end-point and real-time modalities and investigate dielectric metasurface resonance features and design parameters for optimal functionalities.

Novel applications of high-quality-factor (high-Q) dielectric metasurfaces supporting modes rooted in the physics of bound-states-in-the-continuum are exploited. The high-Q metasurface sensors coupled with an imaging-based optical setup and advanced data processing methods have enabled the construction of an end-point sensing platform with superior sensitivity. Our hyperspectral imaging setup provides spectral information from the sensing area with pixel resolution, which, combined with advanced data processing methods, allows for detecting highly diluted samples.

Additionally, a real-time imaging-based biosensor employing an optofluidic chip comprising high-Q dielectric metasurfaces and microfluidics has been demonstrated. The method implements an aided imaging approach based on novel data processing to extract spectral shift information from time-resolved single-wavelength intensity images for highly reliable performance. This approach is suitable for multiplexed detection of biomarkers in real-time for high-throughput monitoring. As a proof-of-concept, we performed real-time in-flow experiments using the optofluidic device to detect extracellular vesicles secreted from breast-cancer tumors with clinically relevant results.

The developed sensing devices rely on a wide range of engineering technologies. Innovative biosensing platforms have been presented by incorporating dielectric metasurfaces with imaging, microfluidics, micro- and nano-fabrication techniques, and novel data processing strategies. These methods hold great promise to overcome the challenges of biomedical diagnostics and pave the way for futuristic point-of-care devices enabling early diagnosis, treatment monitoring, personalized medicine, and democratized healthcare systems.

Keywords

Metasurfaces, Metamaterials, Refractometric sensing, Nanophotonics, Biosensing, Nanofabrication, Label-free biosensor, Hyperspectral imaging, Real-time biosensor, Microfluidics, Estimated spectral shift, Dielectric metasurfaces.

Résumé

Pendant le siècle dernier, notre compréhension du vivant s'est focalisée sur ses éléments constitutifs : les molécules. Les molécules biologiques, comme les protéines présentes dans les fluides corporels, sont d'excellents indicateurs d'une anomalie ou d'une maladie. Cependant, leur échelle minuscule rend difficile leur comptage précise. Les biocapteurs photoniques offrent une méthode réalisable pour sonder les analytes par la lumière. La nanophotonique est apparue comme une plateforme prometteuse pour confiner la lumière et surmonter la barrière d'échelle entre les biomarqueurs et les champs électromagnétiques.

Les métasurfaces ont suscité une attention considérable comme plateforme propice aux applications de biodétection. Les métasurfaces sont des structures bidimensionnelles constituées de cellules unitaires beaucoup plus petites que leur longueur d'onde de fonctionnement. Les nanostructures diélectriques à haut indice sont d'excellents candidats en raison de leur capacité à confiner la lumière avec des pertes d'absorption faibles. Grâce à leurs caractéristiques optiques, les métasurfaces diélectriques peuvent réaliser des résonances aiguës hautement sensibles aux changements infimes de l'indice de réfraction à proximité des nanorésonateurs, propices à une détection réfractométrique sans marqueur.

Cette thèse vise, d'une part, à démontrer l'état de l'art de la technologie des métasurfaces pour la biodétection réfractométrique basée sur l'imagerie et, d'autre part, à étudier les caractéristiques de résonance des métasurfaces diélectriques et les paramètres de conception pour des fonctionnalités optimales.

Nous présentons de nouvelles applications de métasurfaces diélectriques à facteur de qualité (Q) élevé supportant des modes associés à la physique des états liés dans le continuum. Grâce aux capteurs à métasurfaces à Q élevé, couplés à une configuration optique basée sur l'imagerie et à des méthodes avancées de traitement des données, nous avons construit une plateforme de détection de "end-point" avec une sensibilité supérieure. Notre configuration d'imagerie hyperspectrale fournit des informations spectrales de la zone de détection avec une résolution en pixels , ce qui, combiné à des méthodes avancées de traitement des données, permet de détecter des échantillons hautement dilués.

De plus, nous avons réalisé un biocapteur basé sur l'imagerie en temps réel qui utilise une puce optofluidique comprenant des métasurfaces diélectriques à Q élevé et des microfluides. Notre méthode utilise une approche d'imagerie assistée pour extraire les informations de décalage spectral à partir d'images à résolution temporelle et à longueur d'onde unique, ce qui permet d'obtenir des performances très fiables. Cette approche est adaptée au multiplexage pour un suivi en temps réel à haut débit. Comme preuve de concept, nous avons réalisé des expériences d'écoulement en temps réel en utilisant le dispositif optofluidique pour détecter les biomarqueurs du cancer du sein avec des résultats cliniquement pertinents.

En conclusion, nous avons présenté des plateformes de biodétection innovantes en incorporant des métasurfaces diélectriques avec des techniques d'imagerie, de microfluidique, de nanofabrication, et de nouvelles stratégies de traitement des données. Nos méthodes ouvrent la voie à des appareils futuristes permettant un diagnostic anticipé, un suivi du traitement, une médecine personnalisée et un système de santé démocratisé.

Mots-clés

Métasurfaces, métamatériaux, détection réfractomètrique, nanophotonique, biodétection, nanofabrication, biocapteur sans étiquette, imagerie hyperspectrale, biocapteur en temps réel, microfluidique, décalage spectral estimé, métasurfaces diélectriques.

Contents

Dedication .... **i**

Acknowledgments .... **ii**

Abstract .... **iv**

Keywords .... **v**

Résumé .... **vi**

Mots-clés .... **vii**

Contents .... **ix**

List of Figures .... **xi**

List of Tables .... **xxv**

List of Equations .... **xxvi**

Chapter 1 Introduction **27**

- 1.1 Metasurfaces for biosensing 33
  - 1.1.1 Plasmonic metasurfaces for biosensing 35
  - 1.1.2 Dielectric metasurfaces for biosensing 39
- 1.2 Underlying key technologies in developing nanophotonic biosensors 44
  - 1.2.1 Nanofabrication techniques 44
  - 1.2.2 Surface functionalization methodologies 48
  - 1.2.3 Optical interrogation strategies 51
- 1.3 Thesis outline 54

Chapter 2 Dielectric metasurface-based optical biosensors **56**

- 2.1 Surface Enhanced Spectroscopy 56
- 2.2 Chiral Sensing 59
- 2.3 Refractometric Biosensing 62

Chapter 3Ultrasensitive hyperspectral imaging and biodetection enabled by dielectric metasurfaces **66**

3.1 Abstract ... 66

3.2 Main ... 66

3.3 Methods ... 75

3.4 Supplementary information ... 80

Chapter 4 Imaging-based spectrometer-less optofluidic biosensors based on dielectric metasurfaces for detecting extracellular vesicles ... 87

4.1 Abstract ... 87

4.2 Introduction ... 88

4.3 Results ... 90

4.4 Discussion ... 98

4.5 Methods ... 99

4.6 Supplementary information ... 103

Chapter 5 Investigating the resonance characteristics of symmetry-broken dielectric metasurface supporting quasi-BIC modes ... 111

5.1 Numerical and experimental analysis of the asymmetry parameter effect ... 115

5.2 Experimental analysis of the effects of finite sensor dimension ... 119

5.3 Analysis of the effects of illumination angle ... 121

5.3.1 Hyperspectral analysis of illumination angle effect for end-point measurements ... 121

5.3.2 Utilizing the tilt angle towards ultrasensitive handheld imaging-based fluidic biosensors ... 123

Chapter 6 Conclusion ... 125

6.1 The achieved results summary ... 125

6.2 Future development of dielectric metasurfaces for biosensing applications ... 128

References ... 130

Curriculum Vitae ... 145

List of Figures

Figure 1-1 Biosensors could be used in pathogen discovery, drug development, disease detection, and monitoring, food, water, and soil quality assessment, environmental monitoring, and toxin detection. Reproduced with permission from reference [19]. 28

Figure 1-2 Components of a biosensor. Bioreceptors interact with the analyte, a transducer to translate the binding events to a measurable signal, and a detector to record the data for analysis. There are a variety of targets that can be detected by biosensors, including pathogens, biomolecules, and toxins in food, soil, and medical samples. These analytes interact with a biorecognition element such as nucleic acids, antibodies, viruses, or enzymes resulting in a measurable signal transduced via an electrochemical, piezoelectric, or optical system to be recorded and further processed. Reproduced from the open-access article in reference [39]. 30

Figure 1-3 Some optical platforms leverage the evanescent field at the biosensor's surface to enhance light-matter interactions. Resonant microcavities, surface plasmon resonance (SPR), and optical waveguide interferometry are among such sensors. Reproduced with the authors' permission from reference [46]. 32

Figure 1-4 Dielectric particles sustain Mie resonances. A dielectric metasurface is formed by putting together nanoantennas in 2D arrays. It is possible to tailor the unit cell of metasurfaces to provide a variety of functional properties. Reproduced with permission from reference [47]... 33

Figure 1-5 Metasurfaces for biosensing applications. Reproduced with permission from reference [2]. Copyright 2021 American Chemical Society 34

Figure 1-6 Schematic representation of plasmonic metamaterials a) Represents two possible meta-unit of meta-systems: a meta-atom including a plasmonic nanorod and a meta-unit of four split-ring nanoresonators. b-d) Represents a 1D chain (b), a 2D metasurface (c), and a 3D metamaterial made from plasmonic meta-atoms (d). Reproduced with permission from reference [48]. 35

Figure 1-7 (a) Shows the coherent oscillation of gold film's surface conduction electrons to sustain surface plasmon resonance (SPR). (b) Shows gold nanoparticles constraining the oscillations and the resulting electric field to a sub-wavelength dimension leading to the excitation of a localized surface plasmon resonance (LSPR). Reproduced with permission from reference [84]. 36

Figure 1-8 (a) Schematically represents surface plasmon resonance (SPR). The measurement setup is in the Kretschmann configuration. The local changes of refractive index at the surface of the gold thin-film cause shift in the angle of minimum reflected intensity. (b) Schematically represents localized surface plasmon resonance (LSPR). The analyte binding to the nanoparticles induces a shift in the extinction spectrum (c) Schematically represents extraordinary optical transmission through gold nanohole arrays. The analyte binding induces local refractive index changes translated into a shift in the transmission spectrum. Reproduced with permission from reference[83]. 36

Figure 1-9 An overview of plasmonic metasurfaces for biosensing applications. The central pictures are the schematics of typical plasmonic sensing structures. The physical mechanisms are shown on the right, and exemplary analytes are shown on the left side of the diagram. Reproduced from the open-access article in reference [86]. 38

Figure 1-10 Mie resonances in high-index dielectric nanostructures. (a) Schematics of an electric dipole and magnetic dipole induced in a spherical dielectric nanoparticle. The red and blue arrows indicate the direction of the induced magnetic and electric field inside the nanoparticle, respectively. (b) Transmission spectrum and the resonance modes of a 150 nm Si spherical nanoparticle. (c) Dark-field microscopic image of Si nanoparticles on a Si substrate produced by using femtosecond laser ablation [88]. Inset: SEM image of the Si nanoparticles highlighted in the dashed squares. Scale bar of the insets: 200 nm. (a) and (b) are adapted with permission from reference [2] Copyright 2021 American Chemical Society. (c) is reproduced with permission from reference [88]. Copyright 2012 Nature Publishing Group. 40

Figure 1-11 Examples of high-Q dielectric metasurfaces. (a) Fano-resonant metasurface [99]. Left panel: SEM image of the metasurface consisting of Si bars and disks. Insert: the electric field pattern at the resonance wavelength. Right panel: simulation (purple curve) and experiment (red) transmission spectrum of the metasurface. (b) Anapole metasurface [102]. Left panel: SEM image of the metasurface consisting of TiO_2 disks. Insert: the electric field pattern at the resonance wavelength. Right panel: Transmission spectrum of the metasurface. (c) Quasi-BIC metasurfaces with different symmetry breakings [103]. Top panel: Schematic of the metasurface consisting of asymmetric Si asymmetric nanoellipse pairs. Middle panel: Dependence of the transmission spectra versus the rotational angle θ (indicated in the top panel). Bottom panel: Comparison of the electric field patterns for the BIC and quasi-BIC mode, respectively. (d) Ultrahigh-Q factor quasi-

BIC metasurface [104]. Left panel: SEM image of the metasurface consisting of Si nanoresonators. Insert on the top: the electric field pattern at the resonance wavelength. Right panel: Transmission spectra of the metasurfaces with the different cut-out size S. The Q factor of the metasurface is highly sensitive to S. The polarization of the excitation for the metasurfaces shown in this figure is along the x-axis shown in (d). (a) is reproduced with permission from reference [99]. Copyright 2015 ACS. (b) is reproduced with permission from reference [102]. Copyright 2019 ACS. (c) is reproduced with permission from reference [103]. Copyright 2018 APS. (d) is reproduced with permission from reference [104]. Copyright 2017 APS. 42

Figure 1-12 Top-down and bottom-up nanofabrication methods. Top-down nanofabrication starts with a bulk material breaking into smaller fragments and nanostructures. Bottom-up nanofabrication involves putting together attoms to form clusters and nanoscale structures. Reproduced from the open-access article in reference [118]. 45

Figure 1-13 The schematic of photolithography tools. The photomask can be (a) in contact with, (b) in proximity of, and (c) within a distance of the photoresist layer. The third configuration has additional projection optics allowing exposures with factors smaller than the photomask feature based on the magnification of the optical system. Reproduced with permission from reference [117]. 46

Figure 1-14 Two categories of etching directionality. (a) Shows the isotropic etching where the reaction occurs in multiple directions within the substrate leading to an undercut. (b) Shows an anisotropic etching that is highly directional and can make straight walls in the substrate. 47

Figure 1-15 Surface biofunctionalization strategies. (a) Physisorption (b) Chemisorption, and (c) self-assembled monolayers. The red Y-shape molecules represent antibodies. 49

Figure 1-16 The most frequently used molecules for the silanization process to form a self-assembled monolayer on the silica surface, 3-glycidyloxypropyl trimethoxysilane (GPTMS or 3-GPS) and 3-Aminopropyl triethoxysilane (APTES). Reproduced with permission from reference [126] 49

Figure 1-17 Schematic representation of analyte bindings to the pre-functionalized resonators. 51

Figure 1-18 Fundamental interrogation techniques. Schematically represents (a) spectral, (b) intensity and (c) phase interrogation. Reproduced from the open-access article in reference [129]. 51

Figure 2-1 Dielectric metasurfaces for surface-enhanced spectroscopy. (a) Left panel: Electric field enhancement in a Si dimer structure and the temperature dependence on the laser intensity [164]. Right panel: SEM images of Si dimers where the scale bar on the bottom micrographs is 100 nm. (b) SERS signal of β-carotenal monolayer using Si dimer metasurfaces [165]. (c) SERS enhancement of crystal violet molecules using high Q-factor nanohole metasurfaces [166]. (d) Top panel: Illustration of pixelated metasurface and unit cell coated with protein molecules. Bottom panel: Measurements of high Q-factor metasurface response after protein monolayer deposition and imaging-based molecular fingerprint detection [168], [169]. (e) Top panel: unit cell of a Ge metasurface and the spectral response for each light incidence angle. Bottom panel: spectral integration signal that emulates the total reflectance signal and the measured absorbance signals from polylysine, ssDNA aptamers, and ODAM proteins [170]. (a) is reproduced with permission from reference [164]. Copyright 2015 Nature Publishing Group. (b) is reproduced with permission from reference [165]. Copyright 2018 ACS. (c) is reproduced with permission from reference [166]. Copyright 2018 ACS. (d) is reproduced with permission from reference [168], [169]. Copyright 2018 AAAS and the authors. (e) is reproduced with permission from reference [170]. Copyright 2019 AAAS....................................... 58

Figure 2-2 Chiral sensing using dielectric metasurfaces. (a) Left panel: A side-view SEM image of Si nanodisks covered with a dense 200 nm thick phenylalanine film [180]. Right panel: CD signals differentiating molecular enantiomers of phenylalanine using Si nanodisks [180]. (b) Schematic of generating a superchiral field using the electromagnetic duality principle [181]. (c) Schematic of a-Si disk nanostructure with a hole for Kerker-inspired optical chirality enhancement [181]. The plot on the right shows normalized differential transmission from numerical and analytical studies [181]. (d) A dielectric metasurface for chiral field enhancement, based on the asymmetric diamond disk array, capable of boosting the near-field in the UV spectrum [182]. The bottom plot shows its optical chirality enhancement. (e) Asymmetric PbTe bars proposed for VCD measurements by optical chirality intensification [183]. The plot on the right depicts the local optical chirality enhancement. (a) is reproduced with permission from reference [180]. Copyright 2020 ACS. (b) and (c) are reproduced with permission from reference [181]. Copyright 2019 ACS. (d) is reproduced with permission from reference [182].

Copyright 2019 ACS. (e) is reproduced with permission from reference [183]. Copyright 2019 the authors. 61

Figure 2-3 Refractometric biosensing metasurfaces. (a) Picture of a multichannel microfluidic chip (left) with a close-up picture of the eight flow channels showing multiple sensors (middle) and an SEM image of a Si nanodisk metasurface (right) [131]. (b) Schematic of a sandwich bioassay on a Si nanodisk.[184] (c) Extinction spectra of a nanodisk array exposed to six different glucose water mixtures [131]. (d) Normalized calibration curve of the centroid shifts for PSA detection with Si nanodisks and gold nanorods using a sandwich immunoassay for signal amplification. Error bars represent the replicas of the measurement on the same chip. The inset illustrates the extinction spectra of the Si nanodisk arrays and gold nanorod arrays [131]. (e) Calibration curve of the centroid shifts for PSA detection with semi-random Si nanocylinders [184]. (f) Principle of hyperspectral imaging-based biosensing using tilted Si nanoellipses [12]. (g) SEM images of the tilted nanoellipse metasurface (top) and its unit cell (bottom) [12]. (h) The area under the curve (AUC) values of all receiver operating characteristic (ROC) curves show the detection of biomolecules at low concentrations [12]. (i) Resonance shift map for a control measurement, detection of two low concentrations of IgG molecules, and a high concentration of the biomolecule from left to right, respectively [12]. (a), (c), (d) are reproduced with permission from reference [131]. Copyright 2017 ACS. (b) and (e) are reproduced with permission from reference [184]. Copyright 2019 ACS. (f)-(i) are reproduced with permission from reference [12]. Copyright 2019 Nature Publishing Group. 63

Figure 3-1 Principle of hyperspectral imaging-based biomolecule detection using all-dielectric metasurfaces. (a) Sketch of the hyperspectral imaging principle showing a representative dielectric metasurface sensor array illuminated with narrow-band tunable laser source. At each wavelength illumination, images are recorded by a CMOS camera (1,608 × 1,608 pixels) to create a hyperspectral data cube where each CMOS pixel captures high-resolution spectral information. (b) The hyperspectral data cube is processed to extract spatial resonance maps of each individual sensor. For biomolecule detection, the sensing and reference resonance maps are combined to create the resonance shift map, which conveys spectral shift information across the whole sensor. 68

Figure 3-2 Geometrically tunable high-Q dielectric metasurfaces based on quasi-BIC modes. (a),(b) SEM images of the dielectric meta-unit (a) and the metasurface (b). (c) Photograph of a dielectric chip with a 5 × 5 sensor array. (d) Top-view schematic and rendered image of the meta-unit composed of two elliptical dielectric nanoresonators positioned in a mirror symmetry across the major vertical axis, where Wo = 100 nm, Lo = 280 nm, H = 100 nm and θ = 17.5°. Parameter α is used to tune the resonance wavelength (Figure 3-9). (e), Schematic of light scattered by the metasurface. (f), distribution of electric and magnetic fields in the meta-unit showing both BIC and quasi BIC modes. (g) Transmission spectra extracted from the hyperspectral data cube from a single CMOS pixel sampled from sensor regions (~0.5 µm^2) fabricated using three different scaling parameters (n_M = 1.47). The spectra exhibit narrow and spectrally isolated resonance dips in the NIR.(h), Spectral linewidth of the resonance dip measured in the presence of top media with different refractive indices (n_M = 1-1.47), indicating Q-factors as high as 144. The error bars represent the standard deviation of FWHM measurements of 2.5 × 105 pixel spectra acquired from four different sensors. 69

Figure 3-3 Biosensing using dielectric metasurface sensors and image-based data processing. (a) Rendered schematic showing controlled biomolecule delivery to the sensor surface using low-volume (~200 pl) droplets for microarray-based detection.(b) Schematic of the bioassay, in which epoxy-silane-based covalent chemistry is used for biomolecule immobilization.(c) Image of a representative 2 × 2 sensor array showing analyte molecules dispensed using different-volume droplets and a control sensor without analyte molecules.(d) A traditional calibration curve correlating the ensemble-averaged resonance shift from binding spots to the average number of analyte molecules per area (molecules per µm^2). Note that the large standard deviation in the high-concentration regime is caused by the coffee ring effect. (e) Area under the curve (AUC) values of all receiver operating characteristic (ROC) curves. Control measurements revealed an AUC value of 0.5008 ± 0.0291 (N = 68) and the baseline was set at 0.5881. This approach shows that the detection of biomolecules at low concentrations can be achieved, in contrast to traditional ensemble averaging. (f) ROC curve of a sample data set. (g) Resonance shift maps of a sample set from the data presented in (d)-(f). For additional resonance shift maps at low molecule densities, see Figure 3-14. 71

Figure 3-4 Resonance map of the MRS (a), designed according to the scaling parameters in (b), recorded by 275 × 275 CMOS pixels. The distribution of resonance wavelengths within a sensor has a 20 nm spectral range.(c), Resonance vector made by stacking the resonance map column-wise. (d), Sorted resonance vector and its associated index decoder. (e), Intensity images of the MRS recorded at a single excitation wavelength (824 nm) with a top medium of water, 5% glycerol and 10% glycerol. (f), Sensing barcodes created by stacking the individual pixel intensity values from the images in(e). (g),(h), Intensity vectors sorted using the index decoder in (d). (g) resulting in the pseudo-spectra shown in (h), where the difference in the wavelength of pixels that resonate at 824 nm corresponds to the spectral shift associated with the change in the refractive index of the top medium.. 73

Figure 3-5 (a) Rendered representative image of SLG covering dielectric nanoresonators. (b), Hyperspectrally measured and numerically calculated transmission spectra before and after SLG transfer on the bare sensor, extracted from a sub-sensor region. The resonance dip redshifts spectrally and broadens due to graphene's optical properties in the NIR (n = 2.69, k = 1.52) based on both simulation and experiment. (c),(d), Large-area (~3.3 mm^2) image of a sensor array partially covered with a sheet of SLG, the edges of which are marked by white dashed lines (c) and its corresponding resonance shift map extracted from the hyperspectral data cubes before and after SLG transfer (d). (e), Intensity images of the MRS recorded at single excitation wavelength (758 nm) before and after SLG transfer and corresponding sensing barcodes. (f), Index decoder computed from the hyperspectral data cube collected from the bare sensor. (g), The index decoder is used to sort the sensing barcodes in e, resulting in the shown plots. The spectral shift due to SLG is equivalent to the difference in the wavelengths of pixels that resonate at 758 nm. 75

Figure 3-6 Dielectric metasurface fabrication flow chart: (a) LPCVD amorphous silicon deposition (100 nm) on fused silica substrate (b) Double layer PMMA 495K bottom (60 nm) and 950K top (40 nm) (c) EBL exposure and development (d) Aluminum hard mask evaporation (30 nm) (e) Metal lift-off in solvent (f) Dry Si etch (g) Hard mask removal by Al wet etch 80

Figure 3-7 The effect of structural imperfections on the Q-factor. (a) As the tilting angle increases, the FWHM and the resonance suppression efficiency increase. We chose to work at 17.5 degrees as it gives sufficient suppression (>90%) at low FWHM (11 nm). (b) Representative resonance curves at tilting angles of 5 and 17.5 degrees. (c) The effect of the size mismatch between the resonators in a meta-unit showing an increase in the FWHM as the mismatch ratio increases. (d) The effect of tilting angle mismatch between the resonators in a meta-unit, showing the FWHM increase as the angle mismatch increases. The inset shows the measured dispersion curve of amorphous silicon used to fabricate our chips In all the full-wave simulations presented in this work this dispersion curve was used. 80

Figure 3-8 Electric field and intensity enhancement distributions in a meta-unit obtained by full-wave simulation (b) Electric field intensity localization away from the hotspot over a distance d (indicated in Figure 3-8a bottom). (c) Measured bulk refractive index sensitivity of all-dielectric metasurface using hyperspectral imaging method. 81

Figure 3-9 Simulation of the dependence of the resonance wavelength on the tuning parameter a from 0.9 to 1.1, where Wo= 100 nm, Lo =280 nm for a fixed height and angle of H = 100 nm, and θ = 17.5° 81

Figure 3-10 Comparison of spectral characteristics of all-dielectric metasurface extracted from the hyperspectral data cube with ones that are measured with a conventional spectrometer. (a) Transmission spectra measured using a spectrometer. Four regions on a multi-resonant sensor are acquired from a spectral image associated to the narrow slit of the spectrometer. (b) Transmission spectra extracted from hyperspectral data cube associated to analogous regions as in (a). (c) Transmission spectra extracted from hyperspectral data cube associated to a single representative pixel. 82

Figure 3-11 The effect of Q-factor on the estimation of resonance shift. (a) A small and a large full-width-at-half-maximum (FWHM) resonances with the same noise parameters shown with identical resonance shifts of 0.5 nm. (b) Monte Carlo simulation results indicating the increase in the resonance estimation error ($\lambda Res - \lambda Res$, where λRes is the estimate of λRes) as the FWHM increases 82

Figure 3-12 (a) Step-by-step description of the bioassay, indicating non-specifically adsorbed molecules both on the control and the sample sensors. (b) Data processing of the resonance shift maps computed using the sensing and the reference measurements from a control sensor and two sample sensors with low and high areal molecular density. (c) Regions with equal areas are probed both on the spot and off the spot of the control and sample sensors, and the resonance shift values from these pixels are shown as histograms. The on and off the spots are indicated by blue and red boxes in (b) and with the corresponding colored histogram in (c). (d) ROC curves are computed by thresholding the histograms in (c). The thresholding/ROC method is able to accurately discriminate signals coming only from the specific binding of the analytes. 83

Figure 3-13 Simulation results showing the effect of individual IgG molecules binding to the hotspots of the resonators in a meta-unit. The parameters of IgG molecules used in the simulation are from [208], [209]. Due to the highly localized fields at the hotspots, few molecules can create measurable spectral shifts in the resonance position. We calculated 0.12 nm, 0.25 nm, 0.37 nm, and 0.49 nm shifts corresponding to 1 ,2 ,3, and 4 molecules binding, respectively. Moreover, a monolayer of IgG molecules is expected to create ~33 nm spectral shift. 84

Figure 3-14 (a) A representative subset of resonance shift maps of measurements with low detectable molecular concentrations of ~3molecules/µm^2. (b) Resonance shift maps of measurements with very low molecular concentrations of ~1 molecules/µm^2. (c) Summary of all the measurements, where the baseline corresponds to the mean of control measurements plus three times the standard deviation (d) the area under the ROC curve metric illustrated for a representative sample and control. (e) Histogram of the AUC values of control measurements. 84

Figure 3-15 (a) Resonance map array of multi-resonance sensors computed using a single hyperspectral data cube acquired in air medium. The 2x2 mm^2 field-of-view allows for high-throughput spectral data acquisition. (b) Resonance map of a representative multi-resonance sensor in water medium. The multi-resonance sensor was fabricated using four different scaling parameters, as shown in (c). (d) Hyperspectral imaging-based refractometric sensing. The top row shows measured resonance maps of a multi-resonance sensor with different glycerol concentrations of top media. The bottom row shows the resonance shift maps when each measurement is referenced to that of water, indicating bulk sensitivity of 263 nm/RIU, independent of the scaling parameter 85

Figure 3-16 Histogram of 75625 pixels from the resonance map of a multi-resonance sensor, with a bin width of 0.05 nm. The resonance wavelengths are densely distributed in a 20 nm spectral range... 85

Figure 3-17 Raman spectroscopy of the transferred graphene measured at the excitation wavelengths of 532 nm and 785 nm (a) on the metasurface dielectric sensors and (b) off the sensor, on the glass. 86

Figure 4-1 (a) Sketch of a real-time in-flow imaging platform showing a 2D microarray of all-dielectric sensors integrated with a microfluidic cell consisting of three independent flow channels. The metasurface chip is illuminated with a single-wavelength light source and imaged with a large-area CMOS camera to acquire intensity maps of the sensors in pixel resolution (I_1, I_2, …, I_{N+1}, I_{N+2},…). (b) Biomarker binding induces a red-shift in the transmission spectrum ($\Delta\lambda$), which can be detected by tracking the resonance wavelength or by the intensity change (ΔI) at a fixed probing wavelength (λp). ΔI can be approximated as linearly proportional to $\Delta\lambda$ with a constant of α, which is the slope of the transmission spectrum in the linear region near λp . (c) Pictorial representation of time-resolved single-wavelength intensity images. (d) The illustration represents the shortcomings of the basic imaging approach. Time-resolved intensity data from single pixels (A, B, and C) from the sensor area give contradicting responses with noisy signals (red, orange, and pink curves) due to the nonuniformities. Ensemble averaging of the responses from multiple pixels can help to decrease the noise, although it may reduce the final signal, as depicted with the green curve. (e) The illustration represents the implementation and the advantages of our aided imaging approach. By leveraging the optimal linear estimator algorithm and the spectral decoder that incorporates the 2D map of the slope values, time-resolved single-wavelength intensity images are used to reconstruct robust spectral shift ($\Delta\lambda$) information dynamically (purple curve)... 91

Figure 4-2 (a) Scanning electron microscopy (SEM) image of the fabricated dielectric metasurface. To prevent charging while taking SEM images, we applied a thin layer of Electra, a carbon-based conductive polymer. (b), (c) Distributions of electric and magnetic fields, respectively, in four neighboring meta-units from numerical calculations. (d) A region of interest from an intensity image obtained at the resonance wavelength of the integrated optofluidic chip showing 3 × 4 all-dielectric metasurface sensors and borders of the three Polydimethylsiloxane (PDMS) flow channels. (e) Experimentally acquired transmission spectrum of the fabricated dielectric metasurfaces in y-polarization. (f) Top and side-views schematic of the meta-unit composed of an elliptical (long and short axis 180 nm and 100 nm respectively) and a cylindrical (90 nm in radius) a-Si resonators. 92

Figure 4-3 (a) Time-resolved intensity data is fed to the optimal linear estimation algorithm with a spectral decoder, which is the two-dimensional (2D) map of the slope (α) of the transmission spectrum for each CMOS pixel at the probing wavelength (λp). (b) At λp $_p$ = 808.8 nm, the histogram of α values from a single sensor is populated mostly with negative values because, for the majority of the pixels, the resonance is probed at the left flank of the transmission dip (top panel). This case represents a sensor having a relatively homogenous optical response across its surface. For experimental bulk sensing, under a constant running of phosphate buffer saline (PBS) 1x (n = 1.33441), three sensors are exposed to a varying medium with PBS 2x (n = 1.33584) and PBS 3x (n = 1.33731) and their ensemble-averaged intensity changes (ΔI, middle panel) and reconstructed spectral shifts ($\Delta\lambda$, bottom panel) are presented as a function of time. (c) At λp = 811.3 nm, the histogram of the same sensor has a similar number of positive and negative α values (top panel). This case represents a sensor having an inhomogeneous optical response. For the same bulk sensing experiment used in Figure 4-3b, the ensemble-averaged ΔI response of different sensors shows significantly varying signals (middle panel). In contrast, the reconstructed spectral shift data obtained by aided imaging (bottom panel) is consistent between the three sensors. 95

Figure 4-4 (a)The reconstructed spectral shift ($\Delta\lambda$) calibration curve of biotinylated silica nanoparticles (100 nm diameter). The insets are scanning electron microscopy images of the sensors with bound silica nanoparticles on resonators after introducing suspensions with 1.9×10^{8} nanoparticles/mL and 9.5×10^{12} nanoparticles/mL from left to right, respectively. The represented data points in the calibration curves (a), (c) are the mean $\Delta\lambda$ over time from each sensor over a time-interval consisting of 81 consecutive images after the analyte binding reaches the equilibrium state, and the error bars indicate the standard deviations. The reconstructed $\Delta\lambda$ data points are obtained from seven dilutions of silica nanoparticle solutions over three independent sensors to achieve 21 data points on the calibration curve. The reconstructed $\Delta\lambda$ data from the detection sensors are corrected to the non-specific bindings on the control sensor. Some data points are overlapped due to the good agreement between the sensor performance. (b) Biorecognition assay to detect extracellular vesicles (EVs) on the detection sensors and on the control sensor blocked with bovine serum albumin (BSA) to account for non-specific binding is shown on top. (c) The reconstructed spectral shift calibration curve of EVs. The inset is the same plot with a magnified x-axis to better resolve the small error bars for an exemplary data point. The reconstructed shift data points from the detection sensors are corrected to the non-specific bindings on the control sensor. The represented data points are collected from nine different concentrations of EV solutions diluted from three independent batches measured on eight independent sensors to yield 24 data points on the calibration curve. Some data points are overlapped due to the good agreement between the sensors. (d) Transmission electron microscopy images of EVs from the cell culture supernatant of 4T1 mouse breast cancer cells can be seen at the bottom; the magnifications are ×23,000 and ×30,000 from left to the right, respectively. 96

Figure 4-5 Very sharp resonances cannot be resolved using a light source with a broader spectrum 104

Figure 4-6 The trade-offs involved in using higher and lower quality factor (Q) metasurfaces for sensing are shown graphically with representative curves. The narrowband illumination is chosen as a line (at a wavelength of λp probe) for a better illustration of the trade-offs. (a) and (b) show the influence of the Q value on the obtained intensity changes from the red-shifting of the resonance due to the analyte binding. (a) shows that a higher Q resonance (346) with the full-width at half-maximum (FWHM) of 2.4 nm exhibits a 53% intensity change when the resonance is red-shifted for 1 nm. On the other hand, (b) shows that a lower Q resonance (88) with the FWHM of 9.4 nm exhibits only a 14.83% intensity change for the same red-shift of 1 nm. (c) and (d) show the influence of the Q on the dynamic range of the sensor. Here, the dynamic range is chosen as the part of the resonance when the slope has less than 1% of deviation from the linear fit. (c) shows that as the higher Q resonance has smaller bandwidth, it leads to a smaller dynamic range. On the other hand, (d) shows that a lower Q resonance offers a larger dynamic range. 105

Figure 4-7 BICs in diatomic metasurfaces. (a) Different ways to introduce asymmetry for a diatomic metasurface: ellipticity, squeezing, rotation. (b) Dependence of the quasi-BIC quality factor (Q) on the asymmetry parameter of the meta-molecule. Purple squares and blue circles show the radiative and total Q, respectively. The black dashed lines show a fit to the inverse square law and the value of the non-radiative Q. (c) Characteristic evolution of the transmission spectra by changing the meta-molecule asymmetry. (d) Definition of the asymmetry parameter via ellipticity, squeezing, and rotation for the same diatomic metasurface. 107

Figure 4-8 Electric field enhancement in the vicinity of the resonators (a) Electric field enhancement demonstrated for a cluster of four neighboring unit cells. (b) Electric field enhancement along the y-axis of the elliptical (blue) and circular (green) disks. 108

Figure 4-9 Spectral characterizations of the nanofabricated metasurfaces using hyperspectral imaging setup across the sensor surface. (a) The extracted resonance map and (b) The histogram of the resonance wavelength distribution of a fabricated sensor indicate that the mean resonance wavelength of the sensor is 829.05 nm with a standard deviation of 0.97 nm. 109

Figure 4-10 Biorecognition assay to detect silica nanoparticles on the detection sensors and on the control sensor to account for non-specific binding. The control sensor is blocked with bovine serum albumin (BSA), while the detection sensors are functionalized with streptavidin. 110

Figure 5-1 Characteristic features of a resonance. The figure demonstrates schematics of a transmission or a reflection spectrum. The blue curve is a resonance peak, and the red curve is a resonance deep in the VIS-NIR wavelength range below 850 nm. The Resonance wavelength, resonance amplitude for a peak, the resonance suppression for a deep, the full-width-at-half-maximum (FWHM) of resonance, and the quality factor (Q) are illustrated. 112

Figure 5-2 The metasurfaces design geometry and dimensions. The unit cell consists of a disk (with a radius of 90 nm) and an ellipse (with the short and long axis of 50 nm and 90nm, respectively). In this case, the asymmetry parameter is α=0.44. The nanoresonators are 100 nm in height and are made from amorphous silicon placed on a fused silica substrate. Reproduced from the open-access article in reference [8].114

Figure 5-3 The metasurface unit cell and the definition of the asymmetry parameter for this metasurface design 115

Figure 5-4 Visualization of the effect of asymmetry parameter on the resonance features in simulation. (a) Shows the transmission spectrum of the diatomic design while the asymmetry parameter changes. The purple curve with $\alpha = 0.44$ is the transmission spectrum for the design when the changing resonator becomes a disk. (b) Shows the decrease of the quality factor when the asymmetry parameter increases. The fitted curve, illustrated in blue, neatly follows Equation 5-4. (c) Shows the dependence of the suppression on the asymmetry parameter. The green line is a fitted curve, and the Lorentzian approximation is plotted as a dashed red line.................................. 117

Figure 5-5 Visualization of the effect of asymmetry parameter on the resonance features in experiment. (a) Shows the transmission spectrum of the diatomic design while the asymmetry parameter changes. The purple curve with $\alpha = 0.44$ is the transmission spectrum for the design when the changing resonator becomes a disk. (b) Shows the decrease of the quality factor when the asymmetry parameter increases. The fitted curve, illustrated in blue, neatly follows Equation 5-4. (c) Shows the dependence of the suppression on the asymmetry parameter. The inherent nonuniformities strongly affect the suppression. 118

Figure 5-6 The size-dependent response of the metasurfaces. (a) Optical images of the sensors of various sizes surrounded with buffer zones for a fair comparison, mainly to eliminate the fabrication-induced alterations due to the change in the size. (b) The resonance wavelength versus the sensor size shows good stability and homogeneity for 10 µm and bigger sensor sizes. (c) The suppression versus the sensor size shows a decreasing trend in suppression and its homogeneity over the sensor area. (d) The full-width-at-half-maximum (FWHM) versus the sensor size shows a decreasing trend in suppression and its homogeneity over the sensor area. The red, green, and blue lines in a, b, and c, respectively, are the eye guides. 120

Figure 5-7 The effect of illumination angle on the resonance wavelength. (a) Shows the simulation data for the resonance wavelength shift when the illumination is tilted from zero to ±5 degrees. (b) Shows the experimental data for the resonance wavelength shift of 4 independent sensors when the chip is tilted from 3 to 5 degrees. The red, black, blue, and green lines are eye guides to illustrate the resonance shift better. 122

Figure 5-8 The effect of the illumination angle on the resonance features. (a) Shows the experimentally recorded reflection spectrum when the stage is tilted at 4.5 degrees. (b) Illustrates the Full-Width-at-Half-Maximum (FWHM) of the resonance peak against the illumination angle, and it stays almost constant and independent of the tilt. (c) Illustrates the Amplitude of the resonance peak against the illumination angle, and it stays almost constant and independent of the tilt. 122

Figure 5-9 The simulated resonance wavelengths of the dielectric metasurfaces as the function of the tilt angle of the stage. 124

Figure 6-1 Refractive index (n) of low-loss dielectric materials for metasurfaces at (a) the UV−visible regime and (b) the IR regime. The double-headed arrows indicate the wavelength range where the related materials have a near-zero extinction coefficient. The height of the double-headed arrows corresponds to the average value of the refractive index in the wavelength range. Possible sensing techniques of dielectric metasurfaces at different regimes are labeled on the top of the figures. This figure is adapted with permission from reference [2] Copyright 2021 American Chemical Society. 129

List of Tables

Table 1-1 Common biomarkers for cancer detection. Reproduced from the open-access article in reference [31]. 29

Table 3-1 Summary of Raman spectroscopy of graphene deposited on and off the dielectric sensors 86

List of Equations

Equation 2-1 Optical chirality 60

Equation 4-1 The associate slope with pixel i 102

Equation 4-2 The optimal linear estimator of the resonance shift at time k over the sensor area 102

Equation 4-3 Closed-form expression for the total quality factor 106

Equation 5-1 Quality factor 113

Equation 5-2 Dependence of quality factor on asymmetry parameter without non-radiative losses 113

Equation 5-3 Total quality factor 115

Equation 5-4 Dependence of quality factor on asymmetry parameter and non-radiative losses 116

Equation 5-5 Dependence of the suppression and amplitude of resonance on the quality factor 116

Equation 5-6 Approximation of dependence of the suppression and amplitude of a quasi-BIC resonance on asymmetry parameter and non-radiative losses 116

Equation 5-7 Resonance shift 123

Equation 5-8 Resonance shift function 123

Equation 5-9 Constitutive equation set of the hyper-angular spectral decoder elements 123

Chapter 1 Introduction

Disclaimer: Some contents of this chapter are from reference [1] and reference [2]. Reference [1] is an open-access article distributed under the terms of the Creative Commons CC BY license, which permits unrestricted use, distribution, and reproduction in any medium provided the original work is properly cited. The content from reference [2] is adapted with permission. Copyright {2021} American Chemical Society and

- Reference [1]: Phase-sensitive plasmonic biosensor using a portable and large field-of-view interferometric microarray imager. Light Sci Appl 7, 17152-17152 (2018).
  Authors: Filiz Yesilkoy, Roland A Terborg, Josselin Pello, Alexander A Belushkin, **Yasaman Jahani**, Valerio Pruneri, Hatice Altug
  Jahani's Contribution:
  Nanofabrication and characterization of the plasmonic nanohole arrays.
  Carry out numerical simulations of the plasmonic nanohole arrays.
- Reference [2]: Dielectric Metasurfaces Enabling Advanced Optical Biosensors. ACS Photonics 8, 47-60 (2021).
  Authors: Ming-Lun Tseng*., **Yasaman Jahani***, Aleksandrs Leitis*, Hatice Altug.
  Jahani 's Contribution:
  *These authors contributed equally to writing this perspective review

A biosensor is an analytical device that uses certain biological chemicals to send signals that show molecules' presence and sometimes their concentration. This signal can be recorded for future processing and data presentation. There are many applications for biosensors, including environmental monitoring [3]–[5], disease detection [6]–[9], molecular diagnostics [10]–[14], and food safety [15], [16]. Biosensors monitor the presence of pollutants in drinking water[17], food [16], and soil [18] for quality and safety. Analytes, such as pathogens, toxins, and other biologically significant factors, can be detected in small quantities by biosensors, making them invaluable for environmental protection and disease prevention (Figure 1-1) [19].

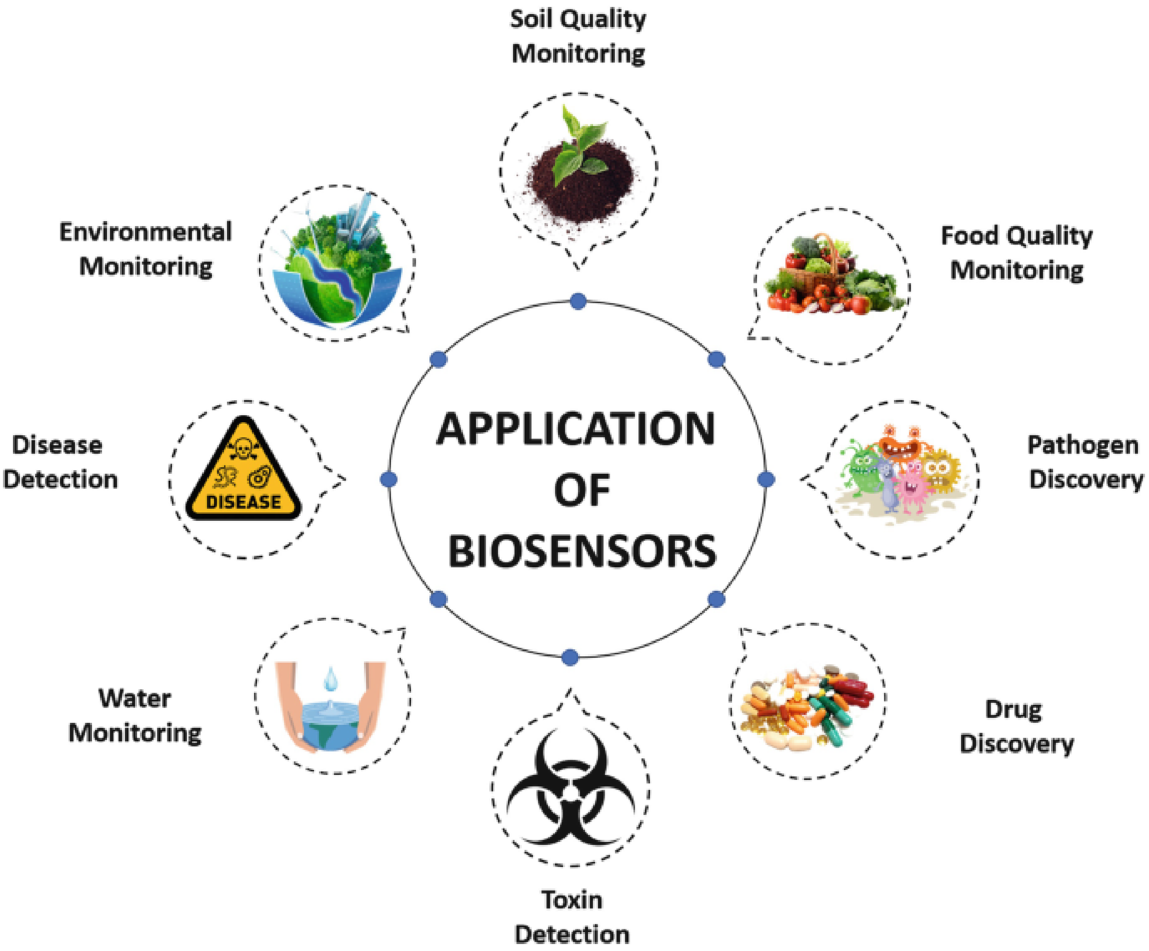
Soil Quality Monitoring
Environmental Monitoring
Food Quality Monitoring
APPLICATION OF BIOSENSORS
Disease Detection
DISEASE
Pathogen Discovery
Water Monitoring
Drug Discovery
Toxin Detection

Figure 1-1 Biosensors could be used in pathogen discovery, drug development, disease detection, and monitoring, food, water, and soil quality assessment, environmental monitoring, and toxin detection. Reproduced with permission from reference [19].

Biosensors are most commonly used in the healthcare sector. There are a number of applications for biosensors in healthcare, including the diagnosis and treatment of infectious diseases [7] and foodborne illnesses [15], the management of chronic diseases such as cancer [8], heart disease [20], and diabetes [21], as well as the general monitoring of personal and public well-being.

Worldwide, foodborne illnesses have become a serious public health problem, which has raised the concerns of the food industry and regulatory organizations [22]–[24]. Some microorganisms are associated with spoiled food, while others are shown to be helpful and beneficial in food production. An example of a beneficial bacterial species is Bifidus, also known as Bifidobacterium, which is a species of probiotic bacteria found in fermented foods like yogurt. According to the centers for disease control and prevention (CDC), the most common foodborne pathogens in the united states include Norovirus, Salmonella, Clostridium perfringens, Campylobacter, and Staphylococcus aureus (Staph). Although Clostridium botulinum (botulism), Listeria, Escherichia coli (E. coli), and Toxoplasma gondii produce fewer diseases, they are more likely to result in hospitalizations [25]. The presence of these microorganisms has been demonstrated to produce cell metabolites and toxins that can potentially cause severe health problems or even death in some cases [26]. Therefore, there is a growing need to develop biosensors targeting foodborne pathogens.

Increasing outbreaks of infectious diseases such as avian influenza, Hendra, Nipah, and SARS are a global concern that requires significant efforts to contain them [27]. In the last month of 2019, a novel human coronavirus was spotted in Wuhan, Hubei Province, China, causing an infectious disease called Coronavirus disease or, in short, COVID-19. In spite of attempts to contain the virus there, it spread to other parts of Asia and eventually to the entire world. The outbreak was called a pandemic and an international public health emergency by the World Health Organization (WHO). There have been more than 600 million cases of infection and 6 million deaths caused by COVID-19 to date, according to Worldometer [28]. There is an urgent need for diagnostic tools to enable the eradication or minimization of the likelihood of an outbreak, given the vital challenges associated with these infectious diseases.

Biosensors have the potential to revolutionize the treatment of chronic diseases. For example, most cancer types involve numerous biomarkers that biosensors can detect for diagnosis and monitoring. The biomarkers can be circulating tumor cells (CTCs), cell-free DNA (cfDNA), extracellular vesicles (EVs), or specific proteins expressed or secreted by tumor cells, as shown in Table 1-1 [29]–[31]. By monitoring tumor biomarkers, biosensors can identify the presence of a tumor and determine whether it is benign or malignant [32]. Furthermore, they can track the patient's response to treatment and determine whether it has effectively decreased or eradicated cancerous cells. Biosensors can enable multiplexing, which means they can screen a panel of biomarkers simultaneously, thereby saving time and resources [33].

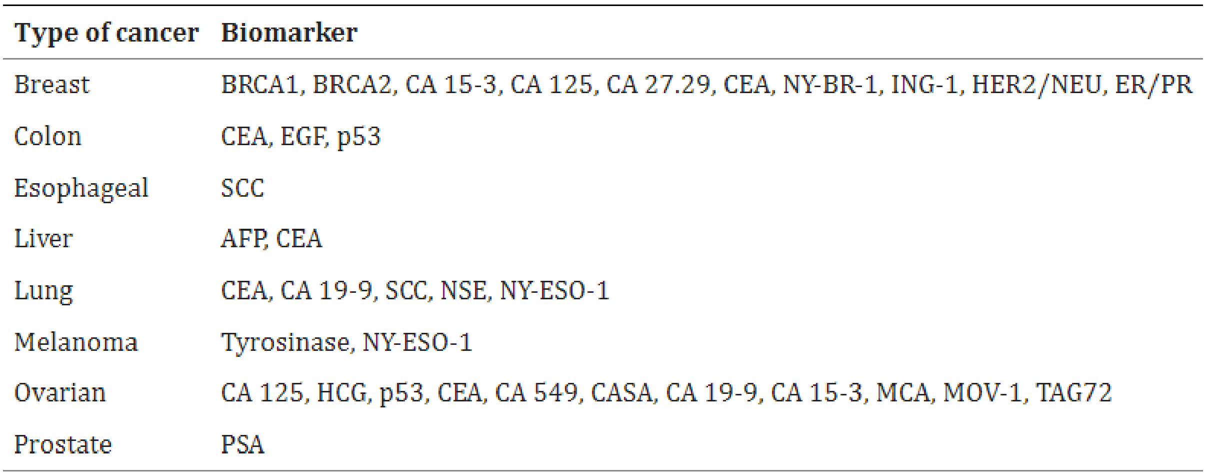

Type of cancer	Biomarker
Breast	BRCA1, BRCA2, CA 15-3, CA 125, CA 27.29, CEA, NY-BR-1, ING-1, HER2/NEU, ER/PR
Colon	CEA, EGF, p53
Esophageal	SCC
Liver	AFP, CEA
Lung	CEA, CA 19-9, SCC, NSE, NY-ESO-1
Melanoma	Tyrosinase, NY-ESO-1
Ovarian	CA 125, HCG, p53, CEA, CA 549, CASA, CA 19-9, CA 15-3, MCA, MOV-1, TAG72
Prostate	PSA

Table 1-1 Common biomarkers for cancer detection. Reproduced from the open-access article in reference [31].

EVs and exosomes in cancer monitoring have recently garnered significant attention. Many bodily fluids contain EVs, including saliva, blood, urine, semen, and breast milk [34]. EVs provide information about the current disease status as they encompass materials from parental cells, such as proteins, microRNAs, and messenger RNAs (mRNAs) [32], [34]. EVs can be of varying sizes. The International Society for Extracellular Vesicles (ISEV) recommends the use of "small extracellular vesicles" (sEVs) for EVs with a diameter of below 200 nm. Previously the EVs with the size of 50 nm to 150 nm diameters were categorized as exosomes [35]. sEVs released by tumor cells contain genetic materials that stimulate breast cancer metastasis [32]. Furthermore, the membrane proteins of sEVs also play a significant role in modifying the functionalities of targeted cells [36]. EVs are emerging as a potent diagnostic marker for early cancer detection, disease monitoring, and treatment evaluation, facilitating minimally invasive assessments thanks to the less intrusive nature of the sampling procedure[37].

The first biosensor, the Clark electrode, was developed by Leland C. Clark, in 1956 to detect oxygen [38]. Since then, a variety of new kinds of biosensors have been introduced, including the revolutionary glucose biosensors to detect diabetes, pregnancy tests, and, most recently, COVID-19 rapid tests, which played a key role in controlling the pandemic. A biosensor consists of three elements: a recognition element, i.e., a layer that is functionalized with biological components, a transducer, and a system that detects and records the signal for further analysis (Figure 1-2).

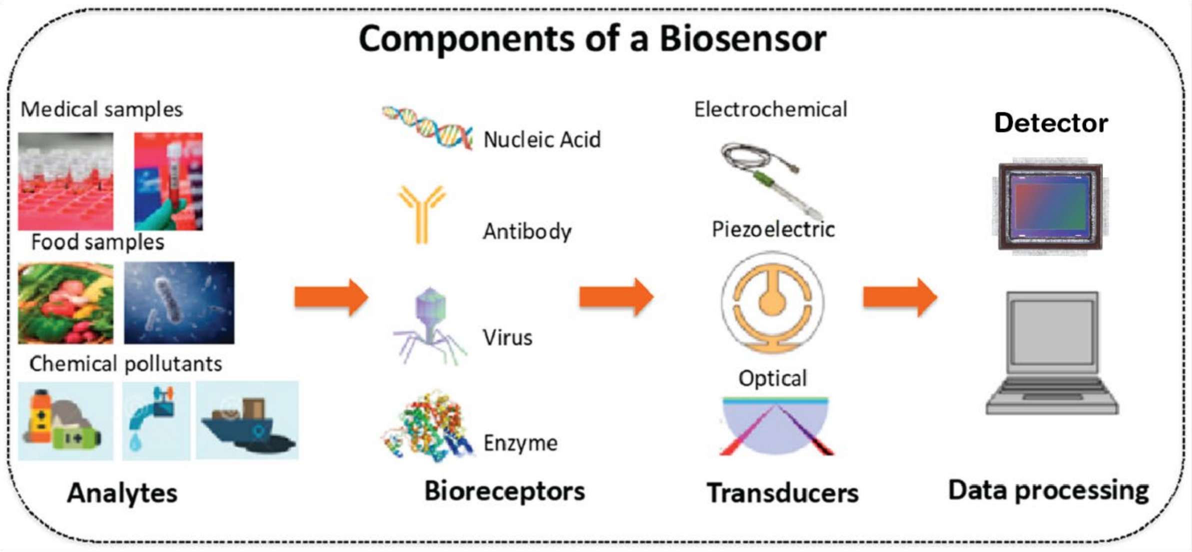

Figure 1-2 Components of a biosensor. Bioreceptors interact with the analyte, a transducer to translate the binding events to a measurable signal, and a detector to record the data for analysis. There are a variety of targets that can be detected by biosensors, including pathogens, biomolecules, and toxins in food, soil, and medical samples. These analytes interact with a biorecognition element such as nucleic acids, antibodies, viruses, or enzymes resulting in a measurable signal transduced via an electrochemical, piezoelectric, or optical system to be recorded and further processed. Reproduced from the open-access article in reference [39].

The recognition element responds to one or more substances in a bio-specimen, known as the analyte. Antibodies, enzymes, nucleic acids, viruses, and even living cells are commonly used as recognition elements. Transducers translate and amplify binding events between analytes and the recognition elements into a detectable signal. This signal is further measured using a detector, such as an electronic or a light-sensitive device, and can be further processed to extract valuable data. It is possible to transduce signals using a variety of methods, including electrochemical, piezoelectric, and optical means [40].

Depending on signal transductions, biosensors are classified into many categories. Electrochemical sensors are the first introduced biosensors. These sensors are based on the principle that molecules interact with biorecognition elements to induce an ionic discharge, resulting in an electrical signal that is directly proportional to the concentration of analytes. Electrochemical sensors convert sensing information into a quantifiable signal by using voltammetry, amperometric, impedimetric, and potentiometric methods [41]. Simple design and low manufacturing costs are two major advantages of electrochemical biosensors. However, electrochemical biosensors and biological processes are both highly sensitive to pH, which can significantly constrain the selection of buffer for biosamples. Furthermore, the multiplexed detection of biomarkers using electrochemical biosensors can pose significant challenges [42].

The piezoelectric biosensors rely on the mass change that occurs due to biomolecular interactions. Also known as mass-based biosensors, these devices are based on the principle that oscillations are changed when a mass is attached to the surface of a piezoelectric crystal, thus generating electrical signals in response to mechanical forces. The biorecognition elements are immobilized on intrinsically piezoelectric crystals. The change in mass caused by the binding of analytes to the recognition element modifies the mechanical vibrations that are translated into electrical signals. A detectable change in oscillations requires quantities of analytes on the order of micrograms [43].

Optical biosensing is another category of biosensors that incorporates a biorecognition sensing element with an optical transducer. Analyte binding at the sensor surface results in changes in a particular characteristic of light that can be measured by optical means. There are various optical biosensing techniques that rely on different phenomena, such as light scattering, absorption, refractometry, fluorescence, or luminescence spectroscopy. Therefore, optical biosensing comprises both label-free and label-based detections. Label-free optical biosensors generally produce a signal proportional to the concentration of the analyte and therefore provide quantitative information [44].

To enhance light-matter interaction and detect binding events, some biosensors, such as surface plasmon resonance (SPR), resonant microcavities, and optical waveguide interferometry, utilize the evanescent field near the surface of the device (Figure 1-3) [45], [46]. The decay length of the evanescent field is in the order of 200 nm to 400 nm which is greatly larger than most biomolecular analytes, therefore, limiting the effective light-matter interactions and the limit of detection (LOD) [44]. The lowest concentration of the analyte that a biosensor can detect with high levels of certainty is the LOD of the device.

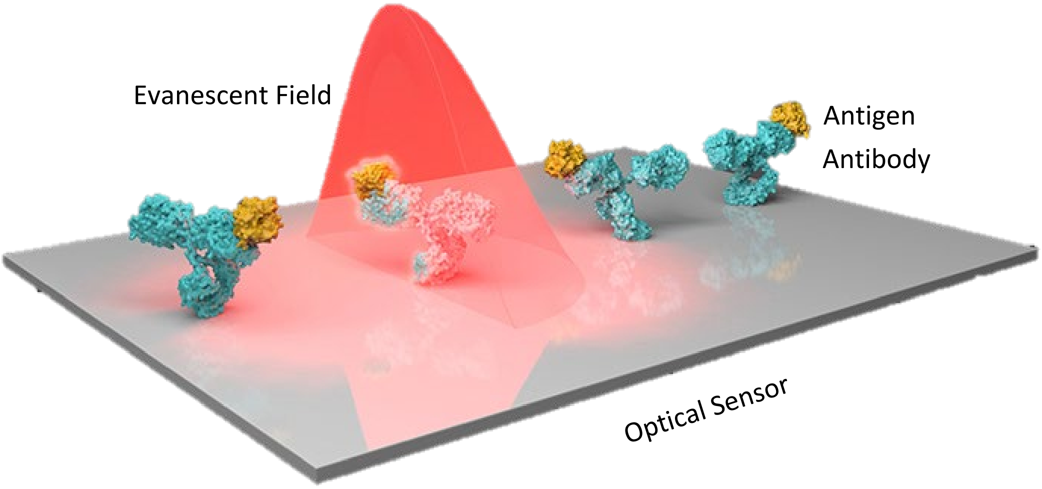

Figure 1-3 Some optical platforms leverage the evanescent field at the biosensor's surface to enhance light-matter interactions. Resonant microcavities, surface plasmon resonance (SPR), and optical waveguide interferometry are among such sensors. Reproduced with the authors' permission from reference [46].

Metallic and dielectric nanostructures are introduced to further localize the electromagnetic fields and push down the LOD. Metallic nanostructure biosensors are mainly based on localized surface plasmon resonance, discussed in the following subchapters. In addition to plasmonic biosensors, dielectric nanoresonators offer new opportunities for the development of subwavelength optics and photonics. High-index dielectric nanoparticles are combined to create dielectric nanophotonic platforms, such as metasurfaces, that exhibit subwavelength electric and magnetic Mie resonances (Figure 1-4). The Mie resonance provides strong field localization and high-quality factor (high-Q) resonances, which are advantageous for biosensing applications requiring strong near-fields to intensify the light-matter interaction [47]. The application of dielectric metasurfaces for biosensing is the main topic of this thesis and is introduced in the following subchapters. Dielectric metasurface biosensors can be compact, rapid, highly sensitive, real-time, and cost-effective, offering multiplexing and a low limit of detection for diagnosing and managing infectious diseases, foodborne illnesses, and chronic diseases such as cancer [8].

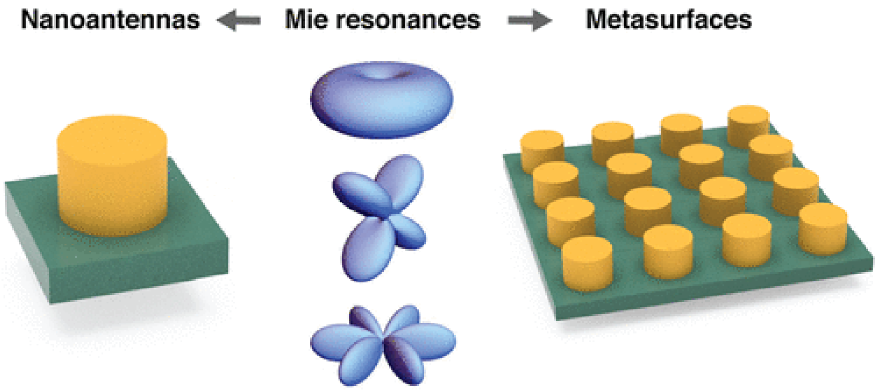

Figure 1-4 Dielectric particles sustain Mie resonances. A dielectric metasurface is formed by putting together nanoantennas in 2D arrays. It is possible to tailor the unit cell of metasurfaces to provide a variety of functional properties. Reproduced with permission from reference [47].

1.1 Metasurfaces for biosensing

Optical sensing techniques are essential in modern biomedical, material, and environmental monitoring applications as they provide fast and robust ways to detect and distinguish target objects from a variety of samples. In recent years, nanophotonic metasurfaces have been emerging as a powerful platform to advance sensing technologies. Metasurfaces are artificial photonic devices composed of subwavelength nanoresonators (called meta-atoms), and their functionalities can be engineered by rationally tailoring their geometric parameters [47]–[50]. Metasurfaces have been used as wavefront control devices, [51]–[54] nanoscale light sources, [55], [56] optical signal modulators, [57], [58] and optical quantum devices [59]–[61]. For optical sensing, their capability to confine light into nanoscale electromagnetic hotspots has been utilized to enhance the sensitivity of various detection techniques [62]–[64]. For instance, plasmonic metasurfaces have enabled the detection of monolayers and their real-time interactions with biomolecules in the mid-infrared (mid-IR) regime [65]–[69], which is challenging by using conventional infrared absorption spectroscopy methods. So far, metasurfaces consisting of metallic nanostructures (e.g., Au, Ag, and Al) have been exploited dominantly, and numerous biosensing devices have been demonstrated [68], [70]–[72]. Although plasmonic metasurfaces provide useful properties, for example, strong electric field enhancement, for various sensing techniques, the intrinsic losses of the constituent metals usually impose limitations. An emerging direction to circumvent such restraints is to replace the constituent materials of metasurfaces with dielectrics that have a low optical loss and high refractive index. Thanks to their striking optical properties, dielectric metasurfaces bring a new horizon for nanophotonic sensing (Figure 1-5) [2].

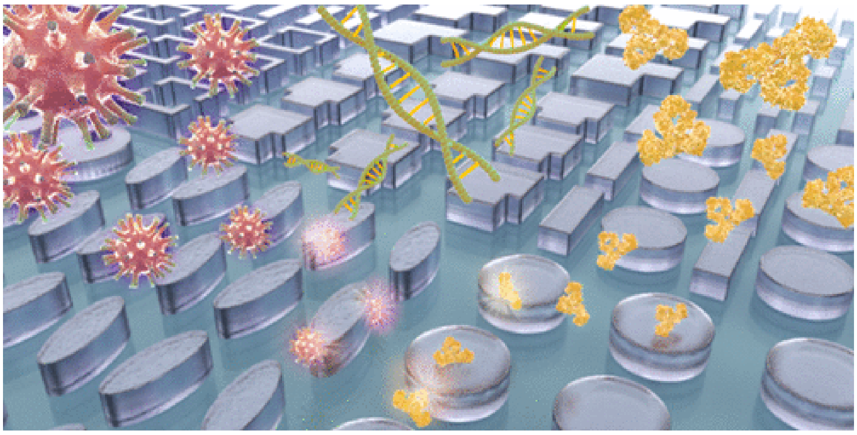

Figure 1-5 Metasurfaces for biosensing applications. Reproduced with permission from reference [2]. Copyright 2021 American Chemical Society

1.1.1 Plasmonic metasurfaces for biosensing

Plasmonic metasurfaces are comprised of metallic elements with subwavelength dimensions that display plasmonic resonances determined by their geometries and material properties [48], [73], [74]. Figure 1-6 shows plasmonic meta-atoms, one-dimensional plasmonic chains, two-dimensional plasmonic metasurfaces, and three-dimensional plasmonic metamaterials [48]. Plasmon resonance is the coherent oscillation of the conduction electrons in the metal, driven by an external electromagnetic field. Recently, significant attention and enormous effort have been devoted to plasmon resonances in metallic nanostructures due to their promising applications in various fields, from negative index metamaterials and perfect lensing to extremely sensitive biosensing and nonlinear optics [75]–[77]. Noble metals such as gold and silver, inheriting large negative permittivity, are commonly used materials for plasmonic metasurfaces; because even a thin layer strongly scatters light [78]. The stimulation of surface plasmons can generate enhanced near-fields, which are suitable for intensifying light-matter interactions. State-of-the-art plasmonic devices highly impacted Raman fluorescent and infrared spectroscopy techniques, improving their conventional capabilities to extract imperative information on complex molecular structures and enabling single-molecule detection [67], [79]–[82].

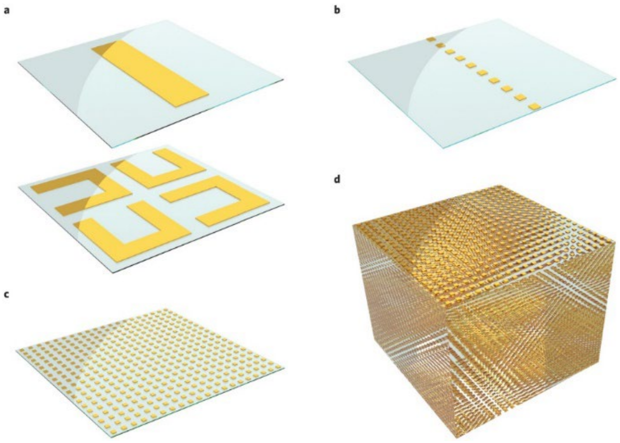

Figure 1-6 Schematic representation of plasmonic metamaterials a) Represents two possible meta-unit of meta-systems: a meta-atom including a plasmonic nanorod and a meta-unit of four split-ring nanoresonators. b-d) Represents a 1D chain (b), a 2D metasurface (c), and a 3D metamaterial made from plasmonic meta-atoms (d). Reproduced with permission from reference [48].

In general, plasmonic systems are based on two different mechanisms: propagating surface plasmons and localized surface plasmons. When surface plasmons interact substantially with electromagnetic radiation, the surface plasmon polariton (SPP) occurs. An SPP can also be referred to as surface plasmon resonance (SPR) or the coherent (resonant) oscillation of surface conduction electrons induced by an electromagnetic field (Figure 1-7a). Further constraining the oscillation to a sub-wavelength metal particle results in the excitation of a localized surface plasmon resonance (LSPR) (Figure 1-7b). LSPRs have greater intensities and spatial resolution than SPPs. Additionally, LSPR offers greater flexibility in tuning optical properties by changing the size, metal, and dielectric environment [83].

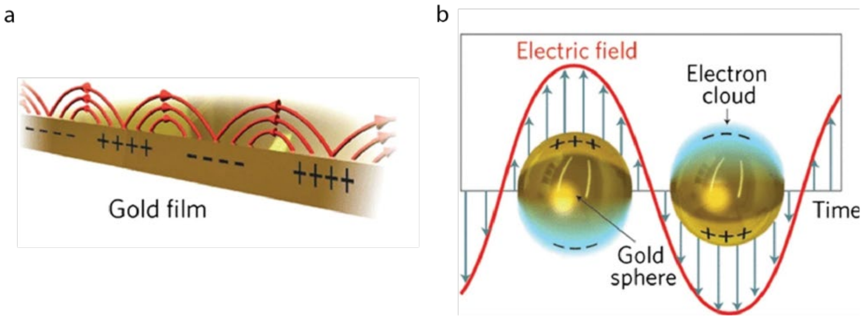

Figure 1-7 (a) Shows the coherent oscillation of gold film's surface conduction electrons to sustain surface plasmon resonance (SPR). (b) Shows gold nanoparticles constraining the oscillations and the resulting electric field to a sub-wavelength dimension leading to the excitation of a localized surface plasmon resonance (LSPR). Reproduced with permission from reference [84].

SPR is restricted to P-polarized modes where the magnetic field vector is in the plane of the metal-dielectric interface, meaning that the S-polarized modes cannot excite surface plasmons. This electromagnetic phenomenon generates transversal electric fields with maximal intensity at the metal-dielectric interface while decaying evanescent waves permeate both adjacent media. Typically, surface plasmons are excited using Kretschmann configurations using coupling prisms in a reflection mode, though this method increases the size of the sensor significantly and inhibits multiplexing (Figure 1-8a) [85].

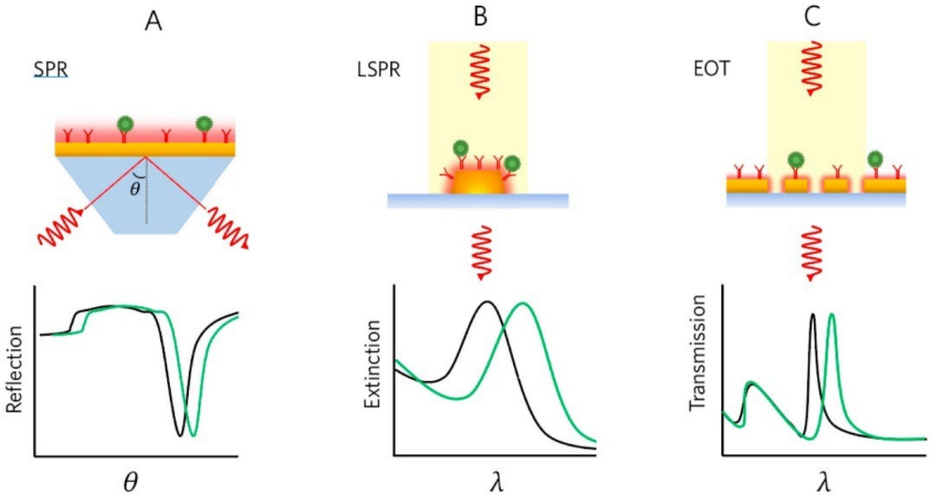

Figure 1-8 (a) Schematically represents surface plasmon resonance (SPR). The measurement setup is in the Kretschmann configuration. The local changes of refractive index at the surface of the gold thin-film cause shift in the angle of minimum reflected intensity. (b) Schematically represents localized surface plasmon resonance (LSPR). The analyte binding to the nanoparticles induces a shift in the extinction spectrum (c) Schematically represents extraordinary optical transmission through gold nanohole arrays. The analyte binding induces local refractive index changes translated into a shift in the transmission spectrum. Reproduced with permission from reference[83].

A metallic nanostructure in the subwavelength range can generate LSPR without the need for coupling elements. The interactions of light with metallic nanostructures can excite specific electronic modes, causing free electrons to oscillate collectively, measurable in their extinction spectra (Figure 1-8b). Furthermore, extraordinary optical transmission (EOT) occurs when incident photons interact with periodic nanohole arrays (NHAs) (Figure 1-8c) [83]. The plasmonic Au-NHAs retain the unique EOT phenomenon induced by the interplay of two resonance coupling mechanisms in a classical asymmetric Fano-type spectral line profile. Perpendicularly incident light generates in-plane surface plasmon polariton sub-radiant modes satisfying Bragg's coupling condition through wavevector matching of the grating's momentum. The sharp dark mode strongly couples to the subwavelength holes in the Au film and generates a bright, radiant mode that scatters light into the free space. These destructive and constructive near-field interactions are strongly dispersive and manifest themselves in the far-field intensity spectrum as multiple dips and peaks that constitute different modes associated with either the supporting substrate or the top medium [1].

The plasmonic properties are responsive to changes in the local refractive index, tailored by the shape, size, and spacing of the metallic nanoresonators [83]–[85]. The analyte binding on the surface of the metallic nanostructures induces a local refractive index change, causing a shift in the resonance peak wavelength. Specifically, refractometric plasmonic sensors, such as those based on SPR or LSPR, have broken fresh grounds in label-free optical biosensing by overcoming the limitations of complicated and time-consuming labeled approaches, including fluorescence detection and enzyme-linked immunosorbents. Holding the advantage of not deteriorating after exposure to surrounding media, such as air and water, plasmonic metasurfaces are interesting sensing platforms for clinically relevant detection of various biomaterials, such as proteins, exosomes, nucleic acids, and viruses [86].

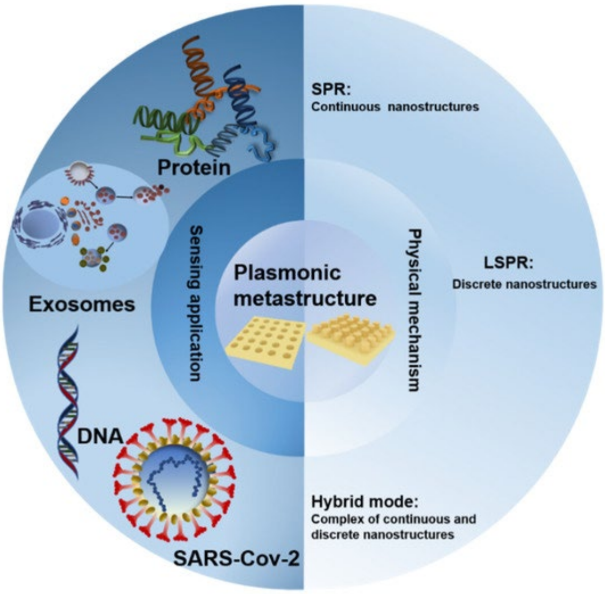
SPR:
Continuous nanostructures
LSPR:
Discrete nanostructures
Hybrid mode:
Complex of continuous and discrete nanostructures
Physical mechanism
Plasmonic metastructure
Sensing application
Protein
Exosomes
DNA
SARS-Cov-2

Figure 1-9 An overview of plasmonic metasurfaces for biosensing applications. The central pictures are the schematics of typical plasmonic sensing structures. The physical mechanisms are shown on the right, and exemplary analytes are shown on the left side of the diagram. Reproduced from the open-access article in reference [86].

Figure 1-9 shows an overview of plasmonic metasurfaces for biosensing applications, the physical mechanisms, and the analytes [86]. While nanoplasmonic sensor technologies have made significant progress in recent years, several challenges remain, including high material losses and joule heating, the need for simple and robust optical readout systems, and mass-scale fabrication of nanostructured chips at low manufacturing costs because gold cannot be used in the same production line as semiconductors due to cross-contamination issues [2], [87].

1.1.2 Dielectric metasurfaces for biosensing

The physics of optical resonances in dielectric metasurfaces is mostly associated with the Mie scattering of subwavelength resonators [53], [87]. As the effective wavelength of the incident light is close to the feature size of a high-index nanoparticle, optical resonances arising from the oscillating displacement currents can be excited. Notably, individual subwavelength dielectric resonators can show a strong response to both electric and magnetic fields of light. This property is in contrast to the plasmonic counterparts that respond weakly to the magnetic field. As a result, electrical and magnetic dipoles, as the first and second Mie-type modes (Figure 1-10a), are usually observed in the spectra of dielectric resonators. A transmission spectrum and the resonance modes of a spherical Si nanoparticle with a diameter of 150 nm were simulated using commercial software CST Microwave Studio (Figure 1-10b). In the transmission spectrum, two dips associated with the electric (at ~490 nm) and the magnetic (at ~600 nm) modes can be observed, respectively. As an experimental demonstration of the resonances in dielectric nanoparticles, a dark-field image of Si nanoparticles made by laser ablation of a Si substrate is presented in Figure 1-10c [88]. The spherical nanoparticles show vibrant colors, ranging from violet to red. As highlighted by the red and green dashed boxes in the images, the red and green spots in the image are associated with Si nanoparticles with different diameters. The dependence of the resonance wavelength and the dimension of a dielectric nanoparticle can be described as $g\left({}^{\lambda}/_{n}\right) = 2\pi r$, where g is a positive integer, λ is the resonance wavelength, and r is the radius, respectively [89], [90]. For different sensing techniques, the resonance wavelengths of dielectric metasurfaces can be precisely tuned from the visible [88], [91] to infrared (IR) [92], [93] by the choices of the feature sizes of the meta-atoms and the materials. This useful property enables the realization of various sensing metasurfaces [2].

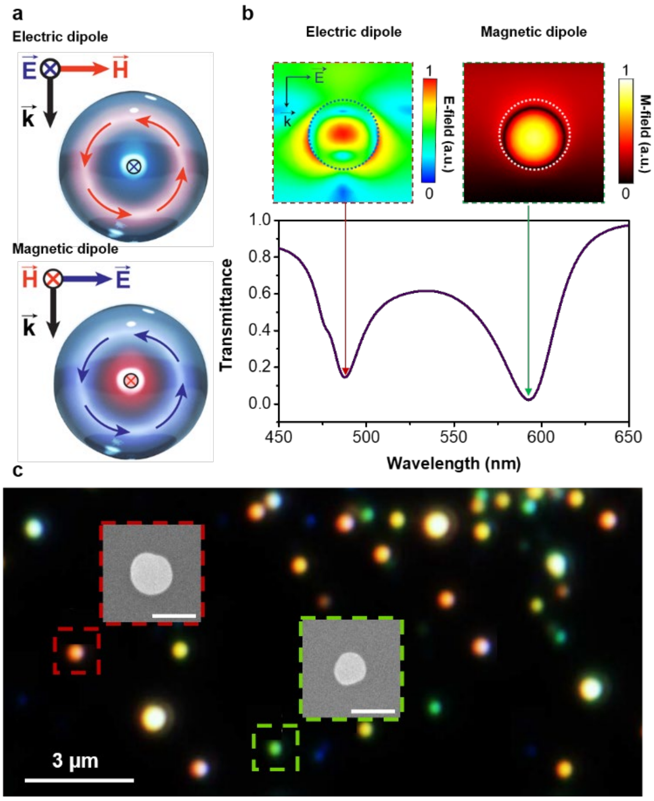

Figure 1-10 Mie resonances in high-index dielectric nanostructures. (a) Schematics of an electric dipole and magnetic dipole induced in a spherical dielectric nanoparticle. The red and blue arrows indicate the direction of the induced magnetic and electric field inside the nanoparticle, respectively. (b) Transmission spectrum and the resonance modes of a 150 nm Si spherical nanoparticle. (c) Dark-field microscopic image of Si nanoparticles on a Si substrate produced by using femtosecond laser ablation [88]. Inset: SEM image of the Si nanoparticles highlighted in the dashed squares. Scale bar of the insets: 200 nm. (a) and (b) are adapted with permission from reference [2] Copyright 2021 American Chemical Society. (c) is reproduced with permission from reference [88]. Copyright 2012 Nature Publishing Group.

In the designs of sensing metasurfaces, several parameters should be carefully considered to achieve the desired functionalities, including the working wavelength, resonance bandwidth, field enhancement, and resonance quality. Especially the resonance quality and near-field enhancement are critical parameters for most of the sensing mechanisms. The quality factor of an optical resonator (Q) is defined as the ratio of the resonance wavelength versus the resonance bandwidth. For instance, in refractometric biosensing, the Q factor influences the resolution to measure refractive index changes [94], [95]. Additionally, the Q factor is closely associated with the field enhancement given by the resonators. Their relationship can be described as $P^2 = \gamma_{rad} \cdot \left({Q^2}/{V} \right)$, where P is the field enhancement, γ_{rad} is the radiative decay ratio, and V is the mode volume of the resonator [96], [97]. Therefore, metasurfaces with a high-Q resonance are also useful for different techniques, such as surface-enhanced spectroscopy [65]–[69]. On the other hand, a higher Q-factor implies a narrower bandwidth, which can bring certain limitations for techniques such as SEIRA and vibrational circular dichroism spectroscopy [98]. It is because a narrower resonance implies a reduced spectral bandwidth, and it might not be able to cover well the molecular absorption bands for chemical-specific detection. Therefore, it is important to be aware of such trade-offs and consider device architectures that can benefit from high-Q while still having a broad spectral coverage. Several examples will be discussed in the following sections related to this point [2].

As a brief overview of the current progress on high-Q dielectric metasurfaces, several state-of-the-art works are presented in Figure 1-11. Yang et al. use the coexistence of strong magnetic and electric dipole resonances in dielectric nanoresonators to achieve a Fano-type resonance in a metasurface [99]. A scanning electron microscopic (SEM) image of the metasurface is presented in Figure 1-11a. It has been designed for operation at the telecommunication wavelength band, and Si was selected as the constituent material due to its low loss property in the IR regime. The meta-atom consists of two nanoresonators, a nanobar, and a nanodisk. The electric dipole mode of the nanobar resonator serves as the bright mode, while the out-of-plane magnetic dipole mode of the nanodisk resonator is optically dark in nature. The coupling of the bright and dark modes suppresses the far-field radiation and results in a sharp spectral feature. As a result, the transmission spectrum of the metasurface reveals a sharp resonance peak at 1371 nm, with a Q factor of 483. Another useful approach for designing high-Q metasurfaces is to introduce a mode interference inside the individual resonators. Semmlinger et al. demonstrate the excitation of an anapole resonance [100]–[102] in a dielectric metasurface. Anapole resonance results from destructive interference between the electric and toroidal dipoles excited in the meta-atoms, and it is useful for boosting light-matter interactions. (Figure 1-11b). The meta-atom of the metasurface is a nanodisk, as can be seen in the left panel of Figure 1-11b. To achieve a proper resonance property in the anapole metasurface, amorphous TiO_2 is used as the constituent material because of its low loss in the visible regime. The anapole resonance produced a sharp dip in the transmission spectrum, as can be observed in the right panel of Figure 1-11b. Notably, the simulation results for both of the metasurfaces (the insets in Figure 1-11a and b) illustrate that electromagnetic energy is confined on the surface of meta-atoms at the resonance condition. This characteristic is beneficial to boost the light-matter interactions at the nanoscale for many applications, including biosensing [2].

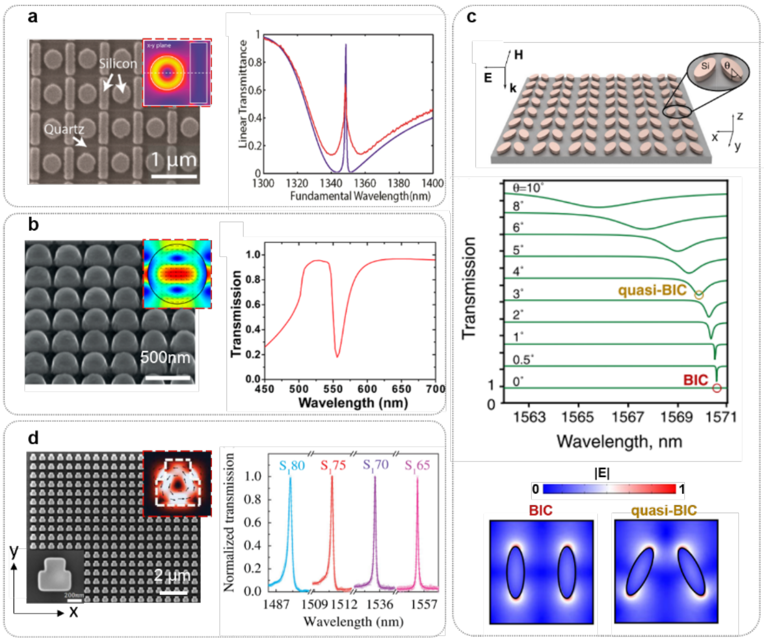

Figure 1-11 Examples of high-Q dielectric metasurfaces. (a) Fano-resonant metasurface [99]. Left panel: SEM image of the metasurface consisting of Si bars and disks. Insert: the electric field pattern at the resonance wavelength. Right panel: simulation (purple curve) and experiment (red) transmission spectrum of the metasurface. (b) Anapole metasurface [102]. Left panel: SEM image of the metasurface consisting of TiO_2 disks. Insert: the electric field pattern at the resonance wavelength. Right panel: Transmission spectrum of the metasurface. (c) Quasi-BIC metasurfaces with different symmetry breakings [103]. Top panel: Schematic of the metasurface consisting of asymmetric Si asymmetric nano-ellipse pairs. Middle panel: Dependence of the transmission spectra versus the rotational angle θ (indicated in the top panel). Bottom panel: Comparison of the electric field patterns for the BIC and quasi-BIC mode, respectively. (d) Ultra-high-Q factor quasi-BIC metasurface [104]. Left panel: SEM image of the metasurface consisting of Si nanoresonators. Insert on the top: the electric field pattern at the resonance wavelength. Right panel: Transmission spectra of the metasurfaces with the different cut-out size S. The Q factor of the metasurface is highly sensitive to S. The polarization of the excitation for the metasurfaces shown in this figure is along the x-axis shown in (d). (a) is reproduced with permission from reference [99]. Copyright 2015 ACS. (b) is reproduced with permission from reference [102]. Copyright 2019 ACS. (c) is reproduced with permission from reference [103]. Copyright 2018 APS. (d) is reproduced with permission from reference [104]. Copyright 2017 APS.

More recently, a new approach for achieving high-Q metasurfaces based on the quasi-bound-state-in-the-continuum (quasi-BIC) has attracted significant attention [103], [105], [106]. BICs are the optical modes that remain ideally confined even though they are compatible with free-space radiation [105], [106]. A true BIC is a mathematical object with an infinite Q factor and a vanishing resonance. Within the concept of metasurfaces, at the BIC condition, the resonance feature in the transmission spectrum collapses due to the transformation of the resonance mode to be optically dark. Symmetry-protected BIC can become quasi-BIC by breaking the in-plane symmetry of the unit cell with a controllable asymmetry parameter. This property provides so-called supercavity modes [107] with finite but high-Q factors. Absorption influences the total Q factor of a quasi-BIC resonance, yet the radiative Q factor for all quasi-BIC supporting metasurfaces has an inverse quadratic relation with the asymmetry parameter of the unit cell. This quadratic correlation, along with the linear scalability of Maxwell's equations, can be employed to engineer metasurfaces with desired properties. BIC modes have been previously observed in plasmonic metasurfaces by Lovera et al. [108]. They proposed a link between Fano resonances and BIC modes in their work. Later, the theory of quasi-BIC was developed and systematically explained by Koshelev et al. within the context of dielectric metasurfaces [103], [107]. An example of a dielectric metasurface based on the physics of BIC is presented in Figure 1-11c [103]. The metasurface consists of pairs of Si nanoellipses. The middle panel of Figure 1-11c represents that when the nanoellipses are parallel, a pure BIC mode appears with an infinite Q factor in the spectra and spectrally vanishes. By breaking the in-plane symmetry with a gradual tilting of the ellipses, a radiation channel is created, and the BIC is turned into a quasi-BIC mode having a finite and tunable Q factor. A resonance dip can be seen in the spectra, and their quality factor varies with the rotation angle. Simulation results of the electric field distribution for the symmetric and asymmetric nanoellipse pair at the resonance wavelength are presented at the bottom of Figure 1-11c. It displays similar field patterns, a characteristic of the transition between the pure BIC mode to the quasi-BIC mode. With such an exceptional type of optical resonance, a Si metasurface with a record-high-Q factor has been recently realized (Figure 1-11d) [97]. Similarly, the authors introduce an in-plane inversion symmetry breaking by cutting out part of the edges. The metasurface provides an experimentally measured Q factor up to 18511 for operation in the telecommunication wavelength range. These recent works show that the type of optical resonances, functionalities, and working wavelengths can be effectively tuned by changing the material, geometry, and arrangement of the unit cell. Chapter 2 will review the implementation of dielectric metasurfaces for sensing [2].

1.2 Underlying key technologies in developing nanophotonic biosensors

Nanostructures are employed as biosensors to localize the electromagnetic fields in near-field hotspots for more efficient light-matter interactions and higher-performance sensors. The initial step toward the realization of a designed nanophotonic biosensor is to fabricate such nanostructures. Multiple nanofabrication steps and a variety of techniques are usually involved in the development of nanophotonic structures. Thereupon, biomolecules must be immobilized on the surface of the fabricated nanostructures using various techniques based on the surface material and the target analyte. The binding reaction of the analyte and biorecognition element occurs upon the delivery of the biosample to the surface of the nanostructures, inducing a change in the optical response of the device. Multiple optical interrogation strategies can be adapted to characterize the change in the optical readout. The following subsections introduce nanofabrication techniques, biofunctionalization methods, and optical interrogation strategies utilized in state-of-the-art nanophotonic biosensors.

1.2.1 Nanofabrication techniques

Nanofabrication is the foundation of virtually every aspect of experimental nanoscience and nanotechnology. In particular, it involves the development of nanostructures and devices with dimensions below 100 nanometers. Nanofabrication focuses on the production of such nanoscale platforms with the goal of integrating them into multifunctional devices that have a variety of applications, including sensing, energy harvesting, and electronic components [109]. The semiconductor integrated circuit industry is largely responsible for the development of most nanofabrication techniques. In 1956 Gordon Moore stated his observation that the number of transistors on a microchip doubles every two years. The constantly advancing nanofabrication techniques have enabled the prediction to be highly accurate, and it was dubbed Moore's Law as a result.

There have been numerous nanofabrication methods developed since the turn of the century, each of which has met or exceeded the lofty expectations placed on nanotechnology and related nanofabrication [110]–[116]. Depending on their procedural concept, nanofabrication techniques fall into one of two broad categories; top-down and bottom-up fabrication approaches. In the top-down method, bulk materials are reduced to nanoscale size, whereas in the bottom-up method, nanomaterials are created by putting together individual atoms (Figure 1-12). Physical, chemical, and biological mechanisms are used in the fabrication of nanomaterials [109], [117].

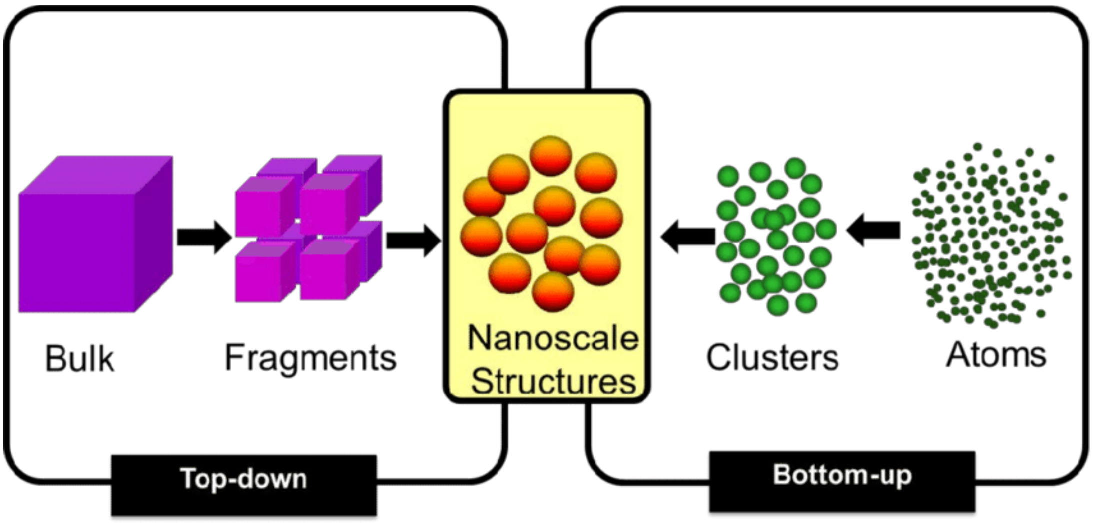

Figure 1-12 Top-down and bottom-up nanofabrication methods. Top-down nanofabrication starts with a bulk material breaking into smaller fragments and nanostructures. Bottom-up nanofabrication involves putting together atoms to form clusters and nanoscale structures. Reproduced from the open-access article in reference [118].

Lithography is one of the most commonly employed top-down fabrication techniques to make two-dimensional patterns on bulk material, for example, a silicon wafer. It is possible to divide lithography techniques into serial and parallel approaches. Conventional photolithography is an example of a parallel technique that incorporates a light source, typically ultraviolet (UV) light, and a photomask that allows light exposure through a defined pattern. The photomask is a high-quality quartz plate patterned with chromium. For nanoscale photolithography, deep and extreme UV rays are typically used. A collimated beam of light exposes a pattern on the surface of a previously coated silicon wafer [117].

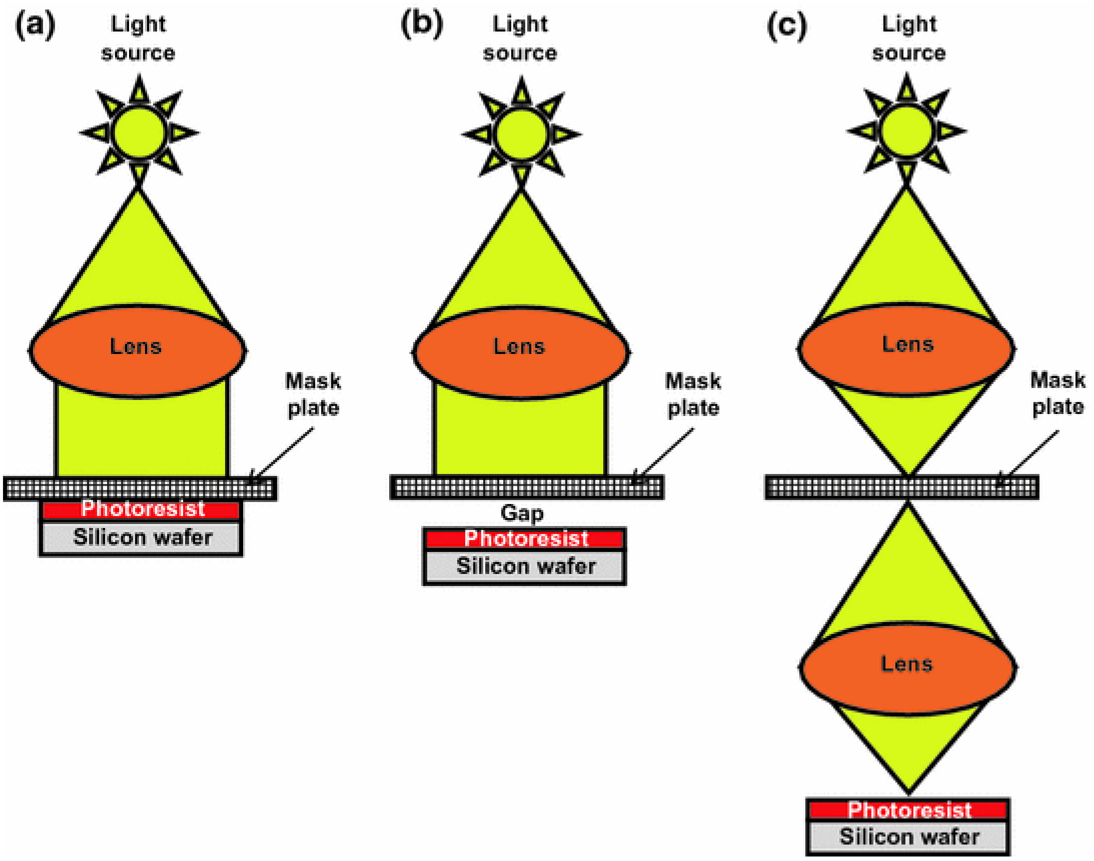
(a)
Light source
Lens
Mask plate
Photoresist
Silicon wafer
(b)
Light source
Lens
Mask plate
Gap
Photoresist
Silicon wafer
(c)
Light source
Lens
Mask plate
Lens
Photoresist
Silicon wafer

Figure 1-13 The schematic of photolithography tools. The photomask can be (a) in contact with, (b) in proximity of, and (c) within a distance of the photoresist layer. The third configuration has additional projection optics allowing exposures with factors smaller than the photomask feature based on the magnification of the optical system. Reproduced with permission from reference [117].

Silicon wafers are coated with a photoresist, a photosensitive organic polymer, and Spin-coating is often used to form a conformal layer on the wafer. In photolithography, the mask may be positioned in contact, in proximity, or apart from the resist layer, spaced by an optical projection system (Figure 1-13). According to the tone of the photoresist, exposed (for positive-tone resists) or non-exposed (for negative-tone resists) areas are dissolved in a solution known as the developer. Lithography results in a thin layer of resist that has been patterned with nanoscale features. The pattern built into the resist layer is later transferred to the bulk material via etching techniques. As shown in Figure 1-14 the etching can be directional (anisotropic) or omnidirectional (isotropic), it can be done chemically, mechanically, or a combination of both, and it can be done in a wet, e.g., using acids or dry process, e.g., reactive-ion etching.

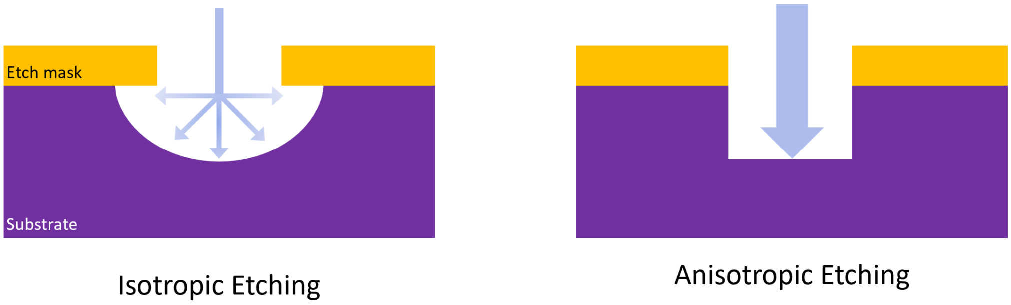

Figure 1-14 Two categories of etching directionality. (a) Shows the isotropic etching where the reaction occurs in multiple directions within the substrate leading to an undercut. (b) Shows an anisotropic etching that is highly directional and can make straight walls in the substrate.

The serial lithography method is referred to as a writing procedure rather than a printing method. Electron beam (e-beam) lithography is an example of serial lithography. E-beam lithography, similar to conventional photolithography, relies on a process by which nanoscale structures are exposed in an electron-sensitive resist and then transferred to the substrate material via etching. E-beam lithography can produce features on the nanoscale level that are below the diffraction limit, which is its key advantage over photolithography. E-beam lithography is a direct writing technique that does not require a mask and can also be used to prepare photomasks. E-beam lithography is a serial writing method in which an electron beam scans over the surface, limiting the process's throughput and making it slower than photolithography. There is also direct laser writing lithography available for writing structures with feature sizes greater than a hundred nanometers or even in the micrometer range. The dielectric metasurfaces introduced in chapters 3 to 5 of this text are fabricated using the e-beam lithography technique. Soft lithography, nanoimprint, block co-polymer, and scanning probe lithography are other examples of top-down fabrication methods [109], [117].

Bottom-up nanofabrication approaches are often referred to as synthesis techniques and encompass methods to create self-assembling functional systems and devices. Implementing bottom-up fabrication techniques, multi-component devices could be produced by controlling the arrangement of atoms and molecules without the need for additional editing or etching steps. The bottom-up fabrication process poses a number of significant challenges, such as preparing the surface for controlled growth of the nanostructure, removing contaminants from the surface, assuring that the reactants are pure enough, and determining the effectuality of surfactants and inhibitors. Although top-down fabrication techniques are mostly employed for nanophotonic biosensors, using a bottom-up approach makes it simpler to produce certain nanostructures, such as nanorods [83], [109].

1.2.2 Surface functionalization methodologies

The biorecognition element is a fundamental part of a biosensor. The modification of the sensor's surface with biological components to specifically target analytes is called surface functionalization. There are two major aspects of biofunctionalization: specificity and biomolecular orientation. Binding specificity is determined by the affinity between receptor biomolecules and the analyte, which is influenced by the chemical and physical interactions between them. Moreover, the antigen recognition efficiency is improved if the receptor molecules' binding sites are exposed to the sample in a proper orientation. The molecular orientation affects the density of receptor molecules on the sensor surface and decreases non-specific binding. Therefore, a densely packed and uniformly oriented immobilization provides high levels of sensing specificity and sensitivity. Functionalization methodologies are determined by considering the surface material, the biorecognition element, and the target analyte [119], [120].

The surface material plays a great role in determining the chemistry for biofunctionalization. Gold is the most promising constituent material in nanoplasmonic biosensing. This inert metal which does not go through oxidation, shows good plasmonic properties while it can be readily processed with standard fabrication techniques [121]. On the other hand, silicon is highly interesting for dielectric nanophotonic biosensors thanks to its low cost and abundance, biocompatibility, complementary metal-oxide-semiconductor (CMOS) compatibility, and, most importantly, its compelling optical properties, such as high refractive index and low loss [2]. Like many other materials in ambient conditions, the silicon surface is covered with a thin self-limit native oxide layer which is called silica. Therefore, the following paragraphs are dedicated to the biofunctionalization of gold and silica as the most important constituent materials for nanophotonic biosensors.

The biorecognition element is another key parameter in establishing a biofunctionalization protocol. Due to the extensive list of bioreceptors, this text focuses on the application of antibodies as biorecognition agents due to their wide use as targeting agents. Antibodies can be synthesized to target almost any type of analyte, such as proteins, drugs, peptides, lipids, live cells, or microorganisms.

There are several approaches to surface biofunctionalization. Physical adsorption is the most basic method of functionalizing sensors. It is the mechanical placement of the receptors on the sensor surface only supported by the electrostatic and hydrophobic interactions. This fast technique is favored due to its simplicity; however, it does not result in a uniformly oriented and densely packed layer of antibodies, and the outcome is not reproducible and stable (Figure 1-15a). The microwell plates used in enzyme-linked immunosorbent assays (ELISAs), the most common analytical biochemistry assay, are physisorption-functionalized [122].

The chemisorption process is another frequently utilized method for biofunctionalizing plasmonic sensors. Specifically, a sulfur-gold anchor chemically binds the receptors to the gold surface through thiol groups.

Proteins are usually rich in thiol groups. In fact, the proteins of every known organism have cysteines in their structure. Having a thiol group, cysteine can chemically bond to the surface of gold. This fast methodology is more efficient than physisorption and results in a more stable receptor layer (Figure 1-15b) [123], [124].

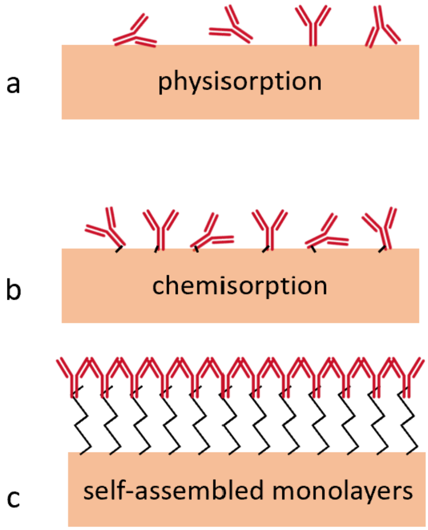

Figure 1-15 Surface biofunctionalization strategies. (a) Physisorption (b) Chemisorption, and (c) self-assembled monolayers. The red Y-shape molecules represent antibodies.

Another approach is to use an intermediate layer, such as a polymeric matrix or a homogenous monolayer, between the sensor's surface and the antibodies (Figure 1-15c). For gold surfaces, dextran-based polymers and alkanethiol self-assembled monolayers (SAMs) are the most frequently used functional chemical scaffolds [125]. For silicon-based sensors, the functionalization, which is called the silanization process, is usually done by covering the surface with alkoxysilane molecules via forming covalent -Si-O-Si- bonds [126], [127].

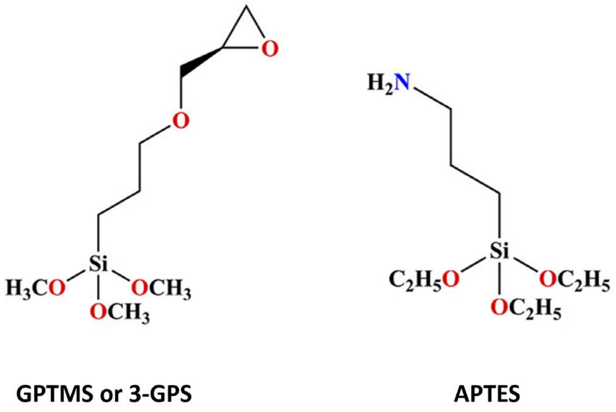

Figure 1-16 The most frequently used molecules for the silanization process to form a self-assembled monolayer on the silica surface, 3-glycidyloxypropyl trimethoxysilane (GPTMS or 3-GPS) and 3-Aminopropyl triethoxysilane (APTES). Reproduced with permission from reference [126]

The formation of a SAM with terminal functional groups has proven to be the most robust and versatile method of functionalization. Using the terminal functional groups of the intermediate SAM layer, bioreceptors may be anchored through covalent cross-linking or through high-affinity molecular systems [125]. The well-controlled and highly reproducible technique provides stable, highly oriented and densely packed immobilization of analytes with minimized nonspecific adsorption (Figure 1-15 c) [128]. 3-glycidyloxypropyl trimethoxysilane (GPTMS or 3-GPS), an epoxysilane and 3-Aminopropyl triethoxysilane (APTES), an amino silane, are two most common coupling agents for the silanization (Figure 1-16).While the epoxy ring of the GPTMS reacts with the amine group of the antibodies, the amine-amine binding (e.g., cross-linking methods) can be employed to chemically link the antibody to APTES [126], [127].

1.2.3 Optical interrogation strategies

When the pre-functionalized surface of the biosensors comes in contact with a biosample, the target analyte specifically binds to the associated biorecognition element immobilized on the sensor surface. (Figure 1-17) The analyte delivery can be done in a static format or in a flow, which requires microfluidics integration.

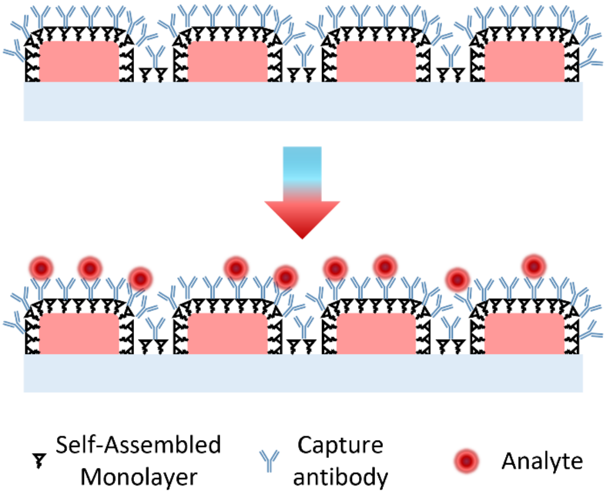

Figure 1-17 Schematic representation of analyte bindings to the pre-functionalized resonators.

The analyte bindings on the surface of the resonators modify the optical characteristics of the biosensors. In fact, the electromagnetics hotspots close to the surface of the resonators are highly sensitive to the local changes in the refractive index in the vicinity of the nanoresonators. This induces a shift in the resonance wavelength of the biosensor that is proportional to the concentration of the analyte. The resonance shift can be plotted against the analyte concentration to build a calibration curve for the sensing device. This detection scheme is known as refractometric biosensing. There are three fundamental interrogation methods within the context of refractometric biosensors: spectral, intensity, and phase (Figure 1-18) [129].

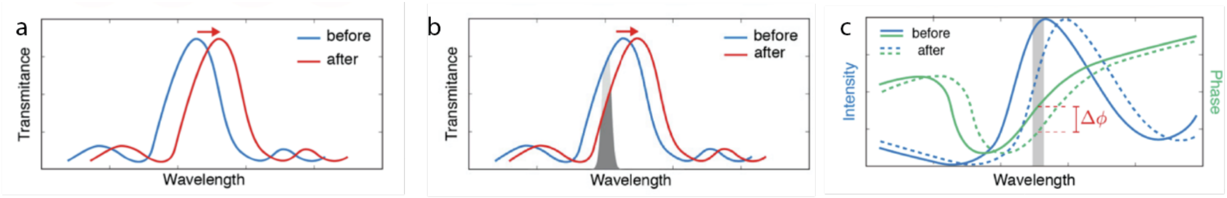

Figure 1-18 Fundamental interrogation techniques. Schematically represents (a) spectral, (b) intensity and (c) phase interrogation. Reproduced from the open-access article in reference [129].

Spectral interrogation is the most traditional optical strategy for the characterization of nanophotonic sensors. The light transmitted through or reflected from the nanophotonic device is analyzed to measure its frequency-dependent intensity. This procedure which is known as spectroscopy is conventionally done using spectrometers. In end-point measurements, the transmission or reflection spectrum before and after the introduction of the analytes are compared to extract the spectral shift caused by the binding events. (Figure 1-18a) It is also possible to record a series of spectra in specific time-intervals for real-time measurements of the binding events.

The most basic spectroscopy is single-point spectroscopy, in which a broadband light illuminates the sensor area. The light passing through a specific location on the nanophotonic device is averaged and analyzed as one data point. The spatial data from the illuminated region, which its size depends on the field of view, is lost due to the averaging. The pioneering works implementing dielectric metasurfaces for refractometric biosensing used this interrogation method [130], [131]. It is also possible to perform imaging spectroscopy by incorporating a slit to narrow the light beam entering the spectrometer. Thereafter, the beam is dispersed by a grating and projected on a two-dimensional imager [132]–[134]. To exploit the full extent of the data-rich light beam passing through an area on the nanophotonic biosensor, hyperspectral imaging is explored, which does not require spectrometers [135], [136]. In hyperspectral imaging, a two-dimensional imager records the transmitted (reflected) light through (from) the biosensors while the narrowband illumination wavelength is swept. This technique provides spatially resolved spectral information from the field of view with the imager pixel resolution [12]. Chapter 3 introduces an ultrasensitive hyperspectral imaging and biodetection platform enabled by dielectric metasurfaces. Moreover, there are some efforts in designing multi-resonant nanophotonic sensors with encoded spectral info to enable single-wavelength measurements granting spectral information, thus simplifying the optical setup [12], [137]. In these settings, pre-recorded data is required to decode the spectral information.

Intensity interrogation is another possible detection scheme with attractive potentials such as simplicity, miniaturization, and low cost because it does not require bulky and expensive spectrometers. In this setting, a narrowband light source, spectrally positioned at the slope of the resonance, illuminates the sensing chip, and the transmitted (reflected) light is recorded by a simple imager. The resonance shift due to the analyte binding results in an intensity change in the optical readout that can be used to make a calibration curve (Figure 1-18b) [138]–[141]. Despite their compelling optical setup, the performance of such platforms is strongly affected by the noise of the system and is not as reliable as spectral interrogation biosensors [8]. A novel methodology incorporating algorithm-aided imaging is proposed in Chapter 4 to fuse the simplicity of intensity-based interrogation with the robustness of spectroscopic biosensing using a pre-recorded spectral decoder [8]. Moreover, an alternative optical setup is suggested in Chapter 5 to enable on-site characterization of the biosensors and remove the need for pre-recorded data [142].

An alternative optical signal transduction mechanism for plasmonic sensing is phase interrogation, which measures phase retardations of electromagnetic wavefronts. Using phase rather than intensity in optical detection has improved microscopy of thin and transparent objects [143], [144] and elucidated the crystal structures of atomically thin layers in the field of X-ray diffraction [145], among many other applications [146]. Phase-based detection was introduced into SPR technology by Kabashin et al [147] to exploit phase shifts varying sharply at plasmonic resonances, first reported by Abeles et al [148] Conventional light sources suffer from high-intensity (amplitude) noise, which in turn reduces the detection sensitivity of intensity-based plasmonic sensors. Instead, phase detection allows for lower noise and versatile signal-processing possibilities, such as spatial and temporal mapping due to the inherent relative measurement of phase with respect to a reference beam [149]. Moreover, in the traditional intensity-based setting, sensing is done at wavelengths that correspond to the side slopes of resonant modes rather than at center wavelengths where the intensity varies minimally as the resonance shifts. Despite that, the side slopes of the intensity spectrum change moderately when compared to the abrupt change that the phase spectrum exhibits at the center of the modes. Therefore, the phase response of the plasmonic sensors allows for superior refractive index sensing [150] (Figure 1-18c) [1].

1.3 Thesis outline

Chapter 1 is the opening to the thesis, starting with introducing biosensors and their multiple applications. The chapter emphasizes the importance of biosensors for the health sector and introduces some disease biomarkers. It covers different types of biosensors, including optical biosensors, specially plasmonic and dielectric metasurfaces, for sensing applications. The chapter is concluded by introducing nanofabrication techniques, surface functionalization methodologies, and optical interrogation strategies for nanophotonic biosensors. The content of this chapter is adapted with permission from references [1] and [2].

Chapter 2 discusses label-free sensing using dielectric metasurfaces through the use of three independent schemes, surface-enhanced spectroscopy through Raman scattering and infrared absorption, chiral sensing, and refractometric sensing. The refractometry sensing is the basis of the following chapters. The content of this chapter is adapted with permission from reference [2].

Chapter 3 introduces a hyperspectral imaging platform leveraging novel data processing techniques for end-point biomolecule detection in the context of refractometric biosensing using dielectric metasurfaces. This chapter presents the first major set of results of this thesis achieved using high-quality-factor resonances rooted in the physics of bound-states-in-the-continuum. The high-quality-factor dielectric metasurfaces are studied numerically, characterized experimentally, and utilized to perform biosensing experiments detecting even highly diluted biosamples. The content of this chapter is adapted with permission from reference [12].

Chapter 4 presents the second major set of results of this thesis. High-quality factor dielectric metasurfaces are leveraged to build an imaging-based spectrometer-less optofluidic platform for detecting cancer-related biomarkers in real time. The dielectric metasurfaces are studied numerically, characterized experimentally, and utilized to perform real-time inflow experiments. Through innovative data processing methods, the intensity readouts of the inflow experiments are translated into highly robust estimated spectral shifts to yield clinically relevant results. The content of this chapter is adapted from the open-access article in reference [8].

Chapter 5 focuses on the investigation of the resonance features and characteristics of the symmetry-broken dielectric metasurface. This chapter covers the influence of the asymmetry parameter, finite sensors size, and the angular dispersion of the metasurfaces and suggests an alternative technique for in-situ characterization of the single-wavelength imaging-based biosensors. The content of this chapter is adapted with permission from reference [142].

Chapter 6 summarizes this thesis's experimental results and the achieved goals, then briefly discusses the outlook for the dielectric metasurfaces for sensing applications. The content of this chapter is adapted with permission from references [2].

Chapter 2 Dielectric metasurface-based optical biosensors

Disclaimer: The content of this chapter is from reference [2], adapted with permission. Copyright {2021} American Chemical Society.

- Reference[2]: Dielectric Metasurfaces Enabling Advanced Optical Biosensors. ACS Photonics 8, 47-60 (2021).
  Authors: Ming-Lun Tseng*., **Yasaman Jahani***, Aleksandrs Leitis*, Hatice Altug.
  Jahani 's Contribution:
  *These authors contributed equally to writing this perspective review

Dielectric metasurfaces have emerged as a powerful platform for novel optical biosensors. Due to their low optical loss and strong light-matter interaction, they demonstrate several exotic optical properties, including sharp resonances, strong near-field enhancements, and the compelling capability to support magnetic modes. They also show advantages such as CMOS-compatible fabrication processes and lower resonance-induced heating compared to their plasmonic counterparts. These unique characteristics enable the advancement of cutting-edge sensing techniques for new applications. The working mechanisms and properties of dielectric metasurfaces are briefly introduced by highlighting several state-of-the-art examples in the previous chapter. In this chapter, we review the recent progress of dielectric metasurface sensors. We describe the application of dielectric metasurfaces for label-free sensing in three different detection schemes, namely, surface-enhanced spectroscopy through Raman scattering and infrared absorption, chiral sensing, and refractometric sensing. In chapter 6, we provide a perspective for the future directions of this exciting research field.

2.1 Surface Enhanced Spectroscopy

Vibrational spectroscopy is a method for biomolecule sensing , which allows not only to detection of surface-bound molecules but also provides chemically specific information about each analyte. Spectroscopy techniques, like Raman and IR absorption spectroscopies, enable label-free sensing and monitoring of chemical reactions and interaction kinetics between various analytes. Raman spectroscopy probes molecular vibrations via the inelastic scattering mechanism of the photons, while IR spectroscopy accesses the chemical information via light absorption measurements. Although these techniques have been well established for chemical analysis, they are fundamentally limited by the low sensitivity, which arises from a weak light-matter interaction in the IR spectral region and a low molecule cross-section for Raman scattering. Therefore, the study of low-concentration analytes is challenging when using conventional spectroscopy methods. This problem can be addressed by employing nanophotonic enhancement from well-designed metasurfaces through surface-enhanced Raman spectroscopy (SERS) [63], [151] and surface-enhanced infrared absorption spectroscopy (SEIRAS) [62], [68], [152].

Heretofore, SERS has been realized mainly with metallic nanostructures [71], [153]–[156] and metasurfaces [157]–[159], which provide strong near-field enhancement. Although their surface enhancement effectively improves the signals, still high laser intensity and tight light focusing on the metasurface are needed. This causes intense heating in metal-based metasurfaces, which can cause damage to the biomolecules [160], [161], change in the local refractive index [162], or even deform the metasurface itself [163]. Therefore, SERS measurements with metal-based metasurfaces are prone to repeatability issues [151]. Recently, dielectric metasurfaces have emerged as an alternative to plasmonic-based metasurfaces for Raman spectroscopy. The near-zero absorption losses in the constituent materials of dielectric metasurfaces allow reducing the generated heat, while the high refractive index enables profound light confinement. An example is presented by Caldarola et al. using a metasurface consisting of a Si dimer array on a Si-on-insulator substrate (Figure 2-1a) [164]. It was successfully implemented for SERS to detect a thin layer of polymethyl-methacrylate (PMMA) coated on the metasurface. A similar Si dimer metasurface was fabricated on a sapphire substrate to detect a self-assembled monolayer of β-carotenal molecules (Figure 2-1b) [165]. Here, the chemically specific β-carotenal signal appears as two pronounced Raman peaks located at 1150 and 1520 cm^{-1}. To further improve the nanophotonic enhancement, a metasurface that sustains quasi-BIC (Q > 103) modes was exploited [166]. It consists of an array of nanoholes in a Si_3N_4 slab and shows Raman enhancement factors larger than 103 for crystal violet molecules (Figure 2-1c). Although there have been initial efforts toward dielectric metasurfaces for SERS, metal-based antennas still provide higher field enhancements and improved SERS signals. Nevertheless, dielectric metasurfaces could be further improved, for instance, by optimizing the designs of the meta-atoms that sustain high-Q resonances and support the highest near-field enhancements outside the resonator volume. In this way, the near-fields can be accessed by the biomolecules and eventually results in higher SERS signals. Furthermore, the wide variety of accessible dielectric materials enables diverse surface functionalization methods for analyte binding [167] and increased chemical enhancement [161].

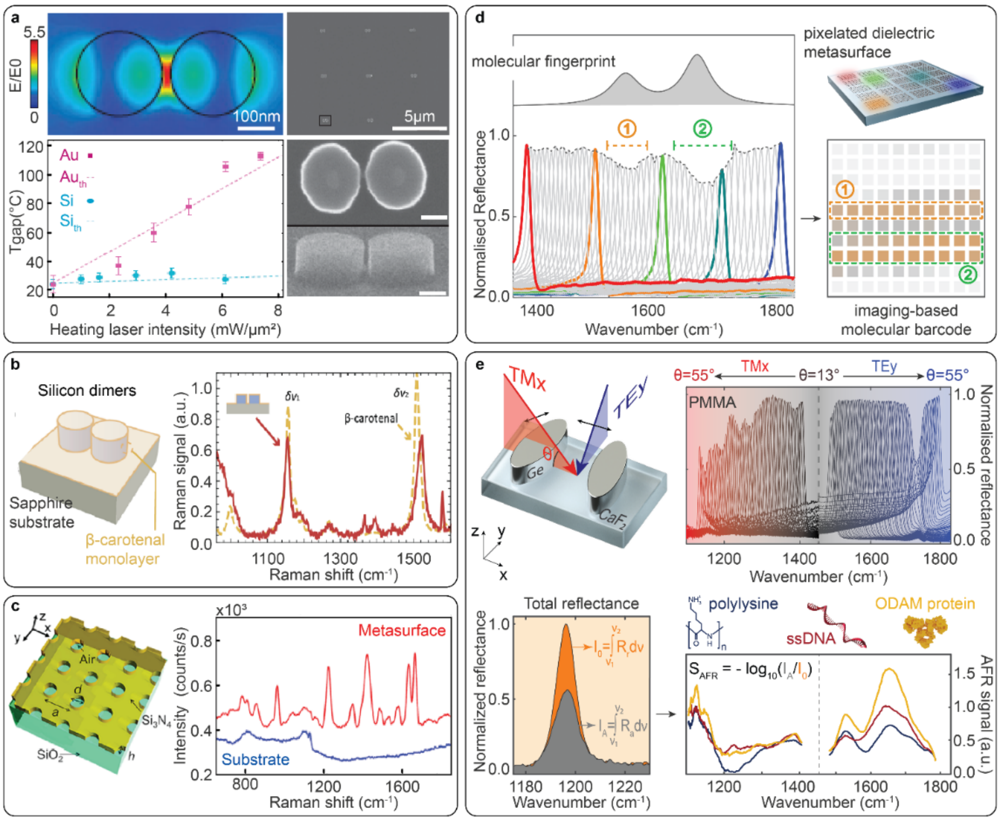

Figure 2-1 Dielectric metasurfaces for surface-enhanced spectroscopy. (a) Left panel: Electric field enhancement in a Si dimer structure and the temperature dependence on the laser intensity [164]. Right panel: SEM images of Si dimers where the scale bar on the bottom micrographs is 100 nm. (b) SERS signal of β-carotenal monolayer using Si dimer metasurfaces [165]. (c) SERS enhancement of crystal violet molecules using high Q-factor nanohole metasurfaces [166]. (d) Top panel: Illustration of pixelated metasurface and unit cell coated with protein molecules. Bottom panel: Measurements of high Q-factor metasurface response after protein monolayer deposition and imaging-based molecular fingerprint detection [168], [169]. (e) Top panel: unit cell of a Ge metasurface and the spectral response for each light incidence angle. Bottom panel: spectral integration signal that emulates the total reflectance signal and the measured absorbance signals from polylysine, ssDNA aptamers, and ODAM proteins [170]. (a) is reproduced with permission from reference [164]. Copyright 2015 Nature Publishing Group. (b) is reproduced with permission from reference [165]. Copyright 2018 ACS. (c) is reproduced with permission from reference [166]. Copyright 2018 ACS. (d) is reproduced with permission from reference [168], [169]. Copyright 2018 AAAS and the authors. (e) is reproduced with permission from reference [170]. Copyright 2019 AAAS.

Similar to SERS, SEIRA measurements have been performed mostly by using metal-based metasurfaces. The plasmonic antennas are well suited for signal enhancement; however, even in the IR spectral region, they are fundamentally limited by Ohmic losses. This significantly broadens their resonances and results in higher Full-Width-at-Half-Maximum (FWHM) when compared to the molecular absorption bands. Therefore, to be able to detect infrared absorption bands and obtain chemical information, bulky spectroscopic equipment is usually required [171]. Dielectric materials empower the realization of higher Q-factor resonances in the mid-IR, where the FWHM of the resonance is sharper than the molecular absorption bands of the bioanalytes. This property allows targeting the molecular absorption bands with better spectral selectivity while maintaining high sensitivity [172]. High Q-factor metasurfaces for SEIRA and their implementation in a large-area imaging configuration was first demonstrated by Tittl et al. In order to maintain a broad bandwidth, they utilized a two-dimensional (2D) array of pixelated metasurfaces over a large-area such that each "metapixel" of the array is tuned to a specific resonant frequency due its high Q-factor and spectrally clean optical response. This feature provided a one-to-one mapping between the spectral and the spatial information and enabled access to the molecular signals across an extended wavelength range at high sensitivity (Figure 2-1d) [168], [169]. Interestingly, with this 2D pixelated metasurface method, the absorbance of the surface-bound analytes (e.g., monolayered protein, see the bottom panels of Figure 2-1d) can be extracted directly from the total reflectance signals, thus eliminating the need for expensive spectroscopy equipment or tunable light sources. Another approach based on high-Q dielectric metasurfaces was demonstrated by Leitis et al. (Figure 2-1e), where the resonance of a single metasurface was tuned by light incidence angle and polarization to retrieve molecular fingerprint information over a broad spectrum ranging from 1100 to 1800 cm^{-1} (i.e., ~5 to ~9 µm in wavelength) [170]. The ellipse-shaped meta-atoms used in both works provide the maximum near-field enhancement at their tips, where the adjacent bioanalytes can interact with the light. Therefore, it enables chemical fingerprint detection with high sensitivity only using broadband light sources and detectors. This method allows for combining the device-level simplicity of the state-of-the-art angle-scanning refractometric sensors with the chemical specificity of infrared spectroscopy. An example of using this metasurface-equipped system for detecting polylysine, single-stranded DNA, and human odontogenic ameloblast-associated proteins (ODAM) is presented in the bottom panel of Figure 2-1e. The high-Q dielectric metasurfaces hold great potential for miniaturizing IR sensors, which could be well suited for point-of-care devices.

2.2 Chiral Sensing

Chirality, a geometric symmetry property in objects, gives rise to pivotal physical and chemical properties and plays a significant role in protein function, cell communication, and in general human physiology. Many naturally occurring biomolecules and drugs are present either in left- or right-handed forms, that is, enantiomers. They can show significant divergences in their metabolic uptake, treatment potential, and toxicologic effects. It has been demonstrated that distortions in the chiral-molecular structure participate in the appearance of neurodegenerative and neuropsychiatric disorders such as Alzheimer's and Parkinson's diseases [173]–[175].

Chiral molecules manifest their chiral attributes when interacting with the chiral state of light, that is, circularly polarized light (CPL). As a result, discrimination of enantiomers can be performed, observing their differential absorption of left and right CPL, conventionally done with circular dichroism (CD) spectroscopy. However, CD spectrometers are sophisticated, bulky, and expensive; hence, their widespread use is hindered by the intrinsically weak chiroptical signals of most small molecules.

Metasurfaces can reinforce the light-matter interaction in chiral sensing by creating so-called superchiral fields with large concentrations of optical chirality, C, defined as

$$C\{E,H\} = \frac{-k_0}{2c_0} Im\{E \cdot H^*\}$$

Equation 2-1 Optical chirality

Here k0 and c0 stand for the wavenumber and speed of light in free space, respectively, while E and H represent the complex electric and magnetic fields [176]. Mohammadi et al. formulated an analytical model to explain the interplay of the characteristics and the performance of an arbitrary metasurface to elucidate the key parameters in their design and unravel the involved trade-offs. The analytical model defines the criteria of the best-performing chirality detection by the nanophotonic platform as follows: (i) Removing the background signal emanated from the sensing device and taking into account the attenuation role of its chiral absorption; (ii) Equal intensity enhancement factors for the right and left CPL to remove the permittivity dependence of the total output signal; (iii) High optical chirality to maximize the output signal.

Metasurfaces can be designed to offer a strong, uniform, and accessible electromagnetic fields for efficient C intensification. Since planar metallic nanostructures usually show weak responses to the magnetic field of the incident light, complex three-dimensional chiral nanostructures were studied as an alternative for chiral enhancement [177]–[179]. However, the experimental realization of such structures is challenging in the context of nanofabrication. Moreover, such chiral nanoresonators are prone to introduce background signals emanating from the chiral nanostructures, which can obscure the CD signal of the analyte.

In contrast to plasmonics, the strong response of dielectric nanoresonators to both the electric and magnetic fields of light makes dielectric metasurface an attractive choice for chirality enhancement. Mohammadi et al. proposed a planar achiral metasurface made from Si nanodisks to successfully enhance the minuscule tail of CD signal in the technology-friendly range of the spectrum, that is, visible and near IR below 1000 nm [176]. The metasurface provides extremely high CD enhancement of the order of 30. Later, Si nanodisks were used to experimentally differentiate l- and d-phenylalanine from a 200 nm thick molecular thermal evaporated layer yielding a dense film (Figure 2-2a) [180]. The spectrometer-based recorded CD signal showed a strong dependence on the electric dipole. Further investigations by Mohammadi et al. led to the tailoring of the spectrally and spatially overlapped electric and magnetic resonances with a π/2 phase difference to maximize the C enhancement by exploiting the Kerker effect with the duality principle (Figure 2-2b) [181]. The authors proposed a Si-based metasurface consisting of Kerker-inspired holey Si nanodisks (Figure 2-2c), [181] which provide uniformly distributed and accessible superchiral near-fields to enhance the differential absorption (also transmission) by a factor of 24.

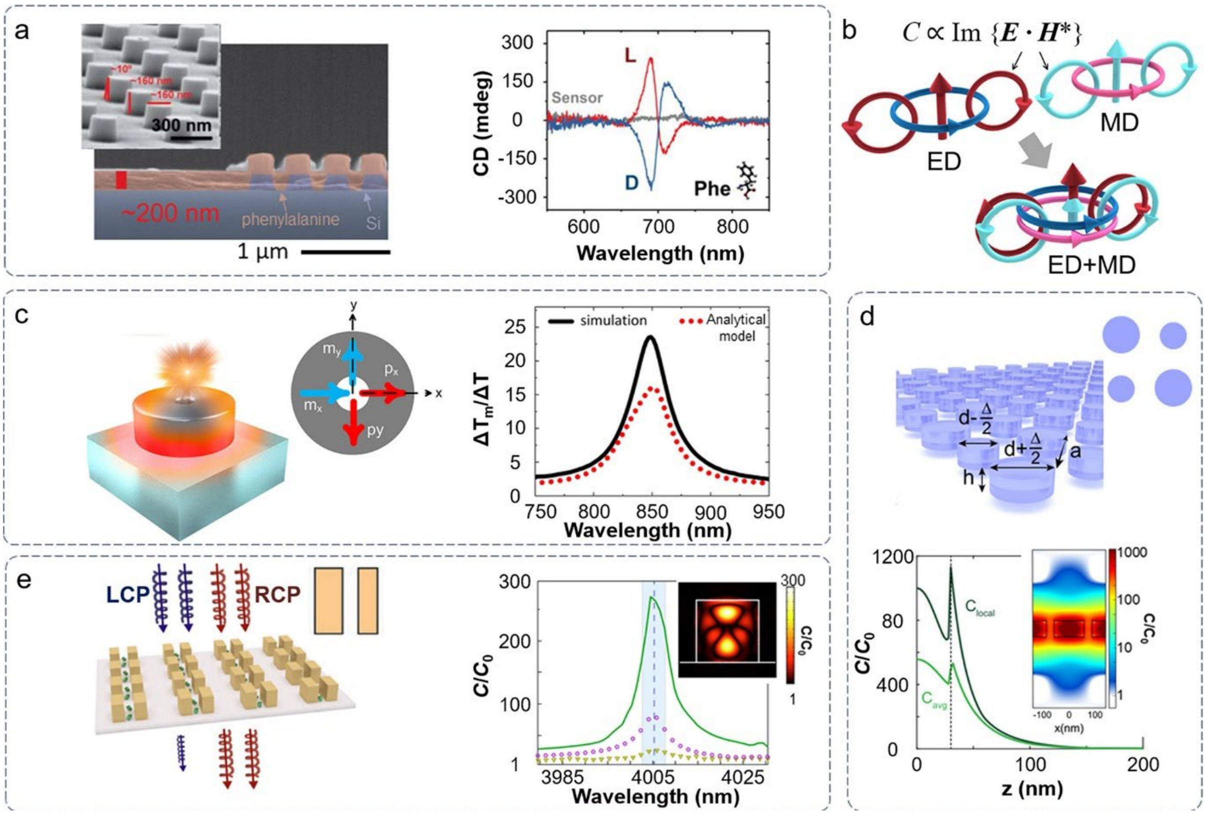

Figure 2-2 Chiral sensing using dielectric metasurfaces. (a) Left panel: A side-view SEM image of Si nanodisks covered with a dense 200 nm thick phenylalanine film [180]. Right panel: CD signals differentiating molecular enantiomers of phenylalanine using Si nanodisks [180]. (b) Schematic of generating a superchiral field using the electromagnetic duality principle [181]. (c) Schematic of a-Si disk nanostructure with a hole for Kerker-inspired optical chirality enhancement [181]. The plot on the right shows normalized differential transmission from numerical and analytical studies [181]. (d) A dielectric metasurface for chiral field enhancement, based on the asymmetric diamond disk array, capable of boosting the near-field in the UV spectrum [182]. The bottom plot shows its optical chirality enhancement. (e) Asymmetric PbTe bars proposed for VCD measurements by optical chirality intensification [183]. The plot on the right depicts the local optical chirality enhancement. (a) is reproduced with permission from reference [180]. Copyright 2020 ACS. (b) and (c) are reproduced with permission from reference [181]. Copyright 2019 ACS. (d) is reproduced with permission from reference [182]. Copyright 2019 ACS. (e) is reproduced with permission from reference [183]. Copyright 2019 the authors.

The maximum chiroptical signature of most small molecules takes place in the UV and IR spectrum termed electronic and vibrational CD (VCD), respectively. Hence, exploiting the capabilities of the nanophotonic platforms in these ranges enlightens the enhancement mechanisms and performances of such devices. A biperiodic diamond disk metasurface in Figure 2-2d was proposed theoretically to enhance the averaged C for more than 2 orders of magnitude in the UV, while the local C enhancement reached 1100 [182]. The Q factor of a resonance correlates with the C enhancement due to its contribution to concentrating the electromagnetic fields. In another theoretical work, a metasurface made of PbTe nanodimers (Figure 2-2e) was conceived to support quasi-BIC modes in mid-IR, [183] exhibiting a resonance with a Q factor of 800 and a local C enhancement of 270 for VCD measurements. Dielectric metasurfaces offer exciting prospects toward developing high-performance sensing devices for easy, fast, and economical stereoisomers differentiation, which is of great importance for the pharmaceutical industry.

2.3 Refractometric Biosensing

The strong Mie-type resonances in dielectric metasurfaces provide near-field hotspots giving rise to pronounced light-matter interactions with the analytes in the vicinity of the resonators. By carefully tailoring the metasurface design, the resonance can be sensitive and responsive to the optical properties of the surrounding media. Analyte binding on the resonators creates local changes in the refractive index, which can be detected and quantified by tracking the resonance wavelength or the induced changes in the transmission or reflection intensity. Sensitivity is a measure of the extent of the resonance shifts for a given change in the refractive index, which depends on the material, geometry, and arrangement of the nanostructures. A comprehensive parameter to appraise the performance of refractometric biosensors is figure-of-merit (FOM), defined as the ratio of the sensitivity divided by the FWHM of the resonance; thus, FOM depends on the Q factor.

One of the initial works of dielectric metasurfaces for biosensing was demonstrated by Si nanodisks for end-point measurements [130]. The metasurface was fabricated by electron beam lithography (EBL) and operated in the telecommunication wavelength regime where Si is nearly lossless. The authors used a spectrometry system to track the resonance wavelength shift. The biosensor shows a resonance at around 1488 nm with a Q factor of 25. It is capable of detecting down to 5 ng/mL of streptavidin when the surface is functionalized with Biotin molecules. Later, EBL-fabricated Si nanodisk structures, optimized for shorter near-IR wavelengths, were integrated with microfluidics to perform bulk refractive index sensing as well as prostate-specific antigen (PSA) detection in a sandwich assay, leveraging single-point spectroscopy [131]. Figure 2-3a shows the microfluidic structure, a close view of eight independent sensing channels, and an SEM image of the Si nanodisks. The setup was equipped with a stage scanning system to acquire data from multiple spatial points on the sensing chip sequentially. The nanodisks, manifesting Mie-type resonances at 844 nm, with a Q factor of 20, bulk sensitivity as high as 227 nm/RIU, and in turn, FOM of 5.4 1/RIU, were reported to have a LOD down to 0.69 ng/mL of PSA when a second antibody was used to amplify the signal (Figure 2-3b). The extinction spectra of the nanodisks in contact with various concentrations of glucose solutions are shown in Figure 2-3c. The sensing performance of the Si nanodisks was compared with the gold nanorod arrays under the same conditions except for the surface chemistry. The normalized calibration curves for both platforms detecting PSA in a sandwich assay are shown in Figure 2-3d. The dielectric metasurface offers a better LOD compared to the plasmonic counterpart, while the plasmonic nanorods afford a wider dynamic range.

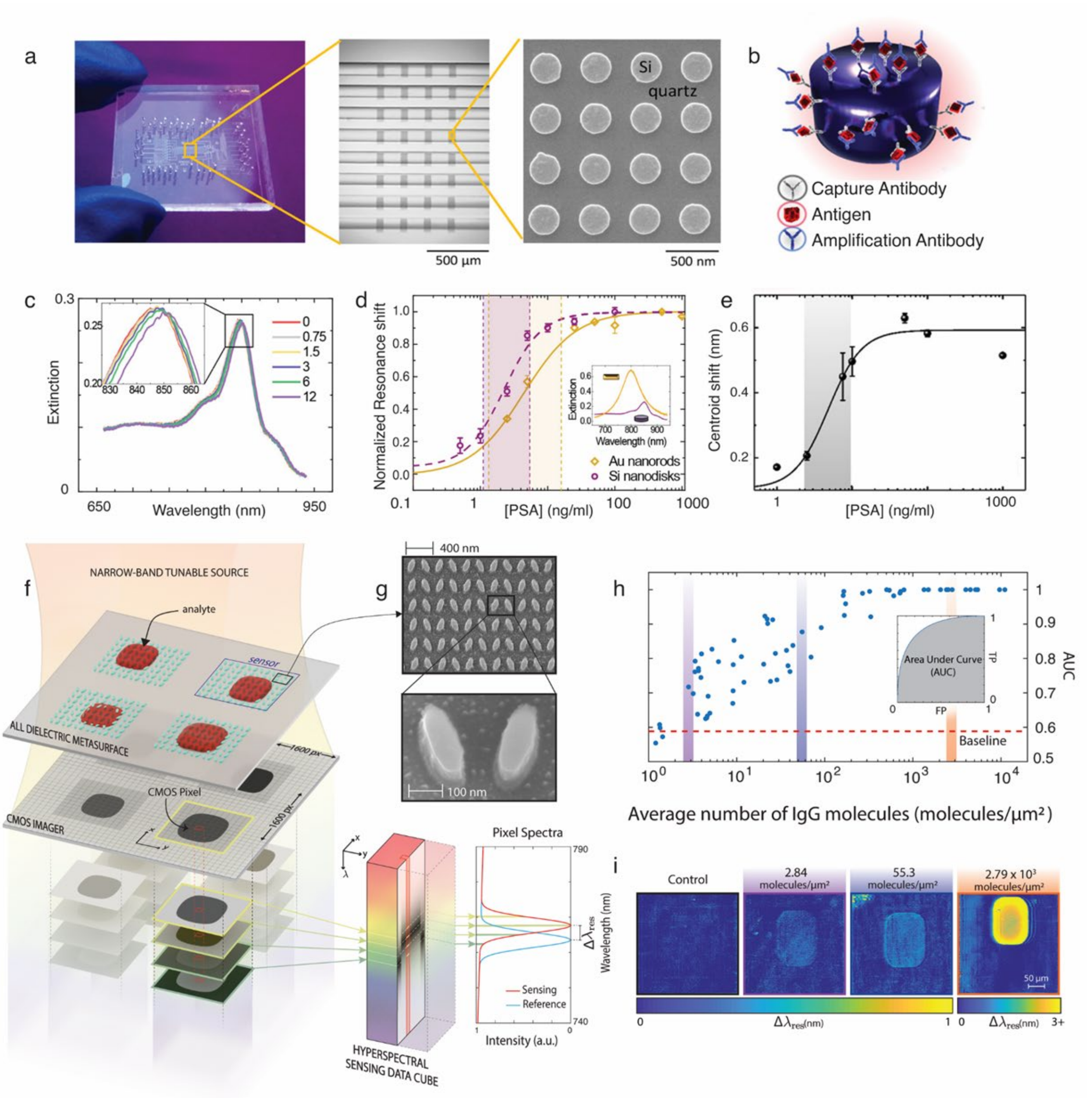

Figure 2-3 Refractometric biosensing metasurfaces. (a) Picture of a multichannel microfluidic chip (left) with a close-up picture of the eight flow channels showing multiple sensors (middle) and an SEM image of a Si nanodisk metasurface (right) [131]. (b) Schematic of a sandwich bioassay on a Si nanodisk.[184] (c) Extinction spectra of a nanodisk array exposed to six different glucose water mixtures [131]. (d) Normalized calibration curve of the centroid shifts for PSA detection with Si nanodisks and gold nanorods using a sandwich immunoassay for signal amplification. Error bars represent the replicas of the measurement on the same chip. The inset illustrates the extinction spectra of the Si nanodisk arrays and gold nanorod arrays [131]. (e) Calibration curve of the centroid shifts for PSA detection with semi-random Si nanocylinders [184]. (f) Principle of hyperspectral imaging-based biosensing using tilted Si nanoellipses [12]. (g) SEM images of the tilted nanoellipse metasurface (top) and its unit cell (bottom) [12]. (h) The area under the curve (AUC) values of all receiver operating characteristic (ROC) curves show the detection of biomolecules at low concentrations [12]. (i) Resonance shift map for a control measurement, detection of two low concentrations of IgG molecules, and a high concentration of the biomolecule from left to right, respectively [12]. (a), (c), (d) are reproduced with permission from reference [131]. Copyright 2017 ACS. (b) and (e) are reproduced with permission from reference [184]. Copyright 2019 ACS. (f)-(i) are reproduced with permission from reference [12]. Copyright 2019 Nature Publishing Group.

In another effort, semi-random Si nanocylinder arrays were fabricated using colloidal lithography as an effective technique to fulfill the need for low-cost and scalable metasurface-based biosensors that are suitable for lab-on-a-chip systems [184]. The structures exhibit a Mie-type resonance at 900 nm in water with a Q factor of slightly lower than the EBL fabricated nanodisks mentioned above and a bulk sensitivity of 86 nm/RIU. The metasurface was assembled to a microfluidic-based spectroscopic platform equipped with spatial scanning arrangements to detect PSA in a sandwich assay. The experimental data are represented both in terms of resonance centroid shift in spectroscopic interrogation and extinction reduction in ensemble-averaged intensity interrogation. They observed that the latter approach provides a wider dynamic range and a lower LOD. The calibration curve for the resonance centroid shift, shown in Figure 2-3e, characterizes the sensor with an LOD and a dynamic range of 1.55 ng/mL and 2.35 - 9.79 ng/mL, respectively, while the intensity interrogation achieved an LOD and a dynamic range of 0.83 ng/mL and 1.87 - 30 ng/mL, correspondingly. The results suggest that further investigations of the intensity interrogation methods are essential toward realizing high-performance spectrometerless biosensing platforms for point-of-care (POC) devices. In the intensity interrogation methods, the spectral location of the resonance also gains special attention as the working wavelength range under 1000 nm allows the use of standard low-cost Si cameras for compact and affordable integrated lab-on-chip systems towards democratization of health care in resource-limited settings.

High-Q factor metasurfaces are favorable for upsurging the sensitivity of refractometric biosensors and for bringing in new functionalities. As an example, a high-Q factor Fano-resonant metasurface [185] consists of symmetry-broken Si nanoresonators, working in the telecommunication wavelength range, was proposed to exhibit a bulk sensitivity as high as 289 nm/RIU and an FOM of 103. Moreover, metasurfaces supporting quasi-BIC offer high-Q factor resonances manifested as supercavity modes. Recently, BIC-type dielectric metasurfaces were used in combination with hyperspectral imaging to perform ultrasensitive biomolecule detection.[12] The unit cell is comprised of EBL fabricated pairs of Si nanoellipses that are tilted around their y-axis in mirror symmetry (Figure 2-3g). The metasurface exhibited a resonance dip around 855 nm for measurements in aqueous media, a Q factor as high as 144, and a bulk sensitivity of 263 nm/RIU. The hyperspectral imaging platform shown in Figure 2-3f consists of a supercontinuum laser source coupled to a narrowband tunable filter for high spectral resolution ($\Delta\lambda$ = 0.1 nm) acquisition. The resonance wavelength range of the metasurface allows the use of a large-area CMOS camera to image simultaneously multiple sensor units on the chip. The transmission spectrum of each sensor is extracted from the hyperspectral data cube with high spatial resolution and processed to create a resonance map, which provides the resonance wavelength at each pixel. The spatially resolved resonance shifts caused by the analyte binding on the resonators are extracted from the resonance shift maps that are computed by subtracting the resonance maps of the metasurface with and without the analyte. For highly diluted analytes, due to the stochastic nature of the binding events, the low number of molecules does not induce measurable spectral shifts, while analyte presence can be confirmed visually from the extracted resonance shift maps (Figure 2-3i). To exploit this feature for high-performance sensing, a thresholding method called receiver operating characteristic (ROC) curve was implemented, and the results (Figure 2-3h) show the ability to detect IgG molecules as low as 3 molecules per μm^2. The work illustrates the superior sensing performance of the imaging techniques in comparison with the ensemble averaging methods commonly used in conventional spectrometer-based measurements. Moreover, it highlights the unexplored potential of data processing techniques for advanced biosensing. Extracting spectral information from spatial data was also utilized with chirped guided-mode resonant gratings [137]. These structures offering a bulk sensitivity of 137 nm/RIU were used for the detection of IgG molecules from a 500 ng/mL solution. Overall, imaging-based schemes hold great promise for ultrasensitive spectrometerless biosensing toward the realization of the POC devices as enabling key technologies for personalized medicine and global healthcare monitoring.

Chapter 3 Ultrasensitive hyperspectral imaging and biodetection enabled by dielectric metasurfaces

Disclaimer: The content of this chapter is from reference [12], adapted with permission from Springer Nature.

- Reference [12]: Ultrasensitive hyperspectral imaging and biodetection enabled by dielectric metasurfaces. Nat. Photonics 13, 390-396 (2019).

Authors: Filiz Yesilkoy, Eduardo R. Arvelo, **Yasaman Jahani**, Mingkai Liu, Andreas Tittl, Volkan Cevher, Yuri Kivshar, Hatice Altug

Jahani's Contribution:
Nanofabrication and characterization of the all-dielectric metasurfaces.
Carry out simulations to extract the distribution of electric and magnetic fields in the meta-unit
Contribution to the bio-measurements.

3.1 Abstract

Metasurfaces based on resonant subwavelength photonic structures enable novel ways of wavefront control and light focusing, underpinning a new generation of flat-optics devices [186]. Recently emerged all-dielectric asymmetric metasurfaces, composed of arrays of meta-units with broken in-plane inversion symmetry [103], [169], [187]–[190] exhibit high-quality resonances originating from the intriguing physics of bound states in the continuum. Here, we combine dielectric metasurfaces and hyperspectral imaging to develop an ultrasensitive label-free analytical platform for biosensing. Our technique can acquire spatially resolved spectra from millions of image pixels and use smart data-processing tools to extract high-throughput digital sensing information at the unprecedented level of less than three molecules per µm^2. We further show spectral data retrieval from a single image without using spectrometers, enabled by our unique sensor design, paving the way for portable diagnostic applications. This combination of nanophotonics and imaging optics extends the capabilities of dielectric metasurfaces to analyze biological entities and atomic-layer-thick two-dimensional materials over large areas.

3.2 Main

BICs were discovered in quantum mechanics [191], but were later employed as the important physical concept of destructive interference [192], expanding to other fields of wave physics, including optics [193], [194].

In practice, BIC can be realized as quasi-BIC in the form of a supercavity mode [195] when both Q and resonance width become finite at the BIC conditions due to absorption and other perturbations [196]. In contrast to their plasmonic counterparts, dielectric nanoresonators do not suffer from inherent material absorption losses [53], [197] and they can support BIC modes generating extremely sharp resonances and strong light confinement. Importantly, dielectric metasurfaces that exhibit these supercavity modes in visible and near-infrared (NIR) wavelengths can be extremely responsive to the local refractive index (RI) changes induced by individual biomolecules, due to their spatial overlap with the surface-confined electromagnetic fields [198]. This is in contrast to conventional Mie-type resonances in silicon subwavelength nanoparticles [197], which store the field mainly inside the high-index material. Previously, silicon nanostructures with Mie-type resonances in NIR were explored for label-free biosensing [130], [131], where traditional spectrometers were used to monitor resonance shifts from spatially limited regions and to quantify analyte mass accumulation using ensemble averaging. Exploration of the BIC-inspired high-Q modes of dielectric metasurfaces in conjunction with imaging-based, high-content data acquisition and processing has yet to be leveraged to launch nanophotonic biosensors as a game changer in the biomedical sciences.

Here, we propose and demonstrate a novel platform based on all-dielectric metasurfaces, supporting geometrically tunable high-Q BIC-inspired resonances in the NIR, and HSI for massively parallel sensing of trace biomolecules as well as optical characterization of two-dimensional (2D) materials at their relevant atomic dimension scale. Our HSI platform spatially resolves spectral information, generating millions of spectra, each associated to a CMOS sensor pixel, without using spectrometers or mechanical scanning. This is particularly important to achieve extreme sensitivities and throughput via the use of various data science techniques. We demonstrate that by employing a pixel-based thresholding method, the detection limit can be improved by three orders of magnitude when compared to ensemble averaging (~3 versus 1,500 molecules per μm^2). Moreover, we introduce a multi-resonance sensor (MRS) design and the new concept of a hyperspectral decoder, which associates spectral information from each CMOS pixel to its spatial index. With the use of this decoder, we demonstrate that high-resolution spectral data can be retrieved from a single image captured at a fixed wavelength. This scheme eliminates the need for bulky and expensive instrumentation and can be used to realize field-deployable sensors. Finally, we subject our sensor to a single atomic layer of graphene and show that our approach is capable of efficiently probing graphene's optical properties over large areas.

Our nanophotonic device comprises an array of all-dielectric sensors, allowing for multiplexed analyte detection in a single measurement. In our optical set-up, we use a continuously tunable bandpass filter coupled to a supercontinuum laser source for excitation in a robust collinear optical path and record images at each illumination wavelength using a CMOS camera (Figure 3-1a). This optical configuration allows us to spatially probe the metasurface spectral response over large areas, in contrast to traditional spectrometers.[199] Specifically, we use an extremely narrow bandwidth (~2 nm) and tunable excitation with high spectral resolution ($\Delta\lambda$ = 0.1 nm) to build a hyperspectral data cube of the field of view that contains full spectral information from the entire sensor array, where each sensor is mapped by tens of thousands of CMOS pixels. The high-content data generated by this method allows for an unprecedented use of data science techniques to best extract insights and information from each sensor [200]. For example, the data cube can be processed to create a resonance map for each sensor (Figure 3-1b), where an individual image pixel represents an area on the metasurface, and its value corresponds to the center wavelength of the area's resonance. This is particularly important for biosensing because resonance shifts caused by the presence of analytes on the sensor's surface are spatially registered by the resonance maps. These maps are then compared with reference maps, acquired without the analyte, to compute resonance shift maps, where each pixel conveys spectral shift information of its corresponding area on the sensor, as shown in Figure 3-1b.

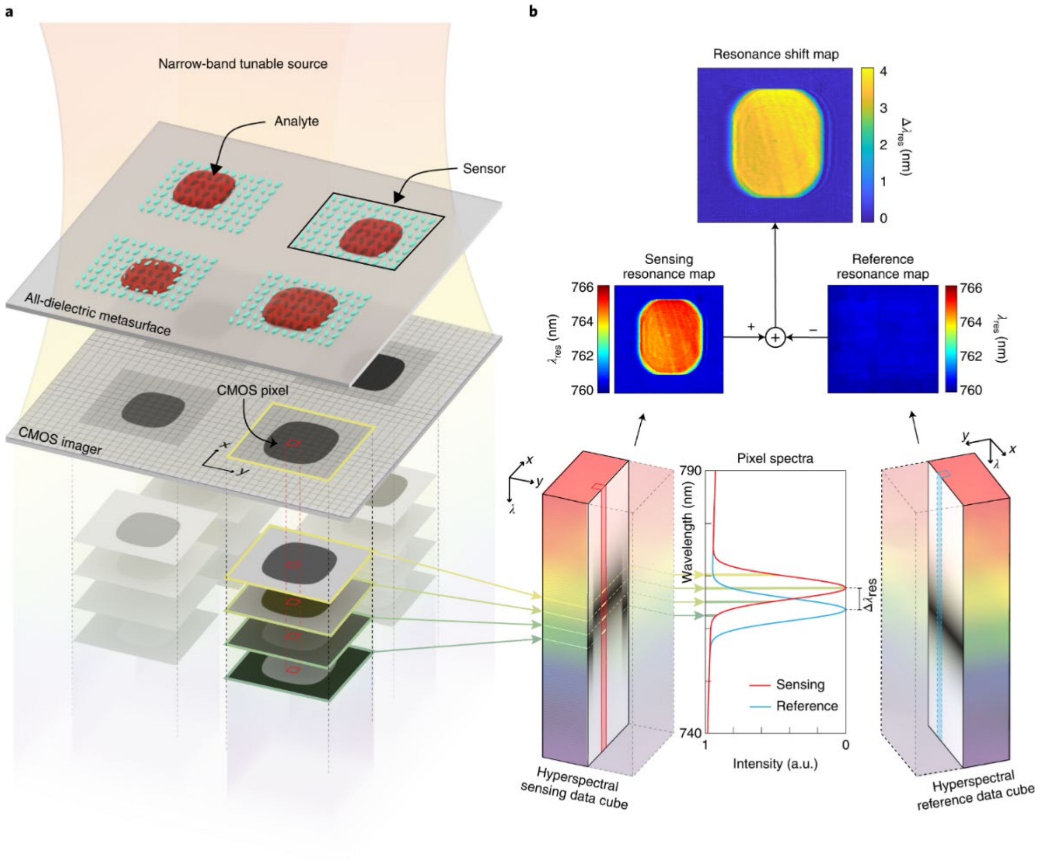
a
Narrow-band tunable source
Analyte
Sensor
All-dielectric metasurface
CMOS pixel
CMOS imager
x
y
b
Resonance shift map
4
3
2
1
0
$\Delta\lambda_{res}$ (nm)
Sensing resonance map
Reference resonance map
766
764
762
760
λ_{res} (nm)
+
−
x
y
λ
Pixel spectra
790
740
Wavelength (nm)
$\Delta\lambda_{res}$
Sensing
Reference
1
0
Intensity (a.u.)
Hyperspectral sensing data cube
Hyperspectral reference data cube

Figure 3-1 Principle of hyperspectral imaging-based biomolecule detection using all-dielectric metasurfaces. (a) Sketch of the hyperspectral imaging principle showing a representative dielectric metasurface sensor array illuminated with narrow-band tunable laser source. At each wavelength illumination, images are recorded by a CMOS camera (1,608 × 1,608 pixels) to create a hyperspectral data cube where each CMOS pixel captures high-resolution spectral information. (b) The hyperspectral data cube is processed to extract spatial resonance maps of each individual sensor. For biomolecule detection, the sensing and reference resonance maps are combined to create the resonance shift map, which conveys spectral shift information across the whole sensor.

Our resonant metasurface consists of pairs of tilted silicon nanobars (Figure 3-2a-f), fabricated using CMOS-compatible processes. Figure 3-2c shows a photograph of a dielectric chip with a 5 × 5 sensor array manufactured by nanostructuring a 100 nm thick amorphous Si film on a glass substrate, followed by dry etching (Supplementary Figure 3-6). SEM images of a meta-unit and metasurface are shown in Figure 3-2a and b, respectively. In our metasurface design, the elliptical Si pairs of nanobars are tilted around the y-axis in mirror symmetry (Figure 3-2d). Normally incident x-polarized light excites the collective lattice resonances, which have their origin in BIC-inspired physics [187], where sharp spectral resonances are controlled by the asymmetry parameter introduced by the tilting angle, such that the Q-factor grows to infinity when the tilting angle vanishes. In our design, we leverage the quasi-BIC states, which are achieved with small but finite values of the tilting angle (17.5°), leading to high-Q and spectrally isolated resonances with high suppression (Figure 3-7). The resulting strong light trapping occurs in such a way that both electric and magnetic fields are localized in the surrounding outer volume of the nanostructures (Figure 3-2f), ideal for sensing applications (Figure 3-8).

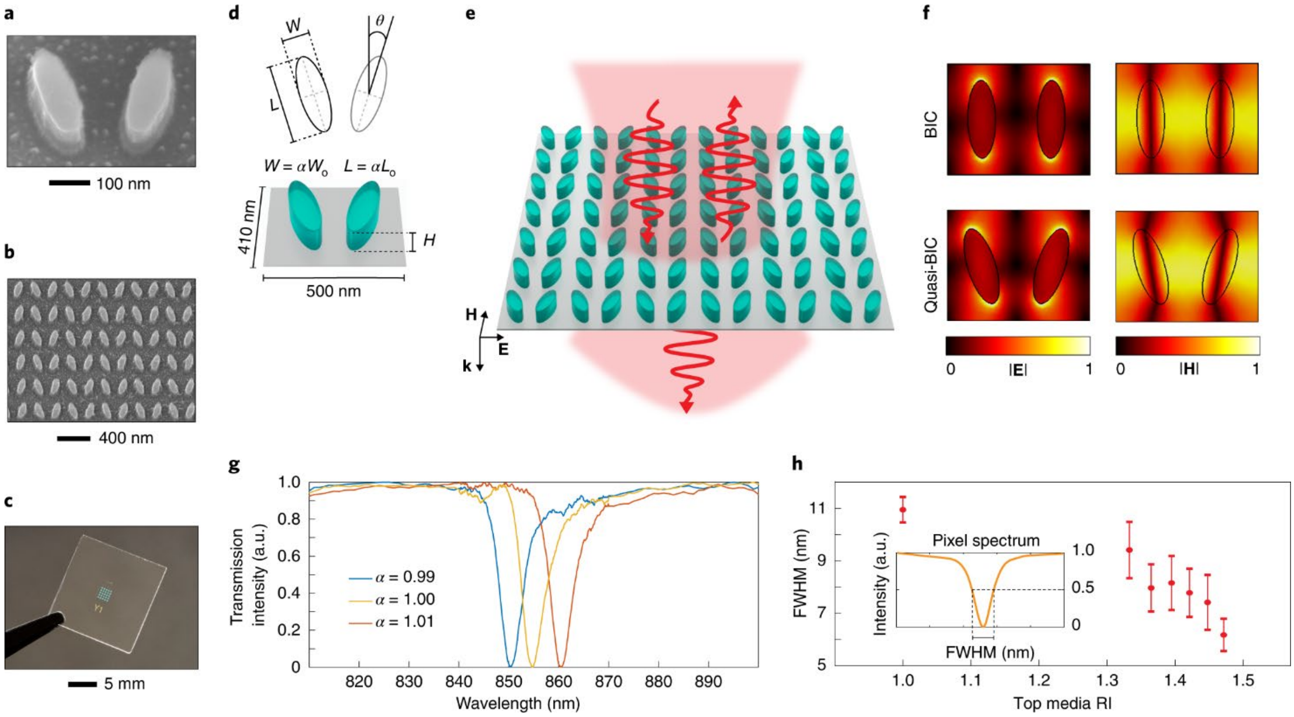

Figure 3-2 Geometrically tunable high-Q dielectric metasurfaces based on quasi-BIC modes. (a),(b) SEM images of the dielectric meta-unit (a) and the metasurface (b). (c) Photograph of a dielectric chip with a 5 × 5 sensor array. (d) Top-view schematic and rendered image of the meta-unit composed of two elliptical dielectric nanoresonators positioned in a mirror symmetry across the major vertical axis, where Wo = 100 nm, Lo = 280 nm, H = 100 nm and θ = 17.5°. Parameter α is used to tune the resonance wavelength (Figure 3-9). (e), Schematic of light scattered by the metasurface. (f), distribution of electric and magnetic fields in the meta-unit showing both BIC and quasi BIC modes. (g) Transmission spectra extracted from the hyperspectral data cube from a single CMOS pixel sampled from sensor regions (~0.5 μm^2) fabricated using three different scaling parameters (n_M = 1.47). The spectra exhibit narrow and spectrally isolated resonance dips in the NIR.(h), Spectral linewidth of the resonance dip measured in the presence of top media with different refractive indices (n_M = 1-1.47), indicating Q-factors as high as 144. The error bars represent the standard deviation of FWHM measurements of 2.5 × 105 pixel spectra acquired from four different sensors.

More importantly, our dielectric metasurface can be spectrally tuned by geometrically scaling the resonator dimensions via parameter α, as shown in Figure 3-2g (Figure 3-9), where the transmission spectra are extracted from single CMOS pixels, each representing a sensor area of 0.5 µm^2, in the presence of a top medium with n_M = 1.47. The measured sharp resonances in the NIR are similar to the spectra obtained using conventional spectrometers (Figure 3-10). To study the Q-factor of the resonance mode, the FWHM of the resonance dip is measured with numerous concentrations of glycerol solutions (n_M = 1:1.47). The measured FWHM results are plotted in Figure 3-2h, showing Q-factors as high as 144, which is a significant achievement for all-dielectric planar metasurfaces in the CMOS detectable spectral range. For more details on the importance of high-Q resonances for sensing small spectral shifts induced by single molecules, see Supplementary Figs. 2 and 6. Furthermore, our dielectric resonators attain high near-field enhancement (40 times), which results in a refractometric sensitivity of 263 nm per RI unit (Figure 3-8).

To demonstrate the compatibility of all-dielectric metasurfaces with biorecognition assays, we used epoxy-silane chemistry to covalently immobilize the capture molecules onto the sensor surface [127]. Mouse-derived immunoglobulin G (M-IgG) solutions were first selectively deposited on the sensor arrays using a low-volume liquid dispenser (Figure 3-3a and c), and the areal molecular density on the sensors was controlled by adjusting the droplet volume and analyte concentration. For control sensors, we deposited bovine serum albumin (BSA) instead of M-IgG. After incubation, the remaining chip surface was blocked with BSA to minimize non-specific binding. Next, the sensors were incubated with rabbit-derived anti-mouse IgG (R-IgG), which has a high affinity to the M-IgG, ensuring that surface-immobilized M-IgG molecules bind to R-IgG (Figure 3-3b). This model bioassay enables the quantification of areal molecular density, as well as the determination of the detection limit of the metasurface, independent of the bioassay affinity parameters (Figure 3-12).

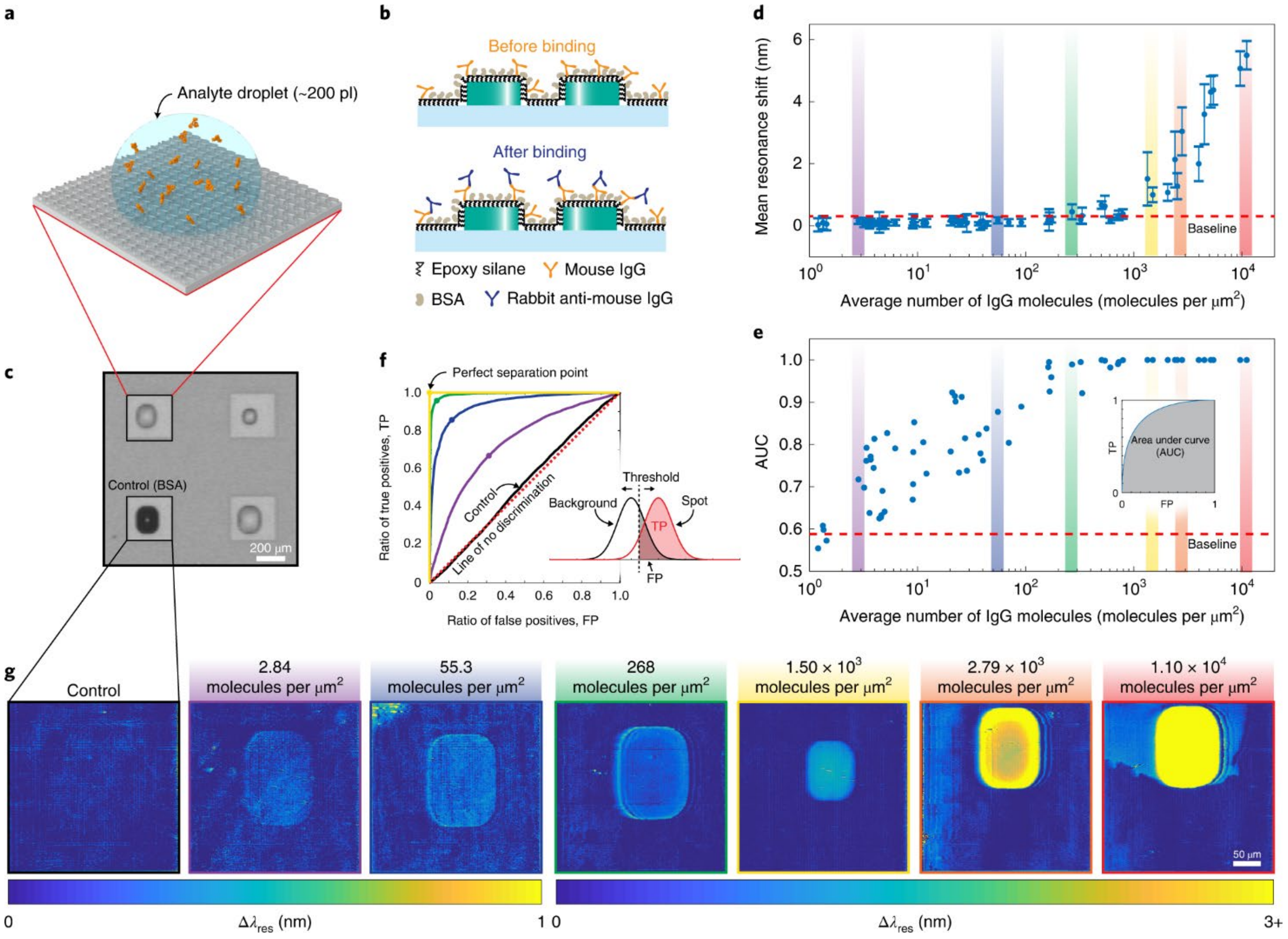

Figure 3-3 Biosensing using dielectric metasurface sensors and image-based data processing. (a) Rendered schematic showing controlled biomolecule delivery to the sensor surface using low-volume (~200 pl) droplets for microarray-based detection.(b) Schematic of the bioassay, in which epoxy-silane-based covalent chemistry is used for biomolecule immobilization.(c) Image of a representative 2 × 2 sensor array showing analyte molecules dispensed using different-volume droplets and a control sensor without analyte molecules.(d) A traditional calibration curve correlating the ensemble-averaged resonance shift from binding spots to the average number of analyte molecules per area (molecules per µm^2). Note that the large standard deviation in the high-concentration regime is caused by the coffee ring effect. (e) Area under the curve (AUC) values of all receiver operating characteristic (ROC) curves. Control measurements revealed an AUC value of 0.5008 ± 0.0291 (N = 68) and the baseline was set at 0.5881. This approach shows that the detection of biomolecules at low concentrations can be achieved, in contrast to traditional ensemble averaging. (f) ROC curve of a sample data set. (g) Resonance shift maps of a sample set from the data presented in (d)-(f). For additional resonance shift maps at low molecule densities, see Figure 3-14.

To evaluate the biosensing performance of our system, we computed the resonance shift maps from sensors with different analyte quantities (N = 66), a subset of which is shown in Figure 3-3g. A traditional calibration curve that correlates the ensemble-averaged resonance shift over the analyte spot to the average number of analyte molecules per area is shown in Figure 3-3d, where the color bars indicate the data points associated to the resonance shift maps shown in Figure 3-3g. The measurements with low areal molecule density (<1 × 103 molecules per µm^2) are not detectable using the traditional ensemble-average method, but the analyte spots are visible on the resonance shift maps. In fact, this is a major challenge that analytical biosensing platforms face, as the signal from ensemble measurements at low concentrations is masked by the background noise [201].

In contrast, our imaging-based platform allows for digitized biomolecular detection, as enhanced analytical characterization is possible by evaluating the information carried by each individual pixel. Due to the highly localized fields of the metasurface, when a few molecules attach to the so-called 'hotspots' a significant spectral shift occurs (Figure 3-13). Yet, as the total number of molecules on the sensor decreases, so does the number of meta-units that have enough molecules to induce a measurable shift due to the stochastic nature of the binding event. We, therefore, use a thresholding method to classify whether a resonance shift map pixel belongs to the region where the analyte is present. The associated receiver operating characteristic (ROC) curves from a sample subset of the data presented in Figure 3-3d, obtained by varying the threshold value, are shown in Figure 3-3f (Figure 3-12). To quantify the signal, we use the metric of the area under the ROC curve (AUC) [202], which is expected to equal 1 when the perfect separation point is achieved and 0.5 for control measurements. Figure 3-3e shows the AUC values for the same data set used in Figure 3-3d. The baseline was computed using the standard criterion of three standard deviations above the mean value of control measurements (0.5008 ± 0.0291, $N = 68$). This approach reveals biomolecular detection information at very low molecular counts (~3 molecules per μm^2), corroborating the strength of our label-free imaging method (Figure 3-14).

The tunable and sharp resonant modes exhibited by our metasurfaces enable the design of unique MRSs for spectrometerless retrieval of spectral information from a single image acquired at a fixed wavelength, which allows for the potential miniaturization of our system. Figure 3-4a shows the resonance map of a 200 µm x 200 µm MRS, which is spatially partitioned into 16 sub-sensors by varying the tuning parameter as described in Figure 3-4b. Each MRS is then hyperspectrally imaged by 275 × 275 CMOS pixels with water as the top medium. The different tuning parameters, aided by intrinsic fabrication variances [203], yield sensors with a wide range of densely distributed resonance wavelengths that respond uniformly to changes in the top medium refractive index. Moreover, because the footprint of each individual MRS is small, sensor arrays over large imaging areas can be imaged in a single snapshot for multiplexed detection (Figure 3-15 and Figure 3-16).

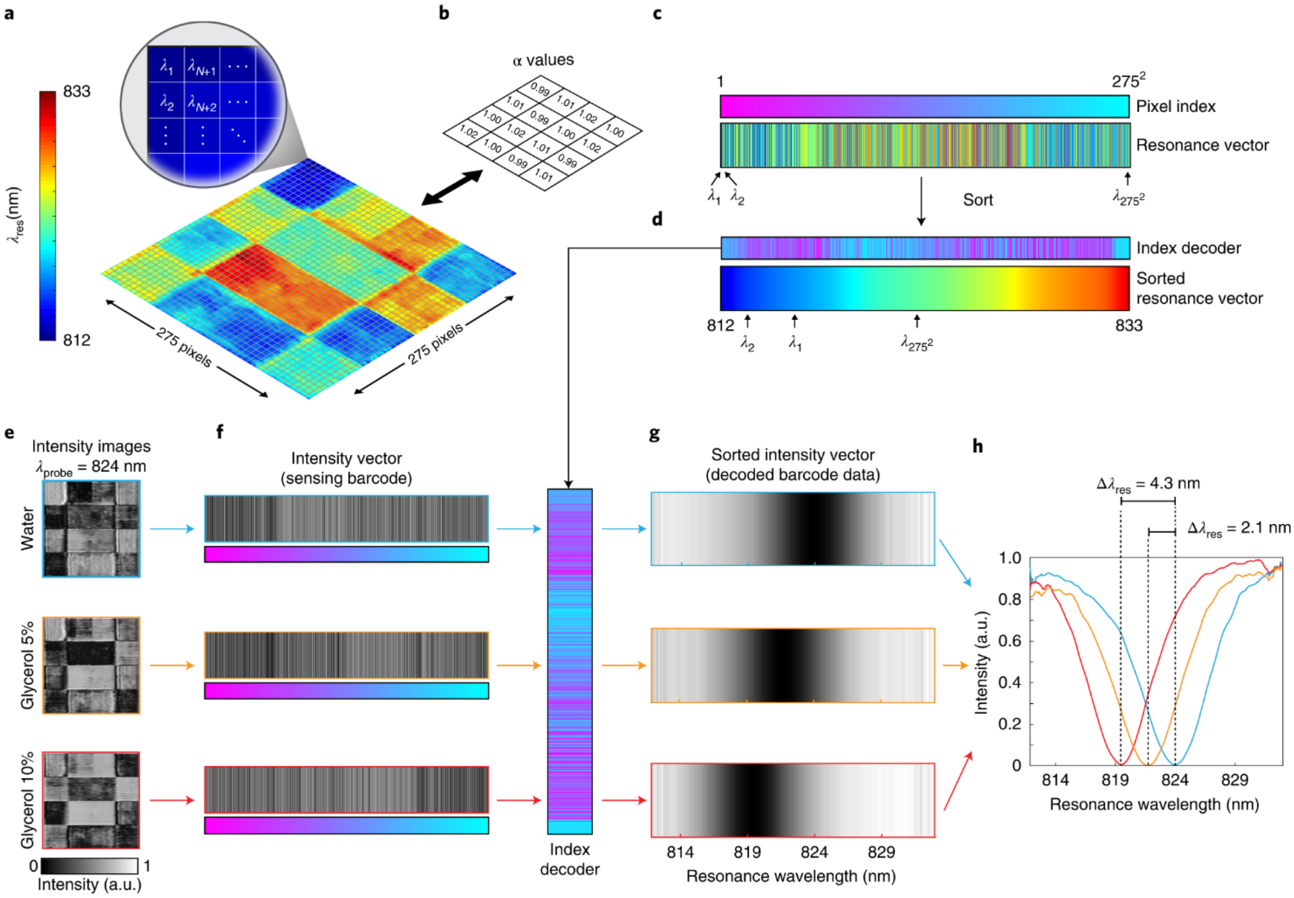
a
b
c
λ_1
λ_{N+1}
λ_2
λ_{N+2}
833
812
λ_{res}(nm)
275 pixels
275 pixels
α values
0.99
1.01
1.02
1.00
1
275^2
Pixel index
Resonance vector
λ_1 λ_2
Sort
λ_{275^2}
d
Index decoder
Sorted resonance vector
812
λ_2
λ_1
λ_{275^2}
833
e
Intensity images
λ_{probe} = 824 nm
Water
Glycerol 5%
Glycerol 10%
0
1
Intensity (a.u.)
f
Intensity vector
(sensing barcode)
Index decoder
g
Sorted intensity vector
(decoded barcode data)
814
819
824
829
Resonance wavelength (nm)
h
$\Delta\lambda_{res}$ = 4.3 nm
$\Delta\lambda_{res}$ = 2.1 nm
1.0
0.8
0.6
0.4
0.2
0
Intensity (a.u.)
814
819
824
829
Resonance wavelength (nm)

Figure 3-4 Resonance map of the MRS (a), designed according to the scaling parameters in (b), recorded by 275 × 275 CMOS pixels. The distribution of resonance wavelengths within a sensor has a 20 nm spectral range.(c), Resonance vector made by stacking the resonance map column-wise. (d), Sorted resonance vector and its associated index decoder. (e), Intensity images of the MRS recorded at a single excitation wavelength (824 nm) with a top medium of water, 5% glycerol and 10% glycerol. (f), Sensing barcodes created by stacking the individual pixel intensity values from the images in(e). (g),(h), Intensity vectors sorted using the index decoder in (d). (g) resulting in the pseudo-spectra shown in (h), where the difference in the wavelength of pixels that resonate at 824 nm corresponds to the spectral shift associated with the change in the refractive index of the top medium.

To translate the intensity data from a single image into spectral information, it is necessary to compute an index decoder using the resonance map. We begin by stacking the resonance map of the MRS column-wise, as shown in Figure 3-4c, where each pixel is indexed from 1 to 2752. Rearranging this resonance wavelength vector in increasing order yields a sorted resonance vector and an associated index decoder, which contains the order in which the pixels must be arranged to achieve sorting (Figure 3-4d). The index decoders are signatures of the sensors and can be used to implement a barcode-based sensing scheme. To illustrate this procedure, three images of the same sensor with different top mediums (water, 5% glycerol, and 10% glycerol) are acquired at a single wavelength of 824 nm (Figure 3-4e). These images are then stacked to reveal the sensing barcodes (Figure 3-4f), which are unique to the optical properties of the sensor and the refractive index of the top medium. The sensing barcodes are decoded by rearranging their elements according to the previously computed index decoder and binning the intensity values to achieve uniform wavelength representation (Figure 3-4g). The resulting vector is a pseudo-spectrum that can be interpreted for spectral shift sensing, as shown in Figure 3-4h. In this example, because the index decoder is computed from reference data acquired with a water medium, the pixels that resonate at the probing wavelength (824 nm) are the darkest for the case with water as the top medium. When the sensor is imaged with a top medium of higher refractive index, some of the pixels whose resonance wavelengths are initially less than 824 nm become resonant due to the redshift of the resonance dip. The difference in the resonance wavelength of such pixels corresponds to the spectral shift associated with the difference in the refractive index of the top medium. This novel technique is particularly important for portable on-site sensing platforms, where an off-the-shelf single-wavelength source, coupled with a CMOS camera and a single-board computer, can be used to build a handheld barcode reader.

To investigate the near-field probing capabilities of our sensing platform, we measured the spectral changes induced by single-layer graphene (SLG) covering the metasurface (Figure 3-5a). The graphene was characterized with Raman spectroscopy to ensure the transfer was in fact of single-layer quality (Figure 3-17 and Table 3-1) [204], [205]. Hyperspectrally measured and simulation extracted transmission spectra with and without ~3.2 Å thick SLG on the dielectric metasurface are shown in Figure 3-5b. Both simulation and experimental results indicate a remarkable ~3 nm redshift and linewidth broadening in the resonance dip due to the optical properties of the SLG in the NIR (n = 2.69, k = 1.52) [206]. When hyperspectral data cubes are used, our nanophotonic imaging set-up can spatially resolve the optical properties of the SLG over large areas (3.3 mm^2), as shown in Figure 3-5c and d. Moreover, our single image-based barcode sensing technique can also be utilized to retrieve the spectral changes that emerge due to the enhanced localized interaction of the metasurface with graphene. Figure 3-5e shows single-wavelength intensity images of MRS with and without SLG along with their corresponding sensing barcodes. Once the index decoder (Figure 3-5f) is used to rearrange the corresponding sensing barcodes, spectral sensing information can be retrieved (Figure 3-5g). Importantly, both the spectral shift and the line-broadening information is recovered in agreement with the hyperspectral results shown in Figure 3-5b. This demonstrates that our method can efficiently characterize the optical parameters of SLG over large areas from a single CMOS image without the need for a spectrometer, which is crucial for the current efforts in understanding and engineering low-dimensional materials [207].

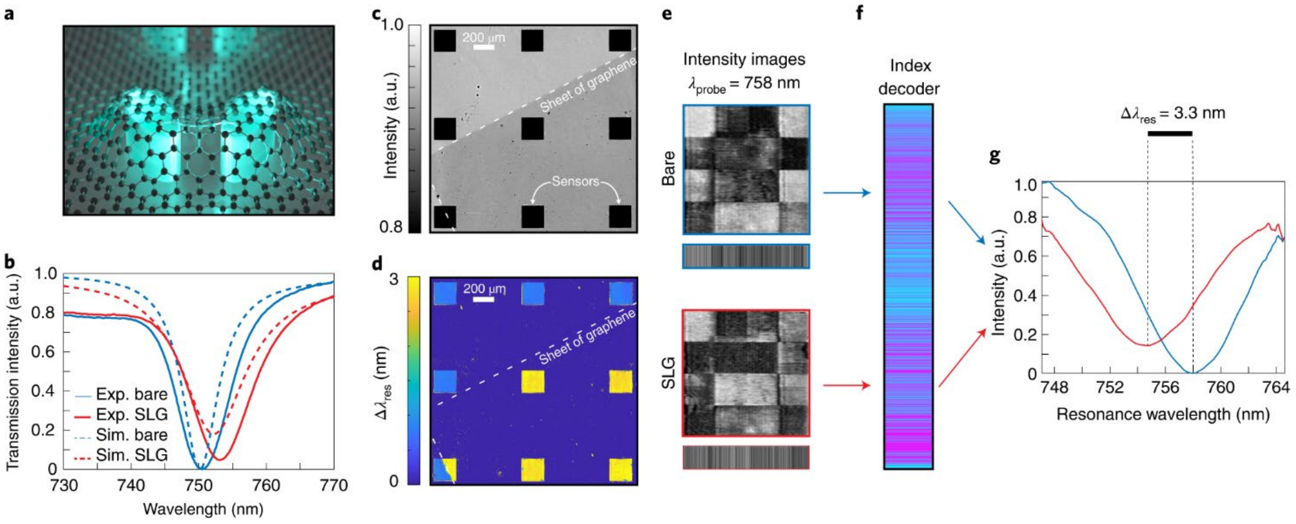

Figure 3-5 (a) Rendered representative image of SLG covering dielectric nanoresonators. (b), Hyperspectrally measured and numerically calculated transmission spectra before and after SLG transfer on the bare sensor, extracted from a sub-sensor region. The resonance dip redshifts spectrally and broadens due to graphene's optical properties in the NIR (n = 2.69, k = 1.52) based on both simulation and experiment. (c),(d), Large-area (~3.3 mm^2) image of a sensor array partially covered with a sheet of SLG, the edges of which are marked by white dashed lines (c) and its corresponding resonance shift map extracted from the hyperspectral data cubes before and after SLG transfer (d). (e), Intensity images of the MRS recorded at single excitation wavelength (758 nm) before and after SLG transfer and corresponding sensing barcodes. (f), Index decoder computed from the hyperspectral data cube collected from the bare sensor. (g), The index decoder is used to sort the sensing barcodes in e, resulting in the shown plots. The spectral shift due to SLG is equivalent to the difference in the wavelengths of pixels that resonate at 758 nm.

We have demonstrated novel applications of high-Q resonant dielectric metasurfaces that support bound states in the continuum, in conjunction with advanced imaging-based optical data acquisition and processing methods, to build a superior and versatile sensing platform. Alternative materials and designs that support such resonant modes can be explored to further enhance the sensitivity and the Q-factor of the resonant metasurfaces. Moreover, the spectral range and density of our single-wavelength spectral retrieval method can be increased by exploiting actively tunable materials or by probing un-utilized dimensions, such as the polarization of the incident light. Finally, machine learning and artificial intelligence methods can introduce new inference tools to expedite our platform as a field-deployable high-throughput single-molecule detector for biomedical applications.

3.3 Methods

All-dielectric metasurface fabrication

The all-dielectric metasurfaces were fabricated using 100 keV EBL by nanopatterning a thin layer (100 nm) of amorphous silicon (a-Si), which was deposited using low-pressure chemical vapor deposition (CVD) on a clean bare fused-silica substrate. First, a-Si coated wafers were diced with a photoresist protective layer into 1.5 cm × 1.5 cm chips and then the individual chips were cleaned using resist remover and oxygen plasma. A double layer of positive tone EBL resists, poly(methyl methacrylate) (PMMA 495K bottom and 950K top) was spin-coated to yield 100 nm total thickness and baked at 180 °C for 5 min. Double-layer PMMA is crucial to create an undercut in the resist layer to enable a successful liftoff process. Because the dielectric metasurfaces were fabricated on non-conductive fused silica substrates, a 5 nm thin Au layer was sputtered on the PMMA as a charge dissipation layer. After EBL exposure, the Au film was first wet etched and then the EBL resist was developed. To transfer the pattern into the a-Si, a hard aluminum mask (30 nm) was deposited using an electron-beam evaporator. The metal liftoff was performed by soaking the chips in a resist remover bath at 70 °C for 6 h. The mask pattern was transferred into the a-Si film by fluorine-based inductively coupled plasma etching. Finally, the Al hard mask was wet-etched to complete the all-dielectric metasurface fabrication (Figure 3-6).

Graphene transfer and Raman spectroscopy characterization

For graphene transfer, CVD-grown graphene was wet-transferred over the clean dielectric metasurface sensor arrays. To certify the presence of a single layer of graphene, Raman spectroscopy was performed using an inViaTM Raman microscope (Renishaw) both on the nanostructured metasurface and on the non-patterned glass area with excitation wavelengths of 532 nm and 785 nm (Figure 3-17 and Table 3-1).

Optical characterization set-up

The all-dielectric metasurfaces were optically characterized using a hyperspectral imaging-based analysis method. To acquire the hyperspectral data cube, individual images were recorded with narrowband illumination using a CMOS camera (DS Qi2, Nikon) coupled to the outlet of an inverted microscope (Eclipse-Ti, Nikon). The illumination source frequency was swept using a laser line tunable filter (LLTF, NKT Photonics) coupled to a supercontinuum laser source (SuperK EXTREME EXR-15, NKT Photonics). The LLTF's operation is based on volume holographic gratings and is capable of tuning wavelengths from 400 nm to 1,000 nm. The bandwidth (FWHM) of the filter output is about 1.75 nm at λ = 700 nm with a maximum FWHM of 2.5 nm at λ = 1,000 nm. The continuously tunable filter can suppress out-of-band transmission efficiently (60 dB @ ±40 nm), enabling a widely tunable narrowband illumination. Non-uniform spectral image sampling was used, where $\Delta\lambda$ = 0.1 nm steps were used to resolve the sharp resonance and $\Delta\lambda$ = 1 nm was used off-resonance to acquire a wide spectral range. To corroborate the hyperspectral data, the all-dielectric surfaces were also spectrally characterized using an imaging spectrometer and a high-performance charge-coupled device camera (IsoPlane 320 spectrometer, Pixis camera, Princeton Instruments). The spectrometer was directly coupled to the outlet of an inverted microscope. The transmission spectra of the dielectric resonators were recorded using a dense grating (600 grooves per mm) with a blaze wavelength of 750 nm under normal broadband illumination and examined for the resonant dip properties (Figure 3-10).

Data acquisition and pre-processing

For each experiment, the hyperspectral cube from a sensor array was partitioned into smaller subsets, each containing the data cube of a single sensor and saved as data sets of a .h5 file. Before using the data cube, the images were corrected for spatial and spectral variations of the light source. This was done by dividing each pixel value by the corresponding pixel value of a data cube collected with the same acquisition parameters but without the sensor chip.

Resonance map computation

To build a resonance map, the spectrum associated with each image pixel was processed in MATLAB to extract the center wavelength of its resonance. To obtain accurate values, data points from a window of 3 nm around the wavelength containing the darkest pixel were used to fit a second-degree polynomial, the minima of which were calculated and assigned to the pixel in question. The process was repeated for every pixel, resulting in the resonance map.

Resonance shift map computation

The resonance shift map was calculated from two resonance maps from the same sensor taken at different time instances (for example, before and after analyte binding). An intensity image containing high contrast between the sensor and off-sensor areas was selected from both data sets. These images were used to compute the geometric transformation matrix aligning them, where only rotation and translation are allowed. The geometric transformation matrix was used to align the previously computed resonance maps. The resonance shift map is the result of the element-wise subtraction of the two aligned resonance maps.

Full-wave numerical analysis

Numerical analysis of the all-dielectric metasurface was performed using a commercially available finite-element frequency-domain solver (CST Microwave Studio 2017). The presented transmittance and field distribution results were produced using periodic boundary conditions for each meta-unit, where polarized (TM00) incident light was launched from the top port at normal incidence. The geometric parameters are specified in the main text and the a-Si thin-film material parameters are shown in Figure 3-7d. The largest mesh element dimension was kept below one-tenth of the smallest wavelength used.

Surface chemistry and chip cleaning

Covalent surface chemistry based on (3-glycidoxypropyl) trimethoxysilane (3-GPS) (Sigma Aldrich) monolayers were used to immobilize the capture antibody microarrays on an all-dielectric metasurface. A continuous monolayer of 3-GPS forms on the dielectric metasurface when the silane end binds to the silicon oxide. The functional terminal group of 3-GPS is epoxide and it reacts with the amine groups of antibodies, which were used as capture molecules in our biorecognition assay. To form the self-assembled monolayer of 3-GPS, the chips were cleaned in RCA first-step solution at 50 °C for 30 min. The clean chips were incubated in 3-GPS solution in toluene (1% vol/vol) for 20 min and rinsed in fresh toluene to remove unbound 3-GPS molecules. The chips were then dried in N2 gas and baked at 120 °C for 30 min. The epoxy-silane-coated chips were shelf-stored under a vacuum to be used within one month of preparation. The all-dielectric metasurfaces were used for multiple biosensing experiments. Between the bio experiments, the chips were cleaned using piranha solution (H_2SO_4: H_2O_2, 3:1), and then the above procedure was repeated. Note that in most of the low-concentration measurements, data were collected exclusively from fresh chips to eliminate any possible effect of chip recycling.

Bioassay details

The biorecognition assays were performed based on immunoassays (Figure 3-12a). For the sample sensors, primary capture antibodies (mouse IgG ab37355, Abcam) were covalently immobilized in a microarray format on the epoxy-silane-coated all-dielectric metasurfaces. A non-contact, low-volume liquid dispenser (sciFLEX-ARRAYER S3, Scienion) was used to create microarrays of antibody droplets (~200 pL) on the sensors. Antibody solutions at various concentrations were prepared in PBS 1× buffer with 0.5% wt/vol Trehalose and 0.01% wt/vol Tween. To control the total quantity of molecules in a microspot, various numbers of droplets were deposited and incubated for ~1 h at room temperature. For control sensors, the bioassay steps were repeated, but, instead of M-IgG, BSA (1% wt/vol) was spotted on the sensor. To block the rest of the surface, the chips were directly soaked in BSA (1% wt/vol in PBS 1× buffer) for 30 min and then washed in PBS (1×) twice for 5 min, rinsed in milli-Q water and dried. Next, the secondary antibody (rabbit anti-mouse IgG ab6725, Abcam) solution (200 µg/mL in PBS 1×) was incubated over the microarray for 1 h at room temperature and washed in PBS (1×) twice for 5 min, rinsed in milli-Q water and dried.

Analyte quantity estimation

The number of mouse IgG molecules per metasurface area was estimated as follows. First, the total number of molecules in a microspot was calculated based on the total volume of dispensed IgG solution and its concentration. For instance, in a single droplet (~200 pL) of 2 µg/mL IgG (150 kDa) solution, there are 1.6 × 106 IgG molecules. The total spot area was thus calculated using the images acquired. A single droplet microspot area usually covered ~1 × 104 μm^2 of the sensor area, which comprises 3.69 × 104 meta-units or 1.9 × 104 image pixels with a ×10 objective. Assuming that every single IgG molecule dispensed in a droplet binds to the metasurface, the number of molecules per area, meta-unit or pixel can be estimated. For the above numerical example, this translated into 160 molecules per μm^2, 43 molecules per meta-unit or 84 molecules per image pixel. Because our optical platform can resolve sensing information from a single image pixel, the molar correspondence of the above example translates to 0.14 zeptomoles. Note that the molecular density of a given experiment depends on several experimental and environmental parameters, including the spot volume, sampling variations, surface hydrophobicity (contributing to spot wetting), humidity in the incubation chamber and structural imperfections in sensor fabrication.

Thresholding and receiver operating characteristic curve

To quantify the presence of an analyte at low concentrations, a threshold method was implemented (Figure 3-12b). For each resonance shift map, two 75 × 75 subsets of pixels were extracted: one from the region where the analyte was spotted and one from the region without analytes. The two sets of 5,625 pixels were labeled positive and negative, respectively. The pixels were then classified using a standard threshold method, where pixels whose associated resonance shifts fell above the threshold t were classified as positive, and the remaining pixels were classified as negative. The ratio of true positives (RTPt) was computed by dividing the number of pixels correctly classified as positive to the total number of pixels labeled positive, whereas the ratio of false positives (RFPt) was computed by dividing the number of pixels incorrectly classified as positive to the total number of pixels labeled negative. The process was repeated for different thresholds, and a receiver operating characteristic curve was built, where each point represents a threshold. To quantify the presence of an analyte, we chose the area under the ROC curve (AUC) as the metric [201]. For control measurements, data were extracted from control areas, either from control-specific sensors or off-spot regions in sample sensors.

3.4 Supplementary information

1) Fabrication Process Flow

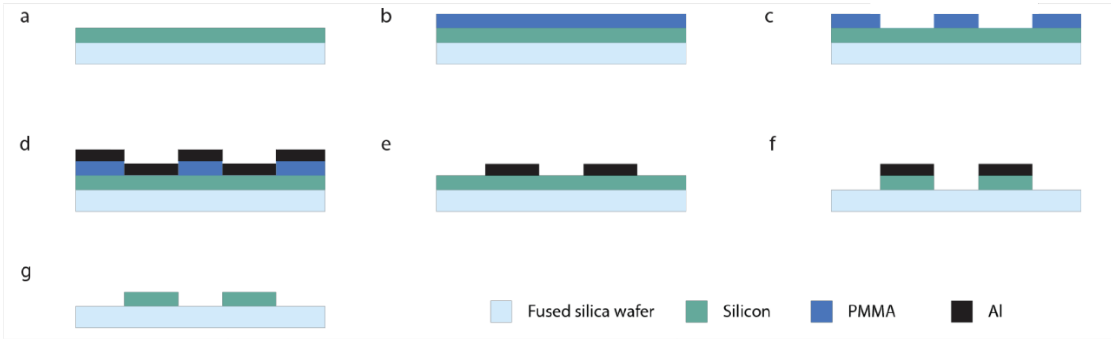

Figure 3-6 Dielectric metasurface fabrication flow chart: (a) LPCVD amorphous silicon deposition (100 nm) on fused silica substrate (b) Double layer PMMA 495K bottom (60 nm) and 950K top (40 nm) (c) EBL exposure and development (d) Aluminum hard mask evaporation (30 nm) (e) Metal lift-off in solvent (f) Dry Si etch (g) Hard mask removal by Al wet etch

2) Effect of geometric parameters and structural imperfections on the Q-factor

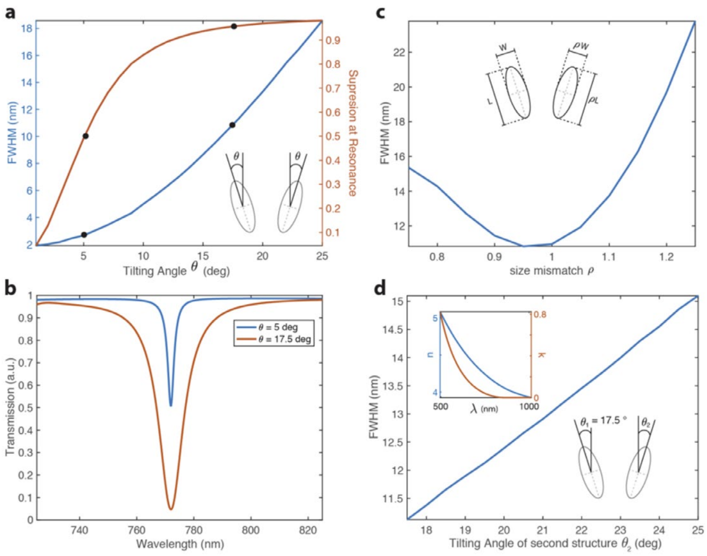

Figure 3-7 The effect of structural imperfections on the Q-factor. (a) As the tilting angle increases, the FWHM and the resonance suppression efficiency increase. We chose to work at 17.5 degrees as it gives sufficient suppression (>90%) at low FWHM (11 nm). (b) Representative resonance curves at tilting angles of 5 and 17.5 degrees. (c) The effect of the size mismatch between the resonators in a meta-unit showing an increase in the FWHM as the mismatch ratio increases. (d) The effect of tilting angle mismatch between the resonators in a meta-unit, showing the FWHM increase as the angle mismatch increases. The inset shows the measured dispersion curve of amorphous silicon used to fabricate our chips In all the full-wave simulations presented in this work this dispersion curve was used.

3) Field enhancement and localization at the resonance and measured sensitivity curve

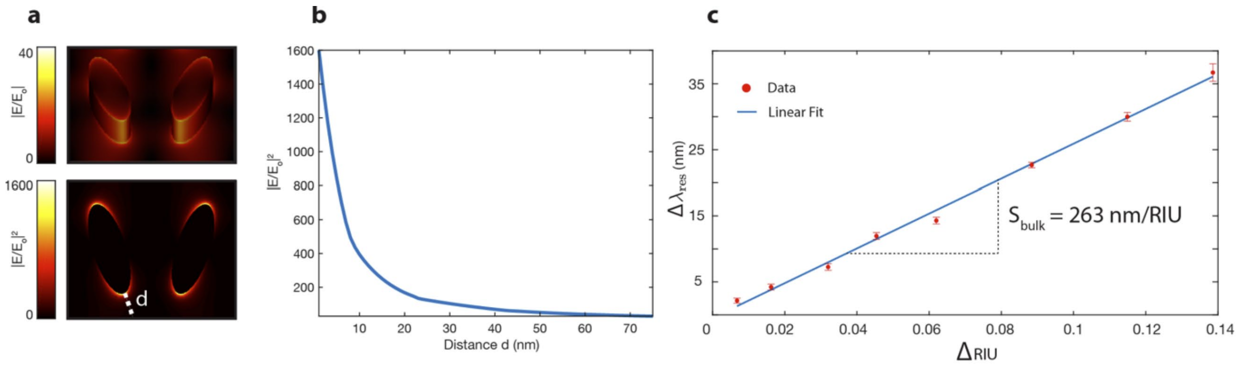

Figure 3-8 Electric field and intensity enhancement distributions in a meta-unit obtained by full-wave simulation (b) Electric field intensity localization away from the hotspot over a distance d (indicated in Figure 3-8a bottom). (c) Measured bulk refractive index sensitivity of all-dielectric metasurface using hyperspectral imaging method.

4) Effect of the geometric tuning parameter α on the resonance wavelength

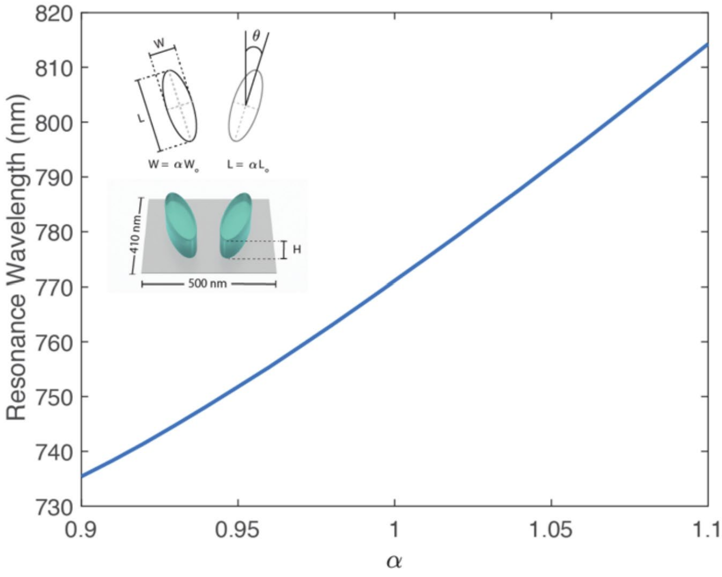

Figure 3-9 Simulation of the dependence of the resonance wavelength on the tuning parameter a from 0.9 to 1.1, where Wo= 100 nm, Lo =280 nm for a fixed height and angle of H = 100 nm, and θ = 17.5°.

5) Spectral characterization of dielectric metasurfaces

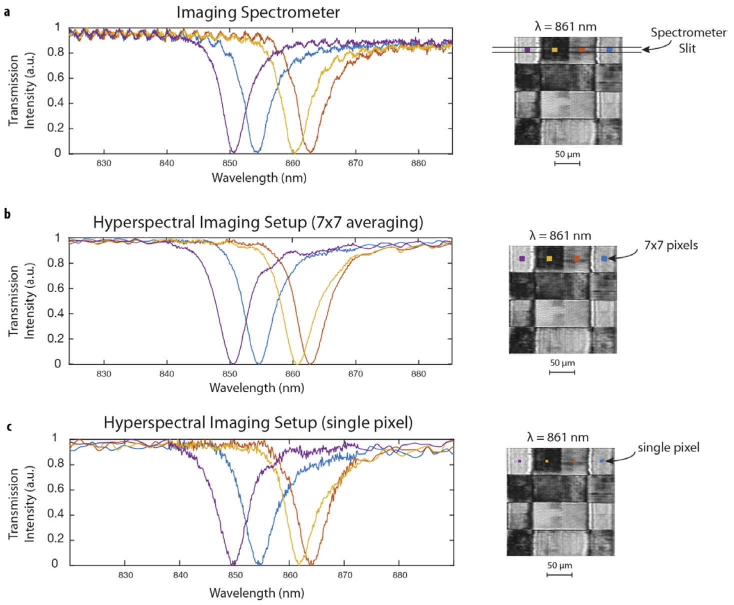

Figure 3-10 Comparison of spectral characteristics of all-dielectric metasurface extracted from the hyperspectral data cube with ones that are measured with a conventional spectrometer. (a) Transmission spectra measured using a spectrometer. Four regions on a multi-resonant sensor are acquired from a spectral image associated to the narrow slit of the spectrometer. (b) Transmission spectra extracted from hyperspectral data cube associated to analogous regions as in (a). (c) Transmission spectra extracted from hyperspectral data cube associated to a single representative pixel.

6) The importance of high-Q resonances for sensing small spectral shifts

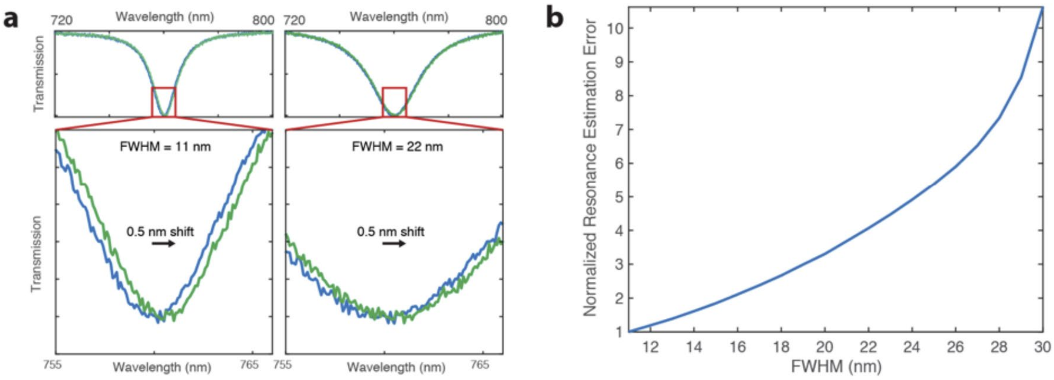

Figure 3-11 The effect of Q-factor on the estimation of resonance shift. (a) A small and a large full-width-at-half-maximum (FWHM) resonances with the same noise parameters shown with identical resonance shifts of 0.5 nm. (b) Monte Carlo simulation results indicating the increase in the resonance estimation error ($\left|\hat{\lambda}_{Res} - \lambda_{Res}\right|$, where $\hat{\lambda}_{Res}$ is the estimate of λ_{Res}) as the FWHM increases

7) Details on the bioassay and the thresholding method

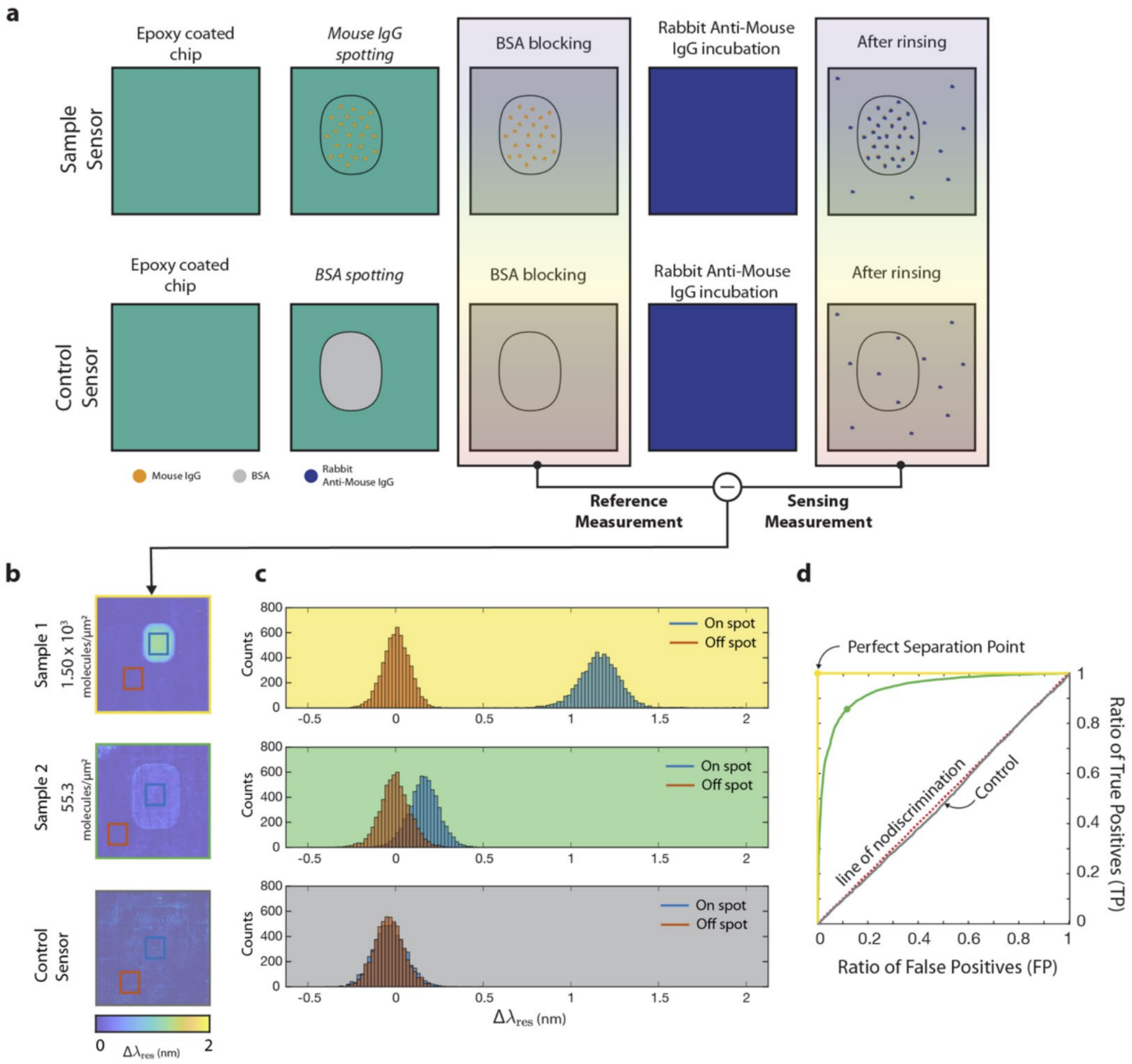

Figure 3-12 (a) Step-by-step description of the bioassay, indicating non-specifically adsorbed molecules both on the control and the sample sensors. (b) Data processing of the resonance shift maps computed using the sensing and the reference measurements from a control sensor and two sample sensors with low and high areal molecular density. (c) Regions with equal areas are probed both on the spot and off the spot of the control and sample sensors, and the resonance shift values from these pixels are shown as histograms. The on and off the spots are indicated by blue and red boxes in (b) and with the corresponding colored histogram in (c). (d) ROC curves are computed by thresholding the histograms in (c). The thresholding/ROC method is able to accurately discriminate signals coming only from the specific binding of the analytes.

8) The effect of a few molecules on the resonance position

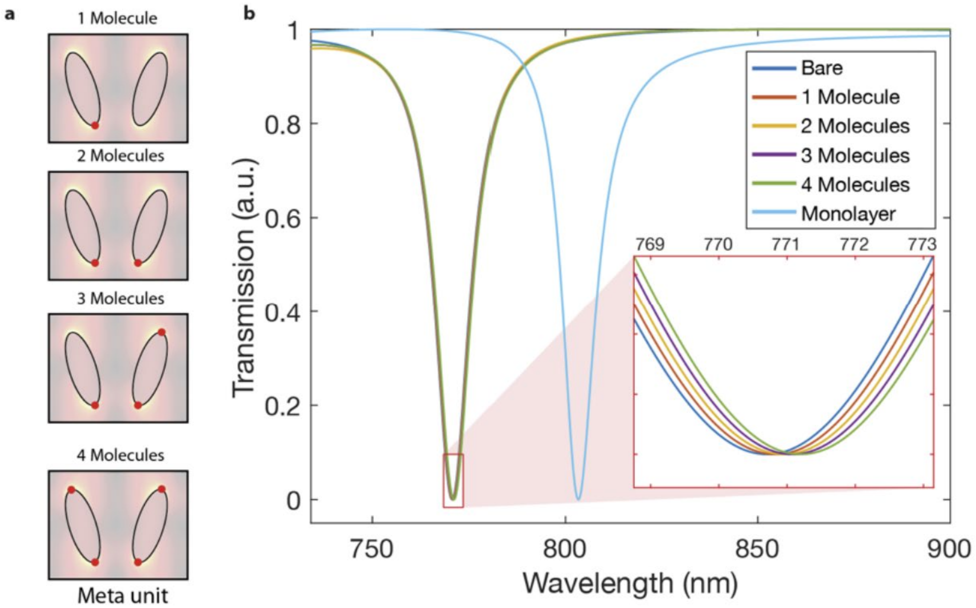

Figure 3-13 Simulation results showing the effect of individual IgG molecules binding to the hotspots of the resonators in a meta-unit. The parameters of IgG molecules used in the simulation are from [208], [209]. Due to the highly localized fields at the hotspots, few molecules can create measurable spectral shifts in the resonance position. We calculated 0.12 nm, 0.25 nm, 0.37 nm, and 0.49 nm shifts corresponding to 1 ,2 ,3, and 4 molecules binding, respectively. Moreover, a monolayer of IgG molecules is expected to create ~33 nm spectral shift.

9) Additional Resonance Maps

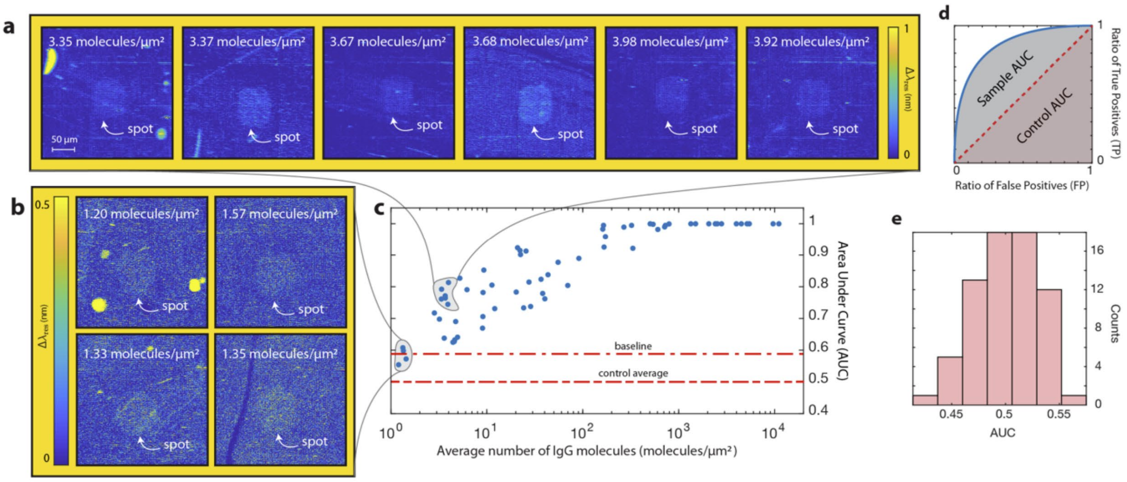

Figure 3-14 (a) A representative subset of resonance shift maps of measurements with low detectable molecular concentrations of ~3molecules/μm^2. (b) Resonance shift maps of measurements with very low molecular concentrations of ~1 molecules/μm^2. (c) Summary of all the measurements, where the baseline corresponds to the mean of control measurements plus three times the standard deviation (d) the area under the ROC curve metric illustrated for a representative sample and control. (e) Histogram of the AUC values of control measurements.

10) High-throughput, large-area, imaging-based sensing using multi-resonance dielectric metasurfaces

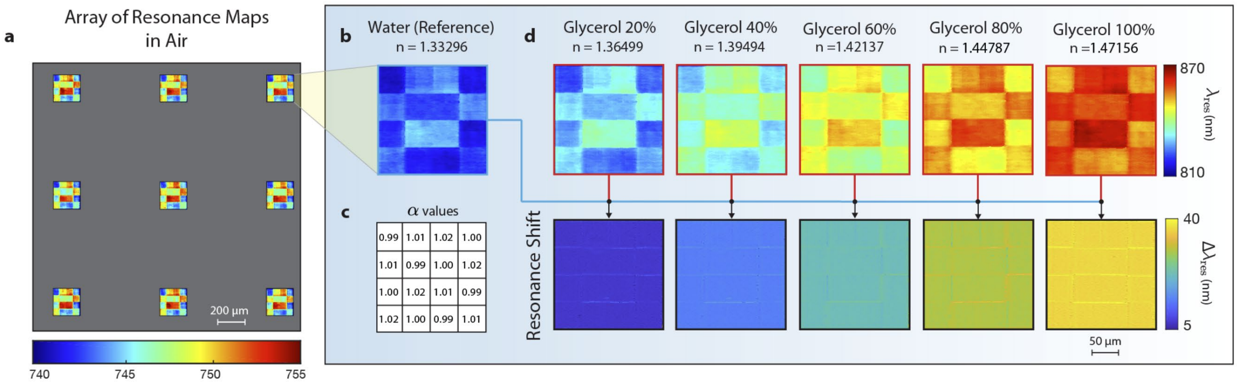

Figure 3-15 (a) Resonance map array of multi-resonance sensors computed using a single hyperspectral data cube acquired in air medium. The 2x2 mm^2 field-of-view allows for high-throughput spectral data acquisition. (b) Resonance map of a representative multi-resonance sensor in water medium. The multi-resonance sensor was fabricated using four different scaling parameters, as shown in (c). (d) Hyperspectral imaging-based refractometric sensing. The top row shows measured resonance maps of a multi-resonance sensor with different glycerol concentrations of top media. The bottom row shows the resonance shift maps when each measurement is referenced to that of water, indicating bulk sensitivity of 263 nm/RIU, independent of the scaling parameter

11) Distribution of pixel resonance wavelengths in a multi-resonance sensor

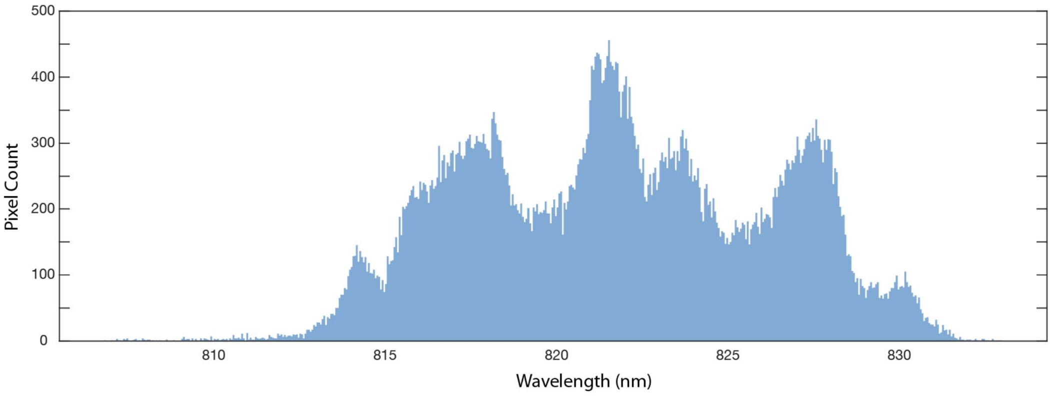

Figure 3-16 Histogram of 75625 pixels from the resonance map of a multi-resonance sensor, with a bin width of 0.05 nm. The resonance wavelengths are densely distributed in a 20 nm spectral range.

12) Raman Spectroscopy of SLG

We have taken the Raman spectra of our graphene chips at two excitation wavelengths: 532 nm and 785 nm, both on the nanostructured metasurface (on sensor) and on the non-patterned glass area (off sensor). The results can be seen in Figure 3-17 and Table 3-1 below. The deposited graphene meets several properties of single-layer graphene reported in the literature. In particular, note that for both excitations, the G peak intensity is much lower than the 2D peak, which is indicative of single-layer graphene [204], [205], [210], [211]. We report 2D/G ratios of 3.4 and 1.7 for excitation wavelengths 532 nm and 785 nm, respectively. Moreover, our measurements show that the G peak position shows a negligible variation (3.8 cm^{-1}) with respect to the excitation wavelengths, as expected [211]. In contrast, the 2D peak position shows a significant variation of 80.6 cm^{-1} based on the excitation wavelength. This translates into 107 cm^{-1}/eV, which is in very good agreement with the rate of ~100 cm^{-1}/eV previously reported by Wu et al. [211]. Finally, we report the FWHM of the 2D band to be 32.4 cm^{-1} and 36.8 cm^{-1} for excitation wavelengths 532 nm and 785 nm, respectively, when measured from the graphene on the nanostructured metasurface. The FWHM values are larger (35.1 cm^{-1} and 38.6 cm^{-1}) in the Raman spectra of graphene on the glass. In agreement with the literature for suspended single-layer graphene, we observe that the Q-values obtained from the graphene that covers the metasurface are higher [205].

	Excitation λ (nm)	I_{2D}/I_G	G CWL (cm^{-1})	2D CWL (cm^{-1})	2D FWHM (cm^{-1})
On sensor	**532 nm**	3.4	1587.5	2675.8	32.4
	785 nm	1.7	1591.3	2595.2	36.8
Off Sensor	**532 nm**	2.3	1580.9	2666.7	35.1
	785 nm	1.5	1583.5	2585.8	38.6

Table 3-1 Summary of Raman spectroscopy of graphene deposited on and off the dielectric sensors

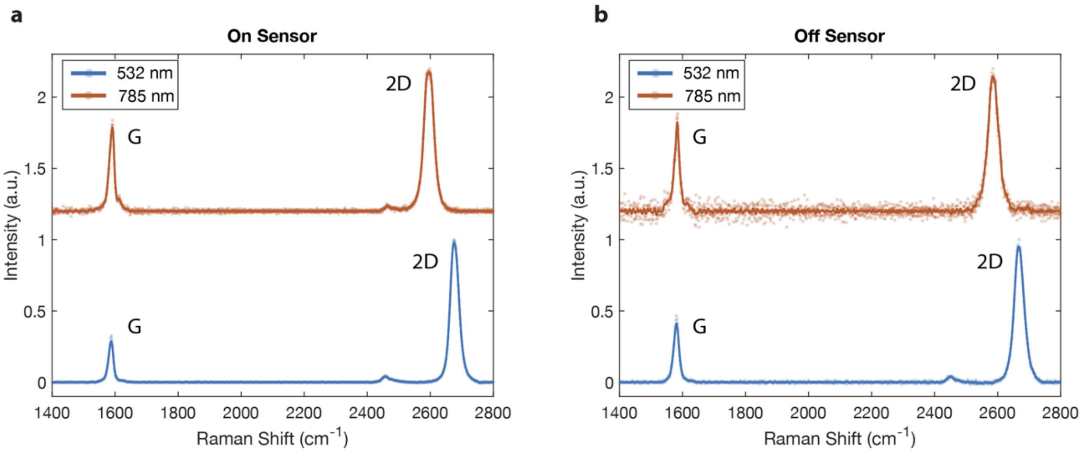

Figure 3-17 Raman spectroscopy of the transferred graphene measured at the excitation wavelengths of 532 nm and 785 nm (a) on the metasurface dielectric sensors and (b) off the sensor, on the glass.

Chapter 4 Imaging-based spectrometer-less optofluidic biosensors based on dielectric metasurfaces for detecting extracellular vesicles

Disclaimer: This chapter is from reference [8], an open-access article distributed under the terms of the Creative Commons CC BY license, which permits unrestricted use, distribution, and reproduction in any medium, provided the original work is properly cited.

- Reference [8]: Imaging-Based Spectrometer-Less Optofluidic Biosensors Based on Dielectric Metasurfaces for Detecting Extracellular Vesicles. Nature Communications 12, 3246 (2021)
  Authors: Yasaman Jahani, Eduardo R. Arvelo, Filiz Yesilkoy, Kirill Koshelev, Chiara Cianciaruso, Michele De Palma, Yuri Kivshar, and Hatice Altug.
  Jahani's Contribution:
  Designing the research and the experiments
  Carry out simulations of dielectric metasurfaces
  Micro/Nanofabrication of the dielectric metasurfaces and the microfluidics
  Building the measurement setup and incorporation of the microfluidic system
  Carry out the real-time in-flow bio-experiments

4.1 Abstract

Biosensors are indispensable tools for public, global, and personalized healthcare as they provide tests that can be used from early disease detection and treatment monitoring to preventing pandemics. We introduce single-wavelength imaging biosensors capable of reconstructing spectral shift information induced by biomarkers dynamically using an advanced data processing technique based on an optimal linear estimator. Our method achieves superior sensitivity without wavelength scanning or spectroscopy instruments. We engineered diatomic dielectric metasurfaces supporting bound states in the continuum that allows high-quality resonances with accessible near-fields by in-plane symmetry breaking. The large-area metasurface chips are configured as microarrays and integrated with microfluidics on an imaging platform for real-time detection of breast cancer extracellular vesicles encompassing exosomes. The optofluidic system has high sensing performance with nearly 70 1/RIU figure-of-merit enabling detection of, on average, 0.41 nanoparticle/μm^2 and real-time measurements of extracellular vesicle bindings from down to 204 femtomolar solutions. Our biosensors provide the robustness of spectrometric approaches while substituting complex instrumentation

with a single-wavelength light source and a complementary-metal-oxide-semiconductor camera, paving the way toward miniaturized devices for point-of-care diagnostics.

4.2 Introduction

Reliable, rapid, and highly sensitive detection of disease indicators is crucial for timely and specific diagnostics and treatments [212]–[214]. POC devices are highly desirable for health monitoring and biosafety applications in the field settings as they offer easy-to-use, low-cost and fast detection of numerous indicative biomarkers, such as proteins, antibodies, nucleic acids, and extracellular vesicles, including exosomes, as well as pathogens such as viruses [1], [215]–[217]. For instance, the 2020 coronavirus outbreak underlines the importance of POC tools that can enable rapid, cost-effective, accurate, and quantitative tests for COVID-19. Optical biosensors based on nanophotonics are eminently sought after as they allow miniaturized lab-on-a-chip technologies for label-free analysis and multiplexed sensing [1], [215], [218], [219]. When integrated with microfluidics, nanophotonic biosensors can perform automated measurements on low sample volumes and provide quantitative and real-time results without requiring time-consuming and expensive external labels [134], [220]–[222]. Nanophotonic resonators can enable label-free detection of biomarkers by means of refractometric sensing that exploit optical resonances to monitor the changes in the dielectric properties in the vicinity of the resonators caused by, for instance, the binding of analytes to the surface-immobilized capture molecules. This change in a local refractive index translates into a resonance wavelength shift, which can be employed to quantify analyte binding events. Spectral interrogation is the conventional method to precisely track the resonance wavelength and measure the spectral shift induced by the analyte presence employing commercial spectrometers. The spectroscopic detection has been implemented with numerous nanophotonic resonators, including plasmonic nanoaperture arrays, nanoparticles, and nanoantennas such as rods, tubes, disks, and bow ties [134], [223]–[226].

In recent years, there has been a surge of efforts to improve both performance and functionalities of nanophotonic biosensors by employing new structures, materials, and devices [2], [216], [227]. While optimizing the nanostructures for refractometric sensing, one should take into account multiple parameters, including the Q of the resonators, the enhancement factor for the near-field intensities, and the spatial overlap of the enhanced fields with the target analytes. As these parameters tend to be coupled with each other, it is also essential to consider their involved trade-offs (see Supplementary Information note 1). For example, high Q resonances with sharp spectral features are desirable to resolve the spectral shift induced by analyte binding at a superior resolution. However, if the high Q values are achieved by confining the mode tightly inside the nanoresonators, then this can reduce the overlap of the near-fields with the analytes and lower the overall sensitivity. Plasmonic sensors have been taking advantage of large near-field enhancement factors, while dissipative losses in metals lead to low Q resonances, which limits their overall sensing performance [228],

[229]. Recently, high-index all-dielectric metasurfaces driven by the physics of optical Mie resonances have emerged as an alternative platform as they do not suffer from losses due to the absence of free charges [53], [130], [197], [230]–[236]. Silicon-based metasurfaces operating within the visible and near-IR (600-900 nm) spectral ranges have been employed for bulk and thin-film sensing using spectrometers [184], [223]. Concurrently, studies show that sharp spectral resonances can be achieved by using the concept of BICs, in which the light wave at the resonance remains completely localized in the metasurface even though the state coexists with a continuous electromagnetic spectrum of the environment.[106], [190] In practice, BICs are realized with high but finite values of the Q due to structural losses and imperfections and are usually termed "quasi BICs" or "supercavity modes" [103], [195]. The BIC-inspired resonances in the symmetry-broken all-dielectric metasurfaces have recently been used for highly sensitive biosensors [12]. This earlier work interrogates dielectric metasurfaces supporting quasi-BIC modes using hyperspectral imaging toward high-performance biomolecule detection.

Although spectrometers and wavelength-scanning systems provide reliable spectral shift information for monitoring the changes in the optical response, they are bulky and expensive. In addition, spectrometers are limited in simultaneously collecting data from an array of sensors for implementing multiplexed bioassays. Wavelength-scanning systems can provide spatially resolved spectral information with hyperspectral imaging in a given field of view for monitoring signals from multiple sensing elements.[12], [136] However, wavelength-scanning is cumbersome and time-consuming; hence, it cannot be used to gather time-resolved images for measuring molecular binding kinetics. Therefore, there is a need for simple and scalable optical read-out mechanisms that can extract both temporally- and spatially-resolved information from large sensor areas. To this end, red-shifting of the resonance spectrum by the binding of the analytes on the sensor surface can be quantified by tracking the changes in intensity over a narrow spectral window instead of collecting spectrally resolved information over a broad bandwidth [218], [237]. In particular, when combined with a small-scale light source - i.e., laser or light-emitting diode (LED) - and an imaging camera (i.e., CMOS or charge-coupled device (CCD) cameras), the intensity-based optical readers can be ultra-compact, low-weight, and portable by eliminating the need for sophisticated spectroscopy instrumentations, including scanning and/or moving parts [85]. Thus, spectrometer-less readers can reduce cost and improve mechanical robustness [238]. Furthermore, by acquiring images over a large field-of-view, they can enable the implementation of microarrays for high-throughput screening applications [1]. For instance, microarrays can be used to detect multiple target analytes from a given sample in a single measurement, saving both time and precious biosamples [239]. Nonetheless, compared to spectral interrogation, intensity interrogation could not achieve sensitive and reliable detection as it is less tolerant of noise factors, such as inhomogeneities in sensors' optical responses and inadequate choice of the light source.

In this work, we introduce single-wavelength imaging-based nanophotonic biosensors for achieving superior sensitivity based on reconstructed spectral shifts without cumbersome wavelength scanning and spectrometers. To achieve this goal, we employ quasi-BIC modes manifesting themselves through high-Q resonances of “diatomic metasurfaces” by generalizing and expanding the concept of BIC developed for asymmetric metasurfaces37. Diatomic metasurfaces are based on a dimer-type unit cell a.k.a “meta-molecule”, in which the dimer symmetry is broken by changing the ellipticity of one of the meta-atoms to support high Q resonance and strong field-analyte overlaps. Compared to single-unit metasurfaces, such diatomic structures provide advanced flexibility in the engineering of the in-plane asymmetry while keeping the design easier to fabricate and making it more feasible for biosensing applications. We combine these metasurfaces with advanced data processing techniques for aided imaging biosensing. Our biosensor acquires large-area intensity images of the metasurface in real-time by using a single wavelength illumination and processes them optimally via a linear estimation algorithm to reconstruct spectral shift data at high accuracy dynamically. For demonstration, we integrated antibody-functionalized metasurface chips in a 2D microarray format with microfluidics and performed in-flow detection and real-time binding of breast cancer extracellular vesicles, which are important biomarkers for diagnostics owing to their connection with disease pathology [32], [240]. Our optofluidic sensor has enabled the detection of on average 0.41 nanoparticle/µm^2 and real-time quantification of extracellular vesicle binding from solutions with as low as 1.23×10^8 particles/mL, the equivalent of 204 femtomolar. By fusing the simplicity of intensity-based large-area and real-time imaging detection with the robustness of spectroscopic systems, our technique paves the way for reliable and ultra-sensitive POC devices powered by temporally and spatially resolved biosensing spectral shift information.

4.3 Results

The experimental platform

Our all-dielectric biosensor, comprising a 2D microarray of metasurfaces, is assembled into a microfluidic unit containing three independent and simultaneously accessible flow channels made of Polydimethylsiloxane (PDMS). The optofluidic chip is illuminated with a single-wavelength light beam that excites the resonators. A CMOS camera acquires 2D images of the whole field of view at fixed time intervals to provide time-resolved intensity information from millions of CMOS pixels (Figure 4-1a). Figure 4-1b shows the red-shift ($\Delta\lambda$) of the spectral response and its corresponding intensity change (ΔI) at a fixed probing wavelength (λ_p) due to the binding of the analytes for each pixel. In contrast to spectral interrogation (i.e., measuring directly $\Delta\lambda$), basic imaging approaches only rely on the detection of the intensity changes. However, this makes basic imaging vulnerable to the noise factors such as the non-uniform optical response of the resonators over the sensor surface due to the fabrication imperfections and the inadequate choice of the illumination source (i.e., λ_p). Figure 4-1d schematically illustrates the problems of the real-time intensity change data extracted from time-resolved images at different pixel locations. The signal coming from a single-pixel is not only noisy, but also contradicts the signals coming from the adjacent pixels (red, orange, and pink curves). Traditional practice to mitigate the noise is to ensemble average the signals from multiple pixels. However, this practice tends to reduce the final signal (green curve) and lowers the sensitivity for operation at low analyte concentrations. To address these shortcomings, we utilized an imaging method relying on the robust spectral shift ($\Delta\lambda$) information that is extracted without requiring bulky and expensive spectroscopy instrumentation. By using an optimal linear estimation algorithm and a spectral decoder that is unique to each metasurface sensor, we reconstruct spectral shift data from time-resolved single-wavelength intensity images dynamically. This algorithm-aided imaging approach can increase the signal-to-noise ratio (SNR) and, consequently, improve LOD by unveiling the signals coming from a highly diluted analyte, which is otherwise unresolvable by conventional ensemble averaging methods (Figure 4-1e).

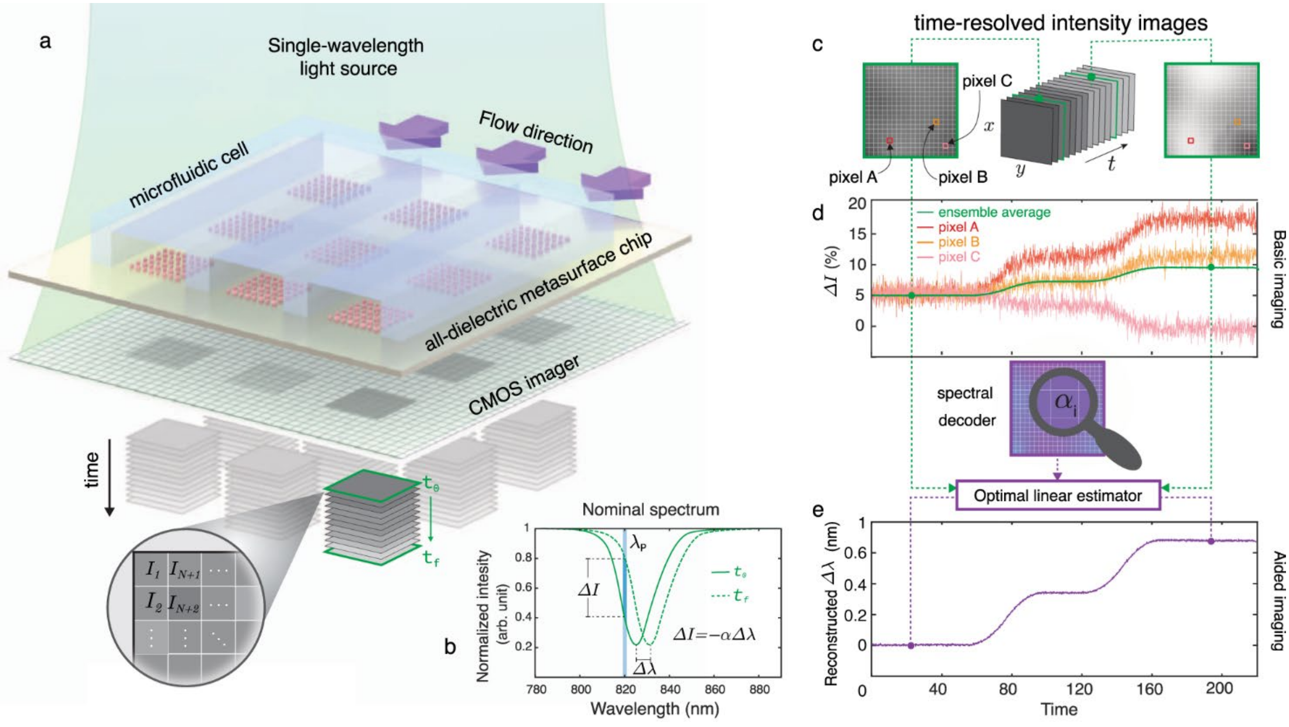
a
Single-wavelength light source
Flow direction
microfluidic cell
all-dielectric metasurface chip
CMOS imager
time
t_0
t_f
I_1 I_{N+1} ⋯
I_2 I_{N+2} ⋯
b
Nominal spectrum
λ_p
ΔI
t_0
t_f
$\Delta I = -\alpha\Delta\lambda$
$\Delta\lambda$
Normalized intesity (arb. unit)
1
0.8
0.6
0.4
0.2
780
800
820
840
860
880
Wavelength (nm)
c
time-resolved intensity images
pixel C
pixel A
pixel B
x
y
t
d
ensemble average
pixel A
pixel B
pixel C
ΔI (%)
20
15
10
5
0
Basic imaging
spectral decoder
α_i
Optimal linear estimator
e
Reconstructed $\Delta\lambda$ (nm)
1
0.6
0.4
0.2
0
0
40
80
120
160
200
Time
Aided imaging

Figure 4-1 (a) Sketch of a real-time in-flow imaging platform showing a 2D microarray of all-dielectric sensors integrated with a microfluidic cell consisting of three independent flow channels. The metasurface chip is illuminated with a single-wavelength light source and imaged with a large-area CMOS camera to acquire intensity maps of the sensors in pixel resolution (I_1, I_2, …, I_{N+1}, I_{N+2},…). (b) Biomarker binding induces a red-shift in the transmission spectrum ($\Delta\lambda$), which can be detected by tracking the resonance wavelength or by the intensity change (ΔI) at a fixed probing wavelength (λ_p). ΔI can be approximated as linearly proportional to $\Delta\lambda$ with a constant of α, which is the slope of the transmission spectrum in the linear region near λ_p . (c) Pictorial representation of time-resolved single-wavelength intensity images. (d) The illustration represents the shortcomings of the basic imaging approach. Time-resolved intensity data from single pixels (A, B, and C) from the sensor area give contradicting responses with noisy signals (red, orange, and pink curves) due to the nonuniformities. Ensemble averaging of the responses from multiple pixels can help to decrease the noise, although it may reduce the final signal, as depicted with the green curve. (e) The illustration represents the implementation and the advantages of our aided imaging approach. By leveraging the optimal linear estimator algorithm and the spectral decoder that incorporates the 2D map of the slope values, time-resolved single-wavelength intensity images are used to reconstruct robust spectral shift ($\Delta\lambda$) information dynamically (purple curve).

All-dielectric metasurfaces

To engineer our all-dielectric metasurfaces for biosensing, we developed the universal theory of quasi-BICs in broken-symmetry dimer-type metasurfaces (see Supplementary Information Note 2). The advantage of such diatomic metasurfaces is a higher number of degrees of freedom to achieve better precision in tuning the accessible enhanced near-fields and the quasi-BIC Q. The meta-molecule consists of a circular and an elliptic disk—this allows the breaking of the in-plane inversion symmetry (Figure 4-2f). The asymmetry is defined as the degree of ellipticity of one of the meta-atoms, which is proportional to the difference between the ellipse's long and short axes. We observed that controlling the asymmetry along one axis improves the tolerance to the fabrication imperfection more than the alternative methods, such as the one used in our previous work.[12] Nonzero ellipticity is a perturbation of a circular disk and induces leakage of radiation out of the metasurface plane at the BIC conditions (Figure 4-7). The BIC transforms into a quasi-BIC with finite radiative losses controlled by the asymmetry of the meta-molecule. Due to the reciprocity, the quasi-BIC manifests itself as a narrow resonant feature in the transmission spectrum for y-polarized incident light (Figure 4-7). Our design supports highly accessible enhanced electric and magnetic fields in the external surface of the dielectric nanoresonator (Figure 4-2b, c). The local electric field enhancement factors can reach as high as almost 5000 times (Figure 4-8), and the enhancement of the electric field averaged over a volume of a 5-nm thick layer in the vicinity of the nanoresonators in an aqueous media is calculated to be 12.4 times. Overall, this design gives rise to a considerable intensification of the optical interaction with the analytes and makes the platform suitable for sensing applications [241]–[243].

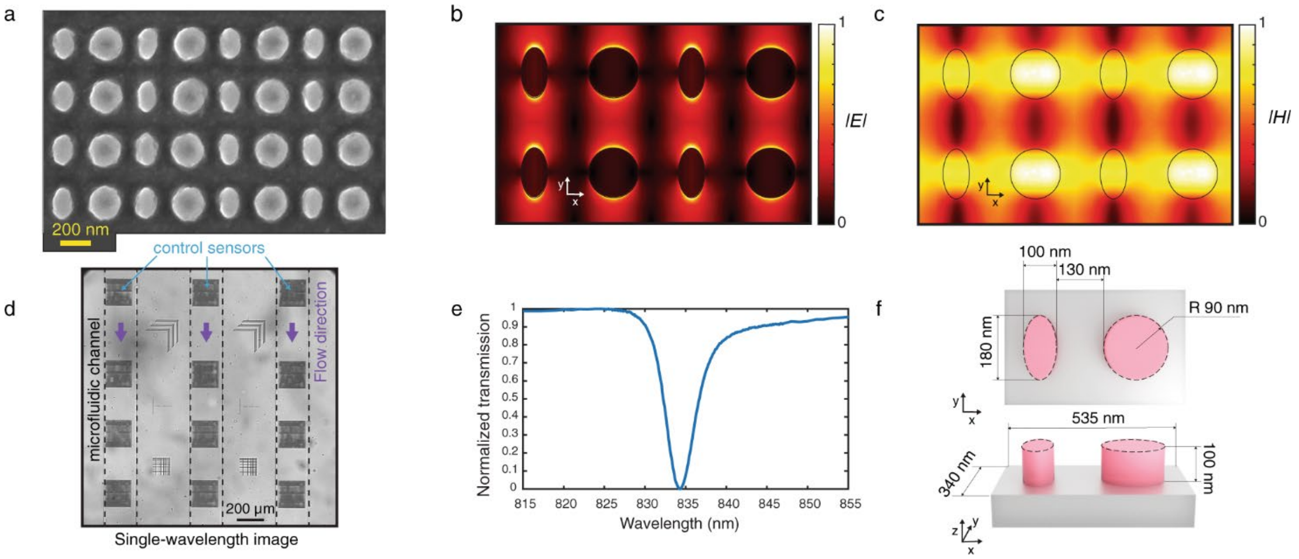

Figure 4-2 (a) Scanning electron microscopy (SEM) image of the fabricated dielectric metasurface. To prevent charging while taking SEM images, we applied a thin layer of Electra, a carbon-based conductive polymer. (b), (c) Distributions of electric and magnetic fields, respectively, in four neighboring meta-units from numerical calculations. (d) A region of interest from an intensity image obtained at the resonance wavelength of the integrated optofluidic chip showing 3 × 4 all-dielectric metasurface sensors and borders of the three Polydimethylsiloxane (PDMS) flow channels. (e) Experimentally acquired transmission spectrum of the fabricated dielectric metasurfaces in y-polarization. (f) Top and side-views schematic of the meta-unit composed of an elliptical (long and short axis 180 nm and 100 nm respectively) and a cylindrical (90 nm in radius) a-Si resonators.

Figure 4-2a shows an SEM image of the resonators fabricated by nanostructuring a 100-nm-thick a-Si on top of a fused silica substrate using a top-down fabrication method with CMOS compatible techniques. Silicon is chosen as the constituent material due to its biocompatibility, well-established surface biofunctionalization methods, and access to mature CMOS fabrication facilities. Also, silicon benefits from desirable optical properties, including a high refractive index and relatively low loss in the near-IR range below 850 nm. The metasurfaces operate in the aqueous media with their resonance in the visible and near-IR spectral range (600 nm to 850 nm). Working in this range offers several unique advantages, including the wide availability of high-performance and cost-effective silicon-based CMOS and CCD cameras. For fabrication, we used the design with geometrical parameters shown in Figure 4-2f, which corresponds to the ellipticity of 0.44. As mentioned above, the metasurface design is tolerant to fabrication imperfections due to the chosen symmetry-breaking strategy. The fabricated resonators were characterized to have <2% size deviations over the sensor area. In turn, a good homogeneity is observed in the optical response of the resonators (see supplementary information note 4).

Our metasurface chip comprises twelve 250 µm by 250 µm sensors in a 3 × 4 microarray format. The optofluidics incorporates three independent microfluidic channels, which allow the sensors to function in aqueous media for in-flow measurements and preserve analyte biofunctionality. The field of view (FOV) of the setup is >7 mm^2; thus, we can acquire the images of all of the twelve sensors on a chip in a single shot. Figure 4-2d shows a subset of an intensity image obtained at the resonance wavelength of the all-dielectric metasurface. The sensors, as well as the borders of the three PDMS fluidic channels, are visible at high contrast. The cross patterns in between the microfluidic channels are alignment and focus monitoring marks, which are used during the subsequent data processing of the time-resolved intensity images. Our aided imaging approach, based on an optimal linear estimation algorithm and a spectral decoder, allows for precise reconstruction of the spectral shift over large areas from the acquired images. The spatially resolved reconstructed shift data from a large FOV has a compelling advantage over the traditional spectrometers by allowing for a concurrent control test and multiplexing to detect a panel of biomarkers in parallel. Figure 4-2e shows the experimentally recorded transmission spectrum of the engineered sensor. The optical characterization of 12 sensors, which are sampled with more than 950,000 CMOS pixels in the field of view, shows that the FWHM of the resonance is as low as 2.3 nm and on average 4.57 nm with a standard deviation of 0.47 nm. Consequently, a Q as high as 250 and, on average 178.6 with a standard deviation of 15.8 was recorded experimentally. Owing to the high-Q resonances and highly accessible enhanced near-fields, we achieved an experimental bulk refractive index sensitivity of 305 nm/RIU and a figure-of-merit (defined as sensitivity divided by FWHM) of 68 1/RIU.

Aided imaging method

Figure 4-3 elucidates the gained robustness and tolerance of the biosensor when the aided imaging method is implemented compared to the basic imaging. To reconstruct spectral shift ($\Delta\lambda$), we fed the time-resolved intensity data to an optimal linear estimation algorithm that uses a "spectral decoder" and the recorded intensity change of each CMOS pixel to compute the best estimate of $\Delta\lambda$ for the entire sensor. The spectral decoder of a sensor is built up by gathering the values of pixel-wise slopes (α) across the sensor area. To do so, we linearize the spectrum associated with each pixel around the probing wavelength λ_p and compute its slope (see Figure 4-3a). This can be simply obtained by recording two images using narrowband illuminations: one at λ_p and a second one at $\lambda_p + \delta$, for a small value of δ. This decoder provides information about the weight of the contribution of each pixel to the spectral shift so that the more sensitive ones have a greater influence on the estimation of $\Delta\lambda$. In this work, the spectral decoder was computed using a hyperspectral imaging system where the sensor was imaged at wavelengths with a small spectral increment of 0.1 nm, and the extracted α values were mapped as a 2D matrix. To experimentally demonstrate the advantages of our aided imaging method over basic imaging, we studied two cases of uniform and non-uniform optical responses over the sensor area at different probing wavelengths. The experiments involved recording simultaneously time-resolved intensity images of three different sensors assembled in a microfluidic channel and comparing their responses under the same condition. This is achieved by flowing aqueous solutions with varying refractive indices across the sensors with consecutive injections of phosphate buffer saline (PBS) at different concentrations. Figure 4-3b, c shows the responses of the three sensors at the illumination wavelengths of 808.8 nm and 811.3 nm, respectively. In the first case shown in Figure 4-3b (top panel), the spectral decoder histogram of a representative sensor (sensor 2) is populated dominantly with negative values, indicating that the probing wavelength intersects the spectra of most pixels on the left flank of the resonance dip. Even with relatively uniform distributions, the responses of the three sensors obtained with basic imaging differ in the intensity change sensorgram (Figure 4-3b, middle panel) compared to the aided imaging method (Figure 4-3b, bottom panel). If the nonuniformity increases, the performance of the basic imaging deteriorates even more, as shown in the second case in Figure 4-3c. In this figure (top panel), the spectral decoder histogram has a similar number of positive and negative values. Consequently, in the ensemble averaging with the absolute intensity change, the pixels with opposite-valued slopes work against one another and result in significant variations between the three responses, leading to poor sensing performance (Figure 4-3c, middle panel). In contrast, when the spectral decoder is used in the context of the optimal estimator, we obtained almost identical responses from all three sensors (Figure 4-3c, bottom panel). The drastically improved performance illustrates that our technique is robust to the inhomogeneity of sensor response that is caused by, for instance, small fabrication imperfections or the improper choice of probing wavelength. This is a significant step toward inexpensive POC instruments for on-site use in resource-limited settings since it eliminates the need for the elusive perfect fabrication of the sensors as well as allows for flexibility in the choice of probing wavelengths. Moreover, our technique provides the reconstruction of the spectral shift without the need for a bulky and expensive spectrometer.

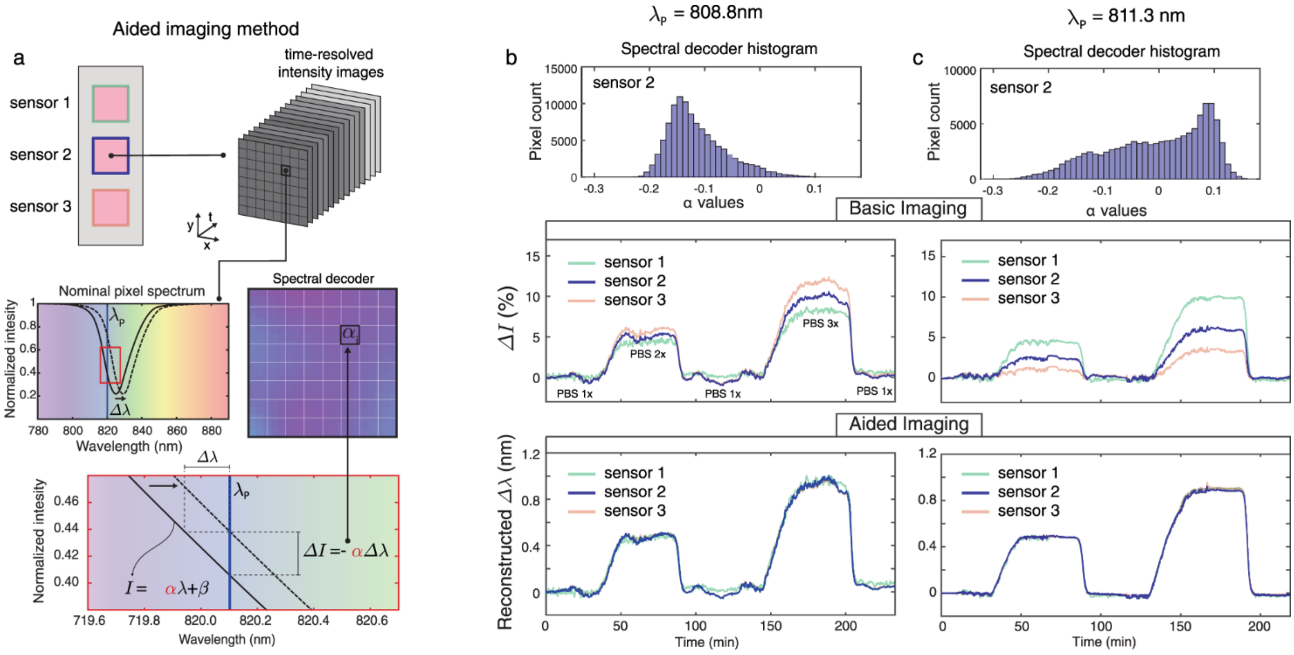

Figure 4-3 (a) Time-resolved intensity data is fed to the optimal linear estimation algorithm with a spectral decoder, which is the two-dimensional (2D) map of the slope (α) of the transmission spectrum for each CMOS pixel at the probing wavelength (λ_p). (b) At λ_p p = 808.8 nm, the histogram of α values from a single sensor is populated mostly with negative values because, for the majority of the pixels, the resonance is probed at the left flank of the transmission dip (top panel). This case represents a sensor having a relatively homogenous optical response across its surface. For experimental bulk sensing, under a constant running of phosphate buffer saline (PBS) 1x (n = 1.33441), three sensors are exposed to a varying medium with PBS 2x (n = 1.33584) and PBS 3x (n = 1.33731) and their ensemble-averaged intensity changes (ΔI, middle panel) and reconstructed spectral shifts ($\Delta\lambda$, bottom panel) are presented as a function of time. (c) At λ_p = 811.3 nm, the histogram of the same sensor has a similar number of positive and negative α values (top panel). This case represents a sensor having an inhomogeneous optical response. For the same bulk sensing experiment used in Figure 4-3b, the ensemble-averaged ΔI response of different sensors shows significantly varying signals (middle panel). In contrast, the reconstructed spectral shift data obtained by aided imaging (bottom panel) is consistent between the three sensors.

Biosensing experiments

To demonstrate the biosensing functionality of our aided imaging method, we performed real-time in-flow detection of nanoparticles (NPs), as well as biological extracellular vesicles (EVs) secreted from cancer cells with an immunoassay. Initially, biotinylated silica nanoparticles (100 nm diameter) were used as the mimics of bioparticles (i.e., EVs and viruses) for the characterization of the sensors [244], [245]. Each microfluidic flow channel interacts with four dielectric metasurface sensors (see Figure 4-2d). The first sensor, which is blocked with bovine serum albumin (BSA), serves as a control sensor. The successive three sensors (detection sensors) are locally functionalized with streptavidin protein to target the biotin molecules on the silica nanoparticles (Figure 4-10). A steady flow of phosphate buffer saline (PBS) 1X delivers a sequence of different dilutions of the NP solution to the sensors, which are continuously illuminated with a linearly polarized single-wavelength light and imaged in time intervals of 14 s by a CMOS camera. The reported $\Delta\lambda$ in the y-axis is the reconstructed shift observed on the detection sensors, from which the reconstructed shift of the control sensor is subtracted to account for any non-specific bindings.

The calibration curve extracted from the reconstructed shift induced by the binding events of the silica nanoparticles on the all-dielectric metasurfaces is shown in Figure 4-4a. The error bars in the figure are representing the standard deviation of $\Delta\lambda$ over time (sensorgram) from each sensor over a time-interval consisting of 81 consecutive images after the analyte binding reaches the equilibrium state. The relative standard deviation for the reproducibility of $\Delta\lambda$ in the working range of sensors is observed to be between 0.33% and 3.97%. LOD is the smallest concentration that can be detected with reasonable certainty for a biosensor [246]. The dashed red line in Figure 4-4a shows the three times the averaged standard deviation, which was calculated by averaging the standard deviation of the sensorgram signals at equilibrium states over at least four time-intervals, each consisting of 81 consecutive images. The LOD of 1.2×10^8 nanoparticles/mL, the equivalent of 199 femtomolar that corresponds to 126 ng/mL, was extracted from the intersection of the dashed red line and the calibration curve. The lowest detected quantity of 1.9×10^8 nanoparticles/mL or 315 femtomolar, corresponding to 200 ng/mL, was measured and further investigated with SEM images revealing the equivalent detection of 0.41 nanoparticles/µm^2 averaged over 78 SEM images, and the total area of 687 µm^2 at randomly chosen locations on the sensors with the standard deviation of 0.26 nanoparticles/µm^2 and 0.34 nanoparticles/µm^2 as the median. The insets of Figure 4-4a shows representative SEM images from the solutions with 1.9×10^8 nanoparticles/mL and 9.5×10^{12} nanoparticles/mL from left to right, respectively.

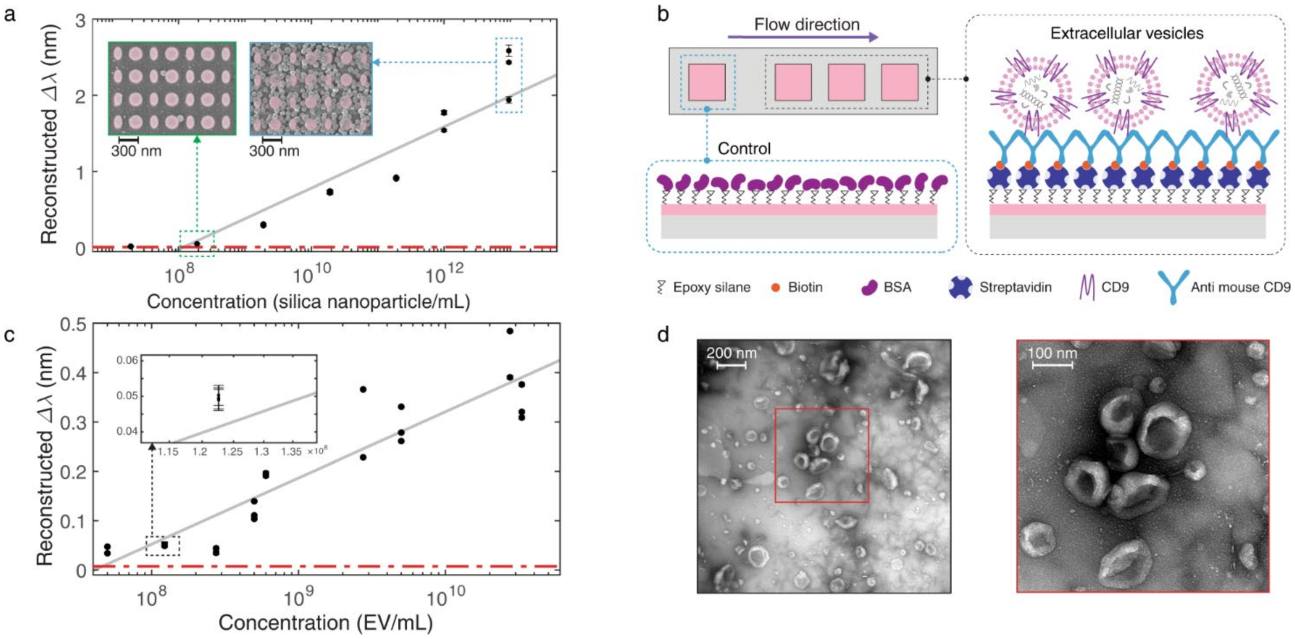

Figure 4-4 (a)The reconstructed spectral shift ($\Delta\lambda$) calibration curve of biotinylated silica nanoparticles (100 nm diameter). The insets are scanning electron microscopy images of the sensors with bound silica nanoparticles on resonators after introducing suspensions with 1.9×10^8 nanoparticles/mL and 9.5×10^{12} nanoparticles/mL from left to right, respectively. The represented data points in the calibration curves (a), (c) are the mean $\Delta\lambda$ over time from each sensor over a time-interval consisting of 81 consecutive images after the analyte binding reaches the equilibrium state, and the error bars indicate the standard deviations. The reconstructed $\Delta\lambda$ data points are obtained from seven dilutions of silica nanoparticle solutions over three independent sensors to achieve 21 data points on the calibration curve. The reconstructed $\Delta\lambda$ data from the detection sensors are corrected to the non-specific bindings on the control sensor. Some data points are overlapped due to the good agreement between the sensor performance. (b) Biorecognition assay to detect extracellular vesicles (EVs) on the detection sensors and on the control sensor blocked with bovine serum albumin (BSA) to account for non-specific binding is shown on top. (c) The reconstructed spectral shift calibration curve of EVs. The inset is the same plot with a magnified x-axis to better resolve the small error bars for an exemplary data point. The reconstructed shift data points from the detection sensors are corrected to the non-specific bindings on the control sensor. The represented data points are collected from nine different concentrations of EV solutions diluted from three independent batches measured on eight independent sensors to yield 24 data points on the calibration curve. Some data points are overlapped due to the good agreement between the sensors. (d) Transmission electron microscopy images of EVs from the cell culture supernatant of 4T1 mouse breast cancer cells can be seen at the bottom; the magnifications are ×23,000 and ×30,000 from left to the right, respectively.

To demonstrate the competence of the proposed method with a biorecognition assay, we detected and quantified EVs purified from the cell culture supernatant of 4T1 mouse breast cancer cells [32]. EVs, which include exosomes and microvesicles, are nanoscale bioactive membrane particles secreted by virtually all types of cells [247]. There is strong evidence that EVs derived from breast cancer cells influence tumor progression [32]. EVs carry molecular information from parental cells; therefore, they can be considered as biomarkers for early-stage cancer detection and for minimally or non-invasive diagnostics [240]. A transmission electron microscopy (TEM) image of the EVs with a mode size between 100 and 150 nm [32] is shown in Figure 4-4d, and their purification process and quantification are briefly explained in the methods section. EVs are highly enriched in tetraspanins [247]. The tetraspanins superfamily is a family of proteins with at least 33 distinct members in mammals; among them, CD9 is the best-studied transmembrane protein and a versatile marker that has been used for EV subtypes, including exosomes [248], [249]. In order to capture the vesicles, we targeted CD9 and immobilized the corresponding biotinylated KMC8 anti-CD9 monoclonal antibody on the detection sensors functionalized with streptavidin. The control sensor was blocked with BSA (Figure 4-4b). As in the nanoparticle experiment, a pressure pump maintains the constant buffer (PBS 1x) flow in the microfluidic channel, and a syringe pump provides successive injections of EV samples in various concentrations. Figure 4-4c shows the calibration curve that uses the reconstructed shifts derived from single-wavelength real-time in-flow experiments to detect EVs from 4T1 mouse breast cancer cells. The error bars in the figure are calculated in the same manner as in Figure 4-4a. In this case, the relative standard deviation for reproducibility varies between 0.50% and 8.11%. Our sensors have a limit of detection of 8×10^7 EV/mL or 133 femtomolar, according to the intersection of the three times the averaged standard deviation (the dashed red line in Figure 4-4c) with the calibration curve, and the lowest detected quantity was measured as 1.23×10^8 EV/mL or 204 femtomolar. The EV protein content at these concentration values corresponds to 267 ng/mL and 423 ng/mL, respectively45. While typically correlating with the tumor burden, the average values of cancer-related EVs range between 10^9 and 10^{10} per mL of human plasma [30], [250],

[251]. With a LOD of 8×10^7 EV/mL and about five orders of magnitude dynamic range, our results indicate that the performance of the proposed sensor is clinically relevant for the detection of cancer-related EVs.

4.4 Discussion

We demonstrated a label-free nanophotonic biosensor, which leverages an aided imaging approach based on novel data processing and an optofluidic chip comprising of all-dielectric metasurfaces. Our method enables the extraction of spectral shift information from single-wavelength intensity images at high accuracy while preserving temporal and spatial resolution. Importantly, it is based on simple imaging optics with fixed-wavelength illumination and a CMOS camera to collect data over a large field of view in real-time. Compared to the basic intensity imaging readers that merely rely on intensity change, our approach, aided by an optimal linear estimation algorithm, provides robustness to the spectral inhomogeneities across the sensor surface that can originate from fabrication imperfections and inadequate operation wavelength. The current device, which images over 7 mm^2 field-of-view, can be used to perform simultaneous measurements from hundreds of individual sensors in a microarray format. Hence our approach is suitable for multiplexed detection of a panel of biomarkers in-real time for high-throughput monitoring. Our diatomic all-dielectric metasurface, emanated from quasi-BIC modes, enables high-performance sensing by supporting high Q resonances with accessible near-fields. Furthermore, its unique symmetry-breaking design makes it more tolerant of nanofabrication. Using CMOS-compatible techniques, we fabricated highly uniform silicon metasurfaces operating below 850 nm in aqueous media and integrated them with microfluidics for in-flow measurements. As a proof-of-concept, we applied the new optofluidic device for real-time detection of breast cancer-derived EVs, and by functionalization of the metasurfaces with specific antibodies, we were able to report the LOD of down to 133 femtomolar.

As an outlook, the flexibility of the detection principle can enable the expansion into various different application areas. For instance, with proper surface functionalization, we can selectively target other bioparticles, such as intact viruses, for infectious disease applications and smaller biomolecules, including proteins, antibodies, and nucleic acids. We anticipate wafer-scale and high-throughput fabrication techniques to eliminate the dependence on high-resolution e-beam lithography. This can drastically reduce the cost and enable disposable biochips customized as consumables for detecting different analytes. We foresee device integration in miniaturized biosensors by using small-scale light sources with tailored bandwidth and low-cost on-chip imagers. The use of large-area imaging data gives the opportunity of implementing other advanced computation techniques (i.e., artificial intelligence methods) toward smarter sensing. By eliminating the need for bulky and expensive instrumentation, the spectrometer-less device architecture can lead to affordable, compact, easy-to-use, and reliable point-of-care systems for disease diagnostics, personalized medicine, and the democratization of health care in resource-limited settings.

4.5 Methods

All-dielectric metasurface fabrication

A thin layer of a-Si with 100 nm thickness was deposited using low-pressure chemical vapor deposition (LPCVD) on a clean bare fused-silica wafer. The wafer was patterned using 100 KeV EBL. First, the wafers were cleaned with radio corporation of America (RCA) cleaning solution and oxygen plasma. A positive-tone resist poly(methyl methacrylate) in a double-layer configuration (PMMA 495 K bottom and 950 K top) was spin-coated and baked for 5 min at 180 °C to yield a total thickness of 160 nm. PMMA double-layer configuration is crucial to make undercut structures to facilitate lift-off. A 10-nm gold layer is sputtered on the PMMA layer to ensure conductivity during electron-beam writing. After EBL exposure, the gold layer was etched away in KI + I_2 solution, and the wafer was developed with a mixture of Methyl isobutyl ketone (MIBK) and IPA(Isopropyl alcohol) in 1-3 ratios. To make a hard mask, a 30-nm-thick aluminum layer was deposited using an electron-beam evaporator, followed by dicing the wafer into 1.5 cm × 1.5 cm chips. Metal lift-off was done by soaking the chips in a resist-remover bath at 70 °C for 6 h. The fabrication process concludes with transferring the nanostructures to the a-Si layer using fluorine-based deep reactive ion etching and, finally, hard mask removal in an aluminum etch solution.

Optical characterization setup

All-dielectric metasurfaces were optically characterized using a hyperspectral imaging platform. The HSI system consists of a supercontinuum laser (SuperK EXTREME EXR-15, NKT photonics) coupled to a tunable filter (LLTF, NKT photonics) integrated with an inverted microscope (Eclipse-Ti, Nikon). The collimated linearly polarized laser line (1.75 nm bandwidth at 700 nm) light was transmitted from the metasurface and collected with a ×10 objective, conveyed through a collinear analyzer and imaged with a CMOS camera (DS Qi 2, Nikon). To extract the transmission spectrum of all-dielectric metasurfaces with pixel size spatial resolution over a large field of view, a hyperspectral data cube was acquired by continuously imaging the chip synchronized with the sweep of the illumination source wavelength. The hyperspectral data cube of a chip was normalized to the hyperspectral data cube of the light source. The normalized intensity profile of each pixel over the wavelength sweep yields the transmission spectra of that pixel. The devices were connected and controlled with a centralized MATLAB code.

Single-wavelength imaging-based real-time biosensing measurements

The optical setup for the real-time in-flow measurements was the same as the optical characterization setup. A biofunctionalized chip was assembled into a microfluidic structure and placed on a microscope stage. The microfluidic system consists of a pressure pump (Elveflow, OB1) to maintain the constant buffer (PBS 1x) flow of 10 µL/min in the microfluidic channel, a syringe pump (Advanced MicroFluidics, LSPone) for analyte injection with a flowmeter (Elveflow, FS3) and tubing. Our data was collected from the net sample volume of 150 µL, which is more than one order of magnitude smaller than a conventional blood test. This volume can be further decreased to few tens of µLs if in-flow measurements and real-time data are not needed and the measurements are performed under static conditions. Image acquisition in 14-second intervals and data pre-processing were handled with the centralized MATLAB code assisted by a macro from NIS Nikon software. The pre-processing module was capable of providing live feedback by plotting the reconstructed spectral shift over time.

Full-wave numerical analysis

Numerical analysis of the all-dielectric metasurfaces was performed using a commercially available finite-element frequency-domain solver (CST Microwave Studio 2018).

Microfluidic structure fabrication

The microfluidic structures were made by soft lithography using a silicon master mold to achieve three 300 µm wide individual flow channels that are simultaneously accessible. The master mold was made with photolithography techniques to achieve the patterns of the final microfluidic channel. A film of positive-tone resist (AZ 1512, 1.3 µm) was coated and patterned on a silicon wafer using an automatic coater and developer (EVG 150, EV Group) and direct laser writer (MLA 150, Heidelberg). The patterned photoresist was used as an etching mask for fluorine-based silicon dry etch in a deep reactive ion etching (DRIE) tool (AMS 200, Adixen) to make 25 µm thick patterns. Finally, the photoresist is removed with oxygen plasma cleaning. One mold can be used repeatedly if the surface is protected from the permanent adhesion of PDMS by silanization. Silanization was done using TriMethylChloroSilane (TMCS) in a desiccator under a vacuum to make TMCS evaporate and form a passivation layer on the mold surface. The base and crosslinker precursors were mixed in a 10 to 1 ratio to make PDMS. The precursor mixture was degassed in a desiccator and poured into the mold. After another degassing step to ensure removing all the bubbles from the mold's surface, it was baked at 80 °C for 4 h. Finally, the inverted replica of the mold in PDMS was peeled off from the mold, and each pattern was cut, punched, and bound to its complementary part with oxygen plasma.

Surface chemistry

Covalent surface chemistry based on (3-glycidoxypropyl) trimethoxysilane (3-GPS) (Sigma-Aldrich) monolayer was used to immobilize the capture molecules on the all-dielectric metasurface. The silane end bonds to the silicon oxide and covers the all-dielectric metasurface with a uniform 3-GPS monolayer. The epoxide functional group of 3-GPS binds to the amine group of the capture molecules. First, the chips were cleaned in RCA solution at 50 °C for 30 min. The clean chips were incubated in the 3-GPS solution in toluene (1% vol/vol) for 20 min and rinsed in fresh toluene to remove the unreacted 3-GPS molecules and dried. The chips were baked for 30 min at 120 °C and were stored under a vacuum to be used within a week.

Biotinylated silica nanoparticles biorecognition assay

To specifically target the Biotinylated silica nanoparticles (Creative Diagnostics) of 100 nm diameter, streptavidin was covalently immobilized on the detection sensors as a capture molecule, and BSA (Sigma-Aldrich) was immobilized on the control sensor. Epoxy-silane chemistry described above is used for the immobilization of a monolayer of Streptavidin and BSA molecules on the detection and control sensors, respectively. 40 droplets (480 pL per droplet) of Streptavidin (Thermo Scientific, 1 mg/mL) and BSA (1% wt/vol) in PBS (Sigma-Aldrich) 1x buffer were spotted on the sensors with a low-volume liquid dispenser (sciFLEXARRAYER S3, Scienion). The spotted chip is incubated for 16 hours at 4 °C.

EV biorecognition assay

All-dielectric metasurfaces were initially treated with epoxy-silane chemistry and functionalized with a monolayer of streptavidin on the detection sensors and BSA on the control sensors by spotting technique. Streptavidin and BSA molecules are incubated for 2 h at room temperature and rinsed consecutively with PBS 1x and Mili-Q water, and then dried. In all, 40 droplets (480 pL per droplet) of a biotinylated capturing molecule, KMC8 monoclonal antibody (Biotin Rat Anti-Mouse CD9, BD biosciences, 0.5 mg/mL) in PBS 1x were spotted on detection sensors and BSA on the control sensors. The spotted chip is incubated for 16 h at 4 °C.

EV isolation

EVs were purified from media conditioned by 4T1 cells. In all, 4T1 cells (mammary adenocarcinoma; from ATCC) were cultured in 15 cm tissue culture-treated dishes in Iscove’s Modified Dulbecco’s Medium (IMDM, Sigma) supplemented with 10% fetal bovine serum (FBS; Gibco), L-glutamine (Amimed), and penicillin/streptomycin (Gibco). Cells at ~40-50% confluence were moved to a medium containing 5% EV-depleted FBS45. EVs were isolated from the conditioned medium using sequential ultracentrifugation (500 × g for 5 min; 2000 × g for 10 min; 4600 × g for 20 min; 134,000 × g for 70 min). The resulting EV pellet was washed in PBS, ultracentrifuged again at 134,000 × g for 70 min, and finally dissolved in PBS, which was obtained by ultracentrifugation of standard FBS at 134,000 × g for 16 h at 4 °C followed by filtration through a 0.1-mm vacuum filtration bottle. After 3 days, the conditioned medium was collected and centrifuged at 500 × g for 5 min, 2000 × g for 10 min to remove dead cells and debris, and ultracentrifuged at 4600×g for 20 min at 4 °C to remove large vesicles. The supernatant was then transferred to new tubes and ultracentrifuged at 134,000 × g for 70 min at 4 °C to collect small EVs. The EV pellet was then washed in 35 mL of PBS and ultracentrifuged again at 134,000 × g for 70 min at 4 °C. All ultracentrifugation steps were performed using a Beckman ultracentrifuge and a SW32Ti rotor. The resulting EV preparation was resuspended in PBS and stored at −80 °C.

Transmission electron microscopy of purified EVs

Purified EVs (5 µg in 15 µL of PBS) were applied to carbon-coated 400 mesh grids (Electron Microscopy Sciences) for 5 min, then washed with PBS and stained with 2% uranyl acetate (Sigma) for 30 s. Excess stain was removed by touching the very edge of the mesh with a piece of filter paper (Whatman). Grids were then let dry completely prior to acquisition. Images were obtained using a transmission electron microscope device (Tecnai Spirit, FEI Company).

Computation of spectral decoder:

Given a probing wavelength λ_p, 11 images are recorded at wavelengths according to the column vector $\lambda = [\lambda p - 0.5, \dots , \lambda p, \dots , , \lambda p + 0.5]$ nm. For each pixel i, the recorded intensities are normalized according to the intensity value corresponding to λ_p, resulting in a vector y^i, where $y^i[6] = 1$. The slope associated with pixel i is then given by Equation 4-1

$$\alpha^i = \frac{(y^i - \overline{y^i})^T(\lambda^i - \overline{\lambda^i})}{(\lambda^i - \overline{\lambda^i})^T(\lambda^i - \overline{\lambda^i})}$$

Equation 4-1 The associate slope with pixel i

(where the bar represents the mean value of the vector. Note that, while we use 11 images to improve the estimation of the slope, two images are sufficient. The computation of the spectral decoder was carried out in MATLAB 2019b.

Optimal linear estimator:

Images acquired over time at the probing wavelength λ_p are first normalized to the average image over 10 acquisitions to establish a baseline. An image pixel i in a sensor area with N pixels has an associated (normalized) intensity value at time k given by y_k^i. The optimal linear estimator of the resonance shift at time k over the sensor area is given by Equation 4-2.

$$\widehat{\Delta\lambda}_k = \frac{1}{\sum_N (\alpha^i)^2} \sum_N \alpha^i (1 - y_k^i)$$

Equation 4-2 The optimal linear estimator of the resonance shift at time k over the sensor area

For the utilized metasurfaces, the optimal linear estimator works well in the neighborhood of λ_p, which ranges from 2 to 3nm, depending on the spectral location of λ_p. For values outside the linear regime, we implemented a correction factor to enable the measurement of large spectral shifts (i.e., silica nanoparticles at high concentrations). All computations were carried out in MATLAB 2019b.

4.6 Supplementary information

Supplementary Note 1: Important parameters in designing refractometric biosensors

Multiple parameters affect the performance of a refractometric biosensor; hence, it is essential to consider the relevant parameters simultaneously. Below, we discuss some of them :

i) The Q contributes to the performance of a biosensor utilizing optical resonances. An ultra-high Q resonance resembling a delta function is not suitable for refractometric imaging-based detection because the intensity changes induced by the wavelength shifts cannot be used to resolve continuous variation of intensity (Figure 4-5). On the one hand, it is preferable to have relatively sharp resonances, i.e., with steep slopes of the intensity profile, to provide bigger changes in the output signal for a given resonance shift. Figures 4-6a and b show realistic cases with a high Q value of 346 and a lower Q of 88. A bigger output value leads to the easier detection of more dilute samples, resulting in a better LOD. On the other hand, a lower Q offers a wider dynamic range of a biosensor, as shown in the example (Figures 4-6c and d). Thus, there is a trade-off between the LOD and dynamic range that we can achieve for a given biosensor.

ii) Another important consideration in designing metasurfaces for sensing applications is the enhancement of the near-fields and their accessibly to the analytes. It is essential that enhanced near-fields extend out of the resonator and spatially overlap with the samples on the sensor surface (see also Section 3). This also brings a trade-off because maximizing the field's spatial overlap with analytes (e.g., by not confining the mode tightly in a high-index meta-unit) reduces the Q value. Here, it is useful to emphasize that BIC designs that can achieve impressively high Qs with tightly confined field enhancements inside the resonators are less suited for biosensing and more appropriate for nonlinear or lasing applications.

iii) In biosensing applications, it is important to show operation in an aqueous environment because water is essential to preserve bioactivity and extend its applicability for real-time and in-flow measurements. However, the optical loss of water hampers the high-Q values of the nanoresonators. In our work, we optimized a design for operation in solution (with the integration of a microfluidic chip) while still supporting suitably high Q value as well as accessible high near-field enhancements at below 850 nm wavelength range.

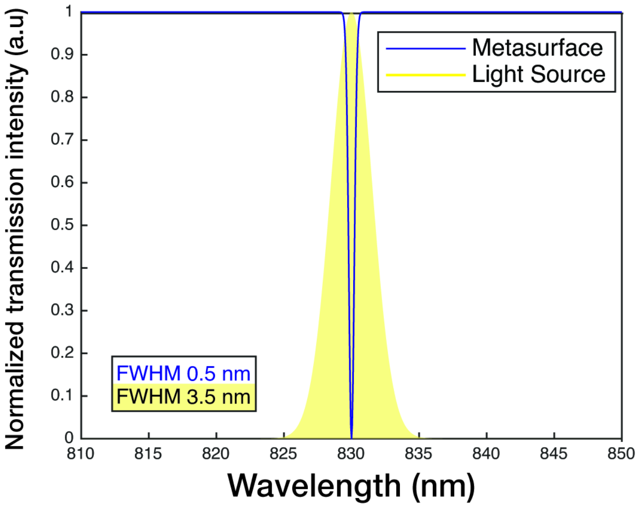

Figure 4-5 Very sharp resonances cannot be resolved using a light source with a broader spectrum

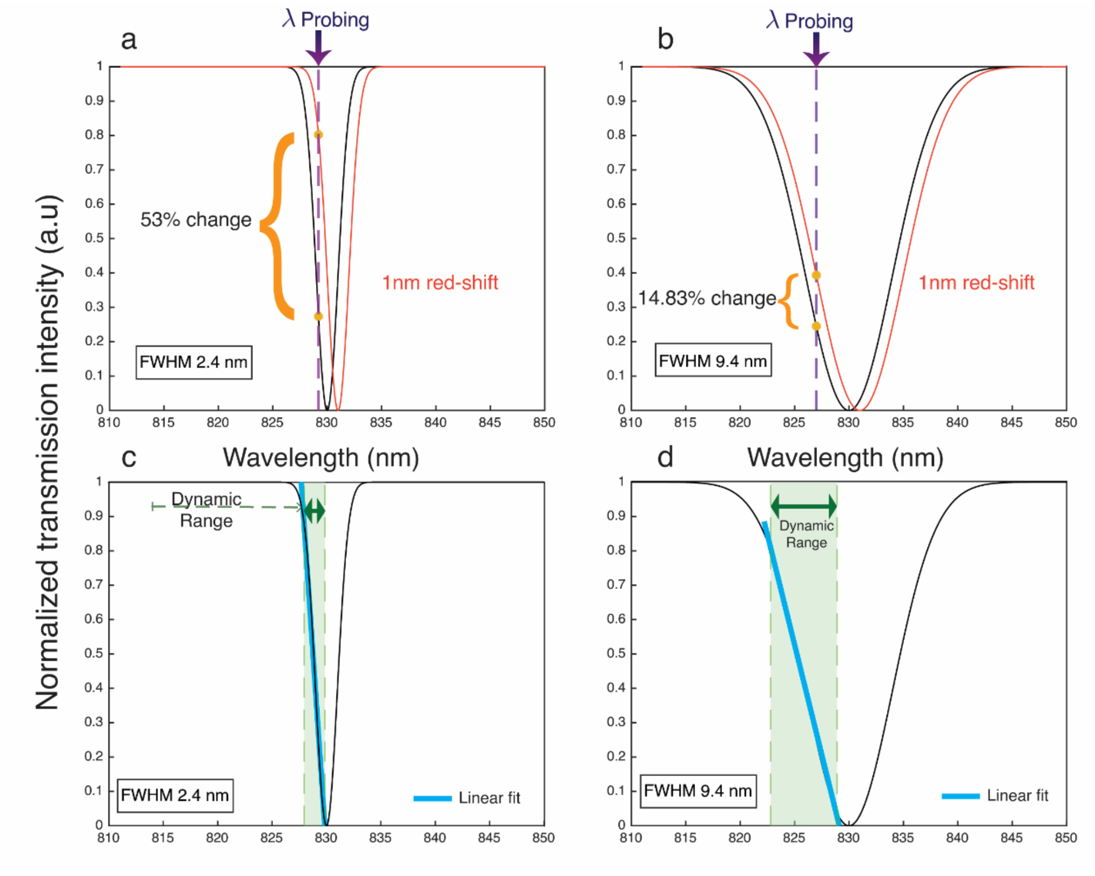

Figure 4-6 The trade-offs involved in using higher and lower quality factor (Q) metasurfaces for sensing are shown graphically with representative curves. The narrowband illumination is chosen as a line (at a wavelength of λ_p probe) for a better illustration of the trade-offs. (a) and (b) show the influence of the Q value on the obtained intensity changes from the red-shifting of the resonance due to the analyte binding. (a) shows that a higher Q resonance (346) with the full-width at half-maximum (FWHM) of 2.4 nm exhibits a 53% intensity change when the resonance is red-shifted for 1 nm. On the other hand, (b) shows that a lower Q resonance (88) with the FWHM of 9.4 nm exhibits only a 14.83% intensity change for the same red-shift of 1 nm. (c) and (d) show the influence of the Q on the dynamic range of the sensor. Here, the dynamic range is chosen as the part of the resonance when the slope has less than 1% of deviation from the linear fit. (c) shows that as the higher Q resonance has smaller bandwidth, it leads to a smaller dynamic range. On the other hand, (d) shows that a lower Q resonance offers a larger dynamic range.

Supplementary Note 2: The general concept of quasi-BICs in asymmetric diatomic metasurfaces

In this section, we develop a general theory of quasi-BICs in dielectric diatomic metasurfaces. Contrary to earlier works, here, we intentionally use a complex unit cell (meta-molecule) with two meta-atoms per unit. Compared to single-atom metasurfaces, diatomic structures provide advanced flexibility in the engineering of the in-plane asymmetry while keeping the design easy to fabricate and feasible for biosensing applications.

We consider a silicon metasurface composed of a square lattice of elliptical dimers on a glass substrate. Parameters: disk height is 100 nm, x-period and y-period are 535 and 340 nm, respectively; the distance between disk centers is 270 nm, the radius of the short and long semi-axis of the ellipse is 50 nm and 90 nm, respectively. The structure supports a true BIC with an infinite quality factor at a wavelength of about 855 nm. To achieve a finite Q of the resonance, we transform the BIC to a quasi-BIC by introducing the in-plane asymmetry of the unit cell. Due to the reciprocity, the quasi-BIC can also be observed in response to an external excitation of the structure. For such a diatomic metasurface, the asymmetry can be introduced in different ways, including squeezing one meta-atom, changing its ellipticity, and rotation of one or two meta-atoms, as shown in Figure 4-7a. The asymmetry parameter α is a linear function of perturbation and has a specific definition for each considered case, as shown in Figure 4-7d. An important difference between diatomic metasurfaces from monoatomic is a higher number of degrees of freedom, which allows for achieving better precision in the control of the quasi-BIC Q. Depending on the application and the device requirements, one can use the most suitable of the mentioned types of asymmetry to obtain a quasi-BIC with a specific Q and field enhancement. We also note that, unlike squeezing and rotation, to the best of our knowledge, changing the ellipticity was not explored earlier as a way to introduce asymmetry for diatomic metasurfaces.

The eigenmode calculations show that for diatomic metasurfaces, the radiative Q of the quasi-BIC decreases with the increase of asymmetry following the inverse square law $Q_{\mathrm{rad}} = Q_0\alpha^{-2}$, as shown in Figure 4-7b. For simulations of the radiative Q, we use the material dispersion for silicon without absorption losses. The total Q factor is limited by the non-radiative quality factor Q_{nrad}, which takes into account the material losses, fabrication imperfections, and sample finite $Q^{-1} = Q_{\mathrm{rad}}^{-1} + Q_{\mathrm{nrad}}^{-1}$. Assuming the weak dependence of Q_{nrad} on the asymmetry, we obtain a closed-form expression for the total Q (Equation 4-3)

$$Q = \frac{Q_{nrad}}{1 + \alpha^2 Q_{nrad}/Q_0}$$

Equation 4-3 Closed-form expression for the total quality factor

The dependence on α is shown with blue circles in Figure 4-7b.

In the transmission spectrum, the quasi-BIC produces a resonant dip with a Fano lineshape, which its width and position depend on the asymmetry parameter. Characteristic normalized transmission spectra are shown in Supplementary Figure 4-7c. For $\alpha = 0$, sharp features in the transmission disappear, and the resonant mode becomes dark, so it does not manifest itself in the scattering spectra.

For the experimental design, we change the disk ellipticity increasing the smaller semi-axis of one of the meta-atoms to 90 nm, making it circular. Such perturbation corresponds to the ellipticity $\alpha = 0.44$. For the designed structure, the quasi-BIC mode is strongly confined to the surface of the resonators, making the metasurface an ideal platform for biosensing applications.

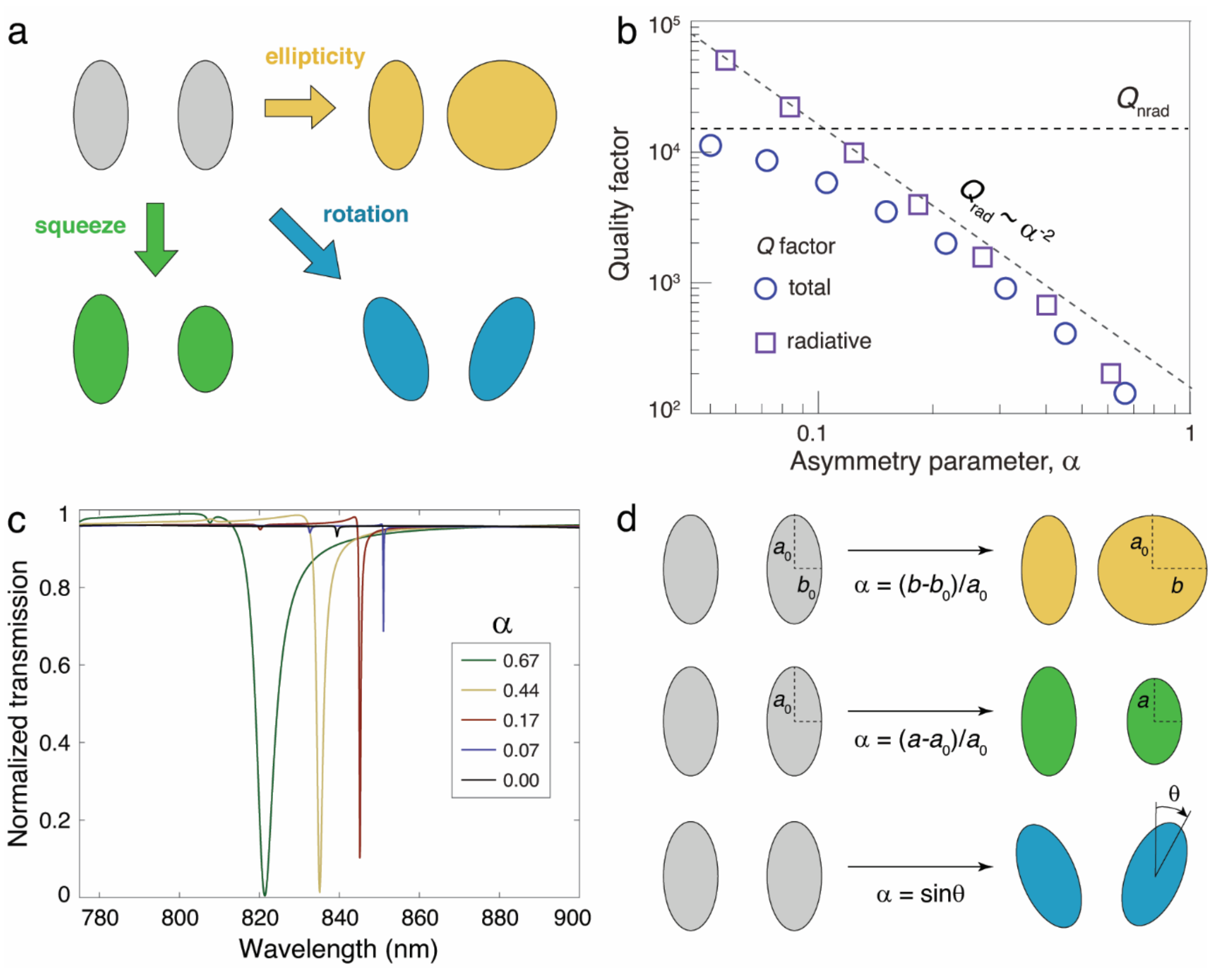

Figure 4-7 BICs in diatomic metasurfaces. (a) Different ways to introduce asymmetry for a diatomic metasurface: ellipticity, squeezing, rotation. (b) Dependence of the quasi-BIC quality factor (Q) on the asymmetry parameter of the meta-molecule. Purple squares and blue circles show the radiative and total Q, respectively. The black dashed lines show a fit to the inverse square law and the value of the non-radiative Q. (c) Characteristic evolution of the transmission spectra by changing the meta-molecule asymmetry. (d) Definition of the asymmetry parameter via ellipticity, squeezing, and rotation for the same diatomic metasurface.

Supplementary Note 3: Numerical calculations of electric field enhancement factors

Electric field enhancement distribution over 4 unit cells and along the y-axis of each meta-atom are shown in Figure 4-8.

Figure 4-8b shows that the local electric field enhancement factors can reach as high as almost 5000 in the close proximity to the elliptical resonators. Moreover, numerical calculations of the enhancement of the electric field averaged over a volume of a 5 nm thick layer in the nanoresonators' vicinity indicate an enhancement of 12.4 times for the averaged field. The significant augmentation of the fields greatly enhances the optical interactions with the analytes making this design compelling for sensing applications.

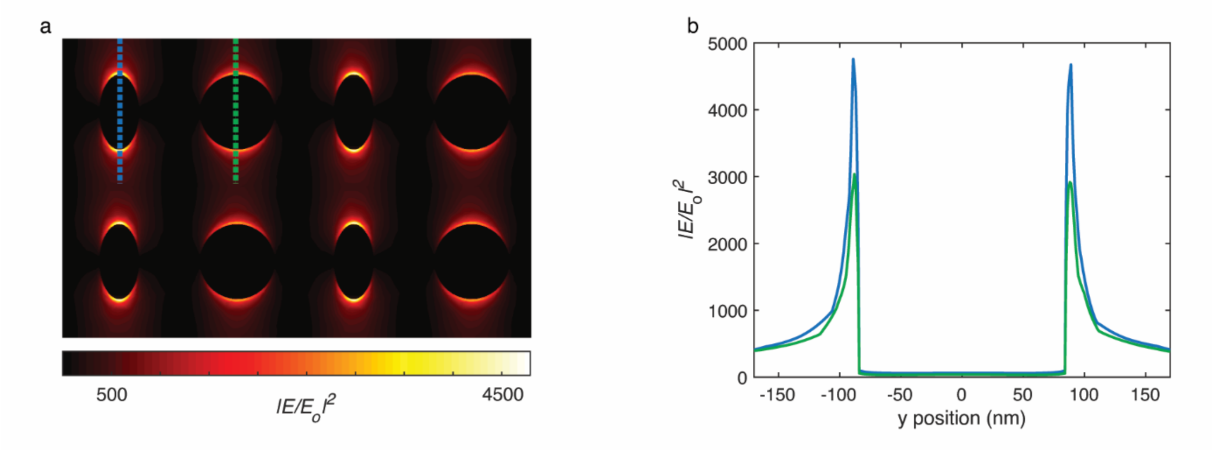

Figure 4-8 Electric field enhancement in the vicinity of the resonators (a) Electric field enhancement demonstrated for a cluster of four neighboring unit cells. (b) Electric field enhancement along the y-axis of the elliptical (blue) and circular (green) disks.

Supplementary Note 4: Characterization of the fabricated resonators over the sensor area

In order to characterize the homogeneity of the nanofabricated resonators over the sensor, we per-formed image processing on over 100 SEM images. The statistics on over 800 resonators revealed the average size of the disk diameter as 182.72 nm with a standard deviation of 1.38 nm (0.75%) and the average size and standard deviation of the long and short axes of the ellipse as 178.25 nm ±3.17 nm (1.78%) and 104.93 nm ±1.72 nm (1.64%), respectively. The probing locations were chosen randomly all around the sensor and on the very edges and corners. The deviation of less than 2% all around the sensor illustrates the high precision of our optimized nanofabrication procedure.

To spectrally characterize the uniformity of the structures, we used our hyperspectral imaging setup [12]. This setup enables the extraction of resonance maps, which gives the resonance wavelength over the entire sensor area at a single-pixel resolution. Supplementary Figures 4-9a and b show the spectral resonance map and the histogram of resonance wavelength distribution for our metasurface, respectively.

The extracted mean value indicates a negligible difference between the simulation (835 nm) and the experiment (829.05 nm). The measurements also reveal a standard deviation of 0.97 nm, highlighting the uniformity in the optical response over the sensor area and the correspondingly high quality of the optimized nanofabrication process.

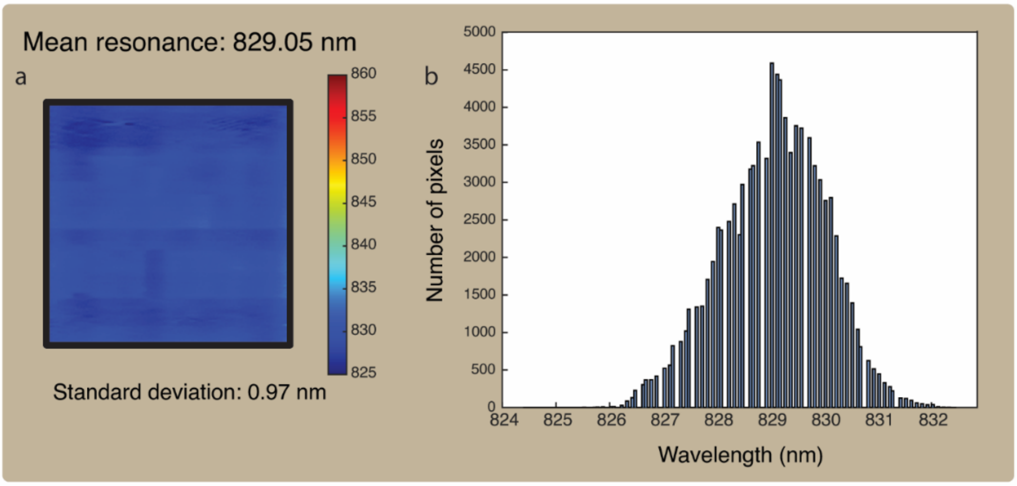

Figure 4-9 Spectral characterizations of the nanofabricated metasurfaces using hyperspectral imaging setup across the sensor surface. (a) The extracted resonance map and (b) The histogram of the resonance wavelength distribution of a fabricated sensor indicate that the mean resonance wavelength of the sensor is 829.05 nm with a standard deviation of 0.97 nm.

Supplementary Note 5: Biorecognition assay for nanoparticles

To demonstrate the biosensing capability of the platform, we performed real-time in-flow detection of nanoparticles to mimic the bioparticles (i.e., extracellular vesicles and viruses). To target the biotinylated silica nanoparticles, streptavidin was immobilized on the detection sensors while the control sensor was blocked with bovine serum albumin (Figure 4-10).

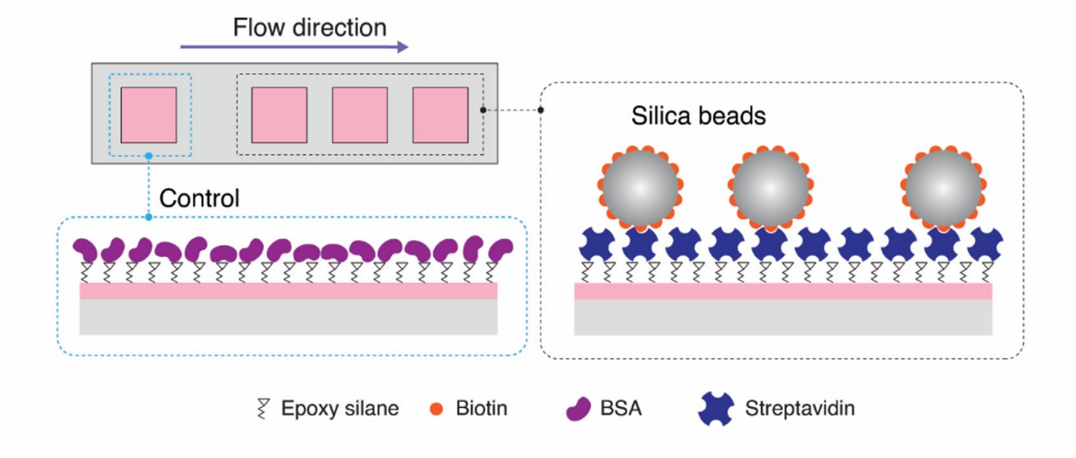
Flow direction
Silica beads
Control
Epoxy silane
Biotin
BSA
Streptavidin

Figure 4-10 Biorecognition assay to detect silica nanoparticles on the detection sensors and on the control sensor to account for non-specific binding. The control sensor is blocked with bovine serum albumin (BSA), while the detection sensors are functionalized with streptavidin.

Chapter 5 Investigating the resonance characteristics of symmetry-broken dielectric metasurface supporting quasi-BIC modes

Disclaimer: Some contents of this chapter are from reference [142], adapted with the author's permission.

- Reference [142]: Towards Ultrasensitive Handheld Imaging-based Optofluidic Biosensors Enabled by All-dielectric Metasurfaces. in Frontiers in Optics, Laser Science 2022 (FIO, LS) (2022),
  Authors: Yasaman Jahani, Hatice Altug.
  Jahani's Contribution:
  The numerical studies of dielectric metasurfaces' angular dispersion are reported in a conference paper.

Most biomolecules exhibit electronic and vibrational absorption in ultraviolet and mid-Infrared ranges, respectively [252], [253]. In the absence of such molecular fingerprints in the visible and near-infrared (VIS-NIR) range of the spectrum, refractometric biosensing becomes the most prominent sensing modal. While targeting molecular absorptions suffers from lower sensitivities, refractometric biosensing offers label-free and highly sensitive detection [44].

In this spectral range, noble metals like gold and silver supporting plasmonic resonances are lossy and subjected to joule heating. The imaginary part of their dielectric constant, which is a measure of dissipation, grows with the wavelengths in VIS-NIR, promoting the low-loss dielectric metasurfaces as an ideal substitute platform for sensing applications in this wavelength range [12], [254]. For example, silicon is characterized by one to two orders of magnitude lower loss in this range, asymptotically reaching zero in telecommunication bands [2], [8]. In addition to its alluring optical properties, silicon is a low-cost and highly abundant material. It is also the main substrate material for CMOS fabrication or, in other words, it is CMOS-compatible. Although the term CMOS-compatible is not strictly defined, it generally refers to the materials and fabrication processes that are not contaminating the CMOS foundries' production lines. The significant advantage of CMOS processes is low cost, high speed, and high volume fabrication. Therefore, the CMOS industry is a great promise for cheap and large-scale fabrication of dielectric metasurfaces in the near future [2].

Furthermore, operating in the VIS-NIR wavelength range below 850 nm offers several unique advantages, including the wide availability of high-performance, cost-effective silicon-based light sources and CMOS and CCD cameras for more efficient technology transfer of these sensors towards POC applications. Consequently, silicon-based metasurfaces, with their resonance in the range of 700 nm to 850 nm, are optimal in terms of lower loss and friendlier technology. Therefore, they hold great promise for lab-on-a-chip and futuristic miniaturized sensing devices.

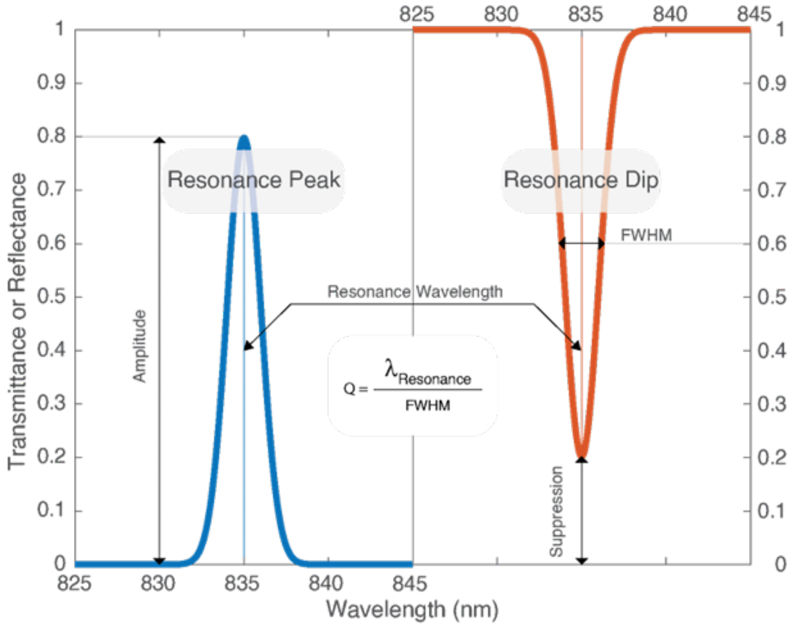

Figure 5-1 Characteristic features of a resonance. The figure demonstrates schematics of a transmission or a reflection spectrum. The blue curve is a resonance peak, and the red curve is a resonance deep in the VIS-NIR wavelength range below 850 nm. The Resonance wavelength, resonance amplitude for a peak, the resonance suppression for a deep, the full-width-at-half-maximum (FWHM) of resonance, and the quality factor (Q) are illustrated.

Figure 5-1 demonstrates the characteristic elements of resonance in a transmission or reflection spectrum. Specifically, in addition to the spectral location of resonance, the amplitude for peaks, or suppression, for deeps, as well as the width of the resonance, are important features. The former, the suppression of dips, can be defined in two ways. It can be considered equivalent to the amplitude of the resonance peaks or, instead, the lowest value a resonance dip reaches, in other words, the optical readout at the center of the resonance dip. In this text, the second definition is more relevant. For imaging-based biosensing, the lower suppression is preferential due to the respective wider dynamic range of an intensity-based reader. The latter, the resonance width, is an indication of the loss of the system affected by both radiative and non-radiative losses [255]. Therefore, it is influenced by the nanophotonic design, material losses, fabrication imperfections that cause scattering losses (and possibly absorption), and nonuniformity in optical responses over the sensor area. Moreover, the finite size of the metasurface contributes to the losses. More specifically, the metasurface resonances are manifested as collective responses of the resonators, and in numerical studies, the metasurfaces are considered infinite dimensions. In experiments, the sensors are fabricated with finite sizes. Therefore, it is of high importance to investigate the impact of the finite sensor size on the optical response.

A derivative parameter to determine the sharpness of resonance is the Q, which is defined as the resonance wavelength divided by the FWHM of the resonance (Equation 5-1).

$$Q = \frac{\lambda_{Resonance}}{FWHM}$$

Equation 5-1 Quality factor

Q is a performance metric of the duration for which the resonators confine light. Higher Q provides more significant light confinement and electromagnetic field enhancement, thus more efficient light-matter interaction [190]. That being said, a more comprehensive perspective is required for the development of biosensors. Even though Q plays a key role, it is not the only essential specification. The interplay of different parameters in optimizing a biosensor [8] is covered in previous chapters, and the influence of Q on the resonance metrics is discussed here.

The BIC is a concept giving rise to high Q resonances. It was first introduced in quantum mechanics but later described in nanophotonics through destructive interferences. Based on the Fridrich-Wintgen scenario, all radiating waves can be accidentally canceled out by finely tuning the resonators' attributes. If destructive interference arises from the system's symmetry, the BIC is symmetry protected. BIC is a mathematical object with infinite Q. Symmetry-protected BICs can be realized in the form of quasi-BICs by breaking the in-plane symmetry.[190] Quasi-BICs support finite but high Q values. In the absence of non-radiative losses, the Q is inversely proportional to the degree of asymmetry or, more precisely,

$$Q = Q_0 \, \alpha^{-2}$$

Equation 5-2 Dependence of quality factor on asymmetry parameter without non-radiative losses

where α is called the asymmetry parameter and Q_0 is a constant determined by the metasurface design [103].

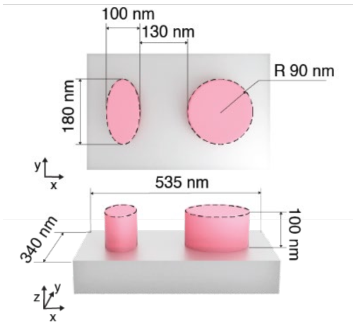

Figure 5-2 The metasurfaces design geometry and dimensions. The unit cell consists of a disk (with a radius of 90 nm) and an ellipse (with the short and long axis of 50 nm and 90nm, respectively). In this case, the asymmetry parameter is α=0.44. The nanoresonators are 100 nm in height and are made from amorphous silicon placed on a fused silica substrate. Reproduced from the open-access article in reference [8].

The content of this chapter is based on the design shown in Figure 5-2. The unit cell of this design, which supports quasi-BIC modes, is made of two meta-atoms, a disk, and an ellipse. The resonators are made of amorphous silicon, and the substrate is fused silica.[8] In addition to the geometry of the resonators, the positioning of the incident beam also alters the resonance features. The effect of the illumination angle is discussed in this chapter in the following sections.

For the experimental data presented in this chapter in sections 5.1 and 5.2, a hyperspectral imaging platform is used to record optical images of the metasurface in normal-incidence configuration while sweeping the illumination wavelength. The optical configuration of the platform is described in 3.3. The optical configuration is slightly modified for the measurements done in the reflection described in section 5.3. The hyperspectral data cube is processed to provide transmission or reflection spectra from the entire field of view with pixel resolution.

5.1 Numerical and experimental analysis of the asymmetry parameter effect

In the absence of non-radiative losses, the Q of a quasi-BIC mode, originated from a symmetry-protected BIC, is only controlled by the asymmetry parameter (α), a geometrical factor introducing radiative losses [103]. For the design shown in Figure 5-2, α is controlled by the ellipticity of the disk resonator. Figure 5-3 gives a better understanding of this variable. The asymmetry parameter (α) controls one resonator's ellipticity by changing its short axis length (b), while all the other dimensions are fixed. If both resonators have the same length of the horizontal axis, thus α=0, the design is symmetric and supports a BIC mode. With a non-zero α, breaking the inversion symmetry creates a quasi-BIC mode manifesting as a high-Q resonance dip in the transmission spectrum.

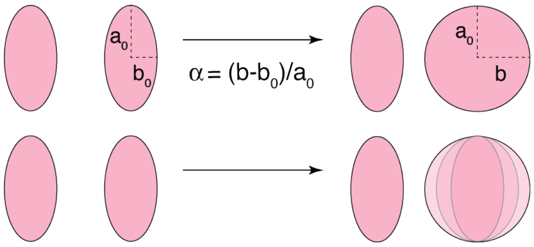

Figure 5-3 The metasurface unit cell and the definition of the asymmetry parameter for this metasurface design

In practice, the Q is not only governed by radiative losses (Q_{rad}), but material losses, fabrication imperfections, finite metasurface size, measurement noise, and tools limitations also affect the quality factor (Q_{nrad}) with the known relation Equation 5-3,

$$Q^{-1} = {Q_{rad}}^{-1} + {Q_{nrad}}^{-1}$$

Equation 5-3 Total quality factor

To maximize the total Q, this relation promptly suggests, $Q_{rad} = Q_{nrad}$ which is called the critical coupling condition [256]–[258]. A higher Q resonance is a sharper resonance; thus, in refractometric sensing, it provides better detection resolution when probing the resonance shift. In intensity interrogation systems, for a given change in the refractive index, higher Q resonance means higher intensity change, thus a higher signal strength. Higher quality factor accounts for stronger confinement of the electromagnetic fields, i.e., more profound hotspots, in turn, higher sensitivity. While high-Q resonances are generally appreciated for biosensing applications, too high Q values limit the dynamic range of a sensor or even result in a step-like resonance spectrum, hindering the efficient performance of intensity-based platforms. Assuming that non-radiative losses are not affected by asymmetry for a quasi-BIC resonance, we can substitute Equation 5-2 in Equation 5-3:

$$Q = \frac{Q_{nrad}}{1 + \alpha^2 \ Qnrad/Q_0}$$

Equation 5-4 Dependence of quality factor on asymmetry parameter and non-radiative losses

The above equation nicely represents the bold effect of asymmetry, and non-radiative losses on total Q [8], [190], [255]. The non-radiative losses influence the resonance amplitude or suppression too. For a Lorentzian resonance, the amplitude $A(\lambda_{res})$ or suppression $Sup(\lambda_{res})$ can be approximated as [259] :

$$A(\lambda_{res}) = 1 - Sup(\lambda_{res}) \approx \left(\frac{{Q_{rad}}^{-1}}{{Q_{rad}}^{-1} + {Q_{nrad}}^{-1}}\right)^2$$

Equation 5-5 Dependence of the suppression and amplitude of resonance on the quality factor

Comparing Equation 5-3 and Equation 5-5, it is clear that the amplitude is more strongly affected by the non-radiative losses than the total Q. Quasi-BIC modes follow a Fano line-shape in their transmission spectra rather than Lorentzian. Therefore, using Equation 5-5 with Equation 5-2 (to reach Equation 5-6) only gives a qualitative understanding of the trend of suppression and not a quantitative analytical model.

$$A(\lambda_{res}) = 1 - Sup(\lambda_{res}) \approx \left(\frac{\alpha^2}{\alpha^2 + Q_0 {Q_{nrad}}^{-1}}\right)^2$$

Equation 5-6 Approximation of dependence of the suppression and amplitude of a quasi-BIC resonance on asymmetry parameter and non-radiative losses

Equation 5-6 suggests that in the absence of non-radiative losses ($Q_{nrad} = \infty$), the suppression is not dependent on the asymmetry and equals zero ($A(\lambda_{res}) = 1$). In practice, the non-radiative losses are always present, and suppression is highly dependent on α. The trend also illustrates that the suppression is maximum, i.e., equal to one, when there is no asymmetry introduced to the system, which is the case of BIC; hence no resonance appears in the spectrum. As the asymmetry parameter increases, this value asymptotically approaches zero. Lower suppression means a deeper resonance, thus, a higher dynamic range for intensity-interrogation systems. Suppression also plays a big role in the LOD [259]. Therefore, it is essential to wisely choose the asymmetry parameter that is most appropriate for a given system according to the available materials, fabrication techniques, and detection methods, to accommodate both high-Q and low-suppression criteria.

The numerical studies shown in Figure 5-4a acknowledge that the resonance becomes broader and lower in suppression as the asymmetry increases. In these simulation studies, the primary source of the non-radiative losses is the material loss implemented using experimentally recorded refractive index dispersion for amorphous silicon. Furthermore, the resonators' sharp corners were blended to achieve more realistic results. The quality factors of the transmission spectra are plotted against the asymmetry parameter in Figure 5-4b showing a nice agreement with the analytical model in Equation 5-4. Importing the Q_0 and Q_{nrad} ,113.7 and 1960 respectively, extracted from the fitting of the quality factor curve into the suppression approximation for the Lorentzian model, leads to the red dashed curve in Figure 5-4c. Even though the model does not pass over the simulation data points, it can still qualitatively describe the general behavior of the graph, starting from one and asymptotically reaching zero as the asymmetry parameter grows. The higher decrease rate of the fitted curve, shown as the solid green line, lies within the fact that quasi-BIC resonances follow a Fano line-shape and not Lorentzian.

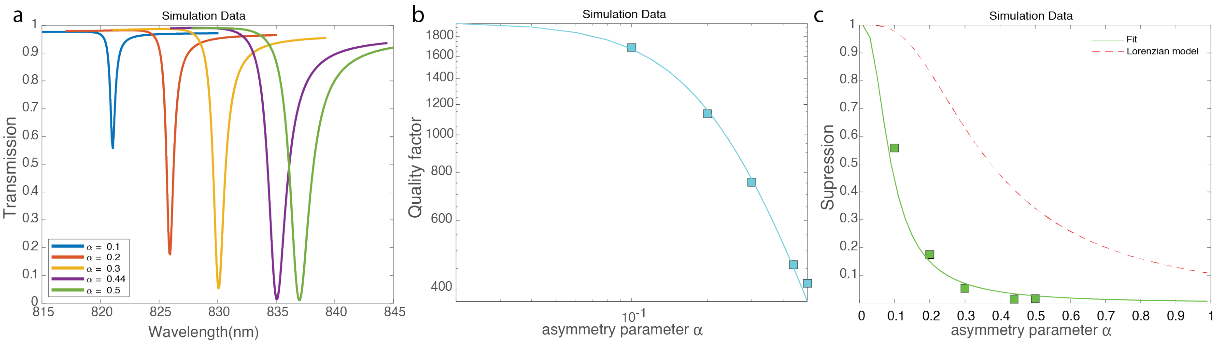

Figure 5-4 Visualization of the effect of asymmetry parameter on the resonance features in simulation. (a) Shows the transmission spectrum of the diatomic design while the asymmetry parameter changes. The purple curve with $\alpha = 0.44$ is the transmission spectrum for the design when the changing resonator becomes a disk. (b) Shows the decrease of the quality factor when the asymmetry parameter increases. The fitted curve, illustrated in blue, neatly follows Equation 5-4. (c) Shows the dependence of the suppression on the asymmetry parameter. The green line is a fitted curve, and the Lorentzian approximation is plotted as a dashed red line.

The experimental results from fabricated dielectric metasurfaces with varying asymmetry parameters are shown in Figure 5-5. Figure 5-5a shows the resonance broadening and suppression decrease as expected from simulation and the analytical models. The quality factors of the transmission spectra are plotted against the asymmetry parameter in Figure 5-5b, showing a nice agreement with the analytical model in Equation 5-4. The extracted $Q_0$and Q_{nrad} from fitting the Equation 5-4 to the experimentally recorded Q, are 112.3 and 203.3, respectively. The experimentally recorded Q_0 decently complies with the one from the simulations, as this parameter only depends on the metasurface design. The decreased Q_{nrad} stands for the higher non-radiative losses in the experiment accounting for measurement noise, tools limitations, finite metasurface size, and fabrication imperfections which cause scattering losses and nonuniformity in optical responses over the sensor area, in addition to the material losses. Moreover, the optical readout non-uniformities, for example, from the geometrical size variation of the resonators, even for low standard deviations as low as 2 nm, strongly affect the resonance amplitude to be reduced in half or even lower; it also widens the FWHM [260]. Therefore, the experimentally recorded suppression is not expected to follow the idealistic case of the simulations. Figure 5-5c shows the experimental suppression against the asymmetry parameter. The fitted curve starts from one and asymptotically reaches 0.5, as expected for the experimentally recorded data.

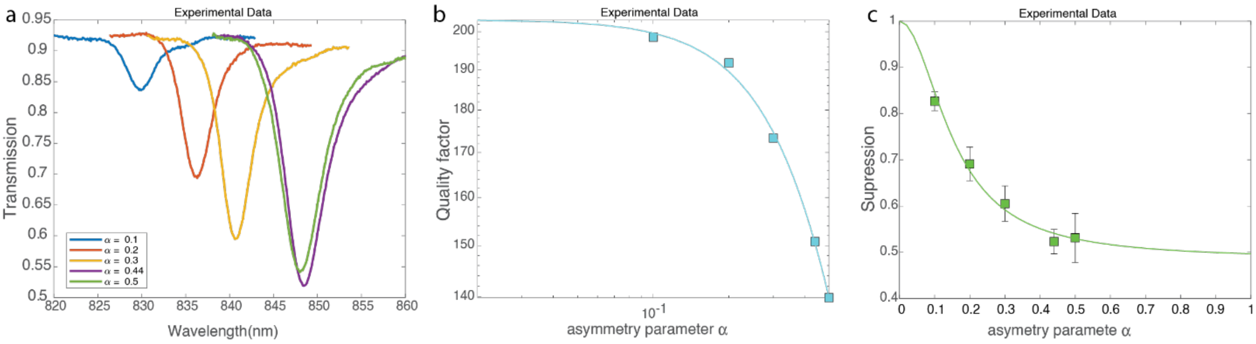

Figure 5-5 Visualization of the effect of asymmetry parameter on the resonance features in experiment. (a) Shows the transmission spectrum of the diatomic design while the asymmetry parameter changes. The purple curve with $\alpha = 0.44$ is the transmission spectrum for the design when the changing resonator becomes a disk. (b) Shows the decrease of the quality factor when the asymmetry parameter increases. The fitted curve, illustrated in blue, neatly follows Equation 5-4. (c) Shows the dependence of the suppression on the asymmetry parameter. The inherent nonuniformities strongly affect the suppression.

Following the analytical, numerical, and experimental investigations, the asymmetry parameter greatly influences the resonance features; thus, it can be considered an important design parameter. A lower asymmetry parameter gives rise to a sharper resonance at the expense of higher suppression. However, experimental investigations show that as the asymmetry parameter increases, the suppression values asymptotically decrease to reach a non-zero value. Consequently, for a quasi-BIC mode, experimental analysis is favored in probing the most appropriate asymmetry parameter for a given system.

5.2 Experimental analysis of the effects of finite sensor dimension

Dielectric metasurfaces can exhibit interesting optical properties such as perfect absorption, cloaking, and effective refractive index [87], [261]–[263]. Notably, the observed modes and resonances result from the metasurfaces' collective response [264]. In numerical studies, such platforms are modeled as a unit cell infinitely repeating in two dimensions. In practice, metasurfaces cannot be infinite. Therefore, it is essential to develop an understanding of the effect of the metasurface finite size on the resonance features experimentally. The motivation behind investigating the smallest operational metasurface size for biosensing stems from the potential cost-effectiveness of fabricating smaller sensors. Furthermore, smaller sensing area is also an interest for micro-array biosensors.

To investigate the effect of sensor size, dielectric metasurfaces were fabricated in various sizes ranging from 5 µm (by 5 µm) to 250 µm (by 250 µm). The square-shaped sensors are made from periodically repeating structures shown in Figure 5-2. The number of unit cell repetition in each direction were calculated by dividing the total targeted sensor size by the unit cell periodicity in that direction. In order to allow a fair comparison and take out the effect of sensor size on the fabrication process, a buffer zone is applied around each sensor. The buffer zone is made from disk resonators with the same area coverage per unit cell as the main design but no resonance at our target range to prevent any interference on the optical readout. The total size of the main sensors and their buffer zone is 250 µm. Figure 5-6 shows optical images of the sensors surrounded by their buffer zones. The resonance wavelength is highly robust to the changes in the sensor size, specifically above 10 µm, as shown in Figure 5-6b. However, as can be seen in Figure 5-6c and Figure 5-6d, FWHM and Suppression require at least the sensor size of 50 µm for stabilization. In addition to this, Figure 5-6c and Figure 5-6d display a descending trend in standard deviation stabilizing from 100 µm for FWHM and suppression. Due to the very different impact of sensor size on the resonance wavelength and the bandwidth and the high standard deviation for smaller sizes, their separate illustration is more meaningful than their derivative metric, the quality factor.

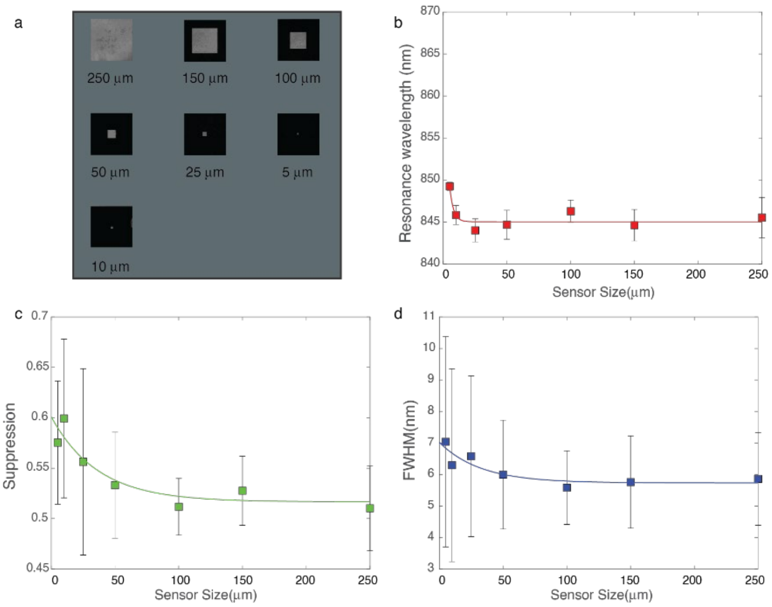

Figure 5-6 The size-dependent response of the metasurfaces. (a) Optical images of the sensors of various sizes surrounded with buffer zones for a fair comparison, mainly to eliminate the fabrication-induced alterations due to the change in the size. (b) The resonance wavelength versus the sensor size shows good stability and homogeneity for 10 µm and bigger sensor sizes. (c) The suppression versus the sensor size shows a decreasing trend in suppression and its homogeneity over the sensor area. (d) The full-width-at-half-maximum (FWHM) versus the sensor size shows a decreasing trend in suppression and its homogeneity over the sensor area. The red, green, and blue lines in a, b, and c, respectively, are the eye guides.

These results suggest different dependence on the sensor size for different applications. Sensor sizes as small as 10 µm could be sufficient to target a specific resonance wavelength homogeneously. However, if the resonance amplitude and sharpness and their homogeneity over the sensor area are playing factors, as per the biosensors, one order of magnitude bigger sensors are required. These values are design- and fabrication-dependent; therefore, experimental analysis is recommended in probing the smallest size for a high-performance dielectric metasurface for a given system.

5.3 Analysis of the effects of illumination angle

The asymmetry parameter and finite sensor size effects are investigated under normal-incidence excitation and in transmission mode. Even though in some cases, the angular dispersion of dielectric metasurfaces is probed for wave-front control applications [265], metasurface-based biosensors were mostly described under normal-incidence illumination, and their angular dispersion is unexplored. Angular dispersion is another degree of freedom when designing dielectric metasurfaces, and the illumination angle affects the resonance characteristics features. The influence of the illumination angle on the dielectric metasurface described in Figure 5-2 is investigated in section 5.3.1, while the potential application of the angular dispersion for a hand-held point-of-care device is probed in section 5.3.2. The hyperspectral platform described in 3.3 is modified to work in reflection. The collimated linearly polarized laser line (1.75 nm bandwidth at 700 nm) light illuminates the metasurface after passing through a low numerical aperture (NA) 4X objective (Nikon Plan Fluor with 0.13 NA). The reflected light is collected with the same objective, conveyed through a cross-polarized analyzer, and imaged with a CMOS camera (DS Qi 2, Nikon). The cross-polarization scheme removes the background signal, thus improving the signal-to-noise ratio of the readout. Moreover, this polarization arrangement leads to a more Lorentzian shape resonance [266]–[268].

5.3.1 Hyperspectral analysis of illumination angle effect for end-point measurements

To experimentally investigate the dielectric metasurface under tilted illumination, a tilting stage is integrated with the microscope to tilt the nanophotonics chip and record the hyperspectral data cube in cross-polarized reflection mode. The cube can be processed to provide reflection spectra from the entire field of view. The recorded data were corrected to remove the background noise and normalized to the source. The numerical simulations using commercially available CST Microwave Studio suggest a resonance red-shift as the tilting happens, as shown in Figure 5-7a. The experimental data confirm the calculated trend, as shown in Figure 5-7b. The smaller slope of the resonance shift is due to the presence of losses and noises in the experiment, while simulation only considers the material loss of the silicon.

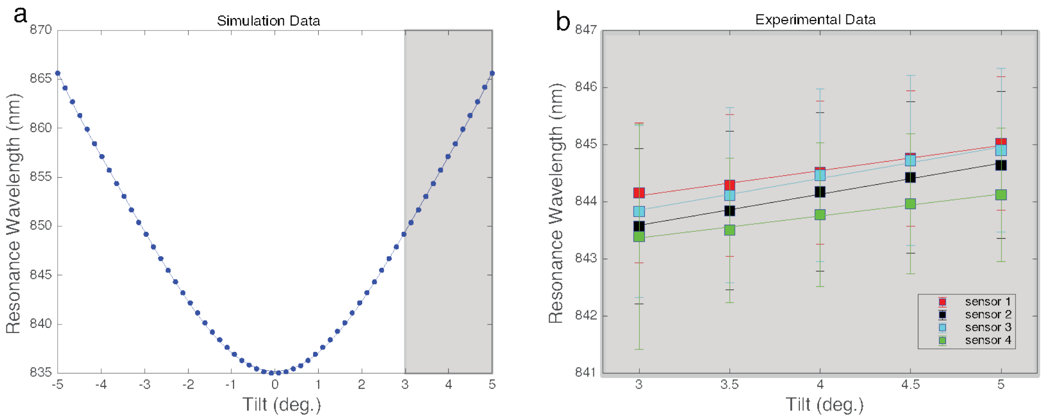

Figure 5-7 The effect of illumination angle on the resonance wavelength. (a) Shows the simulation data for the resonance wavelength shift when the illumination is tilted from zero to ±5 degrees. (b) Shows the experimental data for the resonance wavelength shift of 4 independent sensors when the chip is tilted from 3 to 5 degrees. The red, black, blue, and green lines are eye guides to illustrate the resonance shift better.

The reflection spectrum, a resonance peak, is shown in Figure 5-8a. s 5-8b and c show the resonance FWHM and amplitude, which are almost unaffected by the tilt.

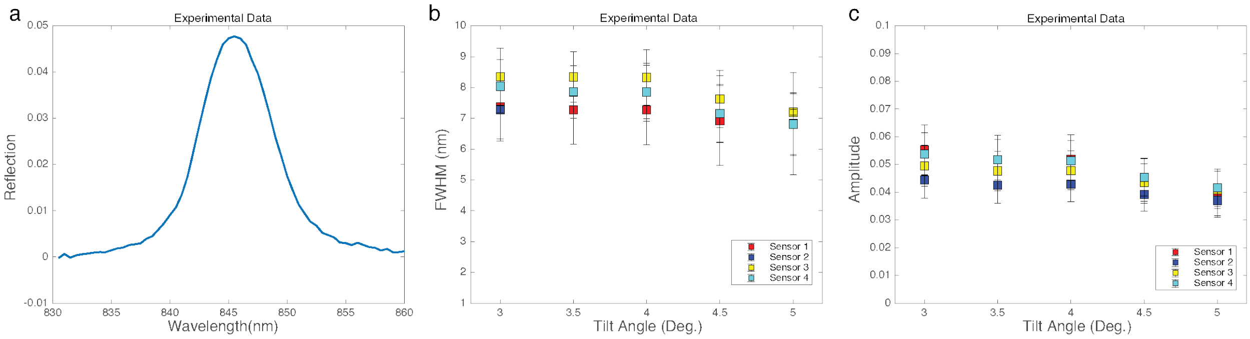

Figure 5-8 The effect of the illumination angle on the resonance features. (a) Shows the experimentally recorded reflection spectrum when the stage is tilted at 4.5 degrees. (b) Illustrates the Full-Width-at-Half-Maximum (FWHM) of the resonance peak against the illumination angle, and it stays almost constant and independent of the tilt. (c) Illustrates the Amplitude of the resonance peak against the illumination angle, and it stays almost constant and independent of the tilt.

The illumination angle plays a significant role in defining the resonance wavelength while minimally affecting the other features of a resonance peak. This peculiar feature of the studied metasurface design can be leveraged for in-situ biosensor characterization, potentially implemented as a point-of-care device, as proposed in the following section.

5.3.2 Utilizing the tilt angle towards ultrasensitive handheld imaging-based fluidic biosensors

Here we introduce a new approach to building a single-wavelength imaging-based platform capable of in-situ characterization of metasurfaces. This approach allows the spectral shift reconstruction algorithm introduced in Chapter 4 to incorporate the on-site recorded spectral decoder instead of the pre-recorded decoder. This is done by adding a tilting stage as an extra degree of freedom to the algorithm-aided imaging optofluidic biosensors.

When the metasurfaces are tilted, the transmission resonance spectra redshift, which induces intensity changes in the optical readouts. The simulation data in Figure 5-9 illustrates the behavior of resonance shift for each pixel as a function of the tilt angle (θ) (Figure 5-9). In practice, due to the inherent fabrication imperfections, the neighboring pixels might have slightly different resonance wavelengths, while the resonance shift is expected to be the same for all pixels. To remove the dependence of the optical readout on the spectral inhomogeneity over the sensor area, the shift function for each pixel is defined as:

$$\Delta\lambda(\theta) = \lambda(\theta) - \lambda(0)$$

Equation 5-7 Resonance shift

Various functions can be fitted to the resonance shift function. For simplicity, we define the shift function as an even polynomial of the degree of six:

$$\Delta\lambda(\theta) = a.\theta^6 + b.\theta^4 + c.\theta^2$$

Equation 5-8 Resonance shift function

Figure 5-9 confirms the adequacy of the fitted polynomial by plotting it over on the simulation data. From $\Delta\lambda = \frac{d\lambda}{dI}.\Delta\mathrm{I}$ and Equation 5-8, we have:

$$a.\theta_n{}^6 + b.\theta_n{}^4 + c.\theta_n{}^2 - \frac{d\lambda}{dI}.\Delta I = 0 \qquad \mathrm{n} = 1,2,3,\ldots \mathrm{N} \geq 4$$

Equation 5-9 Constitutive equation set of the hyper-angular spectral decoder elements

Equation 5-9 can be experimentally set up by acquiring a hyper-angular imaging (HAI) cube from the metasurfaces; thus, intensity shift readouts with pixel resolution from the sensor chip over N different tilt angles. The equation set describes a homogeneous system from which we are able to extract the ratio of the unknowns, including the new spectral decoder components, i.e., $\frac{d\lambda}{dI}$. This solution provides the info regarding the relative performance of the pixels enough for the characterization of the biosensors. Nevertheless, it is possible to introduce a calibration parameter extracted experimentally or through more advanced machine-learning approaches to extract the absolute derivatives. Our technique combines the simplicity of the intensity-interrogation methods and the robustness of spectroscopy while removing the need for sophisticated instrumentation and pre-recorded data towards a reliable handheld point-of-care device [142].

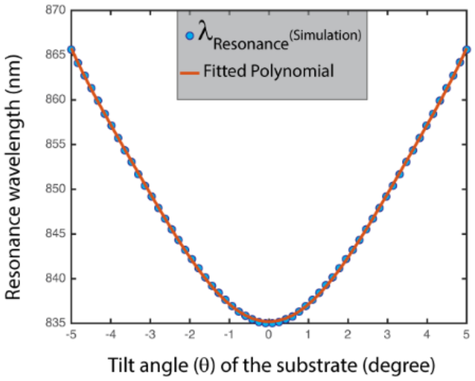

Figure 5-9 The simulated resonance wavelengths of the dielectric metasurfaces as the function of the tilt angle of the stage.

Chapter 6 Conclusion

Disclaimer: Some contents of this chapter are from reference [2], adapted with permission. Copyright {2021} American Chemical Society.

- Reference [2]: Dielectric Metasurfaces Enabling Advanced Optical Biosensors. ACS Photonics 8, 47-60 (2021).
  Authors: Ming-Lun Tseng*., **Yasaman Jahani***, Aleksandrs Leitis*, Hatice Altug.
  Jahani 's Contribution:
  *These authors contributed equally to writing this perspective review

6.1 The achieved results summary

Dielectric metasurfaces have emerged as a powerful platform for biosensing applications, overcoming limitations such as metallic losses and joule heating present in their plasmonic counterparts. These metasurfaces are particularly attractive for enhancing light-matter interactions by amplifying both electric and magnetic fields. To optimize the performance of a refractometric biosensor using dielectric metasurfaces, several factors must be taken into account. The material and design of the unit cell are particularly critical in determining the metasurface's characteristics. The quality factor plays a key role in the performance of the biosensors, influencing the confinement of electromagnetic fields and the limit of detection. The physics of bound-states-in-the-continuum support infinitely high-Q resonances, which can be realized in the form of quasi-BIC by breaking the in-plane symmetry of the unit cell resonators. The degree of symmetry breaking, known as the asymmetry parameter, controls the quality factor. While higher quality factors are achieved when the mode is tightly confined in a high-index resonator, for sensing applications, it is essential to maintain enhanced near-fields extended out of the resonator and spatially overlapped with the samples on the sensor surface. Therefore, while controlling asymmetry parameters helps balance the quality factor, multi-resonator unit cells facilitate extended near-fields, boosting the biosensor performance.

In this thesis, high-Q dielectric metasurfaces with a unit cell made of zigzag nanobars were designed. Quasi-BIC resonances were realized by breaking the in-plane symmetry of the unit cell resonators, i.e., tilting the nanobars. The proposed design was tailored based on numerical studies while considering the fabrication constraints and extended near-fields required for sensing. An optimized nanofabrication process-flow with CMOS-compatible techniques was established to fabricate the fine-tuned dielectric metasurface in a clean-room environment. An imaging-based hyperspectral optical setup was built using a supercontinuum laser source and a tunable filter coupled to an inverted microscope. A MATLAB-based graphical interface was created to control the tunable filter to sweep the illumination wavelength while a scientific CMOS camera imaged the high-Q dielectric metasurfaces. Surface preparation and bio-functionalization protocols using epoxy-silane-based covalent chemistry were developed for silicon nanoresonators to complete all the required components for a biosensor: a biorecognition assay, a transducer, and a recorder.

Incorporating dielectric metasurfaces made from tilted silicon nanobars and a hyperspectral imaging platform, hyperspectral data cubes were constructed. The data cubes were recorded by acquiring 2D images of the metasurfaces while sweeping the illumination wavelength. A hyperspectral data cube contains intensity information of metasurfaces over a large field-of-view with pixel resolution, i.e., millions of transmission spectra that can be processed to generate a resonance map. Each element on a resonance map corresponds to a region on the metasurface, and its value is the resonance wavelength for that region. The metasurfaces were pre-functionalized with mouse IgG to specifically target rabbit anti-mouse IgG molecules. Hyperspectral data cubes were recorded before and after introducing the analyte on the pre-functionalized metasurfaces. The corresponding resonance maps were subtracted to yield a resonance shift map. For higher concentrations of the analyte, a conventional calibration curve was made by plotting the resonance shift against the concentration. Novel data processing methods for classifying the experimental data were exploited to enable the detection of low molecular counts. We plotted the area under the receiver operating curve (ROC) against the concentration to extract a trend from the resonance shift maps in order to detect a very low molecular count, approximately three molecules per μm^2. Furthermore, introducing multi-resonant sensors and hyperspectral barcodes, the metasurfaces were applied to differentiate bulk solutions with different refractive indexes using a single wavelength measurement.

Moreover, using numerical tools, we designed a new diatomic dielectric metasurface based on disks and ellipses supporting high-Q resonances. Compared to the tiled nanobars, this new design supported sharper resonances, was more sensitive to the refractive index change, and easier to fabricate as it did not use tilting to break the in-plane symmetry. Microfluidic PDMS cells were designed, fabricated, and integrated with the dielectric sensors to build an optofluidic chip. We combined a microfluidic system with an imaging platform and the new dielectric metasurfaces to build an imaging-based spectrometer-less optofluidic biosensor. The optofluidic chip was illuminated with a single wavelength light beam that excites the resonators, while a CMOS camera acquired 2D images at fixed intervals in order to provide time-resolved intensity information. The microfluidic system delivered the PBS buffer and the analytes to the pre-functionalized sensors, and the intensity changes due to the analyte bindings were recorded. The intensity changes and a pre-recorded spectral decoder were fed to an optimal linear estimation algorithm to provide an estimated spectral shift. This technique is highly robust compared to simple intensity readout devices, fusing the simplicity of intensity-based biosensors with the reliability of spectroscopy. To demonstrate the functionality of the proposed method with a biorecognition assay, we performed real-time inflow experiments to detect EVs from the mouse breast cancer cells. The lowest detected quantity of 1.23×10^8 EV/mL, the limit of detection of 8×10^7 EV/mL, and almost five orders of magnitude of the dynamic range were reported from the experiments, which are clinically relevant for the detection of cancer-related EVs. It is worth mentioning that the imaging nature of the platform allows for simultaneous control measurement to account for the non-specific bindings. This important feature of the platform facilitates handling samples with potentially complex biological matrices.

In the final chapter, we studied three design parameters that affect the resonance features of dielectric metasurfaces. Specifically, we instantiated our bar and disk design to numerically and experimentally investigate the effects of asymmetry parameters on the quality factor and suppression of the resonance. Moreover, we experimentally demonstrated the minimum required sensor size to achieve an optimal homogeneity for Q and suppression. In addition, we addressed the effect of illumination angle on the resonance features of the bar and disk design. Consequently, we proposed an alternative approach for the in-situ characterization of biosensors that utilizes the angular dispersion of the metasurfaces. The suggested platform can be as simple and compact as a narrow-band light source, a tilt stage, and a CMOS imager. Dielectric metasurfaces present an excellent opportunity for futuristic sensing platforms. Their prospective developments and outlook are discussed in the following section.

6.2 Future development of dielectric metasurfaces for biosensing applications

We anticipate that dielectric metasurfaces will substantially impact designing on-demand functionalities due to the additional degrees of freedom in their optical responses and their unique capabilities to boost light-matter interactions. Although they have shown great promises, several open challenges need to be addressed. One of them is to develop a universal method for the large-scale fabrication of different types of dielectric metasurface sensors. Although some recent works for efficient production of metasurfaces have been reported, including nanoimprinting, [269], [270] laser direct write, [271], [272] and hole-mask lithography [273]–[275] methods that are compatible with standard semiconductor processes are yet to be developed. Another direction for future studies is to improve the sensitives of dielectric metasurfaces. Even though the current studies show that dielectric metasurfaces can provide sufficient sensitives, their overall performance has not reached the levels of their state-of-art plasmonic counterparts. Especially for SERS, there is room to further boost the device's sensitivity.

Furthermore, progress in material science is beneficial for the advancement of dielectric metasurfaces and their device implementation. In Figure 6-1, we provide an overview of low-loss dielectric materials ($k < 0.001$), which are suitable candidates for metasurface sensors in the UV-visible and IR regimes. Some of the suggested materials have already been implemented, such as TiO_2 in the visible regime and Si in the IR regime. On the other hand, the utilization of many others for metasurfaces is yet to be explored, and they can be investigated to open up new territories in dielectric metasurfaces. For example, as shown in Figure 6-1a, by using high bandgap materials, such as diamond, AlN, and HfO_2, the working wavelength of dielectric metasurface sensors can be extended into the UV regime. It will be useful for sensing technologies such as resonance Raman spectroscopy [276] and UV circular dichroism spectroscopy [277]. By using active materials, such as GaAs and GaN, multifunctional metasurfaces capable of not only generating near-field enhancements but also working as on-chip light sources can be realized for ultra-compact sensor integration. In addition, some unconventional materials, including high-index chalcogenides, [278], [279] multiple quantum wells, [280], [281] phase-change media, [282], [283] and perovskites [284], [285] have been recently used for metasurfaces to realize new optical properties. Further investigation of unconventional materials for metasurfaces could lead to high-performance optical biosensors.

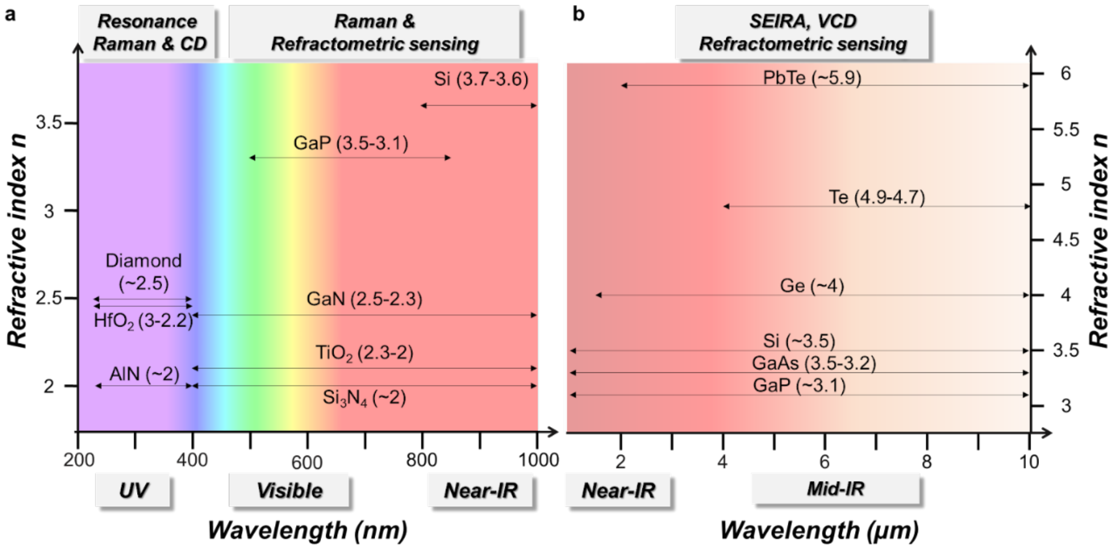

Figure 6-1 Refractive index (n) of low-loss dielectric materials for metasurfaces at (a) the UV–visible regime and (b) the IR regime. The double-headed arrows indicate the wavelength range where the related materials have a near-zero extinction coefficient. The height of the double-headed arrows corresponds to the average value of the refractive index in the wavelength range. Possible sensing techniques of dielectric metasurfaces at different regimes are labeled on the top of the figures. This figure is adapted with permission from reference [2] Copyright 2021 American Chemical Society.

Concurrently, metasurface-based sensing technologies can address the miniaturization of the current bioanalytical and clinical devices. Performing rapid, efficient, and accurate diagnosis is of great importance for the timely treatment of life-threatening diseases. As we have witnessed during the COVID-19 pandemic, devices enabling point-of-care testing and continuous health monitoring are becoming critical for saving lives and improving life quality [286], [287]. While the integration of plasmonic metasurfaces into systems such as CMOS-based chips,[70], [287], [288] microfluidic devices, [68], [69], [289] and lab-on-a-chip systems [215] has been more established, the integration of dielectric metasurfaces is in its infancy and expected to leverage accumulated knowledge for achieving new functionalities. For instance, light-emitting metasurfaces, [54] reconfigurable metasurfaces, [57], [282], [290], [291] and pixelated metasurfaces [169] can enable compact sensors by incorporating on-chip light generation, signal processing, and surface enhancement.

Finally, artificial intelligence can be considered another competent tool to extend the capacity of metasurface sensors. Novel approaches for designing metasurfaces and advanced data processing are the new directions to investigate. Several works have shown the unprecedented capability of machine learning for inverse designs of metasurfaces with the assigned optical properties [292], [293]. Artificial intelligence can provide a novel route toward the development of metasurface sensors with properties that require strict criteria, such as superchiral field generation or spectrally clean sharp resonances. By combining machine learning and novel dielectric metasurfaces, optical sensors capable of performing molecular pattern recognition, distinguishing molecules in complex environments, and the observation of dynamic molecular interactions can be achieved [2].

References

[1] F. Yesilkoy *et al.*, “Phase-sensitive plasmonic biosensor using a portable and large field-of-view interferometric microarray imager,” *Light Sci. Appl.*, vol. 7, no. 2, pp. 17152–17152, Feb. 2018, doi: 10.1038/lsa.2017.152.

[2] M. L. Tseng, Y. Jahani, A. Leitis, and H. Altug, “Dielectric Metasurfaces Enabling Advanced Optical Biosensors,” *ACS Photonics*, vol. 8, no. 1, pp. 47–60, Jan. 2021, doi: 10.1021/acsphotonics.0c01030.

[3] H. Karimi-Maleh *et al.*, “Cyanazine herbicide monitoring as a hazardous substance by a DNA nanostructure biosensor,” *J. Hazard. Mater.*, vol. 423, p. 127058, Feb. 2022, doi: 10.1016/j.jhazmat.2021.127058.

[4] P. Miao, Y. Tang, and L. Wang, “DNA modified Fe3O4@Au magnetic nanoparticles as selective probes for Simultaneous detection of heavy metal ions,” *ACS Appl. Mater. Interfaces*, vol. 9, no. 4, pp. 3940–3947, 2017, doi: 10.1021/acsami.6b14247.

[5] A. Modi, N. Koratkar, E. Lass, B. Wei, and P. M. Ajayan, “Miniaturized gas ionization sensors using carbon nanotubes,” *Nature*, vol. 424, no. 6945, pp. 171–174, 2003, doi: 10.1038/nature01777.

[6] L.-H. Pan, S.-H. Kuo, T.-Y. Lin, C.-W. Lin, P.-Y. Fang, and H.-W. Yang, “An electrochemical biosensor to simultaneously detect VEGF and PSA for early prostate cancer diagnosis based on graphene oxide/ssDNA/PLLA nanoparticles,” *Biosens. Bioelectron.*, vol. 89, pp. 598–605, Mar. 2017, doi: 10.1016/j.bios.2016.01.077.

[7] M. Alafeef, K. Dighe, P. Moitra, and D. Pan, “Rapid, Ultrasensitive, and Quantitative Detection of SARS-CoV-2 Using Antisense Oligonucleotides Directed Electrochemical Biosensor Chip,” *ACS Nano*, vol. 14, no. 12, pp. 17028–17045, 2020, doi: 10.1021/acsnano.0c06392.

[8] Y. Jahani *et al.*, “Imaging-based spectrometer-less optofluidic biosensors based on dielectric metasurfaces for detecting extracellular vesicles,” *Nat. Commun.*, vol. 12, no. 1, Art. no. 1, May 2021, doi: 10.1038/s41467-021-23257-y.

[9] M. Mimee *et al.*, “An ingestible bacterial-electronic system to monitor gastrointestinal health,” *Science*, vol. 360, no. 6391, pp. 915–918, 2018, doi: 10.1126/science.aas9315.

[10] A. Quijano-Rubio *et al.*, “De novo design of modular and tunable protein biosensors,” *Nature*, vol. 591, no. 7850, Art. no. 7850, Mar. 2021, doi: 10.1038/s41586-021-03258-z.

[11] O. Parlak, S. T. Keene, A. Marais, V. F. Curto, and A. Salleo, “Molecularly selective nanoporous membrane-based wearable organic electrochemical device for noninvasive cortisol sensing,” *Sci. Adv.*, vol. 4, no. 7, p. eaar2904, Jul. 2018, doi: 10.1126/sciadv.aar2904.

[12] F. Yesilkoy *et al.*, “Ultrasensitive hyperspectral imaging and biodetection enabled by dielectric metasurfaces,” *Nat. Photonics*, vol. 13, no. 6, Art. no. 6, Jun. 2019, doi: 10.1038/s41566-019-0394-6.

[13] P. Pereira-Silva *et al.*, “Immobilization of Streptavidin on a Plasmonic Au-TiO2 Thin Film towards an LSPR Biosensing Platform,” *Nanomaterials*, vol. 12, no. 9, Art. no. 9, Jan. 2022, doi: 10.3390/nano12091526.

[14] G. Cappi *et al.*, “Label-Free Detection of Tobramycin in Serum by Transmission-Localized Surface Plasmon Resonance,” *Anal. Chem.*, vol. 87, no. 10, pp. 5278–5285, May 2015, doi: 10.1021/acs.analchem.5b00389.

[15] P. Weerathunge *et al.*, “Ultrasensitive Colorimetric Detection of Murine Norovirus Using NanoZyme Aptasensor,” *Anal. Chem.*, vol. 91, no. 5, pp. 3270–3276, Mar. 2019, doi: 10.1021/acs.analchem.8b03300.

[16] R. R. A. Soares *et al.*, “Laser-Induced Graphene Electrochemical Immunosensors for Rapid and Label-Free Monitoring of Salmonella enterica in Chicken Broth,” *ACS Sens.*, vol. 5, no. 7, pp. 1900–1911, Jul. 2020, doi: 10.1021/acssensors.9b02345.

[17] J. K. Jung *et al.*, “Cell-free biosensors for rapid detection of water contaminants,” *Nat. Biotechnol.*, vol. 38, no. 12, Art. no. 12, Dec. 2020, doi: 10.1038/s41587-020-0571-7.

[18] J. A. Hondred *et al.*, “Printed Graphene Electrochemical Biosensors Fabricated by Inkjet Maskless Lithography for Rapid and Sensitive Detection of Organophosphates,” *ACS Appl. Mater. Interfaces*, vol. 10, no. 13, pp. 11125–11134, Apr. 2018, doi: 10.1021/acsami.7b19763.

[19] S. Singh, V. Kumar, D. S. Dhanjal, S. Datta, R. Prasad, and J. Singh, “Biological Biosensors for Monitoring and Diagnosis,” in *Microbial Biotechnology: Basic Research and Applications*, J. Singh, A. Vyas, S. Wang, and R. Prasad, Eds. Singapore: Springer, 2020, pp. 317–335. doi: 10.1007/978-981-15-2817-0_14.

[20] T. Li *et al.*, “Core/Shell Piezoelectric Nanofibers with Spatial Self-Orientated β-Phase Nanocrystals for Real-Time Micropressure Monitoring of Cardiovascular Walls,” *ACS Nano*, vol. 13, no. 9, pp. 10062–10073, Sep. 2019, doi: 10.1021/acsnano.9b02483.

[21] M. Poudineh *et al.*, “A fluorescence sandwich immunoassay for the real-time continuous detection of glucose and insulin in live animals,” *Nat. Biomed. Eng.*, vol. 5, no. 1, Art. no. 1, Jan. 2021, doi: 10.1038/s41551-020-00661-1.

[22] C. Oeser *et al.*, “Epidemiology of Hepatitis E in England and Wales: A 10-Year Retrospective Surveillance Study, 2008–2017,” *J. Infect. Dis.*, vol. 220, no. 5, pp. 802–810, Jul. 2019, doi: 10.1093/infdis/jiz207.

[23] E. M. Glowacki, J. B. Glowacki, A. D. Chung, and G. B. Wilcox, “Reactions to foodborne Escherichia coli outbreaks: A text-mining analysis of the public’s response,” *Am. J. Infect. Control*, vol. 47, no. 10, pp. 1280–1282, Oct. 2019, doi: 10.1016/j.ajic.2019.04.004.

[24] P. Jackson and A. Meah, “Re-assessing vulnerability to foodborne illness: pathways and practices,” *Crit. Public Health*, vol. 28, no. 1, pp. 81–93, Jan. 2018, doi: 10.1080/09581596.2017.1285008.

[25] CDC, “Foodborne Illnesses and Germs,” *Centers for Disease Control and Prevention*, Dec. 19, 2022. https://www.cdc.gov/foodsafety/foodborne-germs.html (accessed Jan. 18, 2023).

[26] A. H. Simonne, “Food safety: bacterial contamination,” in *Reference Module in Food Science*, Elsevier, 2021. doi: 10.1016/B978-0-12-821848-8.00040-8.

[27] R. E. Baker *et al.*, “Infectious disease in an era of global change,” *Nat. Rev. Microbiol.*, vol. 20, no. 4, Art. no. 4, Apr. 2022, doi: 10.1038/s41579-021-00639-z.

[28] “COVID Live - Coronavirus Statistics - Worldometer.” https://www.worldometers.info/coronavirus/ (accessed Jan. 18, 2023).

[29] T. Matsumura *et al.*, “Exosomal microRNA in serum is a novel biomarker of recurrence in human colorectal cancer,” *Br. J. Cancer*, vol. 113, no. 2, Art. no. 2, Jul. 2015, doi: 10.1038/bjc.2015.201.

[30] B. M. Moloney *et al.*, “Investigating the Potential and Pitfalls of EV-Encapsulated MicroRNAs as Circulating Biomarkers of Breast Cancer,” *Cells*, vol. 9, no. 1, Jan. 2020, doi: 10.3390/cells9010141.

[31] B. Bohunicky and S. A. Mousa, “Biosensors: the new wave in cancer diagnosis,” *Nanotechnol. Sci. Appl.*, vol. 4, pp. 1–10, Dec. 2010, doi: 10.2147/NSA.S13465.

[32] I. Keklikoglou *et al.*, “Chemotherapy elicits pro-metastatic extracellular vesicles in breast cancer models,” *Nat. Cell Biol.*, vol. 21, no. 2, pp. 190–202, Feb. 2019, doi: 10.1038/s41556-018-0256-3.

[33] B. Kaur, S. Kumar, and B. K. Kaushik, “Recent advancements in optical biosensors for cancer detection,” *Biosens. Bioelectron.*, vol. 197, p. 113805, Feb. 2022, doi: 10.1016/j.bios.2021.113805.

[34] R. Kalluri and V. S. LeBleu, “The biology, function, and biomedical applications of exosomes,” *Science*, vol. 367, no. 6478, p. eaau6977, Feb. 2020, doi: 10.1126/science.aau6977.

[35] K. W. Witwer and C. Théry, “Extracellular vesicles or exosomes? On primacy, precision, and popularity influencing a choice of nomenclature,” *J. Extracell. Vesicles*, vol. 8, no. 1, p. 1648167, Aug. 2019, doi: 10.1080/20013078.2019.1648167.

[36] D. Huang *et al.*, “Advances in Biological Function and Clinical Application of Small Extracellular Vesicle Membrane Proteins,” *Front. Oncol.*, vol. 11, 2021, Accessed: Dec. 13, 2022. [Online]. Available: https://www.frontiersin.org/articles/10.3389/fonc.2021.675940

[37] F. Urabe, N. Kosaka, K. Ito, T. Kimura, S. Egawa, and T. Ochiya, “Extracellular vesicles as biomarkers and therapeutic targets for cancer,” *Am. J. Physiol.-Cell Physiol.*, vol. 318, no. 1, pp. C29–C39, Jan. 2020, doi: 10.1152/ajpcell.00280.2019.

[38] W. R. Heineman and W. B. Jensen, “Leland C. Clark Jr. (1918–2005),” *Biosens. Bioelectron.*, vol. 21, no. 8, pp. 1403–1404, Feb. 2006, doi: 10.1016/j.bios.2005.12.005.

[39] Y. Zhou, Y. Fang, and R. P. Ramasamy, “Non-Covalent Functionalization of Carbon Nanotubes for Electrochemical Biosensor Development,” *Sensors*, vol. 19, no. 2, Art. no. 2, Jan. 2019, doi: 10.3390/s19020392.

[40] F. Abbasian, E. Ghafar-Zadeh, and S. Magierowski, “Microbiological Sensing Technologies: A Review,” *Bioengineering*, vol. 5, no. 1, Art. no. 1, Mar. 2018, doi: 10.3390/bioengineering5010020.

[41] E. Cesewski and B. N. Johnson, “Electrochemical biosensors for pathogen detection,” *Biosens. Bioelectron.*, vol. 159, p. 112214, Jul. 2020, doi: 10.1016/j.bios.2020.112214.

[42] S. Menon, M. R. Mathew, S. Sam, K. Keerthi, and K. G. Kumar, “Recent advances and challenges in electrochemical biosensors for emerging and re-emerging infectious diseases,” *J. Electroanal. Chem.*, vol. 878, p. 114596, Dec. 2020, doi: 10.1016/j.jelechem.2020.114596.

[43] M. T. Chorsi *et al.*, “Piezoelectric Biomaterials for Sensors and Actuators,” *Adv. Mater.*, vol. 31, no. 1, p. 1802084, 2019, doi: 10.1002/adma.201802084.

[44] H. Altug, S.-H. Oh, S. A. Maier, and J. Homola, “Advances and applications of nanophotonic biosensors,” *Nat. Nanotechnol.*, vol. 17, no. 1, Art. no. 1, Jan. 2022, doi: 10.1038/s41565-021-01045-5.

[45] C. Chen and J. Wang, “Optical biosensors: an exhaustive and comprehensive review,” *Analyst*, vol. 145, no. 5, pp. 1605–1628, Mar. 2020, doi: 10.1039/C9AN01998G.

[46] M. Soler, O. Calvo-Lozano, M.-C. Estevez, and L. M. Lechuga, “Nanophotonic Biosensors: Driving Personalized Medicine,” *Opt. Photonics News*, vol. 31, no. 4, p. 24, Apr. 2020, doi: 10.1364/OPN.31.4.000024.

[47] K. Koshelev and Y. Kivshar, “Dielectric Resonant Metaphotonics,” *ACS Photonics*, vol. 8, no. 1, pp. 102–112, Jan. 2021, doi: 10.1021/acsphotonics.0c01315.

[48] N. Meinzer, W. L. Barnes, and I. R. Hooper, “Plasmonic meta-atoms and metasurfaces,” *Nat. Photonics*, vol. 8, no. 12, Art. no. 12, Dec. 2014, doi: 10.1038/nphoton.2014.247.

[49] F. Monticone and A. Alù, “Metamaterial, plasmonic and nanophotonic devices,” *Rep. Prog. Phys.*, vol. 80, no. 3, p. 036401, Feb. 2017, doi: 10.1088/1361-6633/aa518f.

[50] A. V. Kildishev, A. Boltasseva, and V. M. Shalaev, “Planar Photonics with Metasurfaces,” *Science*, vol. 339, no. 6125, p. 1232009, Mar. 2013, doi: 10.1126/science.1232009.

[51] N. Yu and F. Capasso, “Flat optics with designer metasurfaces,” *Nat. Mater.*, vol. 13, no. 2, Art. no. 2, Feb. 2014, doi: 10.1038/nmat3839.

[52] M. L. Tseng *et al.*, “Metalenses: Advances and Applications,” *Adv. Opt. Mater.*, vol. 6, no. 18, p. 1800554, 2018, doi: 10.1002/adom.201800554.

[53] S. Kruk and Y. Kivshar, “Functional Meta-Optics and Nanophotonics Governed by Mie Resonances,” *ACS Photonics*, vol. 4, no. 11, pp. 2638–2649, Nov. 2017, doi: 10.1021/acsphotonics.7b01038.

[54] S. Colburn, A. Zhan, and A. Majumdar, “Varifocal zoom imaging with large area focal length adjustable metalenses,” *Optica*, vol. 5, no. 7, pp. 825–831, Jul. 2018, doi: 10.1364/OPTICA.5.000825.

[55] D. Wang, W. Wang, M. P. Knudson, G. C. Schatz, and T. W. Odom, “Structural Engineering in Plasmon Nanolasers,” *Chem. Rev.*, vol. 118, no. 6, pp. 2865–2881, Mar. 2018, doi: 10.1021/acs.chemrev.7b00424.

[56] I. Staude, T. Pertsch, and Y. S. Kivshar, “All-Dielectric Resonant Meta-Optics Lightens up,” *ACS Photonics*, vol. 6, no. 4, pp. 802–814, Apr. 2019, doi: 10.1021/acsphotonics.8b01326.

[57] J.-Y. Ou, E. Plum, J. Zhang, and N. I. Zheludev, “An electromechanically reconfigurable plasmonic metamaterial operating in the near-infrared,” *Nat. Nanotechnol.*, vol. 8, no. 4, Art. no. 4, Apr. 2013, doi: 10.1038/nnano.2013.25.

[58] X. Fang, M. Lun Tseng, J.-Y. Ou, K. F. MacDonald, D. Ping Tsai, and N. I. Zheludev, “Ultrafast all-optical switching via coherent modulation of metamaterial absorption,” *Appl. Phys. Lett.*, vol. 104, no. 14, p. 141102, Apr. 2014, doi: 10.1063/1.4870635.

[59] K. Wang *et al.*, “Quantum metasurface for multiphoton interference and state reconstruction,” *Science*, vol. 361, no. 6407, pp. 1104–1108, Sep. 2018, doi: 10.1126/science.aat8196.

[60] L. Li *et al.*, “Metalens-array–based high-dimensional and multiphoton quantum source,” *Science*, vol. 368, no. 6498, pp. 1487–1490, Jun. 2020, doi: 10.1126/science.aba9779.

[61] J. Lee, D.-J. Jeon, and J.-S. Yeo, “Quantum Plasmonics: Energy Transport Through Plasmonic Gap,” *Adv. Mater.*, vol. 33, no. 47, p. 2006606, 2021, doi: 10.1002/adma.202006606.

[62] F. Neubrech, C. Huck, K. Weber, A. Pucci, and H. Giessen, “Surface-Enhanced Infrared Spectroscopy Using Resonant Nanoantennas,” *Chem. Rev.*, vol. 117, no. 7, pp. 5110–5145, Apr. 2017, doi: 10.1021/acs.chemrev.6b00743.

[63] P. Wang, M. E. Nasir, A. V. Krasavin, W. Dickson, Y. Jiang, and A. V. Zayats, “Plasmonic Metamaterials for Nanochemistry and Sensing,” *Acc. Chem. Res.*, vol. 52, no. 11, pp. 3018–3028, Nov. 2019, doi: 10.1021/acs.accounts.9b00325.

[64] N. J. Halas, S. Lal, W.-S. Chang, S. Link, and P. Nordlander, “Plasmons in Strongly Coupled Metallic Nanostructures,” *Chem. Rev.*, vol. 111, no. 6, pp. 3913–3961, Jun. 2011, doi: 10.1021/cr200061k.

[65] C. Wu *et al.*, “Fano-resonant asymmetric metamaterials for ultrasensitive spectroscopy and identification of molecular monolayers,” *Nat. Mater.*, vol. 11, no. 1, Art. no. 1, Jan. 2012, doi: 10.1038/nmat3161.

[66] L. Dong *et al.*, “Nanogapped Au Antennas for Ultrasensitive Surface-Enhanced Infrared Absorption Spectroscopy,” *Nano Lett.*, vol. 17, no. 9, pp. 5768–5774, Sep. 2017, doi: 10.1021/acs.nanolett.7b02736.

[67] D. Rodrigo *et al.*, “Mid-infrared plasmonic biosensing with graphene,” *Science*, vol. 349, no. 6244, pp. 165–168, Jul. 2015, doi: 10.1126/science.aab2051.

[68] D. Rodrigo *et al.*, “Resolving molecule-specific information in dynamic lipid membrane processes with multi-resonant infrared metasurfaces,” *Nat. Commun.*, vol. 9, no. 1, Art. no. 1, Jun. 2018, doi: 10.1038/s41467-018-04594-x.

[69] A. John-Herpin, A. Tittl, and H. Altug, “Quantifying the Limits of Detection of Surface-Enhanced Infrared Spectroscopy with Grating Order-Coupled Nanogap Antennas,” *ACS Photonics*, vol. 5, no. 10, pp. 4117–4124, Oct. 2018, doi: 10.1021/acsphotonics.8b00847.

[70] B. Cerjan and N. J. Halas, “Toward a Nanophotonic Nose: A Compressive Sensing-Enhanced, Optoelectronic Mid-Infrared Spectrometer,” *ACS Photonics*, vol. 6, no. 1, pp. 79–86, Jan. 2019, doi: 10.1021/acsphotonics.8b01503.

[71] S. Gwo *et al.*, “Plasmonic Metasurfaces for Nonlinear Optics and Quantitative SERS,” *ACS Photonics*, vol. 3, no. 8, pp. 1371–1384, Aug. 2016, doi: 10.1021/acsphotonics.6b00104.

[72] J. Lee, J. Park, J.-Y. Lee, and J.-S. Yeo, “Contact Transfer Printing of Side Edge Prefunctionalized Nanoplasmonic Arrays for Flexible microRNA Biosensor,” *Adv. Sci.*, vol. 2, no. 9, p. 1500121, 2015, doi: 10.1002/advs.201500121.

[73] M. L. Brongersma and V. M. Shalaev, “The Case for Plasmonics,” *Science*, vol. 328, no. 5977, pp. 440–441, Apr. 2010, doi: 10.1126/science.1186905.

[74] W. L. Barnes, A. Dereux, and T. W. Ebbesen, “Surface plasmon subwavelength optics,” *Nature*, vol. 424, no. 6950, Art. no. 6950, Aug. 2003, doi: 10.1038/nature01937.

[75] A. D. Boardman and A. V. Zayats, “Chapter 11 - Nonlinear Plasmonics,” in *Handbook of Surface Science*, vol. 4, N. V. Richardson and S. Holloway, Eds. North-Holland, 2014, pp. 329–347. doi: 10.1016/B978-0-444-59526-3.00011-2.

[76] D. R. Smith, J. B. Pendry, and M. C. K. Wiltshire, “Metamaterials and Negative Refractive Index,” *Science*, vol. 305, no. 5685, pp. 788–792, Aug. 2004, doi: 10.1126/science.1096796.

[77] X. Luo, “Subwavelength Optical Engineering with Metasurface Waves,” *Adv. Opt. Mater.*, vol. 6, no. 7, p. 1701201, 2018, doi: 10.1002/adom.201701201.

[78] A. Arbabi and A. Faraon, “Fundamental limits of ultrathin metasurfaces,” *Sci. Rep.*, vol. 7, no. 1, Art. no. 1, Mar. 2017, doi: 10.1038/srep43722.

[79] Y. Zhang, Y.-R. Zhen, O. Neumann, J. K. Day, P. Nordlander, and N. J. Halas, “Coherent anti-Stokes Raman scattering with single-molecule sensitivity using a plasmonic Fano resonance,” *Nat. Commun.*, vol. 5, p. 4424, Jul. 2014, doi: 10.1038/ncomms5424.

[80] B. D. Moore *et al.*, “Rapid and ultra-sensitive determination of enzyme activities using surface-enhanced resonance Raman scattering,” *Nat. Biotechnol.*, vol. 22, no. 9, pp. 1133–1138, Sep. 2004, doi: 10.1038/nbt1003.

[81] D. Punj *et al.*, “A plasmonic ‘antenna-in-box’ platform for enhanced single-molecule analysis at micromolar concentrations,” *Nat. Nanotechnol.*, vol. 8, no. 7, pp. 512–516, Jul. 2013, doi: 10.1038/nnano.2013.98.

[82] V. G. Kravets *et al.*, “Singular phase nano-optics in plasmonic metamaterials for label-free single-molecule detection,” *Nat. Mater.*, vol. 12, no. 4, Art. no. 4, Apr. 2013, doi: 10.1038/nmat3537.

[83] H. Kurt *et al.*, “Nanoplasmonic biosensors: Theory, structure, design, and review of recent applications,” *Anal. Chim. Acta*, vol. 1185, p. 338842, Nov. 2021, doi: 10.1016/j.aca.2021.338842.

[84] M. L. Juan, M. Righini, and R. Quidant, “Plasmon nano-optical tweezers,” *Nat. Photonics*, vol. 5, no. 6, Art. no. 6, Jun. 2011, doi: 10.1038/nphoton.2011.56.

[85] G. A. Lopez, M.-C. Estevez, M. Soler, and L. M. Lechuga, “Recent advances in nanoplasmonic biosensors: applications and lab-on-a-chip integration,” *Nanophotonics*, vol. 6, no. 1, pp. 123–136, Jan. 2017, doi: 10.1515/nanoph-2016-0101.

[86] Z. Wang *et al.*, “Plasmonic Metasurfaces for Medical Diagnosis Applications: A Review,” *Sensors*, vol. 22, no. 1, Art. no. 1, Jan. 2022, doi: 10.3390/s22010133.

[87] S. Jahani and Z. Jacob, “All-dielectric metamaterials,” *Nat. Nanotechnol.*, vol. 11, no. 1, Art. no. 1, Jan. 2016, doi: 10.1038/nnano.2015.304.

[88] A. I. Kuznetsov, A. E. Miroshnichenko, Y. H. Fu, J. Zhang, and B. Luk’yanchuk, “Magnetic light,” *Sci. Rep.*, vol. 2, no. 1, Art. no. 1, Jul. 2012, doi: 10.1038/srep00492.

[89] C. F. Bohren and D. R. Huffman, *Absorption and Scattering of Light by Small Particles*. John Wiley & Sons, 2008.

[90] L. Cao, P. Fan, E. S. Barnard, A. M. Brown, and M. L. Brongersma, “Tuning the Color of Silicon Nanostructures,” *Nano Lett.*, vol. 10, no. 7, pp. 2649–2654, Jul. 2010, doi: 10.1021/nl1013794.

[91] M. Semmlinger *et al.*, “Vacuum Ultraviolet Light-Generating Metasurface,” *Nano Lett.*, vol. 18, no. 9, pp. 5738–5743, Sep. 2018, doi: 10.1021/acs.nanolett.8b02346.

[92] J. C. Ginn *et al.*, “Realizing Optical Magnetism from Dielectric Metamaterials,” *Phys. Rev. Lett.*, vol. 108, no. 9, p. 097402, Feb. 2012, doi: 10.1103/PhysRevLett.108.097402.

[93] M. R. Shcherbakov *et al.*, “Enhanced Third-Harmonic Generation in Silicon Nanoparticles Driven by Magnetic Response,” *Nano Lett.*, vol. 14, no. 11, pp. 6488–6492, Nov. 2014, doi: 10.1021/nl503029j.

[94] J. N. Anker, W. P. Hall, O. Lyandres, N. C. Shah, J. Zhao, and R. P. Van Duyne, “Biosensing with plasmonic nanosensors,” *Nat. Mater.*, vol. 7, no. 6, pp. 442–453, Jun. 2008, doi: 10.1038/nmat2162.

[95] J. Homola, “Surface Plasmon Resonance Sensors for Detection of Chemical and Biological Species,” *Chem. Rev.*, vol. 108, no. 2, pp. 462–493, Feb. 2008, doi: 10.1021/cr068107d.

[96] T. J. Seok *et al.*, “Radiation Engineering of Optical Antennas for Maximum Field Enhancement,” *Nano Lett.*, vol. 11, no. 7, pp. 2606–2610, Jul. 2011, doi: 10.1021/nl2010862.

[97] D. G. Baranov *et al.*, “All-dielectric nanophotonics: the quest for better materials and fabrication techniques,” *Optica*, vol. 4, no. 7, pp. 814–825, Jul. 2017, doi: 10.1364/OPTICA.4.000814.

[98] A. Vázquez-Guardado and D. Chanda, “Superchiral Light Generation on Degenerate Achiral Surfaces,” *Phys. Rev. Lett.*, vol. 120, no. 13, p. 137601, Mar. 2018, doi: 10.1103/PhysRevLett.120.137601.

[99] Y. Yang *et al.*, “Nonlinear Fano-Resonant Dielectric Metasurfaces,” *Nano Lett.*, vol. 15, no. 11, pp. 7388–7393, Nov. 2015, doi: 10.1021/acs.nanolett.5b02802.

[100] P. C. Wu *et al.*, “Optical Anapole Metamaterial,” *ACS Nano*, vol. 12, no. 2, pp. 1920–1927, Feb. 2018, doi: 10.1021/acsnano.7b08828.

[101] A. E. Miroshnichenko *et al.*, “Nonradiating anapole modes in dielectric nanoparticles,” *Nat. Commun.*, vol. 6, no. 1, Art. no. 1, Aug. 2015, doi: 10.1038/ncomms9069.

[102] M. Semmlinger *et al.*, “Generating Third Harmonic Vacuum Ultraviolet Light with a TiO2 Metasurface,” *Nano Lett.*, vol. 19, no. 12, pp. 8972–8978, Dec. 2019, doi: 10.1021/acs.nanolett.9b03961.

[103] K. Koshelev, S. Lepeshov, M. Liu, A. Bogdanov, and Y. Kivshar, “Asymmetric Metasurfaces with High-Q Resonances Governed by Bound States in the Continuum,” *Phys. Rev. Lett.*, vol. 121, no. 19, p. 193903, Nov. 2018, doi: 10.1103/PhysRevLett.121.193903.

[104] Z. Liu *et al.*, “High- Q Quasibound States in the Continuum for Nonlinear Metasurfaces,” *Phys. Rev. Lett.*, vol. 123, no. 25, p. 253901, Dec. 2019, doi: 10.1103/PhysRevLett.123.253901.

[105] K. Koshelev and Y. Kivshar, “Light trapping gets a boost,” *Nature*, vol. 574, no. 7779, pp. 491–492, Oct. 2019, doi: 10.1038/d41586-019-03143-w.

[106] C. W. Hsu, B. Zhen, A. D. Stone, J. D. Joannopoulos, and M. Soljačić, “Bound states in the continuum,” *Nat. Rev. Mater.*, vol. 1, no. 9, p. 16048, Sep. 2016, doi: 10.1038/natrevmats.2016.48.

[107] M. V. Rybin *et al.*, “High- Q Supercavity Modes in Subwavelength Dielectric Resonators,” *Phys. Rev. Lett.*, vol. 119, no. 24, p. 243901, Dec. 2017, doi: 10.1103/PhysRevLett.119.243901.

[108] A. Lovera, B. Gallinet, P. Nordlander, and O. J. F. Martin, “Mechanisms of Fano Resonances in Coupled Plasmonic Systems,” *ACS Nano*, vol. 7, no. 5, pp. 4527–4536, May 2013, doi: 10.1021/nn401175j.

[109] A. Biswas, I. S. Bayer, A. S. Biris, T. Wang, E. Dervishi, and F. Faupel, “Advances in top–down and bottom–up surface nanofabrication: Techniques, applications & future prospects,” *Adv. Colloid Interface Sci.*, vol. 170, no. 1, pp. 2–27, Jan. 2012, doi: 10.1016/j.cis.2011.11.001.

[110] K. Ariga, J. P. Hill, M. V. Lee, A. Vinu, R. Charvet, and S. Acharya, “Challenges and breakthroughs in recent research on self-assembly,” *Sci. Technol. Adv. Mater.*, vol. 9, no. 1, p. 014109, Jan. 2008, doi: 10.1088/1468-6996/9/1/014109.

[111] K. Sakakibara, J. P. Hill, and K. Ariga, “Thin-Film-Based Nanoarchitectures for Soft Matter: Controlled Assemblies into Two-Dimensional Worlds,” *Small*, vol. 7, no. 10, pp. 1288–1308, 2011, doi: 10.1002/smll.201002350.

[112] B. D. Gates, Q. Xu, M. Stewart, D. Ryan, C. G. Willson, and G. M. Whitesides, “New Approaches to Nanofabrication: Molding, Printing, and Other Techniques,” *Chem. Rev.*, vol. 105, no. 4, pp. 1171–1196, Apr. 2005, doi: 10.1021/cr030076o.

[113] J. T. Fourkas, “Nanoscale Photolithography with Visible Light,” *J. Phys. Chem. Lett.*, vol. 1, no. 8, pp. 1221–1227, Apr. 2010, doi: 10.1021/jz1002082.

[114] Y. Ando, K. Miyake, A. Mizuno, A. Korenaga, M. Nakano, and H. Mano, “Fabrication of nanostripe surface structure by multilayer film deposition combined with micropatterning,” *Nanotechnology*, vol. 21, no. 9, p. 095304, Feb. 2010, doi: 10.1088/0957-4484/21/9/095304.

[115] M. Yaman *et al.*, “Arrays of indefinitely long uniform nanowires and nanotubes,” *Nat. Mater.*, vol. 10, no. 7, Art. no. 7, Jul. 2011, doi: 10.1038/nmat3038.

[116] J. A. Liddle and G. M. Gallatin, “Lithography, metrology and nanomanufacturing,” *Nanoscale*, vol. 3, no. 7, pp. 2679–2688, Jul. 2011, doi: 10.1039/C1NR10046G.

[117] V. K. Khanna, “Top-Down Nanofabrication,” in *Integrated Nanoelectronics: Nanoscale CMOS, Post-CMOS and Allied Nanotechnologies*, V. K. Khanna, Ed. New Delhi: Springer India, 2016, pp. 381–396. doi: 10.1007/978-81-322-3625-2_23.

[118] R. S. Rawat, “Dense Plasma Focus - From Alternative Fusion Source to Versatile High Energy Density Plasma Source for Plasma Nanotechnology,” *J. Phys. Conf. Ser.*, vol. 591, no. 1, p. 012021, Mar. 2015, doi: 10.1088/1742-6596/591/1/012021.

[119] M. Oliverio, S. Perotto, G. C. Messina, L. Lovato, and F. De Angelis, “Chemical Functionalization of Plasmonic Surface Biosensors: A Tutorial Review on Issues, Strategies, and Costs,” *ACS Appl. Mater. Interfaces*, vol. 9, no. 35, pp. 29394–29411, Sep. 2017, doi: 10.1021/acsami.7b01583.

[120] O. V. Shynkarenko and S. A. Kravchenko, “Surface Plasmon Resonance Sensors: Methods of Surface Functionalization and Sensitivity Enhancement,” *Theor. Exp. Chem.*, vol. 51, no. 5, pp. 273–293, Nov. 2015.

[121] J.-H. Lee, H.-Y. Cho, H. K. Choi, J.-Y. Lee, and J.-W. Choi, “Application of Gold Nanoparticle to Plasmonic Biosensors,” *Int. J. Mol. Sci.*, vol. 19, no. 7, p. 2021, Jul. 2018, doi: 10.3390/ijms19072021.

[122] Y. Jung, J. Y. Jeong, and B. H. Chung, “Recent advances in immobilization methods of antibodies on solid supports,” *Analyst*, vol. 133, no. 6, pp. 697–701, May 2008, doi: 10.1039/B800014J.

[123] J. R. Nicol, D. Dixon, and J. A. Coulter, “Gold nanoparticle surface functionalization: a necessary requirement in the development of novel nanotherapeutics,” *Nanomed.*, vol. 10, no. 8, pp. 1315–1326, Apr. 2015, doi: 10.2217/nnm.14.219.

[124] T. Bürgi, “Properties of the gold–sulphur interface: from self-assembled monolayers to clusters,” *Nanoscale*, vol. 7, no. 38, pp. 15553–15567, 2015, doi: 10.1039/C5NR03497C.

[125] M. Soler and L. M. Lechuga, “Biochemistry strategies for label-free optical sensor biofunctionalization: advances towards real applicability,” *Anal. Bioanal. Chem.*, vol. 414, no. 18, pp. 5071–5085, Jul. 2022, doi: 10.1007/s00216-021-03751-4.

[126] M. Mousavi and E. Fini, “Silanization Mechanism of Silica Nanoparticles in Bitumen Using 3-Aminopropyl Triethoxysilane (APTES) and 3-Glycidyloxypropyl Trimethoxysilane (GPTMS),” *ACS Sustain. Chem. Eng.*, vol. 8, no. 8, pp. 3231–3240, Mar. 2020, doi: 10.1021/acssuschemeng.9b06741.

[127] V. V. Tsukruk, I. Luzinov, and D. Julthongpiput, “Sticky Molecular Surfaces: Epoxysilane Self-Assembled Monolayers,” *Langmuir*, vol. 15, no. 9, pp. 3029–3032, Apr. 1999, doi: 10.1021/la981632q.

[128] D. R. Shankaran, K. V. Gobi, and N. Miura, “Recent advancements in surface plasmon resonance immunosensors for detection of small molecules of biomedical, food and environmental interest,” *Sens. Actuators B Chem.*, vol. 121, no. 1, pp. 158–177, Jan. 2007, doi: 10.1016/j.snb.2006.09.014.

[129] F. Yesilkoy, “Optical Interrogation Techniques for Nanophotonic Biochemical Sensors,” *Sensors*, vol. 19, no. 19, p. 4287, Oct. 2019, doi: 10.3390/s19194287.

[130] N. Bontempi *et al.*, “Highly sensitive biosensors based on all-dielectric nanoresonators,” *Nanoscale*, vol. 9, no. 15, pp. 4972–4980, 2017, doi: 10.1039/C6NR07904K.

[131] O. Yavas, M. Svedendahl, P. Dobosz, V. Sanz, and R. Quidant, “On-a-chip Biosensing Based on All-Dielectric Nanoresonators,” *Nano Lett.*, vol. 17, no. 7, pp. 4421–4426, Jul. 2017, doi: 10.1021/acs.nanolett.7b01518.

[132] M. E. Stewart *et al.*, “Quantitative multispectral biosensing and 1D imaging using quasi-3D plasmonic crystals,” *Proc. Natl. Acad. Sci.*, vol. 103, no. 46, pp. 17143–17148, Nov. 2006, doi: 10.1073/pnas.0606216103.

[133] X. Li, M. Soler, C. I. Özdemir, A. Belushkin, F. Yesilköy, and H. Altug, “Plasmonic nanohole array biosensor for label-free and real-time analysis of live cell secretion,” *Lab. Chip*, vol. 17, no. 13, pp. 2208–2217, 2017, doi: 10.1039/C7LC00277G.

[134] M. Soler, A. Belushkin, A. Cavallini, C. Kebbi-Beghdadi, G. Greub, and H. Altug, “Multiplexed nanoplasmonic biosensor for one-step simultaneous detection of Chlamydia trachomatis and Neisseria gonorrhoeae in urine,” *Biosens. Bioelectron.*, vol. 94, pp. 560–567, Aug. 2017, doi: 10.1016/j.bios.2017.03.047.

[135] J. A. Ruemmele, W. P. Hall, L. K. Ruvuna, and R. P. Van Duyne, “A Localized Surface Plasmon Resonance Imaging Instrument for Multiplexed Biosensing,” *Anal. Chem.*, vol. 85, no. 9, pp. 4560–4566, May 2013, doi: 10.1021/ac400192f.

[136] H. Yoshikawa, M. Murahashi, M. Saito, S. Jiang, M. Iga, and E. Tamiya, “Parallelized label-free detection of protein interactions using a hyper-spectral imaging system,” *Anal. Methods*, vol. 7, no. 12, pp. 5157–5161, 2015, doi: 10.1039/C5AY00738K.

[137] G. J. Triggs, Y. Wang, C. P. Reardon, M. Fischer, G. J. O. Evans, and T. F. Krauss, “Chirped guided-mode resonance biosensor,” *Optica*, vol. 4, no. 2, p. 229, Feb. 2017, doi: 10.1364/OPTICA.4.000229.

[138] J.-C. Yang, J. Ji, J. M. Hogle, and D. N. Larson, “Multiplexed plasmonic sensing based on small-dimension nanohole arrays and intensity interrogation,” *Biosens. Bioelectron.*, vol. 24, no. 8, pp. 2334–2338, Apr. 2009, doi: 10.1016/j.bios.2008.12.011.

[139] A.-P. Blanchard-Dionne, L. Guyot, S. Patskovsky, R. Gordon, and M. Meunier, “Intensity based surface plasmon resonance sensor using a nanohole rectangular array,” *Opt. Express*, vol. 19, no. 16, p. 15041, Aug. 2011, doi: 10.1364/OE.19.015041.

[140] T.-Y. Chang *et al.*, “Large-scale plasmonic microarrays for label-free high-throughput screening,” *Lab. Chip*, vol. 11, no. 21, pp. 3596–3602, Oct. 2011, doi: 10.1039/C1LC20475K.

[141] L. P. Hackett, A. Ameen, W. Li, F. K. Dar, L. L. Goddard, and G. L. Liu, “Spectrometer-Free Plasmonic Biosensing with Metal–Insulator–Metal Nanocup Arrays,” *ACS Sens.*, vol. 3, no. 2, pp. 290–298, Feb. 2018, doi: 10.1021/acssensors.7b00878.

[142] Y. Jahani and H. Altug, “Towards Ultrasensitive Handheld Imaging-based Optofluidic Biosensors Enabled by All-dielectric Metasurfaces,” in *Frontiers in Optics + Laser Science 2022 (FIO, LS) (2022), paper JW4A.41*, Oct. 2022, p. JW4A.41. doi: 10.1364/FIO.2022.JW4A.41.

[143] F. Zernike, “How I Discovered Phase Contrast,” *Science*, vol. 121, no. 3141, pp. 345–349, Mar. 1955, doi: 10.1126/science.121.3141.345.

[144] N. G. M, “Differential microinterferometer with polarized waves,” *J Phys Radium Paris*, vol. 16, p. 9S, 1955.

[145] E. Wolf, “Solution of the Phase Problem in the Theory of Structure Determination of Crystals from X-Ray Diffraction Experiments,” *Phys. Rev. Lett.*, vol. 103, no. 7, p. 075501, Aug. 2009, doi: 10.1103/PhysRevLett.103.075501.

[146] P. S. Carney, B. Deutsch, A. A. Govyadinov, and R. Hillenbrand, “Phase in Nanooptics,” *ACS Nano*, vol. 6, no. 1, pp. 8–12, Jan. 2012, doi: 10.1021/nn205008y.

[147] A. V. Kabashin and P. I. Nikitin, “Interferometer based on a surface-plasmon resonance for sensor applications,” *Quantum Electron.*, vol. 27, no. 7, p. 653, Jul. 1997, doi: 10.1070/QE1997v027n07ABEH001013.

[148] F. Abelès, “Surface electromagnetic waves ellipsometry,” *Surf. Sci.*, vol. 56, pp. 237–251, Jun. 1976, doi: 10.1016/0039-6028(76)90450-7.

[149] Y. h. Huang, H. p. Ho, S. k. Kong, and A. v. Kabashin, “Phase-sensitive surface plasmon resonance biosensors: methodology, instrumentation and applications,” *Ann. Phys.*, vol. 524, no. 11, pp. 637–662, 2012, doi: 10.1002/andp.201200203.

[150] A. V. Kabashin, S. Patskovsky, and A. N. Grigorenko, “Phase and amplitude sensitivities in surface plasmon resonance bio and chemical sensing,” *Opt. Express*, vol. 17, no. 23, pp. 21191–21204, Nov. 2009, doi: 10.1364/OE.17.021191.

[151] C. Zong *et al.*, “Surface-Enhanced Raman Spectroscopy for Bioanalysis: Reliability and Challenges,” *Chem. Rev.*, vol. 118, no. 10, pp. 4946–4980, May 2018, doi: 10.1021/acs.chemrev.7b00668.

[152] J. A. Dieringer, R. B. Lettan, K. A. Scheidt, and R. P. Van Duyne, “A Frequency Domain Existence Proof of Single-Molecule Surface-Enhanced Raman Spectroscopy,” *J. Am. Chem. Soc.*, vol. 129, no. 51, pp. 16249–16256, Dec. 2007, doi: 10.1021/ja077243c.

[153] P. Mao *et al.*, “Broadband single molecule SERS detection designed by warped optical spaces,” *Nat. Commun.*, vol. 9, no. 1, Art. no. 1, Dec. 2018, doi: 10.1038/s41467-018-07869-5.

[154] M. L. Tseng *et al.*, “Fast Fabrication of a Ag Nanostructure Substrate Using the Femtosecond Laser for Broad-Band and Tunable Plasmonic Enhancement,” *ACS Nano*, vol. 6, no. 6, pp. 5190–5197, Jun. 2012, doi: 10.1021/nn300947n.

[155] S. K. Jha, Z. Ahmed, M. Agio, Y. Ekinci, and J. F. Löffler, “Deep-UV Surface-Enhanced Resonance Raman Scattering of Adenine on Aluminum Nanoparticle Arrays,” *J. Am. Chem. Soc.*, vol. 134, no. 4, pp. 1966–1969, Feb. 2012, doi: 10.1021/ja210446w.

[156] M. F. Cardinal *et al.*, “Expanding applications of SERS through versatile nanomaterials engineering,” *Chem. Soc. Rev.*, vol. 46, no. 13, pp. 3886–3903, Jul. 2017, doi: 10.1039/C7CS00207F.

[157] J. Zhang *et al.*, “Tailoring Alphabetical Metamaterials in Optical Frequency: Plasmonic Coupling, Dispersion, and Sensing,” *ACS Nano*, vol. 8, no. 4, pp. 3796–3806, Apr. 2014, doi: 10.1021/nn500527f.

[158] X. Xu *et al.*, “Flexible Visible–Infrared Metamaterials and Their Applications in Highly Sensitive Chemical and Biological Sensing,” *Nano Lett.*, vol. 11, no. 8, pp. 3232–3238, Aug. 2011, doi: 10.1021/nl2014982.

[159] Y. Lee, S.-J. Kim, H. Park, and B. Lee, “Metamaterials and Metasurfaces for Sensor Applications,” *Sensors*, vol. 17, no. 8, Art. no. 8, Aug. 2017, doi: 10.3390/s17081726.

[160] M. Mahmoudi, S. E. Lohse, C. J. Murphy, A. Fathizadeh, A. Montazeri, and K. S. Suslick, “Variation of Protein Corona Composition of Gold Nanoparticles Following Plasmonic Heating,” *Nano Lett.*, vol. 14, no. 1, pp. 6–12, Jan. 2014, doi: 10.1021/nl403419e.

[161] I. Alessandri and J. R. Lombardi, “Enhanced Raman Scattering with Dielectrics,” *Chem. Rev.*, vol. 116, no. 24, pp. 14921–14981, Dec. 2016, doi: 10.1021/acs.chemrev.6b00365.

[162] Z. Ioffe *et al.*, “Detection of heating in current-carrying molecular junctions by Raman scattering,” *Nat. Nanotechnol.*, vol. 3, no. 12, Art. no. 12, Dec. 2008, doi: 10.1038/nnano.2008.304.

[163] A. Kuhlicke, S. Schietinger, C. Matyssek, K. Busch, and O. Benson, “In Situ Observation of Plasmon Tuning in a Single Gold Nanoparticle during Controlled Melting,” *Nano Lett.*, vol. 13, no. 5, pp. 2041–2046, May 2013, doi: 10.1021/nl400232r.

[164] M. Caldarola *et al.*, “Non-plasmonic nanoantennas for surface enhanced spectroscopies with ultra-low heat conversion,” *Nat. Commun.*, vol. 6, no. 1, p. 7915, Nov. 2015, doi: 10.1038/ncomms8915.

[165] J. Cambiasso, M. König, E. Cortés, S. Schlücker, and S. A. Maier, “Surface-Enhanced Spectroscopies of a Molecular Monolayer in an All-Dielectric Nanoantenna,” *ACS Photonics*, vol. 5, no. 4, pp. 1546–1557, Apr. 2018, doi: 10.1021/acsphotonics.7b01604.

[166] S. Romano *et al.*, “Surface-Enhanced Raman and Fluorescence Spectroscopy with an All-Dielectric Metasurface,” *J. Phys. Chem. C*, vol. 122, no. 34, pp. 19738–19745, Aug. 2018, doi: 10.1021/acs.jpcc.8b03190.

[167] K. E. Sapsford *et al.*, “Functionalizing Nanoparticles with Biological Molecules: Developing Chemistries that Facilitate Nanotechnology,” *Chem. Rev.*, vol. 113, no. 3, pp. 1904–2074, Mar. 2013, doi: 10.1021/cr300143v.

[168] A. Leitis *et al.*, “All-dielectric High-Q Metasurfaces for Infrared Absorption Spectroscopy Applications,” in *2019 Conference on Lasers and Electro-Optics Europe and European Quantum Electronics Conference (2019), paper ch_4_2*, Jun. 2019, p. ch_4_2. Accessed: Jan. 16, 2023. [Online]. Available: https://opg.optica.org/abstract.cfm?uri=CLEO_Europe-2019-ch_4_2

[169] A. Tittl *et al.*, “Imaging-based molecular barcoding with pixelated dielectric metasurfaces,” *Science*, vol. 360, no. 6393, pp. 1105–1109, Jun. 2018, doi: 10.1126/science.aas9768.

[170] A. Leitis *et al.*, “Angle-multiplexed all-dielectric metasurfaces for broadband molecular fingerprint retrieval,” *Sci. Adv.*, vol. 5, no. 5, p. eaaw2871, May 2019, doi: 10.1126/sciadv.aaw2871.

[171] A. Tittl, A. John-Herpin, A. Leitis, E. R. Arvelo, and H. Altug, “Metasurface-Based Molecular Biosensing Aided by Artificial Intelligence,” *Angew. Chem. Int. Ed.*, vol. 58, no. 42, pp. 14810–14822, 2019, doi: 10.1002/anie.201901443.

[172] C. Wu *et al.*, “Spectrally selective chiral silicon metasurfaces based on infrared Fano resonances,” *Nat. Commun.*, vol. 5, no. 1, Art. no. 1, May 2014, doi: 10.1038/ncomms4892.

[173] J. Kumar *et al.*, “Detection of amyloid fibrils in Parkinson’s disease using plasmonic chirality,” *Proc. Natl. Acad. Sci.*, vol. 115, no. 13, pp. 3225–3230, Mar. 2018, doi: 10.1073/pnas.1721690115.

[174] M. Li *et al.*, “Chiral Metallohelical Complexes Enantioselectively Target Amyloid β for Treating Alzheimer’s Disease,” *J. Am. Chem. Soc.*, vol. 136, no. 33, pp. 11655–11663, Aug. 2014, doi: 10.1021/ja502789e.

[175] G. Li, K. DeLaney, and L. Li, “Molecular basis for chirality-regulated Aβ self-assembly and receptor recognition revealed by ion mobility-mass spectrometry,” *Nat. Commun.*, vol. 10, no. 1, Art. no. 1, Nov. 2019, doi: 10.1038/s41467-019-12346-8.

[176] E. Mohammadi, K. L. Tsakmakidis, A. N. Askarpour, P. Dehkhoda, A. Tavakoli, and H. Altug, “Nanophotonic Platforms for Enhanced Chiral Sensing,” *ACS Photonics*, vol. 5, no. 7, pp. 2669–2675, Jul. 2018, doi: 10.1021/acsphotonics.8b00270.

[177] M. Schäferling, D. Dregely, M. Hentschel, and H. Giessen, “Tailoring Enhanced Optical Chirality: Design Principles for Chiral Plasmonic Nanostructures,” *Phys. Rev. X*, vol. 2, no. 3, p. 031010, Aug. 2012, doi: 10.1103/PhysRevX.2.031010.

[178] M. Schäferling, X. Yin, N. Engheta, and H. Giessen, “Helical Plasmonic Nanostructures as Prototypical Chiral Near-Field Sources,” *ACS Photonics*, vol. 1, no. 6, pp. 530–537, Jun. 2014, doi: 10.1021/ph5000743.

[179] M. L. Tseng *et al.*, “Stress-Induced 3D Chiral Fractal Metasurface for Enhanced and Stabilized Broadband Near-Field Optical Chirality,” *Adv. Opt. Mater.*, vol. 7, no. 15, p. 1900617, 2019, doi: 10.1002/adom.201900617.

[180] J. García-Guirado, M. Svedendahl, J. Puigdollers, and R. Quidant, “Enhanced Chiral Sensing with Dielectric Nanoresonators,” *Nano Lett.*, vol. 20, no. 1, pp. 585–591, Jan. 2020, doi: 10.1021/acs.nanolett.9b04334.

[181] E. Mohammadi *et al.*, “Accessible Superchiral Near-Fields Driven by Tailored Electric and Magnetic Resonances in All-Dielectric Nanostructures,” *ACS Photonics*, vol. 6, no. 8, pp. 1939–1946, Aug. 2019, doi: 10.1021/acsphotonics.8b01767.

[182] J. Hu, M. Lawrence, and J. A. Dionne, “High Quality Factor Dielectric Metasurfaces for Ultraviolet Circular Dichroism Spectroscopy,” *ACS Photonics*, vol. 7, no. 1, pp. 36–42, Jan. 2020, doi: 10.1021/acsphotonics.9b01352.

[183] K. Koshelev, Y. Jahani, A. Tittl, H. Altug, and Y. Kivshar, “Enhanced Circular Dichroism and Chiral Sensing with Bound States in the Continuum,” in *Conference on Lasers and Electro-Optics*, San Jose, California, 2019, p. FTh4C.6. doi: 10.1364/CLEO_QELS.2019.FTh4C.6.

[184] O. Yavas, M. Svedendahl, and R. Quidant, “Unravelling the Role of Electric and Magnetic Dipoles in Biosensing with Si Nanoresonators,” *ACS Nano*, vol. 13, no. 4, pp. 4582–4588, Apr. 2019, doi: 10.1021/acsnano.9b00572.

[185] Y. Yang, I. I. Kravchenko, D. P. Briggs, and J. Valentine, “All-dielectric metasurface analogue of electromagnetically induced transparency,” *Nat. Commun.*, vol. 5, no. 1, p. 5753, Dec. 2014, doi: 10.1038/ncomms6753.

[186] F. Capasso, “The future and promise of flat optics: a personal perspective,” *Nanophotonics*, vol. 7, no. 6, pp. 953–957, Jun. 2018, doi: 10.1515/nanoph-2018-0004.

[187] S. Campione *et al.*, “Broken Symmetry Dielectric Resonators for High Quality Factor Fano Metasurfaces,” *ACS Photonics*, vol. 3, no. 12, pp. 2362–2367, Dec. 2016, doi: 10.1021/acsphotonics.6b00556.

[188] M. Liu, D. A. Powell, R. Guo, I. V. Shadrivov, and Y. S. Kivshar, “Polarization-Induced Chirality in Metamaterials via Optomechanical Interaction,” *Adv. Opt. Mater.*, vol. 5, no. 16, p. 1600760, 2017, doi: 10.1002/adom.201600760.

[189] V. R. Tuz *et al.*, “High-quality trapped modes in all-dielectric metamaterials,” *Opt. Express*, vol. 26, no. 3, pp. 2905–2916, Feb. 2018, doi: 10.1364/OE.26.002905.

[190] K. Koshelev, A. Bogdanov, and Y. Kivshar, “Meta-optics and bound states in the continuum,” *Sci. Bull.*, vol. 64, no. 12, pp. 836–842, Jun. 2019, doi: 10.1016/j.scib.2018.12.003.

[191] J. von Neuman and E. Wigner, “Uber merkwürdige diskrete Eigenwerte. Uber das Verhalten von Eigenwerten bei adiabatischen Prozessen,” *Phys. Z.*, vol. 30, pp. 467–470, Jan. 1929.

[192] H. Friedrich and D. Wintgen, “Interfering resonances and bound states in the continuum,” *Phys. Rev. A*, vol. 32, no. 6, pp. 3231–3242, Dec. 1985, doi: 10.1103/PhysRevA.32.3231.

[193] D. C. Marinica, A. G. Borisov, and S. V. Shabanov, “Bound States in the Continuum in Photonics,” *Phys. Rev. Lett.*, vol. 100, no. 18, p. 183902, May 2008, doi: 10.1103/PhysRevLett.100.183902.

[194] E. N. Bulgakov and A. F. Sadreev, “Bound states in the continuum in photonic waveguides inspired by defects,” *Phys. Rev. B*, vol. 78, no. 7, p. 075105, Aug. 2008, doi: 10.1103/PhysRevB.78.075105.

[195] M. Rybin and Y. Kivshar, “Supercavity lasing,” *Nature*, vol. 541, no. 7636, pp. 164–165, Jan. 2017, doi: 10.1038/541164a.

[196] H. M. Doeleman, F. Monticone, W. den Hollander, A. Alù, and A. F. Koenderink, “Experimental observation of a polarization vortex at an optical bound state in the continuum,” *Nat. Photonics*, vol. 12, no. 7, Art. no. 7, Jul. 2018, doi: 10.1038/s41566-018-0177-5.

[197] A. I. Kuznetsov, A. E. Miroshnichenko, M. L. Brongersma, Y. S. Kivshar, and B. Luk’yanchuk, “Optically resonant dielectric nanostructures,” *Science*, vol. 354, no. 6314, p. aag2472, Nov. 2016, doi: 10.1126/science.aag2472.

[198] E. D. Fabrizio *et al.*, “Roadmap on biosensing and photonics with advanced nano-optical methods,” *J. Opt.*, vol. 18, no. 6, p. 063003, May 2016, doi: 10.1088/2040-8978/18/6/063003.

[199] S. H. Lee, N. C. Lindquist, N. J. Wittenberg, L. R. Jordan, and S.-H. Oh, “Real-time full-spectral imaging and affinity measurements from 50 microfluidic channels using nanohole surface plasmon resonance,” *Lab. Chip*, vol. 12, no. 20, pp. 3882–3890, Sep. 2012, doi: 10.1039/C2LC40455A.

[200] Z. S. Ballard, D. Shir, A. Bhardwaj, S. Bazargan, S. Sathianathan, and A. Ozcan, “Computational Sensing Using Low-Cost and Mobile Plasmonic Readers Designed by Machine Learning,” *ACS Nano*, vol. 11, no. 2, pp. 2266–2274, Feb. 2017, doi: 10.1021/acsnano.7b00105.

[201] D. R. Walt, “Optical Methods for Single Molecule Detection and Analysis,” *Anal. Chem.*, vol. 85, no. 3, pp. 1258–1263, Feb. 2013, doi: 10.1021/ac3027178.

[202] A. P. Bradley, “The use of the area under the ROC curve in the evaluation of machine learning algorithms,” *Pattern Recognit.*, vol. 30, no. 7, pp. 1145–1159, Jul. 1997, doi: 10.1016/S0031-3203(96)00142-2.

[203] J. Karst, N. Strohfeldt, M. Schäferling, H. Giessen, and M. Hentschel, “Single Plasmonic Oligomer Chiral Spectroscopy,” *Adv. Opt. Mater.*, vol. 6, no. 14, p. 1800087, 2018, doi: 10.1002/adom.201800087.

[204] A. C. Ferrari and D. M. Basko, “Raman spectroscopy as a versatile tool for studying the properties of graphene,” *Nat. Nanotechnol.*, vol. 8, no. 4, Art. no. 4, Apr. 2013, doi: 10.1038/nnano.2013.46.

[205] Z. H. Ni *et al.*, “Probing Charged Impurities in Suspended Graphene Using Raman Spectroscopy,” *ACS Nano*, vol. 3, no. 3, pp. 569–574, Mar. 2009, doi: 10.1021/nn900130g.

[206] B. G. Ghamsari, J. Tosado, M. Yamamoto, M. S. Fuhrer, and S. M. Anlage, “Measuring the Complex Optical Conductivity of Graphene by Fabry-Pérot Reflectance Spectroscopy,” *Sci. Rep.*, vol. 6, no. 1, Art. no. 1, Sep. 2016, doi: 10.1038/srep34166.

[207] D. F. Ogletree *et al.*, “Revealing Optical Properties of Reduced-Dimensionality Materials at Relevant Length Scales,” *Adv. Mater.*, vol. 27, no. 38, pp. 5693–5719, 2015, doi: 10.1002/adma.201500930.

[208] Y. H. Tan, M. Liu, B. Nolting, J. G. Go, J. Gervay-Hague, and G. Liu, “A Nanoengineering Approach for Investigation and Regulation of Protein Immobilization,” *ACS Nano*, vol. 2, no. 11, pp. 2374–2384, Nov. 2008, doi: 10.1021/nn800508f.

[209] T. L. McMEEKIN, M. L. GROVES, and N. J. HIPP, “Refractive Indices of Amino Acids, Proteins, and Related Substances,” in *Amino Acids and Serum Proteins*, vol. 44, 0 vols., AMERICAN CHEMICAL SOCIETY, 1964, pp. 54–66. doi: 10.1021/ba-1964-0044.ch004.

[210] Z. Ni, Y. Wang, T. Yu, and Z. Shen, “Raman spectroscopy and imaging of graphene,” *Nano Res.*, vol. 1, no. 4, pp. 273–291, Oct. 2008, doi: 10.1007/s12274-008-8036-1.

[211] J.-B. Wu, M.-L. Lin, X. Cong, H.-N. Liu, and P.-H. Tan, “Raman spectroscopy of graphene-based materials and its applications in related devices,” *Chem. Soc. Rev.*, vol. 47, no. 5, pp. 1822–1873, 2018, doi: 10.1039/C6CS00915H.

[212] C. A. K. Borrebaeck, “Precision diagnostics: moving towards protein biomarker signatures of clinical utility in cancer,” *Nat. Rev. Cancer*, vol. 17, no. 3, pp. 199–204, Mar. 2017, doi: 10.1038/nrc.2016.153.

[213] F. V. Paulovich, M. C. F. De Oliveira, and O. N. Oliveira, “A Future with Ubiquitous Sensing and Intelligent Systems,” *ACS Sens.*, vol. 3, no. 8, pp. 1433–1438, Aug. 2018, doi: 10.1021/acssensors.8b00276.

[214] S. A. Walper *et al.*, “Detecting Biothreat Agents: From Current Diagnostics to Developing Sensor Technologies,” *ACS Sens.*, vol. 3, no. 10, pp. 1894–2024, Oct. 2018, doi: 10.1021/acssensors.8b00420.

[215] A. Belushkin *et al.*, “Rapid and Digital Detection of Inflammatory Biomarkers Enabled by a Novel Portable Nanoplasmonic Imager,” *Small*, vol. 16, no. 3, p. 1906108, Jan. 2020, doi: 10.1002/smll.201906108.

[216] B. Spackova, P. Wrobel, M. Bockova, and J. Homola, “Optical Biosensors Based on Plasmonic Nanostructures: A Review,” *Proc. IEEE*, vol. 104, no. 12, pp. 2380–2408, Dec. 2016, doi: 10.1109/JPROC.2016.2624340.

[217] H. Im *et al.*, “Label-free detection and molecular profiling of exosomes with a nano-plasmonic sensor,” *Nat. Biotechnol.*, vol. 32, no. 5, pp. 490–495, May 2014, doi: 10.1038/nbt.2886.

[218] J. Gomez-Cruz, S. Nair, A. Manjarrez-Hernandez, S. Gavilanes-Parra, G. Ascanio, and C. Escobedo, “Cost-effective flow-through nanohole array-based biosensing platform for the label-free detection of uropathogenic E. coli in real time,” *Biosens. Bioelectron.*, vol. 106, pp. 105–110, May 2018, doi: 10.1016/j.bios.2018.01.055.

[219] F. Mazzotta, T. W. Johnson, A. B. Dahlin, J. Shaver, S.-H. Oh, and F. Höök, “Influence of the Evanescent Field Decay Length on the Sensitivity of Plasmonic Nanodisks and Nanoholes,” *ACS Photonics*, vol. 2, no. 2, pp. 256–262, Feb. 2015, doi: 10.1021/ph500360d.

[220] B. Špačková, M. L. Ermini, and J. Homola, “High-performance biosensor exploiting a light guidance in sparse arrays of metal nanoparticles,” *Opt. Lett.*, vol. 44, no. 7, pp. 1568–1571, Apr. 2019, doi: 10.1364/OL.44.001568.

[221] M. Vala, C. T. Ertsgaard, N. J. Wittenberg, and S.-H. Oh, "Plasmonic Sensing on Symmetric Nanohole Arrays Supporting High-Q Hybrid Modes and Reflection Geometry," *ACS Sens.*, vol. 4, no. 12, pp. 3265–3274, Dec. 2019, doi: 10.1021/acssensors.9b01780.

[222] R. Salemmilani, M. Moskovits, and C. D. Meinhart, "Microfluidic analysis of fentanyl-laced heroin samples by surface-enhanced Raman spectroscopy in a hydrophobic medium," *Analyst*, vol. 144, no. 9, pp. 3080–3087, 2019, doi: 10.1039/C9AN00168A.

[223] S.-H. Park, J. Lee, and J.-S. Yeo, "On-chip plasmonic detection of microRNA-106a in gastric cancer using hybridized gold nanoparticles," *Sens. Actuators B Chem.*, vol. 262, pp. 703–709, Jun. 2018, doi: 10.1016/j.snb.2018.02.010.

[224] J. A. Jackman, A. Rahim Ferhan, and N.-J. Cho, "Nanoplasmonic sensors for biointerfacial science," *Chem. Soc. Rev.*, vol. 46, no. 12, pp. 3615–3660, 2017, doi: 10.1039/C6CS00494F.

[225] M. Kaniber *et al.*, "Surface plasmon resonance spectroscopy of single bowtie nano-antennas using a differential reflectivity method," *Sci. Rep.*, vol. 6, no. 1, p. 23203, Mar. 2016, doi: 10.1038/srep23203.

[226] H.-E. Lee *et al.*, "Cysteine-encoded chirality evolution in plasmonic rhombic dodecahedral gold nanoparticles," *Nat. Commun.*, vol. 11, no. 1, p. 263, Jan. 2020, doi: 10.1038/s41467-019-14117-x.

[227] S.-H. Oh and H. Altug, "Performance metrics and enabling technologies for nanoplasmonic biosensors," *Nat. Commun.*, vol. 9, no. 1, Art. no. 1, Dec. 2018, doi: 10.1038/s41467-018-06419-3.

[228] S. V. Boriskina *et al.*, "Losses in plasmonics: from mitigating energy dissipation to embracing loss-enabled functionalities," *Adv. Opt. Photonics*, vol. 9, no. 4, p. 775, Dec. 2017, doi: 10.1364/AOP.9.000775.

[229] B. Doiron *et al.*, "Quantifying Figures of Merit for Localized Surface Plasmon Resonance Applications: A Materials Survey," *ACS Photonics*, vol. 6, no. 2, pp. 240–259, Feb. 2019, doi: 10.1021/acsphotonics.8b01369.

[230] A. Krasnok, M. Caldarola, N. Bonod, and A. Alú, "Spectroscopy and Biosensing with Optically Resonant Dielectric Nanostructures," *Adv. Opt. Mater.*, vol. 6, no. 5, p. 1701094, Mar. 2018, doi: 10.1002/adom.201701094.

[231] J. van de Groep and M. L. Brongersma, "Metasurface Mirrors for External Control of Mie Resonances," *Nano Lett.*, vol. 18, no. 6, pp. 3857–3864, Jun. 2018, doi: 10.1021/acs.nanolett.8b01148.

[232] A. F. Koenderink, A. Alù, and A. Polman, "Nanophotonics: Shrinking light-based technology," *Science*, vol. 348, no. 6234, p. 516, May 2015, doi: 10.1126/science.1261243.

[233] J. Rho, "Metasurfaces: Subwavelength nanostructure arrays for ultrathin flat optics and photonics," *MRS Bull.*, vol. 45, no. 3, pp. 180–187, 2020, doi: 10.1557/mrs.2020.68.

[234] P. Genevet, F. Capasso, F. Aieta, M. Khorasaninejad, and R. Devlin, "Recent advances in planar optics: from plasmonic to dielectric metasurfaces," *Optica*, vol. 4, no. 1, pp. 139–152, Jan. 2017, doi: 10.1364/OPTICA.4.000139.

[235] Y. Zhou, I. I. Kravchenko, H. Wang, J. R. Nolen, G. Gu, and J. Valentine, "Multilayer Noninteracting Dielectric Metasurfaces for Multiwavelength Metaoptics," *Nano Lett.*, vol. 18, no. 12, pp. 7529–7537, Dec. 2018, doi: 10.1021/acs.nanolett.8b03017.

[236] B. Gholipour, D. Piccinotti, A. Karvounis, K. F. MacDonald, and N. I. Zheludev, "Reconfigurable Ultraviolet and High-Energy Visible Dielectric Metamaterials," *Nano Lett.*, vol. 19, no. 3, pp. 1643–1648, Mar. 2019, doi: 10.1021/acs.nanolett.8b04576.

[237] A. E. Cetin *et al.*, "Handheld high-throughput plasmonic biosensor using computational on-chip imaging," *Light Sci. Appl.*, vol. 3, no. 1, Art. no. 1, Jan. 2014, doi: 10.1038/lsa.2014.3.

[238] H. Zhu, S. Mavandadi, A. F. Coskun, O. Yaglidere, and A. Ozcan, "Optofluidic Fluorescent Imaging Cytometry on a Cell Phone," *Anal. Chem.*, vol. 83, no. 17, pp. 6641–6647, Sep. 2011, doi: 10.1021/ac201587a.

[239] E. Chiodi *et al.*, "Highly Multiplexed Label-Free Imaging Sensor for Accurate Quantification of Small-Molecule Binding Kinetics," *ACS Omega*, vol. 5, no. 39, pp. 25358–25364, Oct. 2020, doi: 10.1021/acsomega.0c03708.

[240] N. Kosaka *et al.*, “Exploiting the message from cancer: the diagnostic value of extracellular vesicles for clinical applications,” *Exp. Mol. Med.*, vol. 51, no. 3, pp. 1–9, Mar. 2019, doi: 10.1038/s12276-019-0219-1.

[241] L. Sortino *et al.*, “Enhanced light-matter interaction in an atomically thin semiconductor coupled with dielectric nano-antennas,” *Nat. Commun.*, vol. 10, no. 1, p. 5119, Nov. 2019, doi: 10.1038/s41467-019-12963-3.

[242] X. Luo, D. Tsai, M. Gu, and M. Hong, “Extraordinary optical fields in nanostructures: from sub-diffraction-limited optics to sensing and energy conversion,” *Chem. Soc. Rev.*, vol. 48, no. 8, pp. 2458–2494, 2019, doi: 10.1039/C8CS00864G.

[243] R. W. Ziolkowski and N. Engheta, “Metamaterials: Two Decades Past and Into Their Electromagnetics Future and Beyond,” *IEEE Trans. Antennas Propag.*, vol. 68, no. 3, pp. 1232–1237, Mar. 2020, doi: 10.1109/TAP.2019.2938674.

[244] M. Rippa *et al.*, “Octupolar Plasmonic Nanosensor Based on Ordered Arrays of Triangular Au Nanopillars for Selective Rotavirus Detection,” *ACS Appl. Nano Mater.*, Apr. 2020, doi: 10.1021/acsanm.0c00872.

[245] J. A. Jackman *et al.*, “Plasmonic Nanohole Sensor for Capturing Single Virus-Like Particles toward Virucidal Drug Evaluation,” *Small*, vol. 12, no. 9, pp. 1159–1166, Mar. 2016, doi: 10.1002/smll.201501914.

[246] M. Nič, J. Jirát, B. Košata, A. Jenkins, and A. McNaught, Eds., *IUPAC Compendium of Chemical Terminology: Gold Book*, 2.1.0. Research Triagle Park, NC: IUPAC, 2009. doi: 10.1351/goldbook.

[247] M. Mathieu, L. Martin-Jaular, G. Lavieu, and C. Théry, “Specificities of secretion and uptake of exosomes and other extracellular vesicles for cell-to-cell communication,” *Nat. Cell Biol.*, vol. 21, no. 1, pp. 9–17, Jan. 2019, doi: 10.1038/s41556-018-0250-9.

[248] P. Zhang *et al.*, “Ultrasensitive detection of circulating exosomes with a 3D-nanopatterned microfluidic chip,” *Nat. Biomed. Eng.*, vol. 3, no. 6, Art. no. 6, Jun. 2019, doi: 10.1038/s41551-019-0356-9.

[249] Z. Andreu and M. Yáñez-Mó, “Tetraspanins in Extracellular Vesicle Formation and Function,” *Front. Immunol.*, vol. 5, p. 442, 2014, doi: 10.3389/fimmu.2014.00442.

[250] O. Galindo-Hernandez *et al.*, “Elevated Concentration of Microvesicles Isolated from Peripheral Blood in Breast Cancer Patients,” *Arch. Med. Res.*, vol. 44, no. 3, pp. 208–214, Apr. 2013, doi: 10.1016/j.arcmed.2013.03.002.

[251] K. B. Johnsen, J. M. Gudbergsson, T. L. Andresen, and J. B. Simonsen, “What is the blood concentration of extracellular vesicles? Implications for the use of extracellular vesicles as blood-borne biomarkers of cancer,” *Biochim. Biophys. Acta BBA - Rev. Cancer*, vol. 1871, no. 1, pp. 109–116, Jan. 2019, doi: 10.1016/j.bbcan.2018.11.006.

[252] A. Barth, “Infrared spectroscopy of proteins,” *Biochim. Biophys. Acta BBA - Bioenerg.*, vol. 1767, no. 9, pp. 1073–1101, Sep. 2007, doi: 10.1016/j.bbabio.2007.06.004.

[253] A. P. Demchenko, *Ultraviolet Spectroscopy of Proteins*. Springer Science & Business Media, 2013.

[254] A. Moreau, C. Ciracì, and D. R. Smith, “Impact of nonlocal response on metallodielectric multilayers and optical patch antennas,” *Phys. Rev. B*, vol. 87, no. 4, p. 045401, Jan. 2013, doi: 10.1103/PhysRevB.87.045401.

[255] A. Barreda *et al.*, “The impact of loss on high-Q resonant metasurfaces: A case study for heated a-Si:H,” *J. Quant. Spectrosc. Radiat. Transf.*, vol. 292, p. 108348, Dec. 2022, doi: 10.1016/j.jqsrt.2022.108348.

[256] M. L. Gorodetsky and V. S. Ilchenko, “Optical microsphere resonators: optimal coupling to high-Q whispering-gallery modes,” *JOSA B*, vol. 16, no. 1, pp. 147–154, Jan. 1999, doi: 10.1364/JOSAB.16.000147.

[257] Y. Xu, Y. Li, R. K. Lee, and A. Yariv, “Scattering-theory analysis of waveguide-resonator coupling,” *Phys. Rev. E*, vol. 62, no. 5, pp. 7389–7404, Nov. 2000, doi: 10.1103/PhysRevE.62.7389.

[258] A. Yariv, “Critical coupling and its control in optical waveguide-ring resonator systems,” *IEEE Photonics Technol. Lett.*, vol. 14, no. 4, pp. 483–485, Apr. 2002, doi: 10.1109/68.992585.

[259] D. Conteduca, G. S. Arruda, I. Barth, Y. Wang, T. F. Krauss, and E. R. Martins, “Beyond Q: The Importance of the Resonance Amplitude for Photonic Sensors,” *ACS Photonics*, Apr. 2022, doi: 10.1021/acsphotonics.2c00188.

[260] J. Kühne, J. Wang, T. Weber, L. Kühner, S. A. Maier, and A. Tittl, “Fabrication robustness in BIC metasurfaces,” *Nanophotonics*, vol. 10, no. 17, pp. 4305–4312, Dec. 2021, doi: 10.1515/nanoph-2021-0391.

[261] A. Arbabi, Y. Horie, M. Bagheri, and A. Faraon, “Dielectric metasurfaces for complete control of phase and polarization with subwavelength spatial resolution and high transmission,” *Nat. Nanotechnol.*, vol. 10, no. 11, Art. no. 11, Nov. 2015, doi: 10.1038/nnano.2015.186.

[262] O. Mitrofanov *et al.*, “Perfectly absorbing dielectric metasurfaces for photodetection,” *APL Photonics*, vol. 5, no. 10, p. 101304, Oct. 2020, doi: 10.1063/5.0019883.

[263] A. C. Overvig *et al.*, “Dielectric metasurfaces for complete and independent control of the optical amplitude and phase,” *Light Sci. Appl.*, vol. 8, no. 1, Art. no. 1, Oct. 2019, doi: 10.1038/s41377-019-0201-7.

[264] I. Staude and J. Schilling, “Metamaterial-inspired silicon nanophotonics,” *Nat. Photonics*, vol. 11, no. 5, Art. no. 5, May 2017, doi: 10.1038/nphoton.2017.39.

[265] S. M. Kamali, E. Arbabi, A. Arbabi, and A. Faraon, “A review of dielectric optical metasurfaces for wavefront control,” *Nanophotonics*, vol. 7, no. 6, pp. 1041–1068, Jun. 2018, doi: 10.1515/nanoph-2017-0129.

[266] H. Altug and J. Vučković, “Polarization control and sensing with two-dimensional coupled photonic crystal microcavity arrays,” *Opt. Lett.*, vol. 30, no. 9, pp. 982–984, May 2005, doi: 10.1364/OL.30.000982.

[267] M. Huang, A. A. Yanik, T.-Y. Chang, and H. Altug, “Sub-wavelength nanofluidics in photonic crystal sensors,” *Opt. Express*, vol. 17, no. 26, pp. 24224–24233, Dec. 2009, doi: 10.1364/OE.17.024224.

[268] K. A. Tetz, L. Pang, and Y. Fainman, “High-resolution surface plasmon resonance sensor based on linewidth-optimized nanohole array transmittance,” *Opt. Lett.*, vol. 31, no. 10, pp. 1528–1530, May 2006, doi: 10.1364/OL.31.001528.

[269] T. Das Gupta *et al.*, “Self-assembly of nanostructured glass metasurfaces via templated fluid instabilities,” *Nat. Nanotechnol.*, vol. 14, no. 4, Art. no. 4, Apr. 2019, doi: 10.1038/s41565-019-0362-9.

[270] D. Chanda *et al.*, “Large-area flexible 3D optical negative index metamaterial formed by nanotransfer printing,” *Nat. Nanotechnol.*, vol. 6, no. 7, Art. no. 7, Jul. 2011, doi: 10.1038/nnano.2011.82.

[271] M. l. Tseng *et al.*, “Fabrication of multilayer metamaterials by femtosecond laser-induced forward-transfer technique,” *Laser Photonics Rev.*, vol. 6, no. 5, pp. 702–707, 2012, doi: 10.1002/lpor.201200029.

[272] J. K. Gansel *et al.*, “Gold Helix Photonic Metamaterial as Broadband Circular Polarizer,” *Science*, vol. 325, no. 5947, pp. 1513–1515, Sep. 2009, doi: 10.1126/science.1177031.

[273] S. Cataldo *et al.*, “Hole-Mask Colloidal Nanolithography for Large-Area Low-Cost Metamaterials and Antenna-Assisted Surface-Enhanced Infrared Absorption Substrates,” *ACS Nano*, vol. 6, no. 1, pp. 979–985, Jan. 2012, doi: 10.1021/nn2047982.

[274] L. Yuan *et al.*, “Photocatalytic Hydrogenation of Graphene Using Pd Nanocones,” *Nano Lett.*, vol. 19, no. 7, pp. 4413–4419, Jul. 2019, doi: 10.1021/acs.nanolett.9b01121.

[275] C. Zhang *et al.*, “Al–Pd Nanodisk Heterodimers as Antenna–Reactor Photocatalysts,” *Nano Lett.*, vol. 16, no. 10, pp. 6677–6682, Oct. 2016, doi: 10.1021/acs.nanolett.6b03582.

[276] D. O. Sigle, E. Perkins, J. J. Baumberg, and S. Mahajan, “Reproducible Deep-UV SERRS on Aluminum Nanovoids,” *J. Phys. Chem. Lett.*, vol. 4, no. 9, pp. 1449–1452, May 2013, doi: 10.1021/jz4004813.

[277] M. Meyring *et al.*, “In Vitro Biotransformation of (R)- and (S)-Thalidomide: Application of Circular Dichroism Spectroscopy to the Stereochemical Characterization of the Hydroxylated Metabolites,” *Anal. Chem.*, vol. 74, no. 15, pp. 3726–3735, Aug. 2002, doi: 10.1021/ac0203138.

[278] H. N. S. Krishnamoorthy, G. Adamo, J. Yin, V. Savinov, N. I. Zheludev, and C. Soci, “Infrared dielectric metamaterials from high refractive index chalcogenides,” *Nat. Commun.*, vol. 11, no. 1, Art. no. 1, Apr. 2020, doi: 10.1038/s41467-020-15444-0.

[279] R. Verre, D. G. Baranov, B. Munkhbat, J. Cuadra, M. Käll, and T. Shegai, "Transition metal dichalcogenide nanodisks as high-index dielectric Mie nanoresonators," *Nat. Nanotechnol.*, vol. 14, no. 7, Art. no. 7, Jul. 2019, doi: 10.1038/s41565-019-0442-x.

[280] P. C. Wu *et al.*, "Dynamic beam steering with all-dielectric electro-optic III–V multiple-quantum-well metasurfaces," *Nat. Commun.*, vol. 10, no. 1, Art. no. 1, Aug. 2019, doi: 10.1038/s41467-019-11598-8.

[281] K.-C. Shen *et al.*, "Giant Efficiency of Visible Second-Harmonic Light by an All-Dielectric Multiple-Quantum-Well Metasurface," *Phys. Rev. Appl.*, vol. 12, no. 6, p. 064056, Dec. 2019, doi: 10.1103/PhysRevApplied.12.064056.

[282] A. Leitis *et al.*, "All-Dielectric Programmable Huygens' Metasurfaces," *Adv. Funct. Mater.*, vol. 30, no. 19, p. 1910259, 2020, doi: 10.1002/adfm.201910259.

[283] C. H. Chu *et al.*, "Active dielectric metasurface based on phase-change medium," *Laser Photonics Rev.*, vol. 10, no. 6, pp. 986–994, 2016, doi: 10.1002/lpor.201600106.

[284] B. Gholipour *et al.*, "Organometallic Perovskite Metasurfaces," *Adv. Mater.*, vol. 29, no. 9, p. 1604268, 2017, doi: 10.1002/adma.201604268.

[285] Y. Gao *et al.*, "Lead Halide Perovskite Nanostructures for Dynamic Color Display," *ACS Nano*, vol. 12, no. 9, pp. 8847–8854, Sep. 2018, doi: 10.1021/acsnano.8b02425.

[286] M. Soler, M. C. Estevez, M. Cardenosa-Rubio, A. Astua, and L. M. Lechuga, "How Nanophotonic Label-Free Biosensors Can Contribute to Rapid and Massive Diagnostics of Respiratory Virus Infections: COVID-19 Case," *ACS Sens.*, vol. 5, no. 9, pp. 2663–2678, Sep. 2020, doi: 10.1021/acssensors.0c01180.

[287] T. Yang, Y.-C. Wang, C.-F. Shen, and C.-M. Cheng, "Point-of-Care RNA-Based Diagnostic Device for COVID-19," *Diagnostics*, vol. 10, no. 3, Art. no. 3, Mar. 2020, doi: 10.3390/diagnostics10030165.

[288] L. Hong, H. Li, H. Yang, and K. Sengupta, "Integrated Angle-Insensitive Nanoplasmonic Filters for Ultraminiaturized Fluorescence Microarray in a 65 nm Digital CMOS Process," *ACS Photonics*, vol. 5, no. 11, pp. 4312–4322, Nov. 2018, doi: 10.1021/acsphotonics.8b00440.

[289] C. Chen *et al.*, "High spatial resolution nanoslit SERS for single-molecule nucleobase sensing," *Nat. Commun.*, vol. 9, no. 1, Art. no. 1, Apr. 2018, doi: 10.1038/s41467-018-04118-7.

[290] M. L. Tseng, J. Yang, M. Semmlinger, C. Zhang, P. Nordlander, and N. J. Halas, "Two-Dimensional Active Tuning of an Aluminum Plasmonic Array for Full-Spectrum Response," *Nano Lett.*, vol. 17, no. 10, pp. 6034–6039, Oct. 2017, doi: 10.1021/acs.nanolett.7b02350.

[291] N. I. Zheludev and Y. S. Kivshar, "From metamaterials to metadevices," *Nat. Mater.*, vol. 11, no. 11, Art. no. 11, Nov. 2012, doi: 10.1038/nmat3431.

[292] I. Malkiel, M. Mrejen, A. Nagler, U. Arieli, L. Wolf, and H. Suchowski, "Plasmonic nanostructure design and characterization via Deep Learning," *Light Sci. Appl.*, vol. 7, no. 1, Art. no. 1, Sep. 2018, doi: 10.1038/s41377-018-0060-7.

[293] Z. Liu, D. Zhu, S. P. Rodrigues, K.-T. Lee, and W. Cai, "Generative Model for the Inverse Design of Metasurfaces," *Nano Lett.*, vol. 18, no. 10, pp. 6570–6576, Oct. 2018, doi: 10.1021/acs.nanolett.8b03171.

Curriculum Vitae

Contact

EMAIL: YASI.JAHANI92@GMAIL.COM

LINKEDIN: LINKEDIN.COM/IN/YASAMAN-JAHANI/

Education

SWISS FEDERAL INSTITUTE OF TECHNOLOGY OF LAUSANNE (*EPFL*)
PH.D. IN MICROSYSTEMS AND MICROELECTRONICS: BIONANOPHOTONIC SYSTEMS LABORATORY (BIOS)
Lausanne, Switzerland
NOV. 2017 – PRESENT

Swiss Federal Institute of Technology of Lausanne (*EPFL*)
MASTER THESIS: ALL-DIELECTRIC METAMATERIALS FOR BIOSENSING
Lausanne, Switzerland
Sep. 2016 – Sep. 2017

Politecnico di Milano
M.SC. IN MATERIAL ENGINEERING AND NANOTECHNOLOGY
Milan, Italy
SEP. 2014 – SEP. 2017

Amirkabir University of Technology
B.SC. IN MECHANICAL ENGINEERING
Tehran, Iran
SEP 2010 – JUL 2014

Core Experience

BIOnanophotonic Systems Laboratory, EPFL
FULL-TIME RESEARCHER
Lausanne, Switzerland
NOV. 2017 – PRESENT

Optical sensors: Design, fabrication, characterization of silicon-based metasurfaces and their implementation for detecting cancer-related biomarkers
Surface biofunctionalization,
Building a real-time imaging-based diagnostic platform (Optical setup and Microfluidics)
Training, on-boarding, mentoring and supervising lab members
Scientific writing and science communication
Project management, Teamwork, Intercultural team

Center of MicroNanoTechnology, EPFL
FULL-TIME RESEARCHER
Lausanne, Switzerland
Sep. 2016 – Sep. 2017

Process flow development
Electron-beam lithography, Photo-lithography
Thin film deposition (Evaporation, Sputtering, ALD, PECVD) (also at IBM Zurich cleanroom),
Wet etching (Acid/Base), Dry etching (DRIE, IBE, Plasma)
Metrology (SEM, AFM, ellipsometry, Profilometry)
Packaging (PDMS line)

PROFESSIONAL EXPERTISE

Programming:
MATLAB, Python, C++, Pascal, Visual Basic

Simulation Tools:
CST Studio, COMSOL

Graphical and 2D and 3D design:
Adobe Illustrator, Blender, Luxrender,

CleWin4, L-edit, Inventor, Solidworks

Typesettings:
Microsoft office

Experimental Safety Certifications
Laser operation, Acid/Base handling

Soft Skills:
Fast learner, Coordinator, Passionate, Openminded,

Team Player and Supportive

ADDITIONAL EXPERIENCES

EPFL Photonics Chapter (EPC)
Lausanne, Switzerland
Feb. 2020 – Present
President (2021) and member
EPFL association for optics and photonics, supported by OPTICA (formerly OSA) and SPIE leading professional societies for optics and photonics technology, Keeping the chapter active and the members safe during the extraordinary times of COVID with creative academic and social activities, Teamwork

EPFL Teaching
Lausanne, Switzerland
Feb. 2018 – Sep. 2020
Teaching Assistant
Biomicroscopy I, Biomicroscopy II, Optics experimental laboratory
(Nanoparticles and gold nanohole array modules)
teaching, assisting in the conduct of experiment and report writing

Ofogh Journal of Amirkabir University of Technology
Tehran, Iran
Sep. 2012 – Sep. 2013
Editor and Responsible for public relations
Ofogh was a peer-reviewed journal of mechanical engineering in Persian.
It is currently known as the Amirkabir Journal of Mechanical Engineering

AUT CUP Broadcasting Group
Tehran, Iran
Team Leader *Nov. 2012*
AUT CUP is Amirkabir Robotic and Artificial Intelligence 5-day competition.

PUBLICATIONS

Towards Ultrasensitive Handheld Imaging-based Optofluidic Biosensors Enabled by All-dielectric Metasurfaces
Frontiers in Optics
2022

Yasaman Jahani, Hatice Altug

All-dielectric Metasurfaces Enabling Imaging-based Real-time Biosensing
European Quantum Electronics Conference
2021

Yasaman Jahani, Eduardo R Arvelo, Filiz Yesilkoy, Kirill Koshelev, Chiara Cianciaruso, Michele De Palma, Yuri Kivshar, Hatice Altug

Imaging-based spectrometer-less optofluidic biosensors based on dielectric metasurfaces for detecting extracellular vesicles
Nature Communications
2021

Yasaman Jahani, Eduardo R Arvelo, Filiz Yesilkoy, Kirill Koshelev, Chiara Cianciaruso, Michele De Palma, Yuri Kivshar, Hatice Altug

Imaging-based Optofluidic Biosensors Enabled by All-dielectric metasurfaces
CLEO: Science and Innovations
2021

Yasaman Jahani, Eduardo R Arvelo, Filiz Yesilkoy, Kirill Koshelev, Chiara Cianciaruso, Michele De Palma, Yuri Kivshar, Hatice Altug

Membrane activity detection in cultured cells using phase-sensitive plasmonics

Optics Express
2020

Foozieh Sohrabi, **Yasaman Jahani**, Jose Vicente Sanchez-Mut, Ershad Mohammadi, Zahra Barzegar, Xiaokang Li, Liliane Glauser, Johannes Gräff, Seyedeh Mehri Hamidi

Dielectric metasurfaces enabling advanced optical biosensors

ACS Photonics
2020

Ming Lun Tseng, **Yasaman Jahani**, Aleksandrs Leitis, Hatice Altug

Blue-shift ultrasensitivity using rhombus-shaped plasmonic crystal on Si_3N_4 membrane

Optical Materials Express
2020

Foozieh Sohrabi, Dordaneh Etezadi, **Yasaman Jahani**, Ershad Mohammadi, Bahareh Ghadiani, Mahdi Tamizifar, Seyedeh Mehri Hamidi

Phase-sensitive optical neural recording of cerebellum tissue on a flexible interface

Journal of Applied Physics
2020

Foozieh Sohrabi, Dordaneh Etezadi, Rodrigo Perin, **Yasaman Jahani**, Ershad Mohammadi, Seyedeh Mehri Hamidi

Lens-Free Interferometric Microscope for Point-of-Care Label-Free Detection of Sepsis Biomarkers

Frontiers in Optics
2019

Roland A Terborg, Luc Duempelmann, Josselin Pello, Alican Noyan, Filiz Yesilkoy, Alexander A Belushkin, **Yasaman Jahani**, Nuria Fabri-Faja, Priyanka Dey, Olalla Calvo-Lozano, M-Carmen Estevez, Anna Fàbrega, Juan J González-López, Laura M Lechuga, Hatice Altug, Valerio Pruneri

Accessible superchiral near-fields driven by tailored electric and magnetic resonances in all-dielectric nanostructures

ACS Photonics
2019

Ershad Mohammadi, Ahad Tavakoli, Parisa Dehkhoda, **Yasaman Jahani**, Kosmas L Tsakmakidis, Andreas Tittl, Hatice Altug

Nanophotonic biosensors: From plasmonic to dielectric metasurfaces

Optical Sensors
2019

Filiz Yesilkoy, Eduardo R Arvelo, **Yasaman Jahani**, Alexander Belushkin, Mingkai Liu, Andreas Tittl, Yuri Kivshar, Hatice Altug

Ultrasensitive hyperspectral imaging and biodetection enabled by dielectric metasurfaces

Nature Photonics
2019

Filiz Yesilkoy, Eduardo R Arvelo, **Yasaman Jahani**, Mingkai Liu, Andreas Tittl, Volkan Cevher, Yuri Kivshar, Hatice Altug

Enhanced circular dichroism and chiral sensing with bound states in the continuum

CLEO: QELS Fundamental Science
2019

Kirill Koshelev, **Yasaman Jahani**, Andreas Tittl, Hatice Altug, Yuri Kivshar

Integrated Nanophotonic Biosensors for Point-of Care Diagnostics and Bioanalytical Applications

Optical Fiber Communication Conference
2019

Filiz Yesilkoy, Alexander Belushkin, **Yasaman Jahani**, Roland Terborg, Xiaokang Li, Valerio Pruneri, Hatice Altug

Photonic metasurfaces for next-generation biosensors

Integrated Photonics Research, Silicon and Nanophotonics
2019

Hatice Altug, Filiz Yesilkoy, Xiaokang Li, Maria Soler, Alexander Belushkin, **Yasaman Jahani**, Roland Terborg, Josselin Pello, Valerio Pruneri

Phase-sensitive plasmonic biosensor using a portable and large field-of-view interferometric microarray imager

Light: Science & Applications
2018

Filiz Yesilkoy, Roland A Terborg, Josselin Pello, Alexander A Belushkin, **Yasaman Jahani**, Valerio Pruneri, Hatice Altug